STATE OF CALIFORNIA • DEPARTMENT OF TRANSPORTATION

TECHNICAL REPORT DOCUMENTATION PAGE

TR-0003 (REV 04/2024)

1. REPORT NUMBER	2. GOVERNMENT ASSOCIATION NUMBER	3. RECIPIENT'S CATALOG NUMBER
CA 24-3674		

4. TITLE AND SUBTITLE	5. REPORT DATE
Analysis of Lateral Spreading Effects on Bridge Foundations	April 2024
	6. PERFORMING ORGANIZATION CODE

7. AUTHOR	8. PERFORMING ORGANIZATION REPORT NO.
Zhijian Qiu, Jinchi Lu, Ahmed Ebeido, Athul Parayancode, Axel Arnold Yarahuaman Chamorro, Ahmed Elgamal, Geoffrey R. Martin and John S. McCartney	SSRP-24/05

9. PERFORMING ORGANIZATION NAME AND ADDRESS	10. WORK UNIT NUMBER
Department of Structural Engineering School of Engineering University of California, San Diego La Jolla, California 92093-0085	11. CONTRACT OR GRANT NUMBER 65A0786

12. SPONSORING AGENCY AND ADDRESS	13. TYPE OF REPORT AND PERIOD COVERED
California Department of Transportation Division of Engineering Services 1801 30th St., MS-9-2/5i Sacramento, California 95816	Final Report (2019-2022) 14. SPONSORING AGENCY CODE

15. SUPPLEMENTARY NOTES

16. ABSTRACT

This research is directed towards enhancements to the assessment and mitigation of liquefaction induced lateral spreading effects on bridge foundation systems. The conducted research scope and outcomes are presented. On this basis, insights are derived for improvement of the current assessment procedures, and mitigation of this detrimental mechanism. Finally, a number of future additional research needs are outlined.

17. KEY WORDS	18. DISTRIBUTION STATEMENT	
Bridge, Pile Foundations, Seismic, Liquefaction, Lateral Spreading, Finite Element	Unlimited	
19. SECURITY CLASSIFICATION *(of this report)*	20. NUMBER OF PAGES	21. COST OF REPORT CHARGED
Unclassified	307	

DISCLAIMER STATEMENT

This document is disseminated in the interest of information exchange. The contents of this report reflect the views of the authors who are responsible for the facts and accuracy of the data presented herein. The contents do not necessarily reflect the official views or policies of the State of California or the Federal Highway Administration. This publication does not constitute a standard, specification or regulation. This report does not constitute an endorsement by the Department of any product described herein.

For individuals with sensory disabilities, this document is available in alternate formats. For information, call (916) 654-8899, TTY 711, or write to California Department of Transportation, Division of Research, Innovation and System Information, MS-83, P.O. Box 942873, Sacramento, CA 94273-0001.

STRUCTURAL SYSTEMS RESEARCH PROJECT

Report No.
SSRP–24/05

ANALYSIS OF LATERAL SPREADING EFFECTS ON BRIDGE FOUNDATIONS

by

ZHIJIAN QIU

JINCHI LU

AHMED EBEIDO

ATHUL PARAYANCODE

AXEL ARNOLD YARAHUAMAN CHAMORRO

AHMED ELGAMAL

GEOFFREY R. MARTIN

JOHN S. MCCARTNEY

Final Report Submitted to the California Department of Transportation (Caltrans) under Contract No. 65A0786.

April 2024

Department of Structural Engineering
University of California, San Diego
La Jolla, California 92093-0085

Analysis of Lateral Spreading Effects on Bridge Foundations

Report No. SSRP-24/05

by

Zhijian Qiu

Graduate Student Researcher, UC San Diego

Jinchi Lu

Associate Project Scientist, UC San Diego

Ahmed Ebeido

Graduate Student Researcher, UC San Diego

Athul Parayancode

Graduate Student Researcher, UC San Diego

Axel Arnold Yarahuaman Chamorro

Graduate Student Researcher, UC San Diego

Ahmed Elgamal

Professor of Geotechnical Engineering, UC San Diego

Geoffrey R. Martin

Professor Emeritus of Geotechnical Engineering, USC

John S. McCartney

Professor of Geotechnical Engineering, UC San Diego

Final Report Submitted to the California Department of Transportation under Contract No. 65A0548

Department of Structural Engineering

University of California, San Diego

La Jolla, California 92093-0085

April 2024

ACKNOWLEDGMENTS

The research described in this report was supported by the California Department of Transportation (Caltrans) under Contract No. 65A0548 with Dr. Charles Sikorsky as the project manager. This support is most appreciated. In addition, we are grateful for the valuable technical suggestions, comments and contributions provided by Dr. AnhDan Q. Le, Mr. Thomas Shantz, Dr. Foued Zayati of Caltrans, and Dr. Arul Arulmoli, Dr. Amir Zand and Mr. Raj Varatharaj of Earth Mechanics, Inc.

ABSTRACT

This research is directed towards enhancements to the assessment and mitigation of liquefaction induced lateral spreading effects on bridge foundation systems. The conducted research scope and outcomes are presented. On this basis, insights are derived for improvement of the current assessment procedures, and mitigation of this detrimental mechanism. Finally, a number of future additional research needs are outlined.

TABLE OF CONTENTS

LIST OF TABLES

LIST OF FIGURES

1. INTRODUCTION

This report is comprised of stand-alone chapters, each concerned with an element of the overall research scope. Three main themes of this research scope are highlighted as:

Element I: Significance of Integrated Bridge-Ground System Analyses

Building on work by the authors that was reported earlier (Qui et al. 2020), several significant aspects related to the overall bridge response were shown to be highly dependent on handling the analysis within an integrated bridge-ground system framework. In this regard:

Chapter 2 further extends (Qui et al. 2020), using a full three-dimensional Finite Element (FE) analysis framework. It illustrates: i) the increased demands on outer piles that are adjacent to the surrounding free-field, and ii) the increasing feasibility of conducting such fully 3D analyses.

Chapter 3 addresses the important configuration of bridges in narrow waterways. In particular, the interaction between potential deformations on both sides of the waterway might significantly reduce the detrimental consequences of liquefaction. The study clearly shows the necessity of a full bridge-ground analysis framework in such cases.

Element II: Mitigation Concepts against liquefaction-induced lateral spreading scenarios.

Chapter 4 discusses the extent of ground deformation at its specific location within the slope, under the scenario of liquefaction induced lateral spreading. Generally, lower levels of deformation are to be expected with distance away from the crest and toe of the sliding zone. As such, it lays the background for the subsequent chapter that aims, when feasible, to locate the deep foundation systems away from these locations.

Chapter 5 discusses bridge configurations that aim to reduce the detrimental consequences of potential liquefaction-induced lateral spreading. A number of bridge configurations are suggested, in which: i) the foundations are placed at locations of potentially lower lateral deformations, ii) a shallow foundation is employed, iii) the bridge deck is employed as a strut to shore the slopes on both sides of the canyon, and iv) the canyon slopes are braced using the bridge superstructure and its foundation. The presented outcomes and conclusions provide insights for bridge retrofit efforts and/or for new construction.

Chapter 6 conceptually proposes a shallow foundation integral-bridge configuration, particularly for narrow waterway scenarios. Where applicable in terms of the underlying soil profile and waterway geometry, such an integral bridge-foundation system will counteract downslope ground deformation via; i) the bridge superstructure acting as a brace or strut that self-reacts against the sloping sides of the waterway, and ii) the bridge self-weight being employed as a potential additional stabilizing mechanism.

Chapter 7 investigates a valuable bridge seismic response case history from the relatively nearby 2010 7.2 M_w El Mayor-Cucapah earthquake. In this regard, liquefaction-induced lateral spreading demands on a pair of adjacent parallel bridges, along with the bridge responses are well-documented. On this basis, this case history is studied with additional effort undertaken to address the damaged bridge configuration shortcomings, with retrofit scenarios such as: i) extensions of the seat width, ii) structural retrofit to enhance the deck-bent connectivity, and iii) ground modification to mitigate the consequences of liquefaction.

Finally, Appendix I is directed towards development of a new approach for mitigating the effects of liquefaction induced lateral spreading on bridge foundation systems. Specifically, this study is focused on evaluating the feasibility of using a layer of tire derived aggregate (TDA) placed upslope from the bridge foundation system to absorb the lateral spreading deformations.

Element III: Insights for simplified analysis frameworks and procedures

Chapter 8 is concerned with insights related to further development of simplified analysis procedures. Some potential enhancements to the current MTD 20-15 (2017) are outlined. In addition, a new simplified procedure framework is proposed. This new framework places emphasis on representing the entire bridge-foundation-ground configuration, along with possibilities for more direct application of lateral loads, rather than the current logic which employs displacements to generate these loads.

References

MTD 20-15 (2017): https://dot.ca.gov/-/media/dot-media/programs/engineering/documents/memotodesigner/20-15-a11y.pdf

Qiu, Z., Ebeido, A., Almutairi, A., Lu, J., Elgamal, A., Shing, P. B., and Martin, G. (2020). "Aspects of bridge ‐ ground seismic response and liquefaction ‐ induced deformations." Earthquake Engineering & Structural Dynamics 49, no. 4: 375-393.

2. THREE-DIMENSIONAL BRIDGE-GROUND LIQUEFACTION-INDUCED DEFORMATIONS

Zhijian Qiu and Ahmed Elgamal

Abstract

Global response of bridges is dictated by soil-structure interaction considerations of the entire bridge-ground system. In this study, the three-dimensional (3D) longitudinal response of such a bridge-ground system is numerically investigated. A realistic multi-layer soil profile is considered with interbedded liquefiable/non-liquefiable strata. Effect of the resulting liquefaction-induced ground deformation on the bridge-ground system is explored. The analysis techniques as well as the derived insights are of significance for general bridge-system configurations under liquefaction-induced ground deformation.

2.1 Introduction

Liquefaction and related damage to large bridges remained as a main concern in recent earthquakes, including the events of 2010 Maule (Arduino et al. 2010) and 2011 Christchurch (Cubrinovski et al. 2011, 2014). Generally, the observed response is highly influenced by the global bridge-ground overall characteristics as an integral system. As a consequence, investigators have been increasingly studying the entire bridge and the surrounding ground response within an integrated framework (Boulanger et al. 2007; Shin et al. 2008; Zhang et al. 2008; Ashford et al. 2009, 2011). Such studies indicated that global analysis is paramount in realistically evaluating the performance of liquefaction-induced lateral spreading and its consequences. On this basis, a three-dimensional (3D) finite element (FE) bridge-ground model was developed herein to capture salient characteristics of the involved response mechanisms. In developing this model, a realistic bridge geometric layout and ground stratification profile are represented. In the following sections, details of this modeling effort are presented and discussed.

2.2 Computational Framework

The Open System for Earthquake Engineering Simulation (OpenSees, McKenna 2011) framework was employed. Developed by the Pacific Earthquake Engineering Research (PEER) Center, OpenSees is widely used for simulation of geotechnical systems and soil-structure interaction applications (Qiu et al. 2020). The OpenSees elements and materials used in this study are briefly described below.

Three-dimensional solid-fluid *u-p* elements (Chan 1988) were employed for simulating soil response, where *u* is displacement of the soil skeleton and *p* is pore water pressure. Calibrated in a large number of earlier studies, the employed soil constitutive models (Parra 1996; Yang 2000; Yang and Elgamal 2002; Elgamal et al. 2003) were the PressureDependMultiYield03 and the PressureIndependMultiyield (PIMY). In these models, the shear stress-strain backbone curve is represented by the hyperbolic relationship with the shear strength based on simple shear. The PressureDependMultiYield03 (Khosravifar et al. 2018) includes new modifications to better capture the established guidelines on liquefaction triggering (Idriss and Boulanger 2008).

Details concerning the employed time integration scheme are described in Qiu et al. (2020). A relatively low level of stiffness proportional viscous damping was used to enhance numerical stability (coefficient = 0.003), with the main damping emanating from the soil nonlinear shear stress-strain hysteresis response (Qiu et al. 2020).

2.3 Bridge-Ground System

Figure 2-1depicts the investigated bridge-ground configuration (Qiu 2020, Qiu et al. 2020). This 18-span reinforced concrete bridge is approximately 197 m long and 9.9 m wide, composed of a reinforced concrete deck on vertical pier walls with pile groups, and on single piles. Along the bridge deck, two expansion joints are located adjacent to the Piers (Figure 2-1b). In general, the site soil profile consists of shallow, fine-grained soils underlain by medium dense to dense sands (Table 2-1 and Table 2-2), with loose sand layers (the red zone in Figure 2-1b). The water table was prescribed at an elevation of 30.5 m (Figure 2-1b). Cross sections of the bridge structural components are presented in Qiu (2020) and Qiu et al. (2020).

Based on the soil profiles (Qui 2020 and Qiu et al. 2020) and ground configuration (Figure 2-1), a 3D bridge-ground FE model is developed (Figure 2-2). Along both the West and East side mesh boundaries (Figure 2-2), soil columns of large size (not shown) are included (Qiu et al. 2020). These soil columns, at an adequate distance (around 100 m) away from the bridge structure to minimize boundary effects, efficiently reproduce the desired free-field response at these locations. Figure 2-2 shows the full 3D FE models (half mesh due to symmetry), comprising 58,801 nodes and 52,292 brick elements. In this model, seismic response is investigated only in the longitudinal

direction, no out-of-plane motion is allowed. As such, loading was implemented in a staged fashion as follows:

1) Gravity was applied to activate the initial static state for the soil domain only with: i) linear elastic properties (Poisson's ratio of 0.47 for all layers), ii) nodes on both side planes of the model fixed against longitudinal translation, iii) nodes along the base fixed against vertical translation, iv) water table prescribed (Figure 2-2) with related water pressure and nodal forces specified along the canyon boundary. At the end of this step, the static soil state was imposed and displacements under own-weight application were re-set to zero using the OpenSees command InitialStateAnalysis.

2) Soil properties were switched from linear elastic to plastic.

3) Nonlinear force-based beam-column elements of pile and elastic beam-column elements of reinforced concrete deck were added. The pile nodes were connected to the soil nodes by rigid links, zerolength and zerolengthSection elements as described in Qiu et al. (2020). Thereafter, self-weight of the bridge structure was applied.

In this study, the Lysmer-Kuhlemeyer 1969 boundary is applied along the base of the FE model (base V_s = 600 m/s, slightly higher than the stiffness of the overlying stratum), so as to avoid spurious wave reflections along this model boundary. For the shaking phase (purely in the longitudinal x-direction), seismic motion was simply taken as that of the 1994 Northridge earthquake ground surface Rinaldi Receiving Station record (Component S48W), scaled down to a peak amplitude of about 0.2 g (Figure 2-3). Via deconvolution (using Shake91 by Idriss and Sun, 1993), an incident earthquake motion (Figure 2-3) was derived and imparted (Elgamal et al. 2008) along the base of the FE model (elevation 0.0 in Figure 2-1). In this representation, free-field site response along both the side mesh boundaries is generated by the included 2D plane strain soil columns mentioned above.

2.4 Computed Response

Figure 2-3b displays the full 3D model lateral bridge deck displacement, along with that predicted by the slice approach of Qiu et al. (2020). Maximum displacement of the full 3D model is slightly higher than that of the slice model (0.13 m), reaching about 0.16 m. Post peak, permanent displacement of the full 3D model is significantly higher than that of the slice model by about 30

%. This makes sense in light of the additional imposed demands from lateral deformation of the large ground domain surrounding the bridge in the full 3D model simulation.

Figure 2-4 displays the displacement contours of the two bridge-ground system models at end of shaking. For the slice model (Figure 2-4a), maximum displacement of the overall bridge-ground system reached about 0.15 m (in the vicinity of the bridge model). In Figure 2-4b, noticeable localized east-side slope deformations of the free-field (away from the bridge) is seen. In Figure 2-5, deformation of the outer bents (Figure 2-1) is significantly higher than those of the inner bents, due to the large permanent downslope displacement of the surrounding sloping ground. Computed moment curvature of bents 1-4 and 17-19 (Figure 2-1) in the slice and full 3D models are displayed in Figure 2-6. It can be seen clearly that the outer piles in full 3D model sustain more loads than the inner piles. In addition, the loads of both outer and inner piles in the full 3D model are higher than the corresponding counterparts of the slice model.

2.5 Conclusions

A 3D FE analysis framework was presented to study the liquefaction-induced seismic response of bridge-ground systems as dictated by soil-structure interaction. For that purpose, results of two 3D FE models representing the same ground-bridge-foundation configuration were presented. Permanent deformation patterns resulting from the liquefaction-induced lateral spreading were explored. Comparison results of the two 3D models demonstrated that a holistic assessment of such response generally requires a highly demanding full three-dimensional (3D) model of the bridge and surrounding ground. In such a full 3D modeling representation, the outer piles of each bent will encounter higher demands than their corresponding inner piles, due to the larger imposed lateral deformations of the soil domain, transversally around the bridge's footprint.

2.6 References

Arduino, P., Ashford, S., Assimaki, D., Bray, J., Eldridge, T., Frost, D., Hashash, Y., Hutchinson, T., Johnson, L., Kelson, K., Kayen, R.: Geo-engineering reconnaissance of the 2010 Maule, Chile earthquake. GEER Association Report No. GEER-022, 1 (2010).

Ashford, S.A., Boulanger, R.W., Brandenberg, S.J., Shantz, T.: Overview of recommended analysis procedures for pile foundations in laterally spreading ground. In: TCLEE 2009: Lifeline Earthquake Engineering in a Multihazard Environment, pp. 1–8 (2009).

Ashford, S.A., Boulanger, R.W., Brandenberg, S.J.: Recommended design practice for pile foundations in laterally spreading ground. Pacific Earthquake Engineering Research Center. University of California, Berkeley, Calif. PEER Rep, (2011/04) (2011).

Boulanger, R.W., Chang, D., Brandenberg, S.J., Armstrong, R.J., Kutter, B.L.: Seismic design of pile foundations for liquefaction effects. Earthquake Geotechnical Engineering, pp. 277–302. Springer, Dordrecht (2007).

Chan, A.H.C.: A unified finite element solution to static and dynamic problems in geomechanics. PhD Thesis, University College of Swansea (1988) Cubrinovski, M., Bradley, B., Wotherspoon, L., Green, R., Bray, J., Wood, C., Pender, M., Allen, J., Bradshaw, A., Rix, G., Taylor, M.: Geotechnical aspects of the 22 February 2011 Christchurch earthquake. Bull. N. Z. Soc. Earthq. Eng. 44(4), 205–226 (2011).

Cubrinovski, M., Winkley, A., Haskell, J., Palermo, A., Wotherspoon, L., Robinson, K., Bradley, B., Brabhaharan, P., Hughes, M.: Spreading-induced damage to short-span bridges in Christchurch. N. Z. Earthq. Spectra 30(1), 57–83 (2014).

Elgamal, A., Yang, Z., Parra, E.: Modeling of cyclic mobility in saturated cohesionless soils. Int. J. Plasticity 19(6), 883–905 (2003).

Elgamal, A., Yan, L., Yang, Z.: Three-dimensional seismic response of Humboldt Bay bridge-foundation- ground system. J. Struct. Eng. 134(7), 1165–1176 (2008).

Idriss, I.M., Sun, J.I.: User's Manual for SHAKE91: A Computer Program for Conducting Equivalent Linear Seismic Response Analyses of Horizontally Layered Soil Deposits. Center for Geotechnical Modeling, Dept. of Civil and Environmental Engineering, University of

California Press, Davis (1993).

Idriss, I.M., Boulanger, R.W.: Soil Liquefaction During Earthquakes. Earthquake Engineering Research Institute, San Francisco (2008).

Khosravifar, A., Elgamal, A., Lu, J., Li, J.: A 3D model for earthquake-induced liquefaction triggering and post-liquefaction response. Soil Dyn. Earthq. Eng. 110, 43–52 (2018)

Lysmer, J., Kuhlemeyer, R.L.: Finite dynamic model for infinite media. J. Eng. Mech. Div. 95, 859–878 (1969).

McKenna, F., Scott, M.H., Fenves, G.L.: Nonlinear finite-element analysis software architecture using object composition. J. Comput. Civ. Eng. 24(1), 95–107 (2010).

Parra, E.: Numerical modeling of liquefaction and lateral ground deformation including cyclic mobility and dilation response in soil systems. PhD Thesis. Rensselaer Polytechnic Institute (1996).

Qiu, Z., Ebeido, A., Almutairi1, A., Lu, J., Elgamal, A., Shing, B., Martin, G.: Aspects of bridge-ground seismic response and liquefaction-induced deformations. Earthq. Eng. Struct. Dyn. 49 (4), 375–393 (2020).

Qiu, Z.: Computational Modeling of Ground-Bridge Seismic Response and Liquefaction Scenarios. Ph.D. thesis, Department of Structural Engineering, University of California, San Diego, La Jolla, CA (2020).

Shin, H., Arduino, P., Kramer, S.L., Mackie, K.: Seismic response of a typical highway bridge in liquefiable soil. In: Geotechnical Earthquake Engineering and Soil Dynamics IV, pp. 1–11 (2008)

Yang, Z.: Numerical modeling of earthquake site response including dilation and liquefaction. PhD Thesis, Columbia University (2000).

Yang, Z., Elgamal, A.: Influence of permeability on liquefaction-induced shear deformation. J. Eng. Mech. 128(7), 720–729 (2002).

Zhang, Y., Conte, J.P., Yang, Z., Elgamal, A., Bielak, J., Acero, G.: Two-dimensional nonlinear earthquake response analysis of a bridge-foundation-ground system. Earthq. Spectra 24(2),

343–386 (2008).

Table 2-1 Sand (Figure 2-1) PressureDependMultiYield03 model parameters

Model Parameters	LS2	MS2	DS1	DS2	VDS
Reference mean effective pressure, p'_r (kPa)	170*	210*	270	340	430
Mass density, ρ (t/m^3)	1.98*	2.03*	2.08	2.08	2.13
Maximum shear strain at reference pressure, $\gamma_{max,r}$	0.1*	0.1*	0.1	0.1	0.1
Low-strain shear modulus at reference pressure, G_r (MPa)	80.4*	118*	164	256	435
Stiffness dependence coefficient n, $G = G_r(\frac{\boldsymbol{P'}}{\boldsymbol{P'_r}})^{\boldsymbol{n}}$	0.5*	0.5*	0.5	0.5	0.5
Poisson's ratio v for dynamic analysis	0.4*	0.4*	0.4	0.4	0.4
Shear strength at zero confinement (kPa)	2.0*	2.0*	2.0	2.0	2.0
Friction angle ϕ, with resulting shear strength defined as $p'\sin\phi$	29°	31°	34°	36°	40°
Phase transformation angle, ϕ_{PT}	29°	27°	29°	31°	33°
Contraction coefficient, c_1	0.1	0.035	0.015	0.015	0.001
Contraction coefficient, c_2	5.0	3.0	1.0	1.0	0.0
Contraction coefficient, c_3	0.05	0.2	0.45	0.45	0.8
Dilation coefficients, d_1	0.1	0.15	0.2	0.2	0.6
Dilation coefficients, d_2	3	3	3	3	3
Dilation coefficient, d_3	0.05	0.2	0.45	0.45	0.5
Permeability (m/s)	10^{-5}	10^{-5}	10^{-5}	10^{-5}	10^{-5}
Additional contraction parameters					
b_1	0.35	0.2	0.2	0.1	0.1
b_2	30	30	15	10	10
b_3	0.0	0.0	0.06	0.06	0.06
b_4	0.001	0.001	0.001	0.001	0.001

Note: For each involved soil layer, the soil-pile friction angle δ and/or the soil-pile adhesion c_A are assumed equal to the corresponding friction angle and/or cohesion, respectively.

*Sands LS1 and MS1 (Figure 3) include the same model parameters as LS2 and MS2 except for friction angles, respectively.

Table 2-2 Clay (Figure 2-1) PIMY model parameters

Model parameters (PressureIndependMultiYield)	SC	SC1	SC2
Mass density, ρ (t/m^3)	2.07	2.1	2.1
Low-strain shear modulus, G (MPa)	52.9	95.5	82.3
Poisson's ratio v for dynamic analysis	0.4	0.4	0.4
Cohesive strength, c_u (kPa)	24	96	48
Maximum shear strain at reference pressure, $\gamma_{max,r}$	0.1	0.1	0.1
Permeability (m/s)	10^{-9}	10^{-9}	10^{-9}

Note: For each involved soil layer, the soil-pile adhesion c_A is assumed equal to the corresponding cohesive strength.

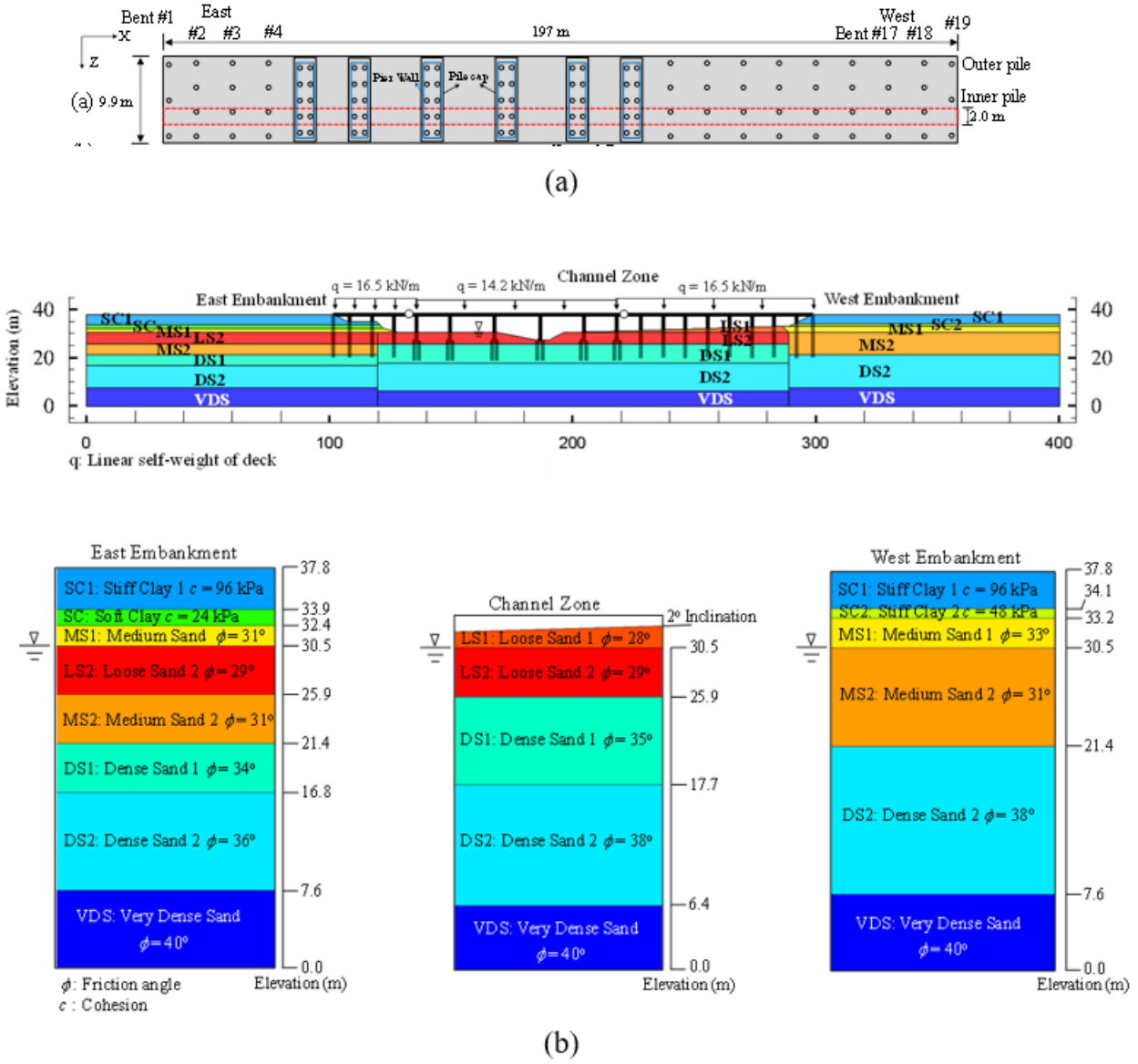

Figure 2-1. Bridge-ground system: (a) Schematic plan view of the bridge (not to scale); (b) Bridge-Ground configuration.

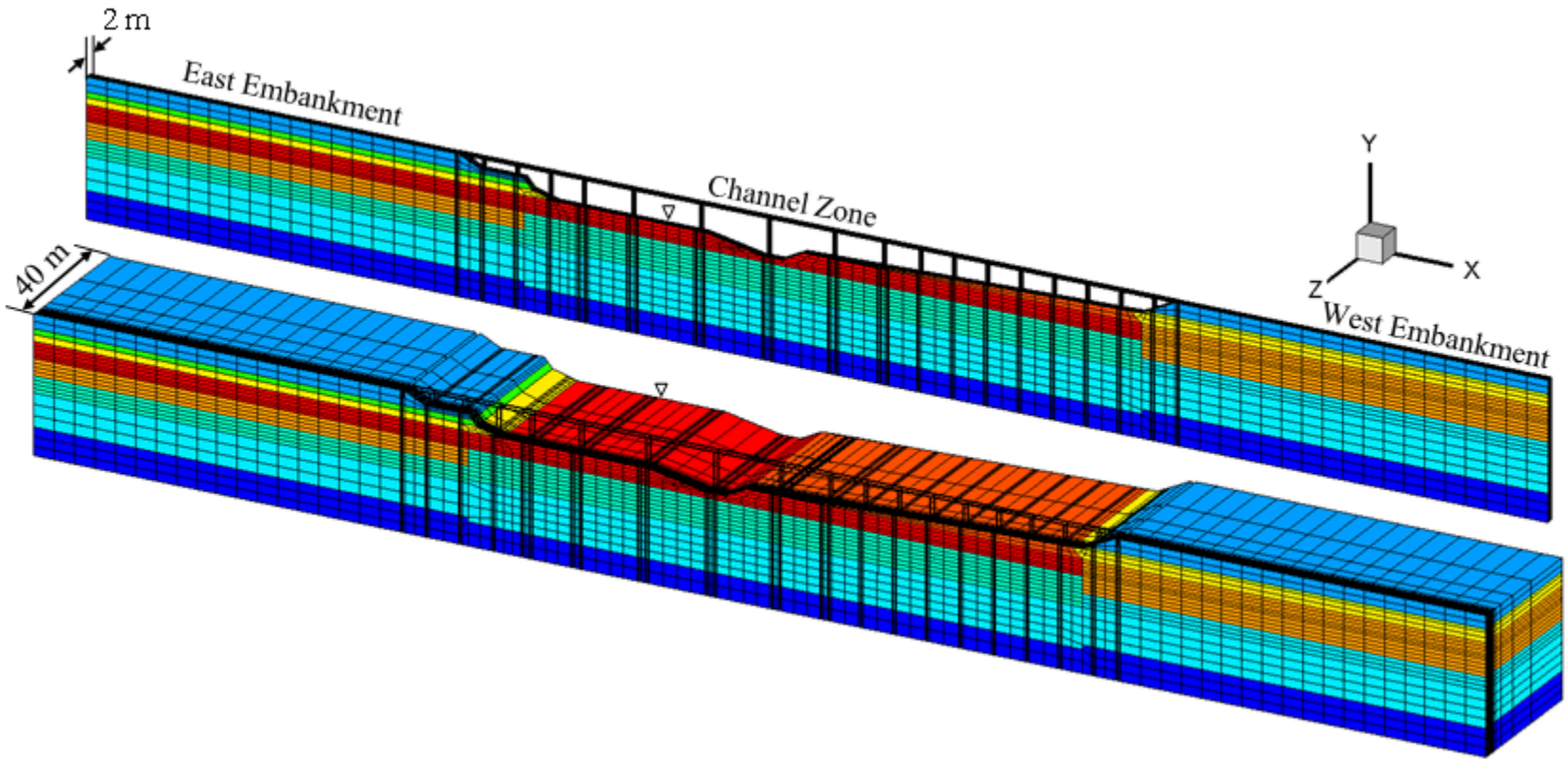

Figure 2-2. FE mesh: (a) Slice model; (b) Full 3D model shown below (half mesh due to symmetry)

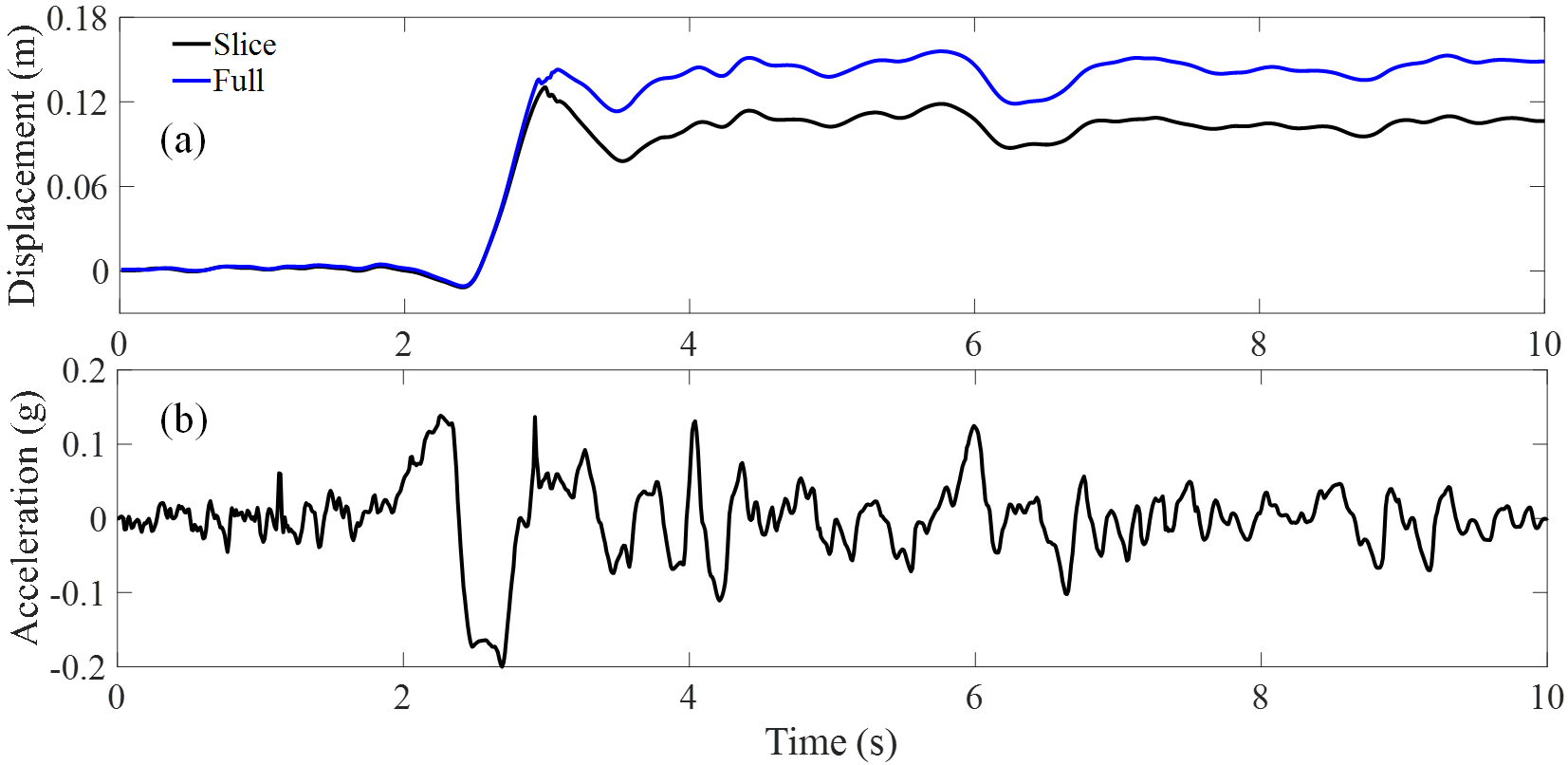

2Figure 2-3. Incident input motion and computed bridge deck relative displacement time history.

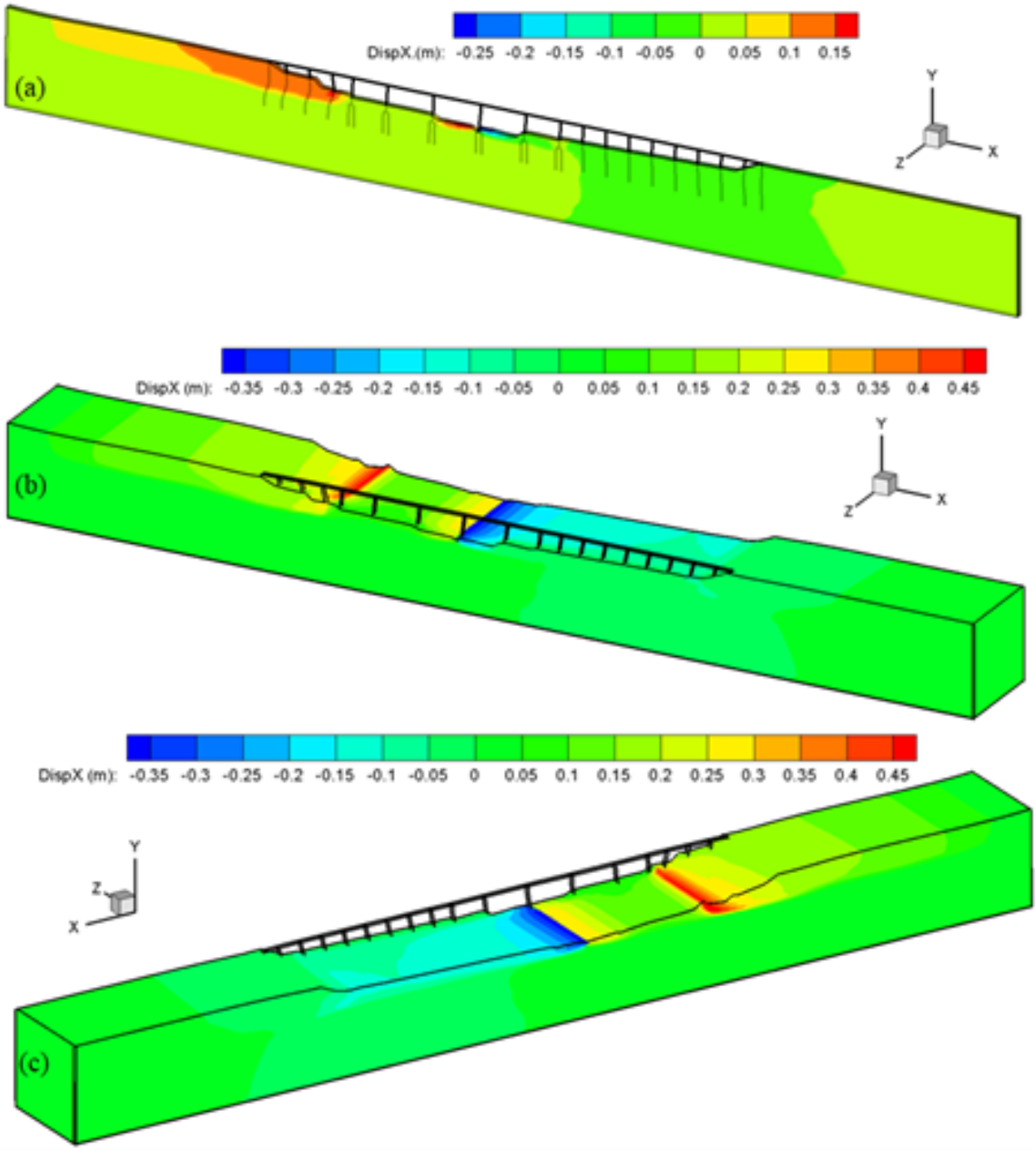

Figure 2-4. Displacement contours at end of shaking: (a) Slice model (Qiu et al. 2020); (b), (c) Full 3D model

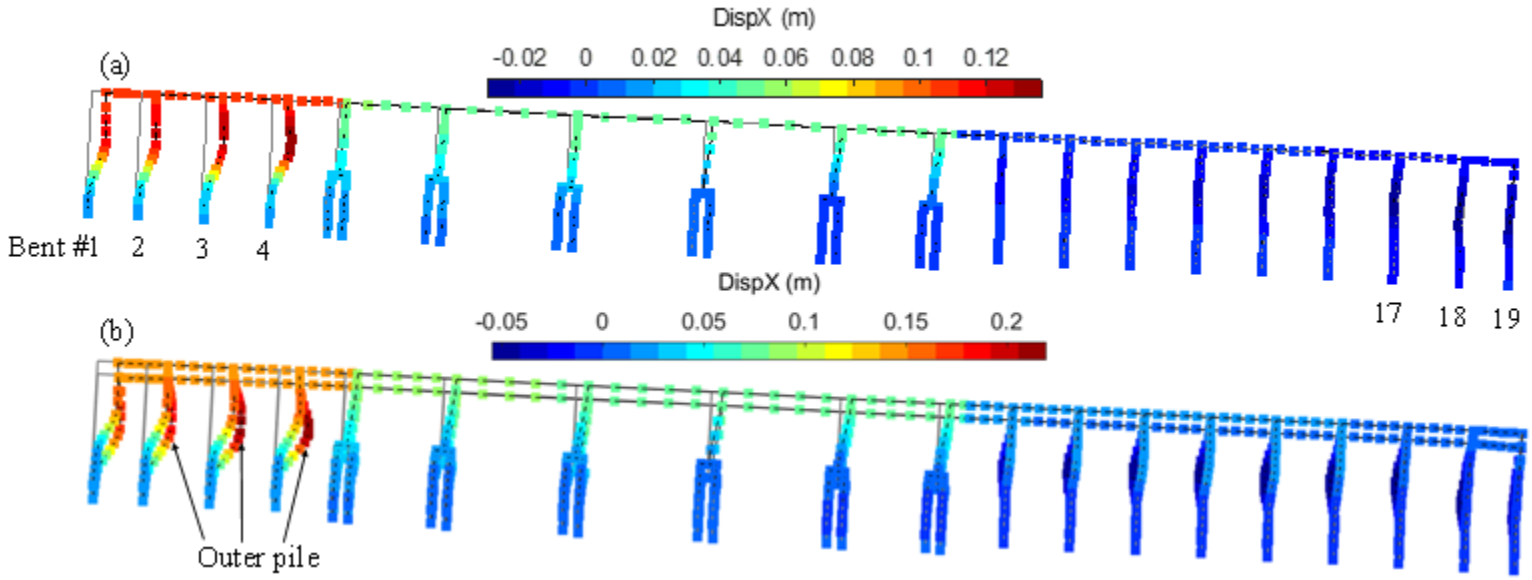

Figure 2-5. Deformed FE mesh of bridge at end of shaking: (a) Slice model; (b) Full 3D model

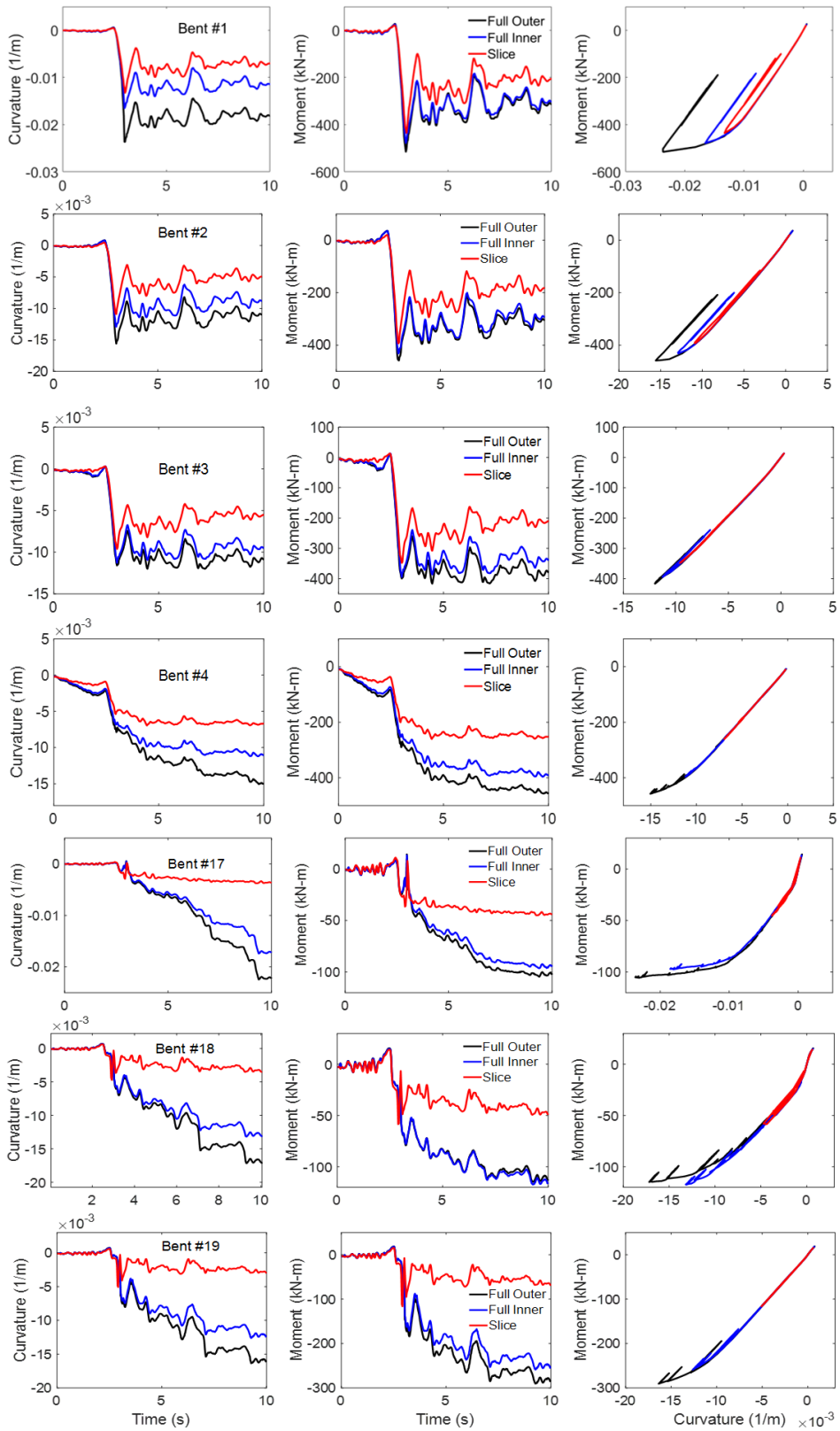

Figure 2-6. Computed maximum moment-curvature response of bents 1-4, 17-19 as shown in Figure 2-1

3. BRIDGE IN NARROW WATERWAY: SEISMIC RESPONSE AND LIQUEFACTION-INDUCED DEFORMATIONS

Zhijian Qiu, Jinchi Lu, Ahmed Ebeido, Ahmed Elgamal, Chia-Ming Uang, Fadel Alameddine, and Geoffrey Martin

Abstract

Considerable bridge-ground interaction effects are involved when evaluating the consequences of liquefaction-induced deformations. Due to seismic excitation, liquefied soil layers may result in substantial accumulated permanent deformation due to the sloping ground near the abutments. Ultimately, global response of the bridge is dictated by soil-structure interaction considerations of the entire bridge-ground system. Of particular interest is the scenario of narrow waterways where interaction between downslope deformations at both ends of the bridge takes place. In order to highlight the involved salient mechanisms, this study investigates the longitudinal response of an overall bridge-ground system. For that purpose, a full three-dimensional (3D) Finite Element (FE) model is developed, motivated by details of an existing narrow waterway bridge-ground configuration. As such, a realistic multi-layer soil profile is considered with interbedded liquefiable/non-liquefiable strata. Specific attention is given to global response of the bridge structure as an integral entity due to ground deformation in the vicinity of the abutments. The overall results indicated that downslope deformations at both ends of the bridge may result in significant interference within the narrow waterway central section. As such, analysis of deformations at each slope separately might lead to unrealistic outcomes. Generally, the analysis technique as well as the derived insights are of significance for the seismic response of bridge systems with downslope ground deformations.

3.1 Introduction

Liquefaction-induced damage to bridge foundations has been observed frequently during earthquakes (Youd 1993; Hamada *et al.* 1996; Tokimatsu and Asaka 1998; Berrill *et al.* 2001), including the recent 2010 Maule (Arduino *et al.* 2010; Ledezma *et al.* 2012; Verdugo *et al.* 2012), the 2011 Christchurch (Cubrinovski *et al.* 2011, 2014; Wotherspoon *et al.* 2011), and the El Mayor-Cucapah events (Turner *et al.* 2013, 2016). Figure 3-1illustrates typical response of a short span bridge as discussed earlier by Cubrinovski *et al.* (2011, 2014).

To study the entire bridge and surrounding narrow waterway within an integrated framework (Figure 3-1), different approaches to the representation of ground response at the location of each bridge foundation were presented by Boulanger *et al.* 2007, Ashford *et al.* 2009, 2011, Aygün *et al.* 2009, 2010, Ledezma and Bray 2010, Padgett *et al.* 2013, Turner *et al.* 2013, 2016, Wang *et al.* 2013a, b, McGann and Arduino 2015, Ghofrani *et al.* 2016, Soltanieh *et al.* 2019, and Qiu *et al.* 2020. Results of these studies show that consideration of the entire bridge-ground system provides a more realistic distribution of force and displacement demands.

Currently, three-dimensional (3D) Finite Element (FE) analyses for seismic response of bridges, with consideration of soil liquefaction, are rather limited. For instance, McGann and Arduino 2014 conducted quasi static analysis of the Mataquito River Bridge abutment and foundation system subjected to liquefaction-induced lateral spreading. Similarly, McGann and Arduino 2015 and McGann 2020 conducted parametric studies to investigate the influence of 3D site geometry on seismic response of the bridge piles and abutments.

In view of the observed system response as depicted schematically in Figure 3-1, a full 3D bridge-ground FE investigation is undertaken herein. Focus is placed on a narrow waterway configuration, motivated by the details of an actual bridge-ground system (Caltrans 2017). In such a configuration, significant interaction between the lateral downslope ground deformations at both ends of the bridge takes place.

As such, the following sections of this paper outline the: 1) computational framework, 2) specifics and model properties of the bridge-ground system, 3) details of the employed FE modeling techniques, and 4) computed response and insights derived from the study. Finally, a number of conclusions are presented and discussed.

3.2 Computational Framework

The Open System for Earthquake Engineering Simulation (OpenSees, McKenna *et al.* 2010, http://opensees.berkeley.edu) framework was employed to conduct the nonlinear bridge-ground system analysis subjected to seismic excitation. OpenSees is developed by the Pacific Earthquake Engineering Research (PEER) Center, and it is widely used for simulation of geotechnical systems and soil-structure interaction applications (Yang and Elgamal 2002; Lu *et al.* 2011; Su *et al.* 2017). The OpenSees elements and materials used in this FE model are briefly described below.

Three-dimensional solid-fluid brick elements (i.e., bbarBrickUP element in OpenSees) following the *u-p* formulation (Chan 1988) were employed for simulating saturated soil response, where *u* is displacement of the soil skeleton and *p* is pore-water pressure. As such, the 3D soil domain is represented by effective-stress solid-fluid fully coupled brick elements (Parra 1996; Yang 2000; Lu 2006; Yang *et al.* 2008) to describe the solid translational degrees of freedom (DOFs) and the fluid pressure.

The OpenSees soil material PressureDependMultiYield03 (typically used with the solid-fluid fully coupled brick elements, Khosravifar *et al.* 2018) is employed to simulate the liquefaction-induced shear strain accumulation mechanism in cohesionless soils (Yang and Elgamal 2002; Elgamal *et al.* 2003; Yang *et al.* 2003, 2008). In order to more closely capture the established guidelines concerning triggering of liquefaction (Idriss and Boulanger 2008), the PressureDependMultiYield03 material has been recently updated (Khosravifar *et al.* 2018). In addition, the PressureIndependMultiYield material (Elgamal *et al.* 2008; Yang *et al.* 2008; Lu *et al.* 2011) is employed for simulating elasto-plastic undrained clay-type shear response.

The FE matrix equation of the bridge-ground system is integrated in time using a single-step predictor multi-corrector scheme of the Newmark type (Chan 1988; Parra 1996) with integration parameters $\gamma = 0.6$ and $\beta = 0.3025$. The equation is solved using the modified Newton-Raphson approach with Krylov subspace acceleration (Carlson and Miller 1998; Mazzoni *et al.* 2009). A relatively low level of stiffness proportional viscous damping was used to enhance numerical stability (coefficient = 0.003), with the main damping emanating from the soil nonlinear shear stress-strain hysteresis response (Su *et al.* 2017; Qiu *et al.* 2020).

3.3 Piles and Soil-pile Interface

Three-dimensional nonlinear force-based beam-column elements with fiber-section (Scott and Fenves 2006; Scott and Ryan 2013) were employed to represent the piles, for the purpose of this liquefaction-induced downslope deformation study (Elgamal and Lu 2009; He *et al.* 2017). In order to represent the geometric space occupied by the pile within the soil domain, rigid beam-column links ($EI = 10^5$ times the linear EI of the pile) were used normal to the vertical axis of the pile, effectively defining its surface for skin friction and its base for end bearing resistance. The soil nodes of 3D brick elements surrounding the pile were connected to the outer nodes of these rigid links by using: 1) zerolength elements to axially connect the rigid links to adjacent soil nodes

without separation, 2) zerolengthSection elements to provide yield shear force in each link, and 3) the OpenSees equalDOF translation constraint. Finally, the yield shear force was simply defined as $F = [c_A + \sigma' \tan(\phi)] \cdot l \cdot h / N$, where l is the perimeter of the pile, h is center to center contributing height (according to the adjacent soil element heights), c_A is the soil-pile adhesion, ϕ is the soil-pile friction angle, σ' is the lateral effective stress and N is the number of zeroLengthSection elements along the pile perimeter (Su *et al.* 2017; Qiu *et al.* 2020).

3.4 Finite Element Model

3.4.1 Ground Configuration

The overall ground configuration based on existing boring data and site conditions (Caltrans 2017) is shown in Figure 3-2. Inclination angle of the slopes (2H:1V) is about 27 degrees, and water table elevation is 35.5 m, at the interface between Layers Q3a and Q3b. In this ground profile (Figure 3-2), Layers Q2 and Q4 are deemed to be potentially liquefiable, and Layer Q3b is a relatively weak soft clay. Table 3-1 and Table 3-2 list the sand and clay model parameters, respectively. For illustration, the clay and sand (initial confinement = 100 kPa) constitutive model responses under undrained monotonic loading conditions are presented in Figure 3-3. It can be seen that shear strength of the soft clay Q3b is comparatively low (Figure 3-3a), further promoting the potential for seismically induced downslope deformations. As shown in Figure 3-3b, shear strength of the saturated medium dense and dense sands (Q2 and Q4) increases with shear strain amplitude (undrained response, due to the prescribed dilative tendency as noted in Table 3-1).

For the purpose of this investigation, seismic excitation is applied only in the longitudinal downslope-deformation direction (i.e., no transverse or vertical shaking is imparted), thus allowing for the use of a half-mesh due to symmetry (Figure 3-4 Finite Element model of bridge-ground system (half mesh due to symmetry): (a) Isometric view; (b) Elevation view.). In the transverse direction, an additional 35 m wide soil domain is included in order to capture the narrow waterway response away from the bridge structure. On this basis, a 3D bridge-ground FE mesh (Figure 3-4 Finite Element model of bridge-ground system (half mesh due to symmetry): (a) Isometric view; (b) Elevation view.) is generated comprising 65,714 nodes, 60,060 brick elements, 725 nonlinear and 30 linear elastic beam-column elements, 2988 rigid beam-column links, 2988 zerolength elements and 2988 zerolengthSection elements.

Along the left- and right-side mesh boundaries (Figure 3-4), 2D plane strain soil columns of large size and depth (not shown) are included (Qiu *et al.* 2020). These soil columns, at an adequate distance (around 100 m) away from the bridge structure so as to minimize boundary effects (Figure 3-4), efficiently reproduce the desired shear beam free-field response at these locations (Qiu *et al.* 2020).

3.4.2 Bridge Structure

Figure 3-5 depicts the three-span reinforced concrete bridge layout. The bridge is approximately 96 m long (spans of equal length) and 10.4 m wide (Caltrans 2017), composed of reinforced concrete pier walls, seat-type abutments and wing walls founded on Steel H-piles (Figure 3-5b). Four hinge-type connections (Figure 3-5a) are located along the bridge deck. Cross sections of the bridge structural components are displayed in Figure 3-5c.

All structural components except for the reinforced concrete deck (modeled by linear elastic beam-column elements with self-weight q as shown in Figure 3-2) were modeled using 3D nonlinear force-based beam-column elements with fiber-section. In this fiber section formulation, the widely used OpenSees uniaxial materials Concrete01 (Kent and Park 1971; Mander *et al.* 1988) and Steel02 (Giuffrè A and Pinto 1970; Menegotto and Pinto 1973; Filippou *et al.* 1983) were employed to simulate the core and cover concrete, and reinforcement steel, respectively (Figure 3-3c and d). Geometry and fiber discretization of the bridge pile cross sections (Figure 3-5c) are shown in Figure 3-6. In this figure, moment-curvature for each section under different axial load levels is displayed. It can be seen that the flexural strength of the Steel H-pile 10´57 is comparatively low (Figure 3-6), promoting the potential for damage at the corresponding locations of A1-A11 and D1-D11 near the abutments (Figure 3-5).

In addition, axial force-strain response for each fiber section is shown in Figure 3-6. In this regard, the Concrete01 material only displays strength in compression, with tension supported by the reinforcing steel (Figure 3-6).

3.4 Boundary and Loading Conditions

As mentioned above, both lateral mesh boundaries (X = 0 m and X = 300 m) are located away from the bridge structure (Figure 3-2and Figure 3-4). Along the longitudinal symmetry plane (Z =

40 m) of the model (Figure 3-4), no out of plane motion is allowed. Loading was implemented in a staged fashion following the steps outlined earlier in Su *et al.* (2017) and Qiu *et al.* (2020).

In this study, the base of the soil domain is located at a depth of 50 m from the ground surface (Figure 3-2), about 10 m away from the bridge foundations which were tipped into bedrock (layer TM). Lateral response of the soil strata below this 50 m depth was represented by the Lysmer-Kuhlemeyer (Lysmer and Kuhlemeyer 1969) dashpot boundary, applied along the base of the FE model (base V_s = 600 m/s, in the range of soft rock, slightly higher than stiffness of the overlying TM stratum), so as to avoid spurious wave reflections. As such, a dashpot is activated in the longitudinal X-direction at each node along the base, and the incident seismic wave excitation is defined by dynamic equivalent nodal forces (details of this process are presented earlier in Zhang *et al.* 2008 and Elgamal *et al.* 2008).

For the shaking phase (purely in the longitudinal direction), a realistic input motion was selected to demonstrate the liquefaction-induced key outcomes for the global bridge-ground system. As such, seismic motion (Figure 3-7) was simply taken as that of the 1994 Northridge earthquake ground surface Rinaldi Receiving Station record (Component S48W), scaled down to a peak amplitude of 0.3 g. This shaking level is similar to that of recorded motions that resulted in liquefaction and ground deformations in past California earthquakes such as Loma Prieta (Seed *et al.* 1990) and Superstition Hills (Zeghal and Elgamal 1994).

For the purpose of this study, deconvolution was employed as a simple approach (using Shake91 by Idriss and Sun 1993), to derive an incident earthquake motion (Figure 3-7), imparted (Elgamal *et al.* 2008) along the base of the FE model (elevation 0.0 in Figure 3-4). In this representation, free-field motion along both the left and right-side mesh boundaries (Figure 3-4) is generated by the included left and right boundary soil columns mentioned above.

3.5 Acceleration Response

Figure 3-7 shows acceleration response at various locations of the bridge-ground system (Figure 3-4). Motion along the ground surface is amplified and appears to be rather similar, in view of the stiff TM ground formation that surrounds the narrow waterway (Figure 3-2 and Figure 3-4). Since there is a larger extent of softer soils at the right-side slope compared to that at the left (Figure 3-2), peak spectral acceleration at R1 is slightly lower than that at L1. Nevertheless, the relatively

small difference in acceleration along the bridge deck and its abutments denotes influence of the connectivity exerted by the bridge structure.

3.6 Displacement

In the following, the computed results will be discussed at two specific time instants (Figure 3-8 - Figure 3-12) during the shaking phase: i) time step at maximum deck displacement (labeled as max time step, t = 2.9 s) to recognize inertial effects of the bridge-ground system, and ii) time step at the end of shaking (labeled as final time step, t = 20 s) to investigate permanent deformation.

3.6.1 Deformation at Maximum Deck Displacement

Figure 3-8 shows the longitudinal (i.e., X-direction) relative displacement contours at max deck displacement. It can be seen that the entire bridge-ground system is moving leftwards (Figure 3-8) at this specific time instant, with displacement of the TM soil narrow waterway on both side boundaries (X = 0 and X = 300 m) reaching about 0.07 m near the ground surface. Away from the bridge (Z = 0 m), slope crest displacements are significantly higher downslope (at R0), and lower upslope (at L0). At Z = 40 m, with the bridge deck connecting both sides, slope crest displacement (at R1) is lower than that at R0, restrained by resistance from the left side where L1 displacement became larger than that of L0.

3.6.2 Deformation at End of Shaking

Figure 3-9 depicts the longitudinal relative displacement contours at end of shaking. At the left and right boundaries, deformation of the TM soil narrow waterway was minimal, only reaching about 0.01 m (Figure 3-9 and Figure 3-10). Within the narrow waterway, the left and right downslope deformations are seen to interact, pushing against each other. Away from the bridge (Z = 0 m), downslope crest displacements were about -0.36 m at R0, compared to +0.03 m only at L0. At Z = 40 m, the bridge through its deck and foundations acted as a strut that reduced deformations from the R0 -0.36 m to R1 of about -0.09 m, with resistance mobilized from the left side where downslope deformation was reversed from the L0 of +0.03 m (downslope) to the L1 of -0.09 m (Figure 3-9 and Figure 3-10).

Figure 3-11 displays the vertical relative displacement contours at end of shaking. Peak settlement occurred near the right-side slope (location R0) and showed slumping of as much as 0.3 m (Figure 3-11). For this relatively narrow waterway geometry, the interaction of both slopes (Figure 3-11)

resulted in the narrow waterway central section experiencing upward ground heave of about 0.5 m (Figure 3-10and Figure 3-11). Such a response mechanism (Figure 3-1, Figure 3-11 and Cubrinovski *et al.* 2011, 2014) differs from the assumptions of the conventional 1D site liquefaction response and warrants further attention and scrutiny. Finally, settlement is significantly lower at Z = 40 m, due to presence of the bridge's structural system (location R1 compared to R0).

It is worth noting that considerable interaction is taking place in terms of downslope permanent displacements of both slopes. In this regard, if unrestrained by the slope on the other side of this narrow waterway (based on conducted 2D plane-strain simulations, not shown), the right- and left-side slopes would experience much higher displacements of 5.0 m and 0.24 m (Figure 3-12), respectively (compared to the 3D narrow waterway-influenced values of 0.65 m, and 0.05 m).

3.6.3 Bridge Deck Displacement

Figure 3-13 displays relative displacement of the bridge deck, and pile caps B and C. Permanent displacement is initiated during the 2.4 - 2.9 s time interval due to the large fling motion pulse in the base input acceleration (Figure 3-7). The bridge lurches first slightly to the right in the downslope direction for pile cap B. Thereafter, pile cap C moves sharply to the left (downslope at this location) and continues to accumulate displacements throughout the remainder of the shaking phase. Along with these longitudinal displacements, vertical settlement (Figure 3-13b) is also seen to be much larger at the right embankment compared to its left counterpart. As discussed above, this significant right-side downslope deformation has potentially helped to impede the corresponding left slope deformations, with pile cap B only exhibiting a permanent downslope value of +0.04 m. At the deck level, the large right-side downslope deformation forced the bridge to move leftwards, pushing into the left-side slope as an additional restraining mechanism.

3.6.4. Liquefaction and Accumulated Shear Strains

Figure 3-14 shows time histories of effective confinement p' divided by the initial value p'_0 (before shaking) at locations M2 and M3 (Figure 3-4). The ratio p'/p'_0 reaching 0 indicates loss of effective confinement due to liquefaction. With the medium dense Q2 sand at the elevation range of about 18.1-29.1 m, it is noted that the ratio p'/p'_0 at Z = 0.0 m decreased slightly faster than that at Z = 40 m closer to the bridge. Upon liquefaction, Q2 at both locations M2 and M3 attains its low specified residual shear strength of 2 kPa at zero p'/p'_0 (Figure 3-14c and Table 3-1). In light of the

large deformations of the right-side slope (Figure 3-9), accumulated shear strains in this Q2 stratum and in the soft Q3b (Figure 3-14c) are seen to be quite high. Away from the bridge (Z = 0.0 m), larger shear strains are noted within the Q3b (Figure 3-14d) and near the base of the liquefied Q2 strata (Figure 3-14c).

From the overall picture of shear strains γ_{xy} at the end of shaking (Figure 3-15), it may be noted that:

1. At the left and right boundaries of the ground domain, shear strain is relatively small reaching only about 0.5 %, mainly due to the high shear strength afforded by the stiff narrow waterway AF, Q3a and TM strata (Figure 3-2 and Table 3-2).

2. At the right-side slope (locations M2 and M3), downslope shear strains accumulated, reaching peak values of about 15 % near the base of the liquefied sand Q2 layer. As shown in Figure 3-15, the overall shear strain at location M3 (Z = 40 m close to the structure) is lower than that at location M2 (Z = 0 m away from the bridge), due to restraining effects of the bridge structure and its foundation.

3.7 Response of Bridge Structure

3.7.1 Axial Force

Figure 3-16 displays longitudinal displacement of the bridge structure and the deck axial forces at max time step and at end of shaking. At max time step, the entire bridge moves leftwards with peak displacement of about 0.18 m at pile cap C (Figure 3-16a). As such, axial compressive forces were imposed on the deck (Figure 3-16a).

Figure 3-16b shows longitudinal response at end of shaking with a peak displacement of about 0.5 m. As discussed above, both sides moved downslope towards the center of the narrow waterway, such that the entire bridge deck was in a compressive state (Figure 3-16b). Since there was no inertial effect, the axial force along the deck is constant within each span.

Figure 3-17 presents axial forces in the foundation piles before shaking, at max time step, and at end of shaking. As a reference, Figure 3-17a shows the computed self-weight axial forces, with all supporting elements under compression throughout (i.e., negative axial force). At max time step, pile groups B1-B10, C1-C10 (below elevation 30 m) and piles A9-A11 are under tension (positive axial force). For this particular deformed configuration, peak axial compressive force reached a

high value of about 3200 kN in piles D1-D5 (axial compressive yielding force being 3300 kN in Figure 3-6a) at the elevation range of about 21-35 m where the soft clay Q3b is encountered. These high values of axial force in piles D1-D5 are attributed to ground settlement at the right-side slope which exerted additional downdrag loads on these piles.

Nevertheless, all pile forces remained within the elastic capacity of the corresponding cross-sections (Figure 3-6). At end of shaking, most piles are in compression, except for sustaining a low level of tensile force (about 100 kN) at the lower zones of piles C1-C10 (Figure 3-17).

3.7.2 Bending Moment and Ductility Demand

Figure 3-18 depicts the bending moment profiles. Generally, it can be seen that the highest values occur at: i) the pier cap connection, ii) the interface between liquefied and non-liquefied soils, and iii) the pile-deck connections. Consequences of these observed moments are addressed next in the form of ductility demand defined as the ratio of ultimate attained curvature f to yield curvature f_y (= M_y/EI), where M_y denotes yield moment (NIST 2017) with reduction according to the acting axial compressive load (Figure 3-17c) as described in Appendix 3-A.

As such, Figure 3-19 shows the ductility demand profiles for the bridge foundations (values < 1 are not shown for clarity). It can be seen that the highest values occurred at: i) the pile-deck connection for piles A, D, (ii) the interface between liquefied and non-liquefied soils, and iii) pile segments within the zone of the soft clay Q3b for piles D. The attained peak values, reaching as much as 30 would generally be considered of much concern and would warrant closer scrutiny.

A note of considerable importance is that some of these highest values are occurring on the left side that experienced much lower downslope deformation. The reason being that the large downslope displacements of the right-side slope pushed the bridge structure leftwards causing these piles to experience significant lateral deformations at the top, in opposite direction to the underlying downslope ground movements at this location. As such, due to the interaction of the left and right-side slopes through the relatively rigid bridge deck, substantial deformations occurred at the abutment piles on both sides.

3.8 Bridge-ground System under Reverse Motion

To assess influence of input motion polarity, an additional numerical simulation was conducted reversing direction of the employed input motion (Figure 3-7a). The fling motion pulse in this

particular shaking record, which dictated a substantial level of the accumulated global deformations (Figure 3-9), motivated the investigation of this additional scenario. The results in terms of end of shaking displacement are shown in Figure 3-20 and Figure 3-21. From Figure 3-20, it can be seen that the right-side slope displacement (0.6 m) is slightly lower when compared to that of Figure 3-9(0.65 m). However, it is also seen that the left side downslope displacement became substantially higher.

The ductility demand at end of shaking is displayed in Figure 3-21. Despite the difference in the ground deformation pattern (Figure 3-9 and Figure 3-20), it appears that ductility demand ended up being rather similar under this particular shaking scenario (Figure 3-19 and Figure 3-21).

3.9 Retrofit Analyses

For illustration, potential use of the numerical model to conduct retrofit studies is addressed briefly in this section. For that purpose, two additional numerical simulations were conducted by adding concrete walls (linear elastic, with Young's modulus E = 30 GPa) around the abutment and wing walls (Figure 3-22). In configuring this mitigation approach, attention was given to the option where retrofit is implemented at the abutments rather than within the narrow waterway, where cost and effort would substantially increase. The conceptual mitigation mechanisms discussed below, would be implemented in practice by appropriate techniques to introduce equivalent stiffness and strength into the existing foundations.

The first scenario (Figure 3-22a and Figure 3-23a) was investigated for direct comparison to the original results (Figure 3-19) by adding a concrete wall on the outer side of the wing walls. As seen in Figure 3-23a, the ductility demand was significantly reduced at the upper section of piles A, D. Furthermore, the overall ductility demand values for abutment piles D in the soft clay Q3b stratum were reduced below 1. In the second scenario (Figure 3-22b), an additional wall was placed behind the abutment along with a pile cap of about 1.6 m in thickness. As seen in Figure 3-23b, ductility demand values were lower than 1 throughout, except for few locations with values close to 1 at top of abutment piles D. As such, repairs would be needed only close to the ground surface.

Along with the above ductility demand, Figure 3-24 shows the relative displacement time histories of bridge deck, and pile caps B and C. It can be seen that the longitudinal displacement of pile cap C and vertical settlement of location R1 are also reduced, in light of the increased overall stiffness and strength of the ground around the piles (scenarios 1 and 2).

3.10 Discussion

As discussed above, the employed 3D finite element model has been useful for the purpose of exploring key mechanisms associated with the overall bridge-ground system response. When applicable, closer semblance to actual conditions or scenarios can be achieved by refinements such as: i) a more detailed representation of the soil variability and its spatial distribution, ii) tracking of the construction sequence during the FE model own-weight application, iii) inclusion of numerical features to represent expansion/construction joints within the bridge deck, and details of the connectivity between the deck and its piers and abutments, iv) accounting for the effects of geometric nonlinearity with the evolution of large deformations, and v) subjecting the model to the full 3D picture of seismic excitation.

3.11 Summary and Conclusions

A full 3D FE analysis framework was presented to study a number of salient features associated with the liquefaction-induced seismic response of a bridge-ground system in a narrow waterway configuration (Cubrinovski *et al.* 2014). For that purpose, an idealized 3D FE model was developed, motivated by the details of an actual bridge-ground configuration. The bridge-ground system and the corresponding numerical analysis details were discussed. Displacement, moment, axial forces, and ductility demand of the structure, resulting from the liquefaction-induced ground deformations were explored. In addition, the bridge's restraining influence, and effect of input motion polarity were investigated. The numerical framework and the insights derived from this study are of general relevance to bridge-ground seismic response in narrow waterway scenarios. Specific observations and conclusions include:

1) For relatively narrow waterway geometries, downslope displacement of the side slopes may result in significant interference within the narrow waterway central section. For such situations, analysis of deformations at each slope separately might lead to unrealistic outcomes. The interference manifests in the form of upward heave within the central section. Such a deformation mechanism differs from the assumptions of conventional 1D site liquefaction response and might warrant further scrutiny in terms of liquefaction susceptibility and its consequences.

2) As highlighted in earlier studies (Shin *et al.* 2008; Zhang *et al.* 2008; Cubrinovski *et al.* 2014, McGann and Arduino 2015; Qiu *et al.* 2020), response is highly dependent on the soil ground system as an integral global entity. Connectivity provided by the bridge deck, soil profile and its

spatial variability, and geometric configuration of the narrow waterway are all factors that would significantly influence the outcome.

3) Damage mainly occurred at the pile-deck connection as observed by Cubrinovski *et al.* (2014) in an actual short-span bridge configuration. Other vulnerable locations include the interfaces between liquefiable and non-liquefiable or soft clay and stable soil strata.

4) The bridge structure and its foundations acted as a strut that exerted a significant added restraint to the slope deformations on both sides. These restraining effects partially stem from the bridge's global connectivity and the corresponding abutment-to-abutment interaction, which can be of much influence.

5) Peak demands might occur due to the combined inertial and kinematic load during the shaking event. In a simplified analysis, both inertial as well as kinematic load cases should be considered.

6) Sensitivity studies may be undertaken to further elucidate the significance of site stratigraphy, soil model properties, and ground motion characteristics on global response of the bridge-ground system. In addition, higher fidelity can be attained by subjecting the 3D model to the full picture of 3D seismic excitation.

3.12 References

Arduino, P., Ashford, S., Assimaki, D., Bray, J., Eldridge, T., Frost, D., Hashash, Y., Hutchinson, T., Johnson, L., Kelson, K. and Kayen, R. (2010). "*Geo-engineering reconnaissance of the 2010 Maule, Chile earthquake*." GEER Association Report No. GEER-022, 1.

Ashford, S.A., Boulanger, R.W., Brandenberg, S.J. and Shantz, T. (2009). "Overview of Recommended Analysis Procedures for Pile Foundations in Laterally Spreading Ground." In TCLEE 2009: *Lifeline Earthquake Engineering in a Multihazard Environment*, 1-8.

Ashford, S.A., Boulanger, R.W. and Brandenberg, S.J. (2011). "Recommended design practice for pile foundations in laterally spreading ground." *Pacific Earthquake Engineering Research Center. University of California, Berkeley, Calif.* PEER Rep, (2011/04).

Aygün, B., Dueñas-Osorio, L., Padgett, J.E. and DesRoches, R. (2009). "Seismic Vulnerability of Bridges Susceptible to Spatially Distributed Soil Liquefaction Hazards." *In Structures Congress 2009: Don't Mess with Structural Engineers: Expanding Our Role*, 1-10.

Aygün, B., Dueñas-Osorio, L., Padgett, J.E. and DesRoches, R. (2010). "Efficient longitudinal seismic fragility assessment of a multispan continuous steel bridge on liquefiable soils." *Journal of Bridge Engineering*, 16(1), 93-107.

Berrill, J.B., Christensen, S.A., Keenan, R.P., Okada, W. and Pettinga, J.R. (2001). "Case study of lateral spreading forces on a piled foundation." *Geotechnique*, 51(6), 501-517.

Boulanger, R.W., Chang, D., Brandenberg, S.J., Armstrong, R.J. and Kutter, B.L. (2007). "Seismic design of pile foundations for liquefaction effects." In *Earthquake Geotechnical Engineering*, 277-302. Springer, Dordrecht.

Caltrans (2017). Personal Communications.

Carlson, N.N. and Miller, K. (1998). "Design and application of a gradient-weighted moving finite element code I: in one dimension." *SIAM Journal on Scientific Computing*, 19(3), 728-765.

Chan A.H.C. (1988). "A unified finite element solution to static and dynamic problems in geomechanics." *PhD Thesis*, University College of Swansea.

Cubrinovski, M., Bradley, B., Wotherspoon, L., Green, R., Bray, J., Wood, C., Pender, M., Allen, J., Bradshaw, A., Rix, G. and Taylor, M. (2011). "Geotechnical aspects of the 22 February 2011

Christchurch earthquake." *Bulletin of the New Zealand Society for Earthquake Engineering*, 44(4), 205-226.

Cubrinovski, M., Winkley, A., Haskell, J., Palermo, A., Wotherspoon, L., Robinson, K., Bradley, B., Brabhaharan, P. and Hughes, M. (2014). "Spreading-induced damage to short-span bridges in Christchurch, New Zealand." *Earthquake Spectra*, 30(1), 57-83.

Elgamal, A., Yang, Z. and Parra, E. (2003). "Modeling of cyclic mobility in saturated cohesionless soils." *International Journal of Plasticity*, 19(6), 883-905.

Elgamal, A., Yan, L. and Yang, Z. (2008). "Three-dimensional seismic response of Humboldt Bay bridge-foundation-ground system." *Journal of Structural Engineering*, 134(7), 1165-1176.

Elgamal, A. and Lu, J. (2009). "A framework for 3D finite element analysis of lateral pile system response." *Contemporary Topics in In Situ Testing, Analysis, and Reliability of Foundations*, 616-623.

Elgamal, A., Lu, J., and Forcellini, D. (2009). "Mitigation of liquefaction-induced lateral deformation in a sloping stratum: Three-dimensional numerical simulation." *Journal of Geotechnical and Geoenvironmental Engineering*, 135(11), 1672-1682.

Filippou, F.C., Popov, E.P. and Bertero, V.V. (1983). "Effects of bond deterioration on hysteretic behavior of reinforced concrete joints. EERC Report 83-19." *Earthquake Engineering Research Center, University of California, Berkeley, Calif*.

Ghofrani, A., McGann, C. R. and Arduino, P. (2016). "Influence of modeling decisions on three-dimensional finite element analysis of two existing highway bridges subjected to lateral spreading." Transportation Research Record: *Journal of the Transportation Research Board*, (2592), 143-150.

Giuffrè, A. and Pinto, P. (1970). "II comportamento del cemento armato per sollecitazioni ciclichedi forte intensità." *G Genio Civ*. 5(1):391-408, [Italian].

Hamada, M., Isoyama, R. and Wakamatsu, K. (1996). "Liquefaction-induced ground displacement and its related damage to lifeline facilities." *Soils and foundations*, 36(Special), 81-97.

He, L., Ramirez, J., Lu, J., Tang, L., Elgamal, A. and Tokimatsu, K. (2017). "Lateral spreading near deep foundations and influence of soil permeability." *Canadian Geotechnical Journal*, 54(6):846-861.

Idriss, I.M. and Sun, J.I. (1993). "User's manual for SHAKE91: A computer program for conducting equivalent linear seismic response analyses of horizontally layered soil deposits." *Center for Geotechnical Modeling, Dept. of Civil and Environmental Engineering, University of California Press, Davis, CA*.

Idriss, I.M. and Boulanger, R.W. (2008). Soil liquefaction during earthquakes. *Earthquake Engineering Research Institute*.

Kent, D.C. and Park. R. (1971) "Flexural members with confined concrete." *Journal of the Structural Division*, No ST7, Proc Paper 8243, 97(11), 1969-1990.

Khosravifar, A., Elgamal, A., Lu, J. and Li, J. (2018). "A 3D model for earthquake-induced liquefaction triggering and post-liquefaction response." *Soil Dynamics and Earthquake Engineering*, 110, 43-52.

Ledezma, C. and Bray, J.D. (2010). "Probabilistic performance-based procedure to evaluate pile foundations at sites with liquefaction-induced lateral displacement." *Journal of Geotechnical and Geoenvironmental Engineering*, 136(3), 464-476.

Ledezma, C., Hutchinson, T., Ashford, S.A., Moss, R., Arduino, P., Bray, J.D., Olson, S., Hashash, Y.M., Verdugo, R., Frost, D. and Kayen, R. (2012). "Effects of ground failure on bridges, roads, and railroads." *Earthquake Spectra*, 28(S1), S119-S143.

Lu, J. (2006). "Parallel finite element modeling of earthquake ground response and liquefaction." *PhD Thesis*, UC San Diego.

Lu, J., Elgamal, A., Yan, L., Law, K. H. and Conte, J. P. (2011). "Large-scale numerical modeling in geotechnical earthquake engineering." *International Journal of Geomechanics*, 11(6), 490-503.

Lu, J., Kamatchi, P. and Elgamal, A. (2019). "Using stone columns to mitigate lateral deformation in uniform and stratified liquefiable soil strata." *International Journal of Geomechanics*, *19*(5), 04019026.

Lysmer, J. and Kuhlemeyer, R.L. (1969). “Finite Dynamic Model for Infinite Media.” *Journal of Engineering Mechanics Division*, 95, 859-878.

Mander, J.B., Priestley, M.J. and Park, R. (1988). “Theoretical stress-strain model for confined concrete.” *Journal of Structural Engineering*, 114(8), 1804-1826.

Mazzoni, S., McKenna, F., Scott, M. H. and Fenves, G. L. (2009). “Open System for Earthquake Engineering Simulation, User Command-Language Manual.” *Pacific Earthquake Engineering Research Center, University of California, Berkeley*, OpenSees version 2.0, May.

Menegotto, M. and Pinto, P. (1973). “Method of analysis for cyclically loaded RC plane frames including changes in geometry and non-elastic behavior of elements under combined normal force and bending.” In *Proc., IABSE Symp. on Resistance and Ultimate Deformability of Structures Acted on by Well Defined Repeated Loads*, 15-22. Zurich, Switzerland: International Association for Bridge and Structural Engineering.

McGann, C.R. and Arduino, P. (2014). “Numerical assessment of three-dimensional foundation pinning effects during lateral spreading at the Mataquito River Bridge.” *Journal of Geotechnical and Geoenvironmental Engineering*, 140(8), 04014037.

McGann, C. R. and Arduino, P. (2015). “Numerical assessment of the influence of foundation pinning, deck resistance, and 3D site geometry on the response of bridge foundations to demands of liquefaction-induced lateral soil deformation.” *Soil Dynamics and Earthquake Engineering*, 79, 379-390.

McGann, C.R. (2020). “Parametric Assessment of Equivalent Static Procedure Accounting for Foundation-Pinning Effects in Analysis of Piled Bridge Abutments Subject to Lateral Spreading.” *Journal of Geotechnical and Geoenvironmental Engineering*, 146(7), 04020055.

McKenna, F., Scott, M. and Fenves, G. (2010). “Nonlinear finite-element analysis software architecture using object composition.” *Journal of Computing in Civil Engineering*, 24(1), 95-107.

NIST (2017). “Guidelines for Nonlinear Structural Analysis for Design of Buildings, Part IIa – Steel Moment Frames.” NIST GCR 17-917-46v1, prepared by the Applied Technology Council for the National Institute of Technology and Standards, Gaithersburg, Maryland (https://doi.org/10.6028/NIST.GCR.17-917-46v2).

Padgett, J.E., Ghosh, J. and Dueñas-Osorio, L. (2013). "Effects of liquefiable soil and bridge modelling parameters on the seismic reliability of critical structural components." *Structure and Infrastructure Engineering*, 9(1), 59-77.

Parra, E. (1996). "Numerical modeling of liquefaction and lateral ground deformation including cyclic mobility and dilation response in soil systems." *PhD Thesis*, Rensselaer Polytechnic Institute.

Qiu, Z., Ebeido, A., Almutairi, A., Lu, J., Elgamal, A., Shing, P.B. and Martin, G. (2020). "Aspects of bridge-ground seismic response and liquefaction-induced deformations." *Earthquake Engineering & Structural Dynamics*, 49(4), 375-393.

Seed, R.B., Dickenson, S.E., Riemer, M.F., Bray, J.D., Sitar, N., Mitchell, J.K., Idriss, I.M., Kayen, R.E., Kropp, A., Harder, Jr. L.F. and Power, M.S. (1990). "Preliminary report on the principal geotechnical aspects of the October 17, 1989 Loma Prieta earthquake," Report No. UCB/EERC-90/05, UC Berkeley, Berkeley, CA.

Scott, M. and Fenves, G. (2006). "Plastic hinge integration methods for force-based beam-column elements." *Journal of Structural Engineering*, 132(2), 244-252.

Scott, M. and Ryan, K. (2013). "Moment-rotation behavior of force-based plastic hinge elements." *Earthquake Spectra*, 29(2), 597-607.

Shin, H., Arduino, P., Kramer, S.L. and Mackie, K. (2008). "Seismic response of a typical highway bridge in liquefiable soil." In *Geotechnical Earthquake Engineering and Soil Dynamics IV*, 1-11.

Soltanieh, S., Memarpour, M. M. and Kilanehei, F. (2019). "Performance assessment of bridge-soil-foundation system with irregular configuration considering ground motion directionality effects." *Soil Dynamics and Earthquake Engineering*, 118, 19-34.

Su, L., Lu, J., Elgamal, A. and Arulmoli, A.K. (2017). "Seismic performance of a pile-supported wharf: Three-dimensional finite element simulation." *Soil Dynamics and Earthquake Engineering*, 95, 167-179.

Tokimatsu, K. and Asaka, Y. (1998). "Effects of liquefaction-induced ground displacements on pile performance in the 1995 Hyogoken-Nambu earthquake." *Soils and Foundations*, 38(Special), 163-177.

Turner, B., Brandenberg, S.J. and Stewart, J.P. (2013). "Evaluation of collapse and non-collapse of parallel bridges affected by liquefaction and lateral spreading," *Proc. 10th International Conf. on Urban Earthquake Engin.*, Center for Urban Earthquake Engineering, March 1-2, 2013, Tokyo Institute of Technology, Tokyo, Japan.

Turner, B.J., Brandenberg, S.J. and Stewart, J.P. (2016). "Case study of parallel bridges affected by liquefaction and lateral spreading." *Journal of Geotechnical and Geoenvironmental Engineering*, 142(7), 05016001.

Verdugo, R., Sitar, N., Frost, J.D., Bray, J.D., Candia, G., Eldridge, T., Hashash, Y., Olson, S.M. and Urzua, A. (2012) "Seismic performance of earth structures during the February 2010 Maule, Chile, earthquake: dams, levees, tailings dams, and retaining walls." *Earthquake Spectra*, 28(S1), S75-S96.

Wotherspoon, L., Bradshaw, A., Green, R., Wood, C., Palermo, A., Cubrinovski, M. and Bradley, B. (2011). "Performance of bridges during the 2010 Darfield and 2011 Christchurch earthquakes." *Seismological Research Letters*, 82(6), 950-964.

Wang, Z., Dueñas-Osorio, L. and Padgett, J.E. (2013a). "Seismic response of a bridge–soil–foundation system under the combined effect of vertical and horizontal ground motions." *Earthquake Engineering and Structural Dynamics*, 42(4), 545-564.

Wang, Z., Padgett, J.E. and Dueñas-Osorio, L. (2013b). "Influence of vertical ground motions on the seismic fragility modeling of a bridge-soil-foundation system." *Earthquake Spectra*, 29(3), 937-962.

Yang, Z. (2000). "Numerical modeling of earthquake site response including dilation and liquefaction." *PhD Thesis*, Columbia University.

Yang Z. and Elgamal A. (2002). "Influence of permeability on liquefaction-induced shear deformation." *Journal of Engineering Mechanics*, 128(7), 720-729.

Yang, Z., Elgamal, A. and Parra, E. (2003). "Computational model for cyclic mobility and associated shear deformation." *Journal of Geotechnical and Geoenvironmental Engineering*, 129(12), 1119-1127.

Yang, Z., Lu, J. and Elgamal, A. (2008). "OpenSees soil models and solid-fluid fully coupled elements." User's manual: Version 1. La Jolla, CA: Univ. of California, San Diego.

Youd, T.L. (1993). “Liquefaction-induced damage to bridges.” *Transportation Research Record*, 1411, 35-41.

Zeghal, M. and Elgamal, A.W. (1994). “Analysis of site liquefaction using earthquake records.” *Journal of geotechnical engineering*, 120(6), 996-1017.

Zhang, Y., Conte, J.P., Yang, Z., Elgamal, A., Bielak, J. and Acero, G. (2008). “Two-dimensional nonlinear earthquake response analysis of a bridge-foundation-ground system.” *Earthquake Spectra*, 24(2), 343-386.

Appendix 3-A

As presented in NIST (2017), the yield moment M_y of a steel column refers to its effective flexural yield strength ($= 1.15ZR_yF_y$) reduced by the acting axial compressive load, where the factor 1.15 accounts for the effects of cyclic hardening, Z is the section plastic modulus, R_y (taken as 1 in this paper) is the ratio of the steel expected yield stress to the specified yield stress F_y. As such, M_y is defined as (NIST 2017):

$$\begin{aligned} &\text{If } P/P_{ye} \le 0.2,\ M_y = 1.15ZR_yF_y(1-P/P_{ye}) \\ &\text{If } P/P_{ye} > 0.2,\ M_y = 1.15ZR_yF_y\left[\frac{9}{8}(1-P/P_{ye})\right] \end{aligned} \tag{A-1}$$

where, P is the compressive axial load, $P_{ye} = R_yF_yA$ is the expected column yield force, and A is the cross-sectional area of the Steel H-pile. On this basis, at end of shaking, the yield curvature ϕ_y for calculation of ductility demand ($= \phi/\phi_y$) is shown in Figure 3-25.

Table 3-1 Sand PressureDependMultiYield03 (Khosravifar *et al.* 2018) model parameters (Figure 3-2).

Model Parameters		Q2	Q4
Reference mean effective pressure, p'_r (atm)		2.0	2.7
Mass density, □ (t/m^3)		1.89	1.92
Maximum shear strain at reference pressure, $g_{max,r}$		0.1	0.1
Low-strain shear modulus at reference pressure, G_r (MPa)		73.8	104
Stiffness dependence coefficient d, $G = G_r(\frac{P'}{P'_r})^d$		0.5	0.5
Poisson's ratio v for dynamics		0.4	0.4
Shear strength at zero confinement, c (kPa)		2.0	2.0
Friction angle f, with resulting shear strength defined as $p'\sin f$		35°	37°
Phase transformation angle		29°	30°
Contraction coefficient, c_1		0.035	0.02
Contraction coefficient, c_2		3.0	3.0
Contraction coefficient, c_3		0.2	0.2
Dilation coefficient, d_1		0.15	0.2
Dilation coefficient, d_2		3.0	3.0
Dilation coefficient, d_3		0.2	0.2
Additional contraction parameters			
	b_1	0.2	0.15
	b_2	20	20
	b_3	0.0	0.0
	b_4	0.001	0.001

Note: For each involved soil layer, the soil-pile friction angle δ and/or the soil-pile adhesion c_A are assumed equal to the corresponding friction angle and/or cohesion, respectively.

Table 3-2 Clay (PressureIndependMultiYield in OpenSees, PIMY) model parameters (Figure 3-2).

Model parameters	AF	Q1	Q3a	Q3b	TM
Mass density, □ (t/m^3)	1.92	1.84	1.92	1.84	2.16
Shear modulus, *G* (MPa)	117	71	139.3	75.2	293.0
Poisson's ratio for dynamics, *v*	0.4	0.4	0.4	0.4	0.4
Shear strength (kPa)	80.0	40.0	108.0	53.0	400.0
Shear strain at maximum shear strength	0.1	0.1	0.1	0.1	0.1

Note: For each involved soil layer, the soil-pile adhesion c_A is assumed equal to the corresponding cohesive strength.

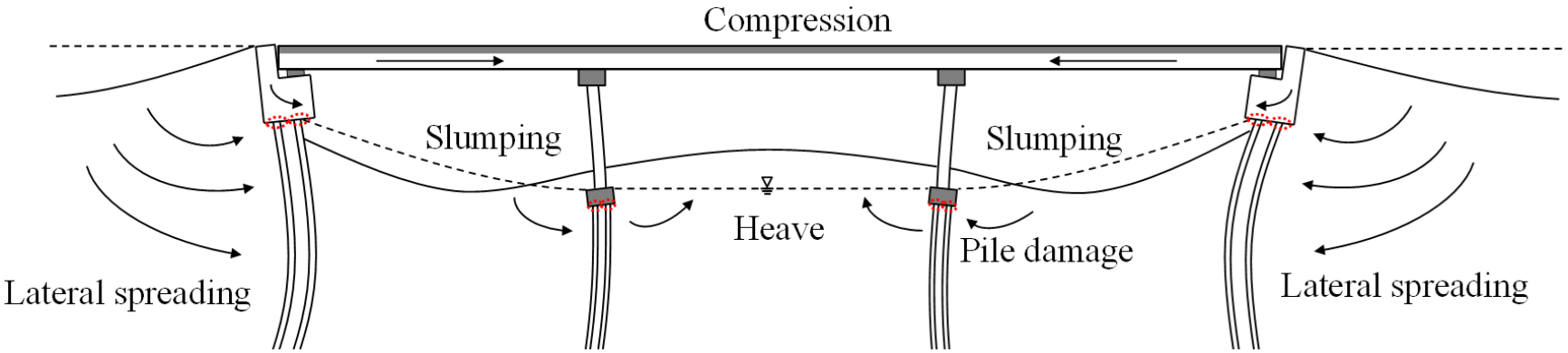

Figure 3-1. Schematic illustration of the liquefaction-induced bridge and ground deformation mechanism.

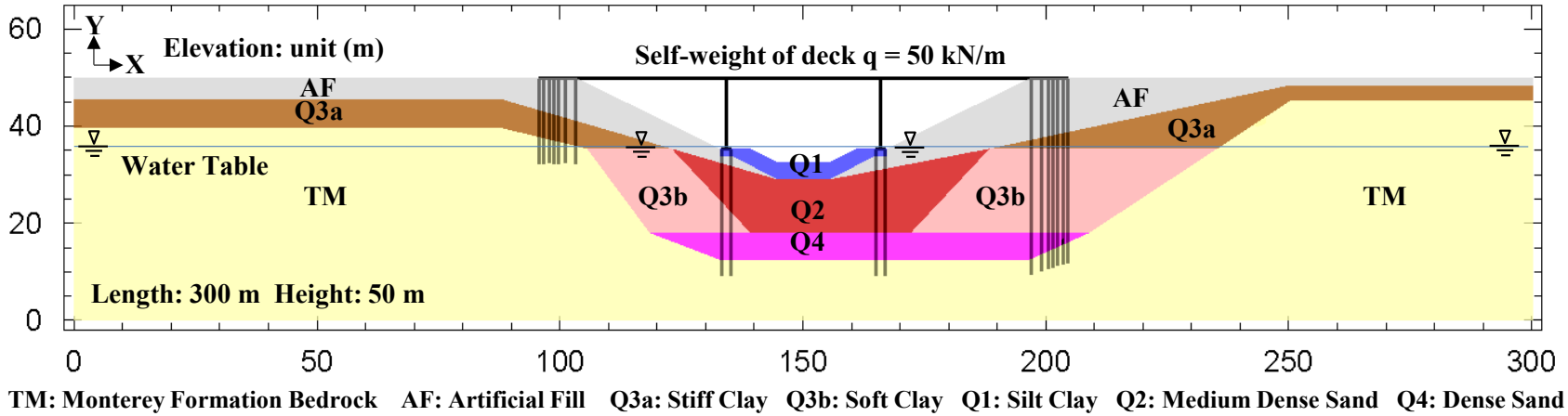

Figure 3-2. Ground configuration.

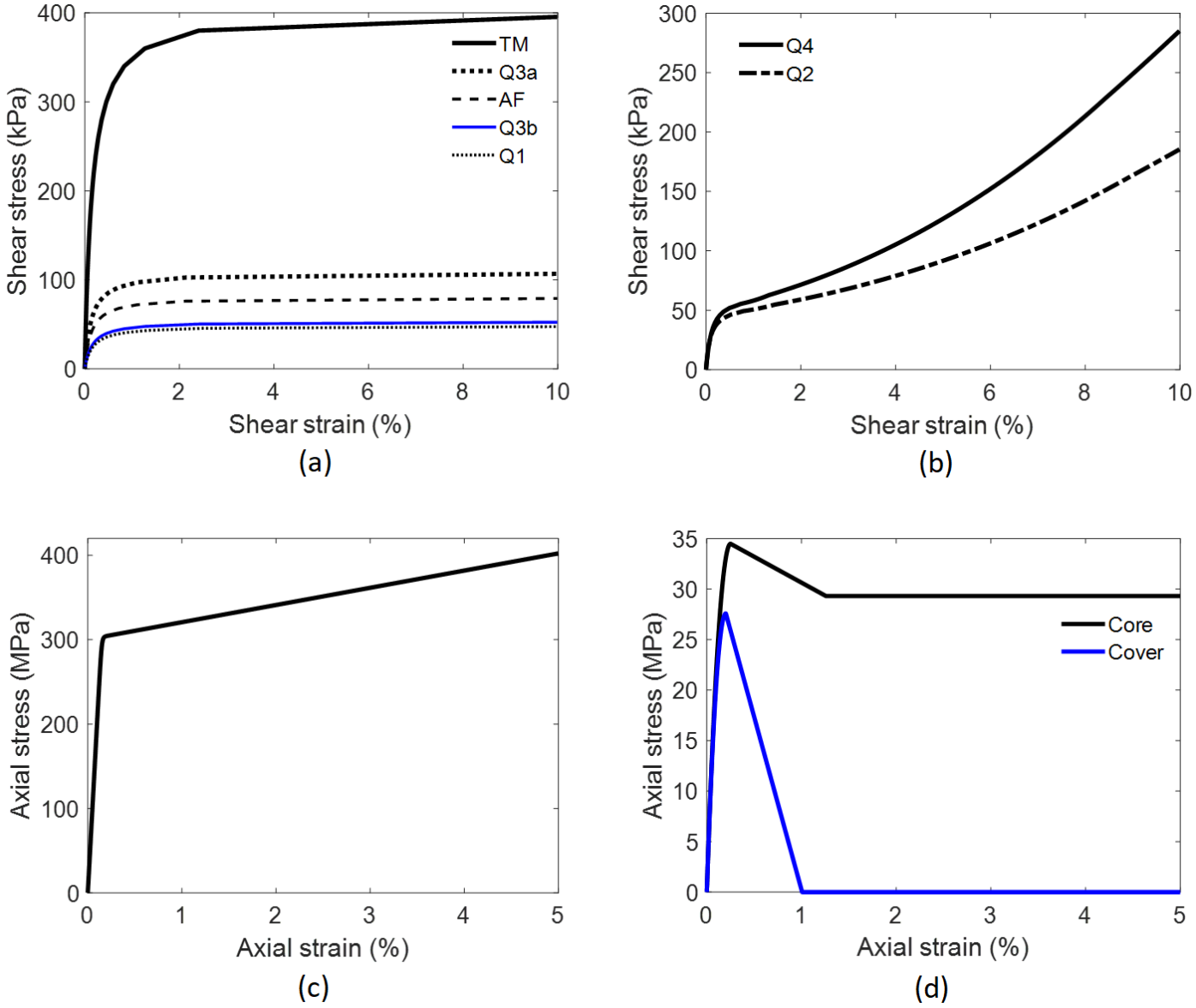

Figure 3-3. Material model response: (a) Clay (PIMY); (b) Sand model under undrained condition; (c) Steel02; (d) Concrete01.

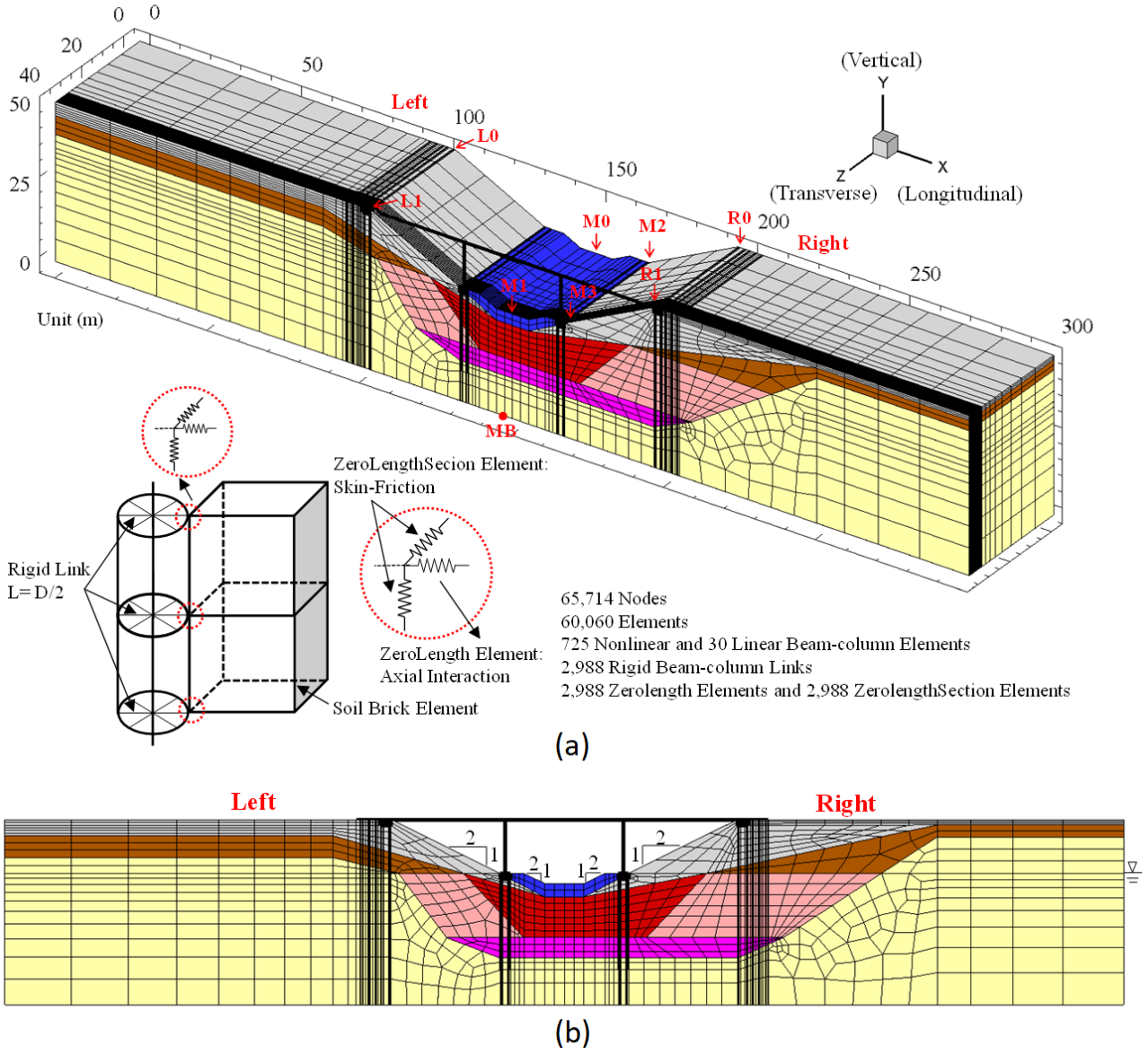

Figure 3-4. Finite Element model of bridge-ground system (half mesh due to symmetry): (a) Isometric view; (b) Elevation view.

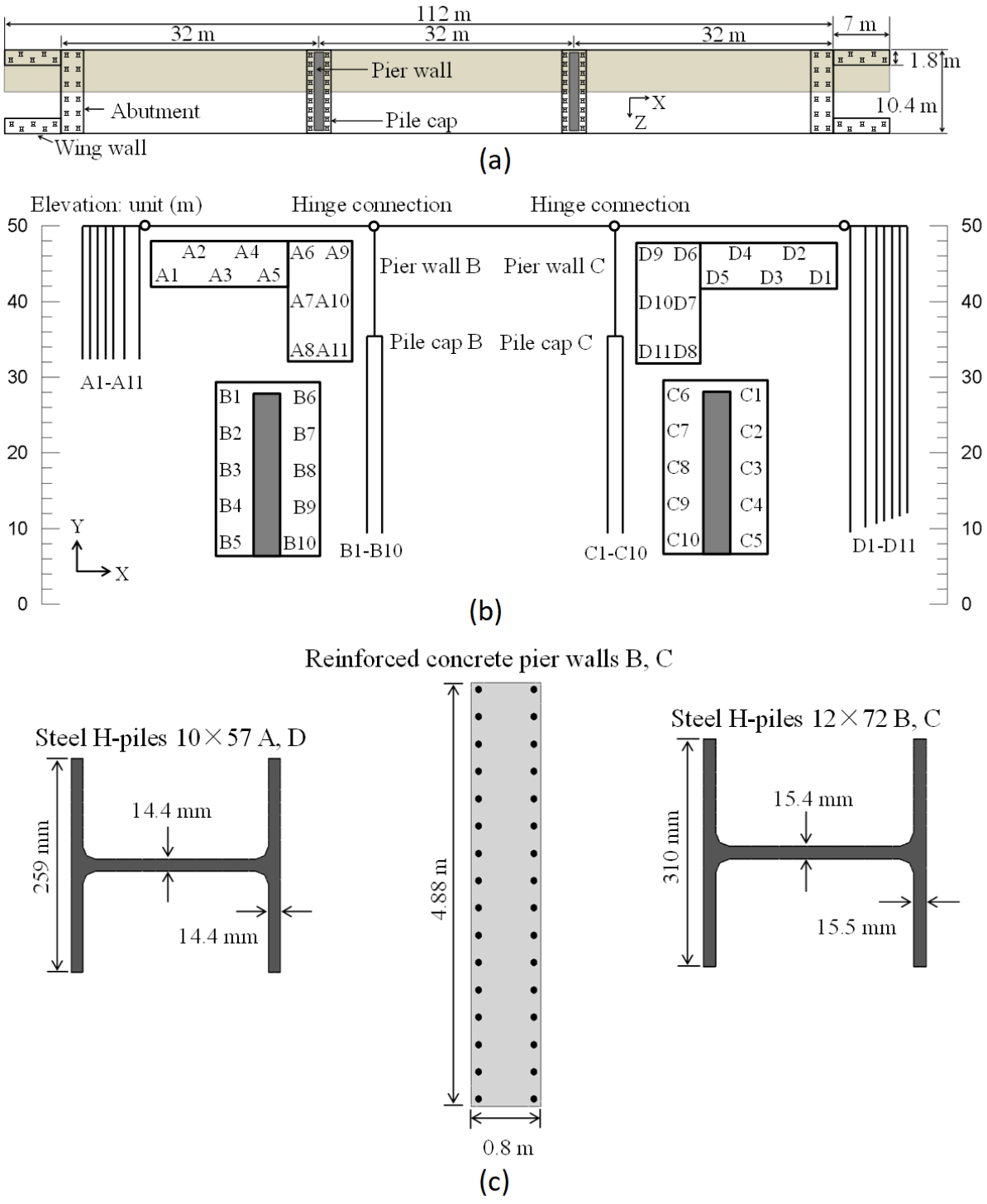

Figure 3-5. Bridge configuration: (a) Plan view (upper half of bridge is modeled in view of symmetry); (b) Elevation view of bridge and plan view of foundations systems in the FE half mesh configuration; (c) Cross sections.

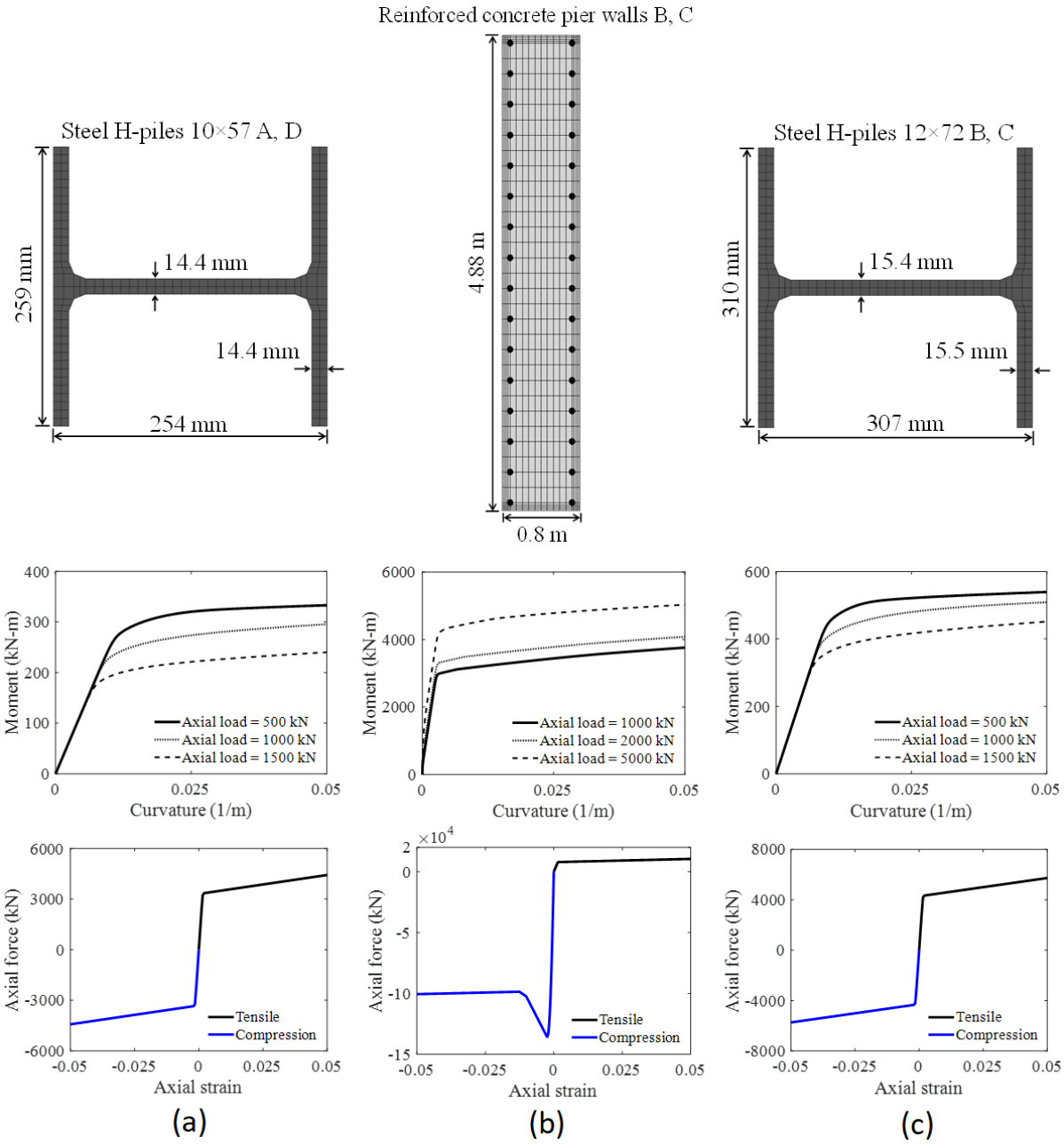

Figure 3-6. Fiber sections and response: (a) Piles A, D; (b) Pier walls B, C; (c) Piles B, C.

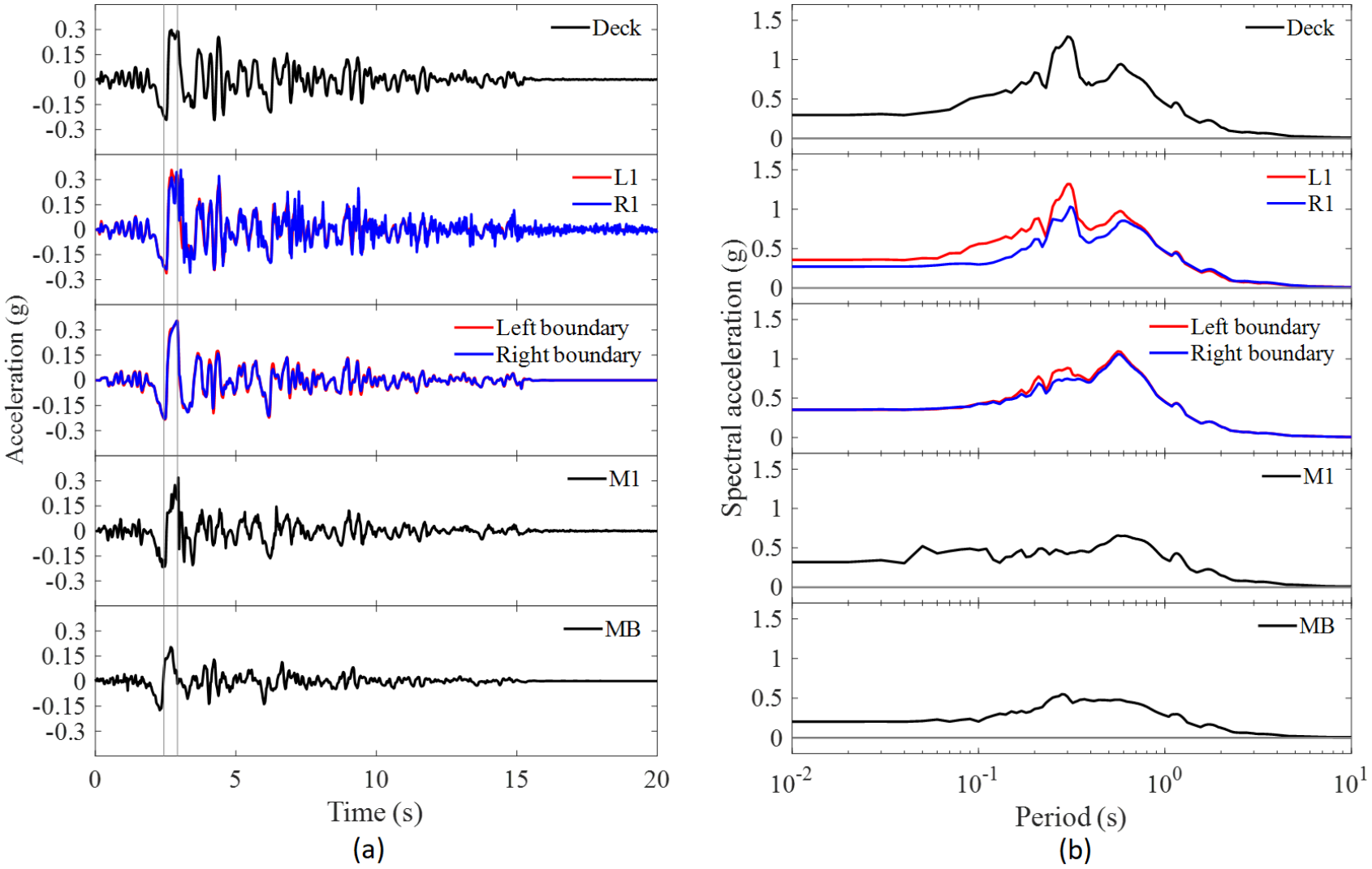

Figure 3-7. Acceleration response (locations are summarized in Figure 3-4): (a) Time histories; (b) Spectra (5 % damped).

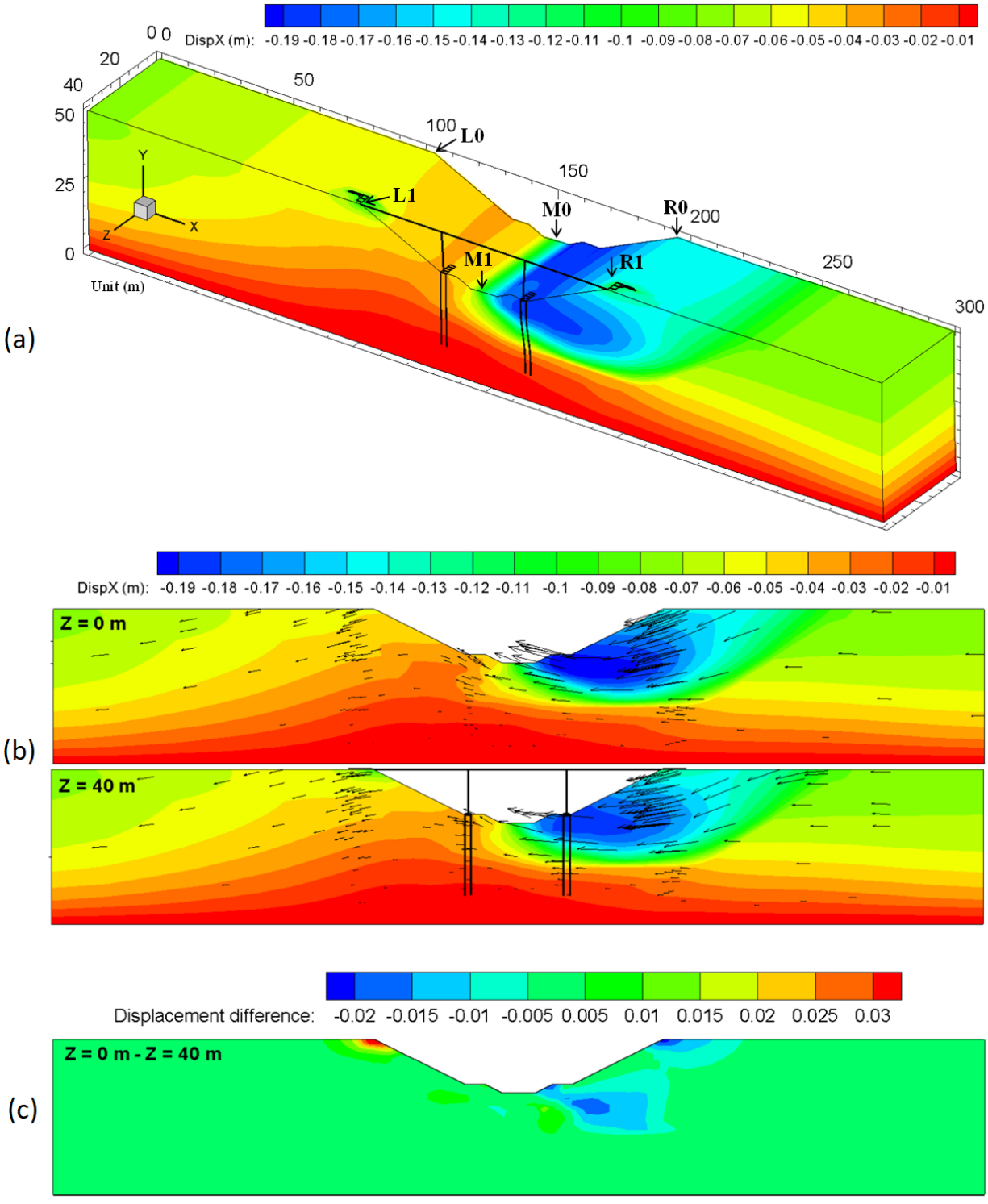

Figure 3-8. Longitudinal displacement contours at maximum deck displacement: (a) Isometric view (factor = 10); (b) Side views at Z = 0 m, 40 m (factor = 10; arrows displaying direction of ground movement); (c) Difference between Z = 0 and 40 m.

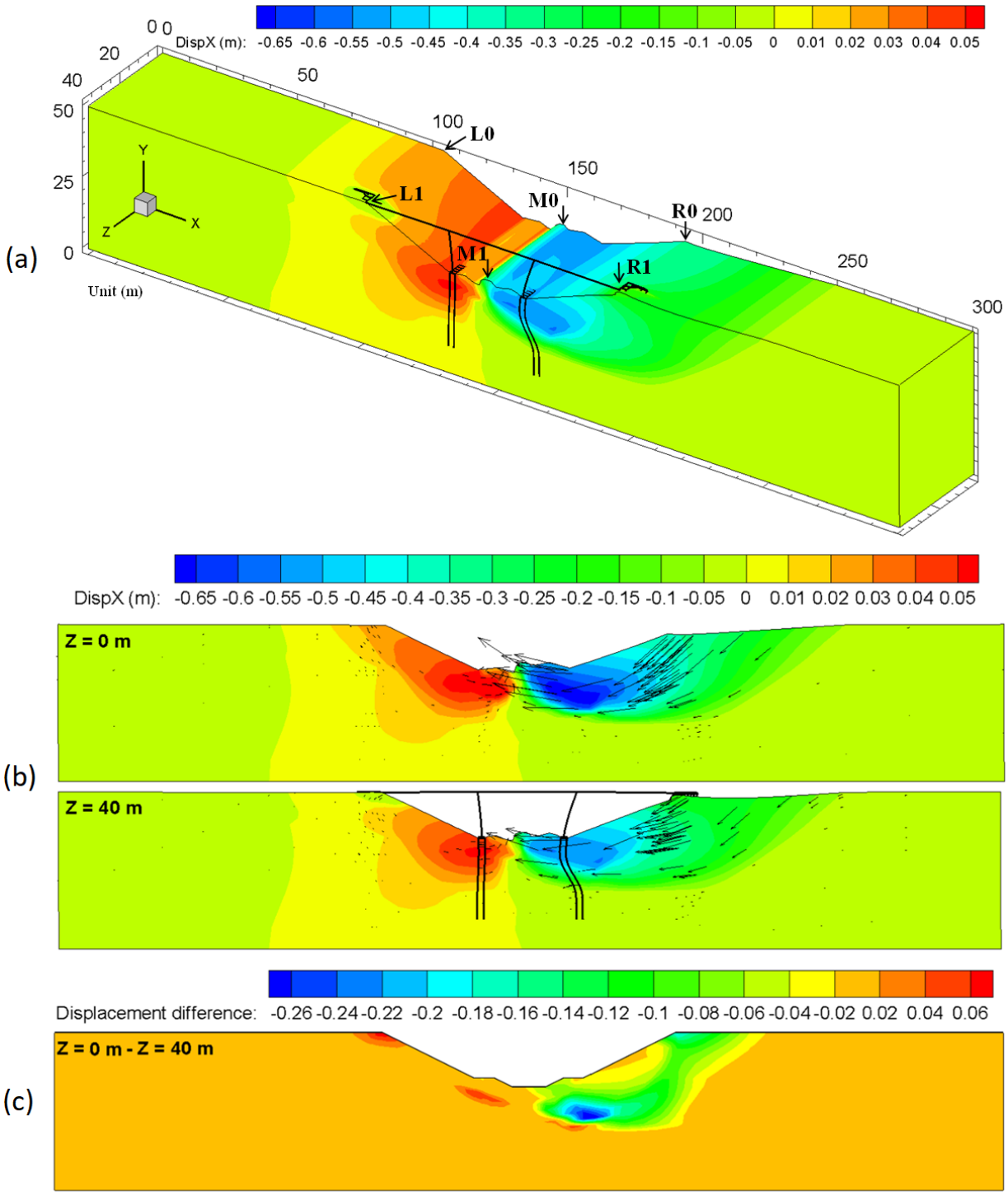

Figure 3-9. Longitudinal displacement contours at end of shaking: (a) Isometric view (factor = 10); (b) Side views at Z = 0 m, 40 m (factor = 10; arrows displaying direction of ground movement); (c) Difference between Z = 0 and 40 m.

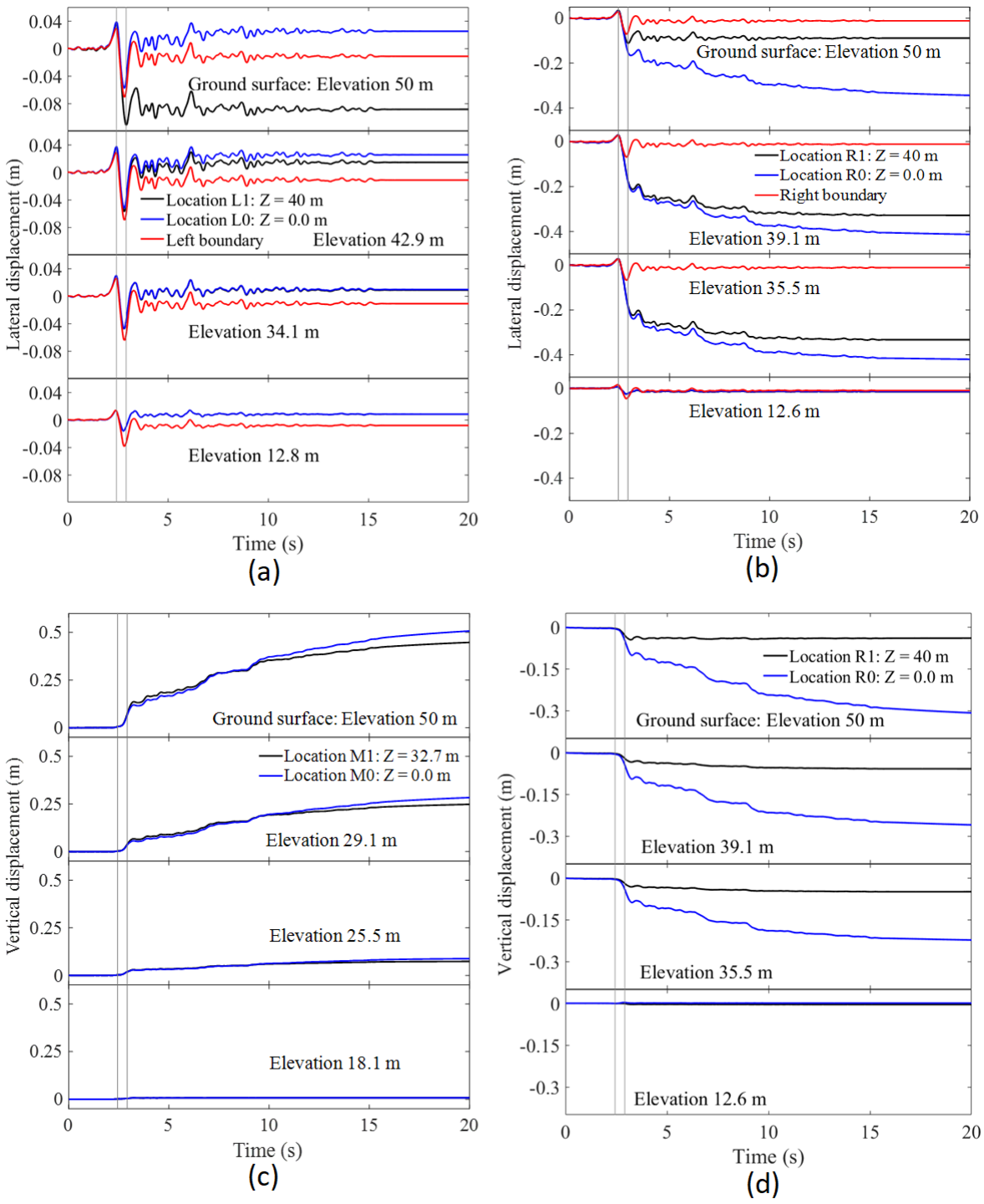

Figure 3-10. Ground displacement time histories (locations are summarized in Figure 3-4): (a) Locations L0, L1; (b) Locations R0, R1 (horizontal); (c) Locations M0, M1; (d) Locations R0, R1 (vertical).

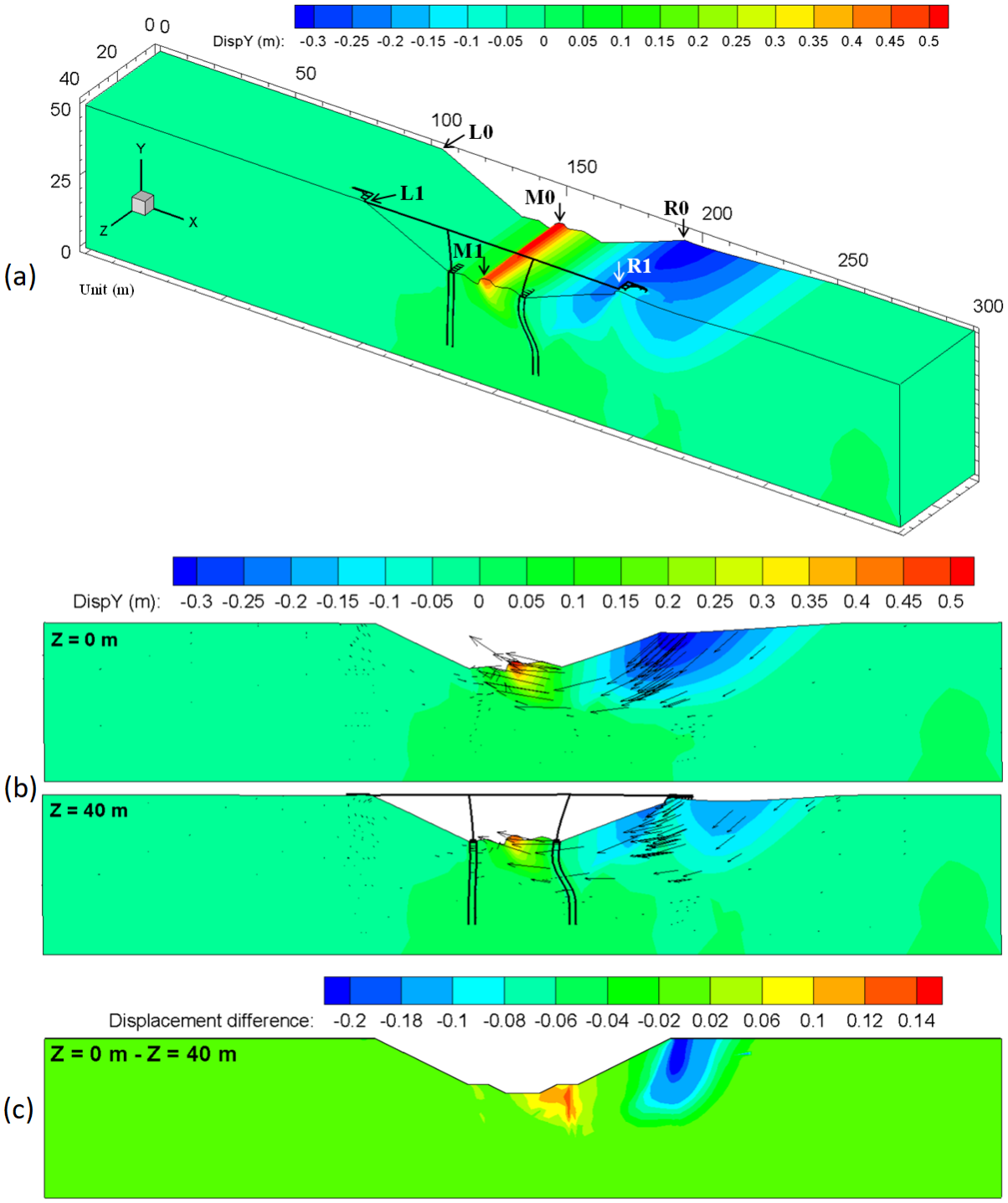

Figure 3-11. Vertical displacement contours at end of shaking: (a) Isometric view (factor = 10); (b) Side views at Z = 0 m, 40 m (factor = 10; arrows displaying direction of ground movement); (c) Difference between Z = 0 and 40 m.

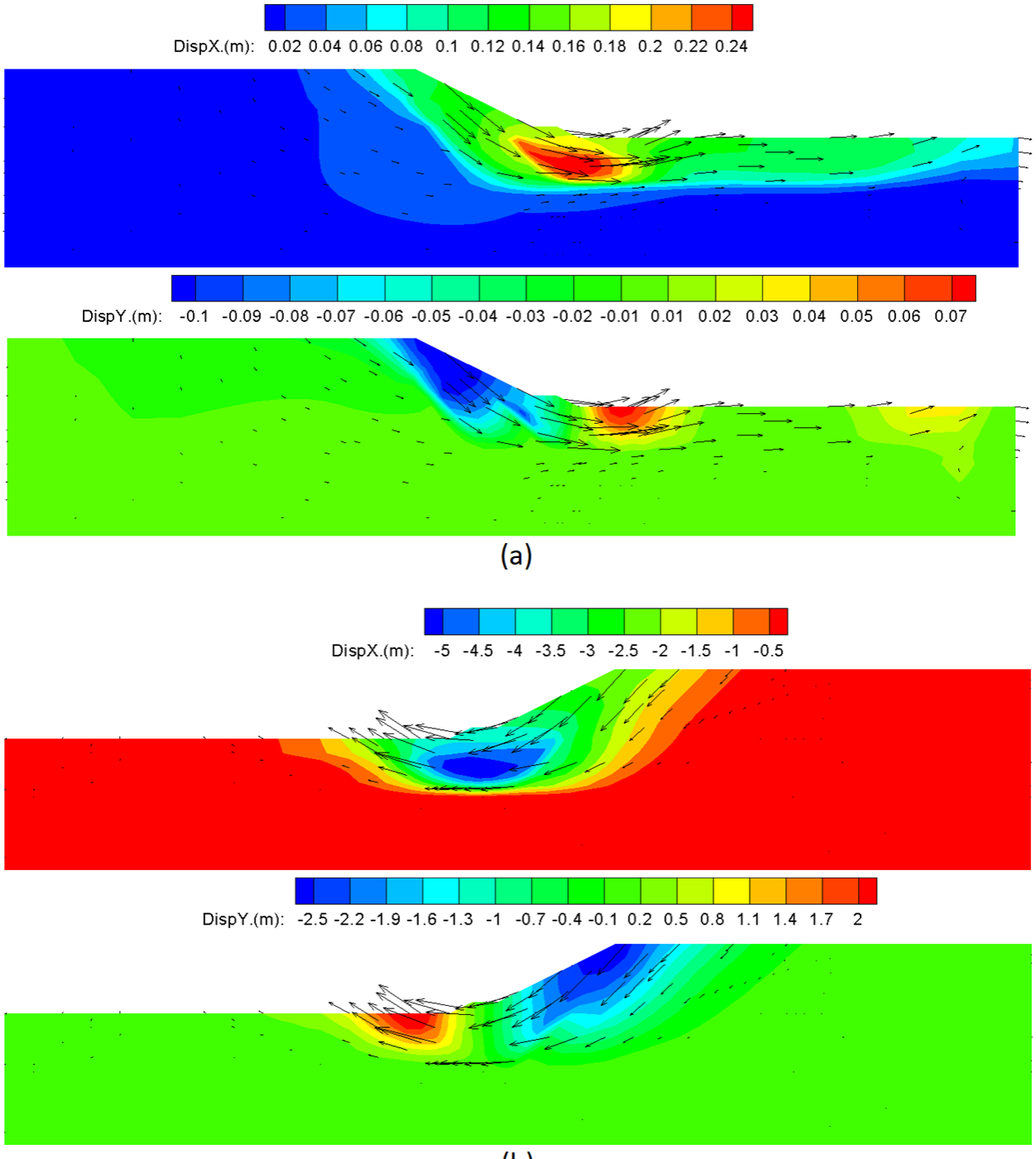

Figure 3-12. Longitudinal and vertical displacement contours of 2D plane-strain simulations at end of shaking: (a) Left-side slope; (b) Right-side slope.

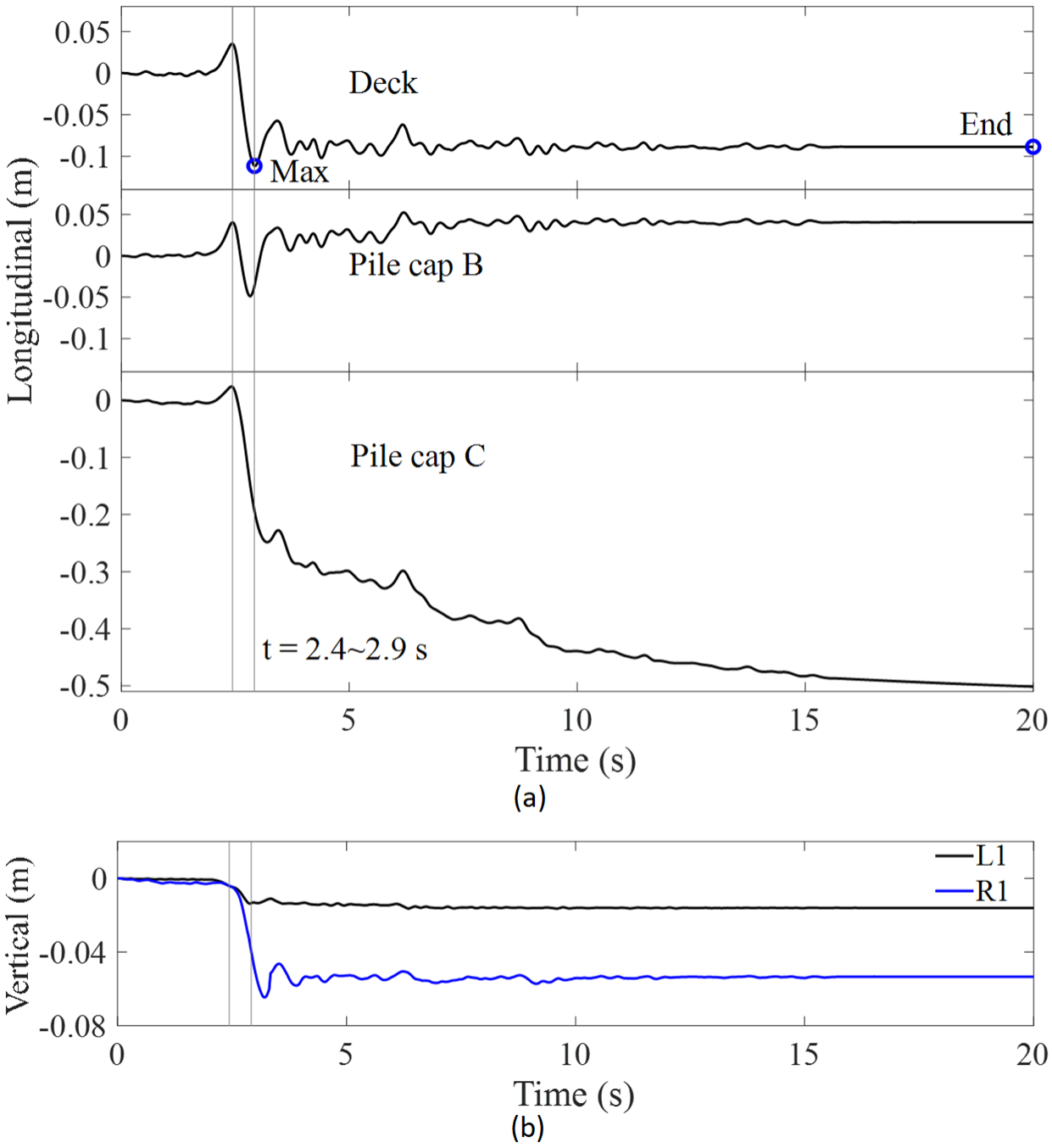

Figure 3-13. Bridge relative displacement time histories (locations are summarized in Figure 3 4): (a) Longitudinal (positive towards the right and negative towards the left); (b) Vertical (negative is settlement).

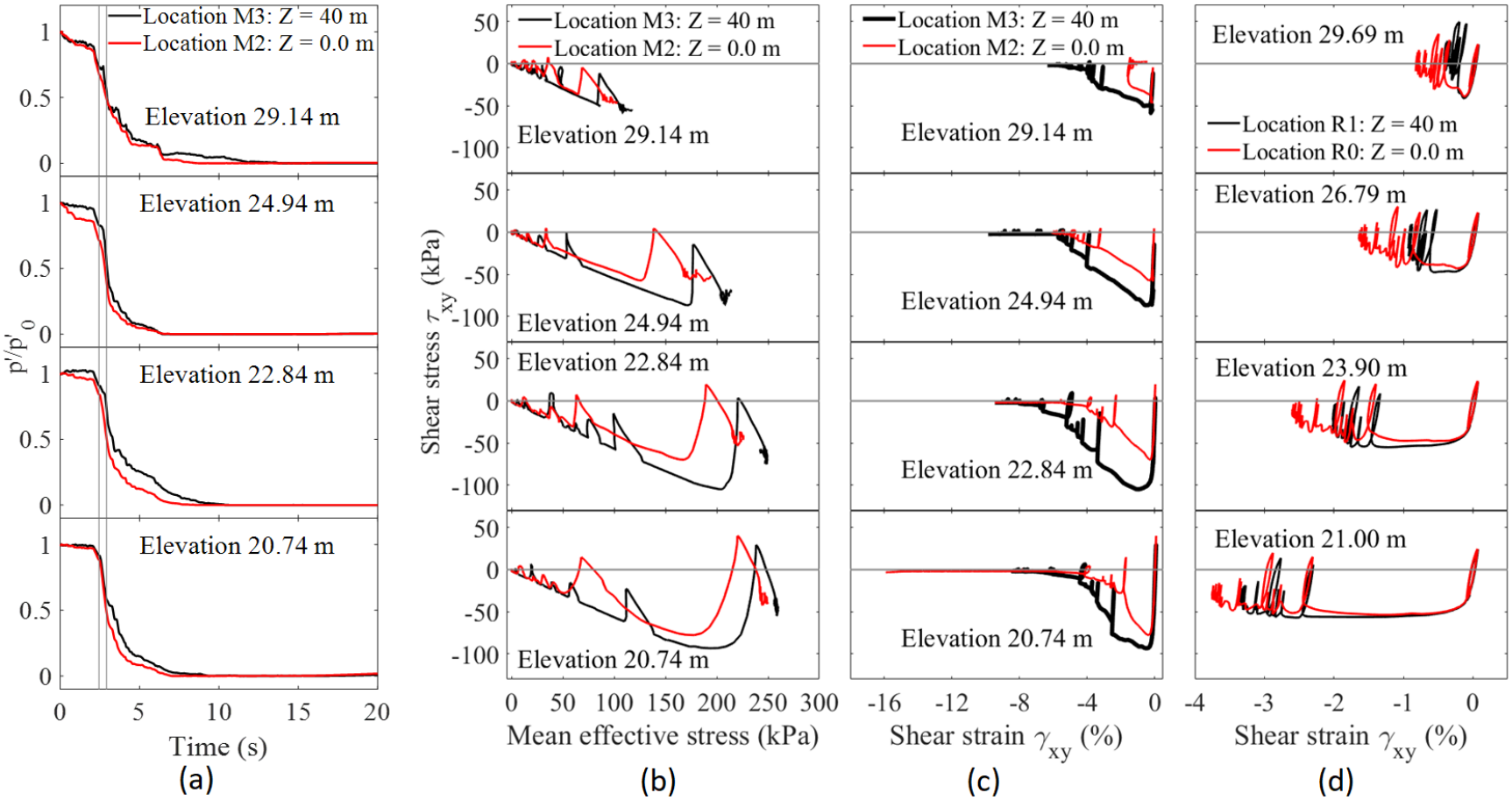

Figure 3-14. Soil response (locations are summarized in Figure 3-4): (a) Effective confinement ratio at locations M2, M3; (b) Mean effective stress-shear stress at locations M2, M3; (c) Shear stress-strain at locations M2, M3; (d) Shear stress-strain in Q3b clay layer at locations R0, R1.

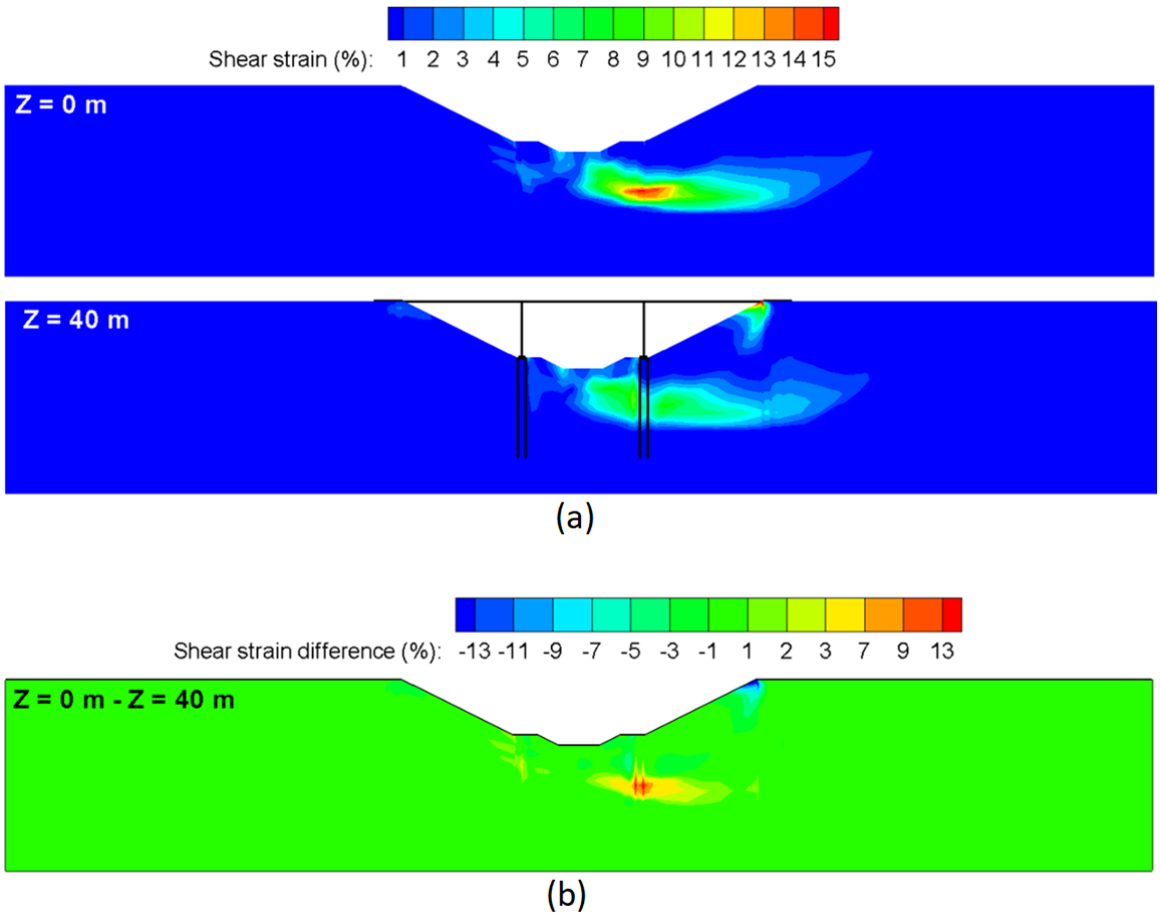

Figure 3-15. Contour of shear strain γ_{xy} at end of shaking: (a) Side views at Z = 0 m, 40 m; (b) Difference between Z = 0 and 40 m.

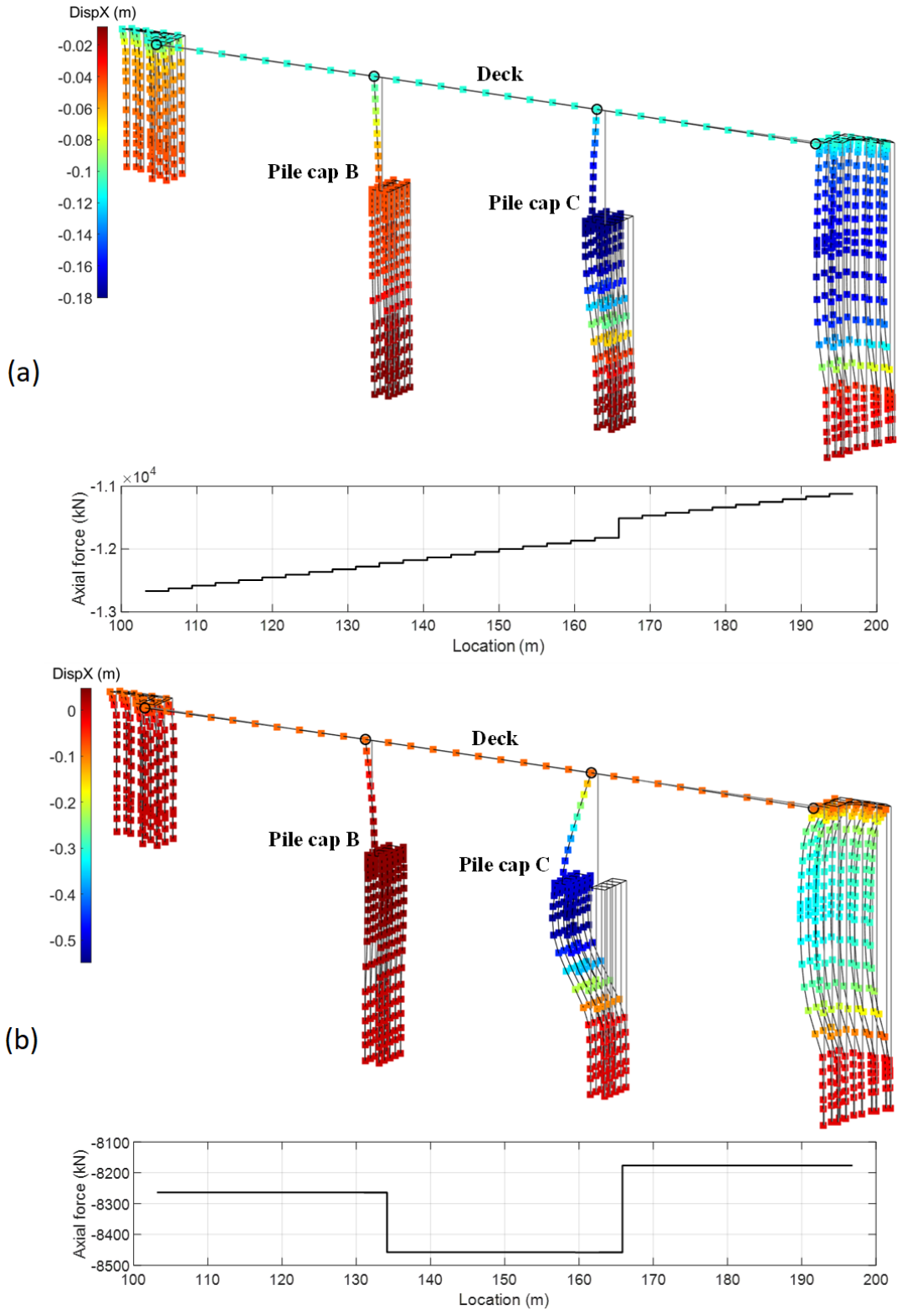

Figure 3-16. Deformed FE mesh of bridge and deck axial forces: (a) At maximum deck displacement; (b) At end of shaking (contour fill shows the horizontal displacement; factor = 10).

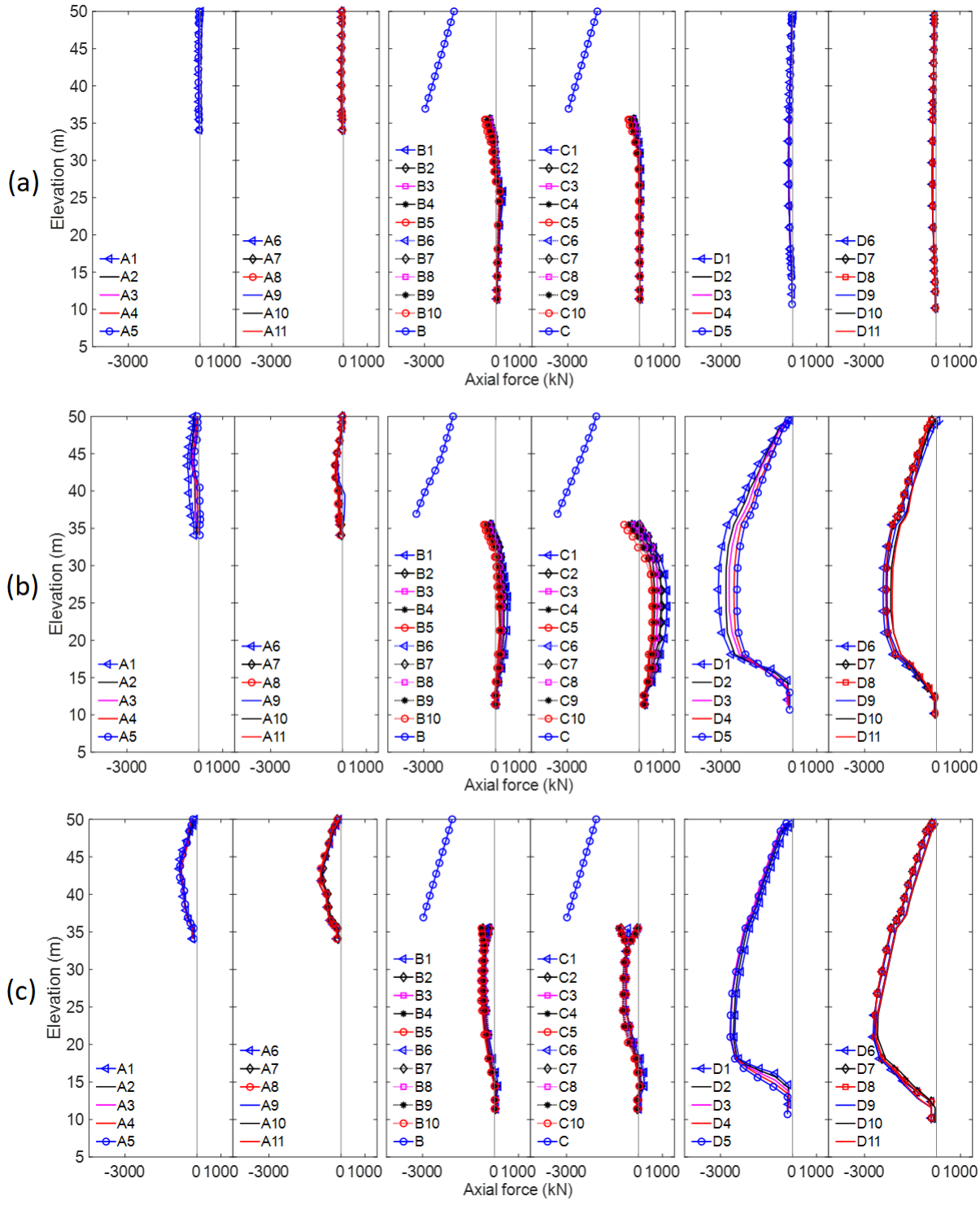

Figure 3-17. Axial force: (a) Before shaking; (b) At maximum deck displacement; (c) At end of shaking (negative represents compression and positive represents tension).

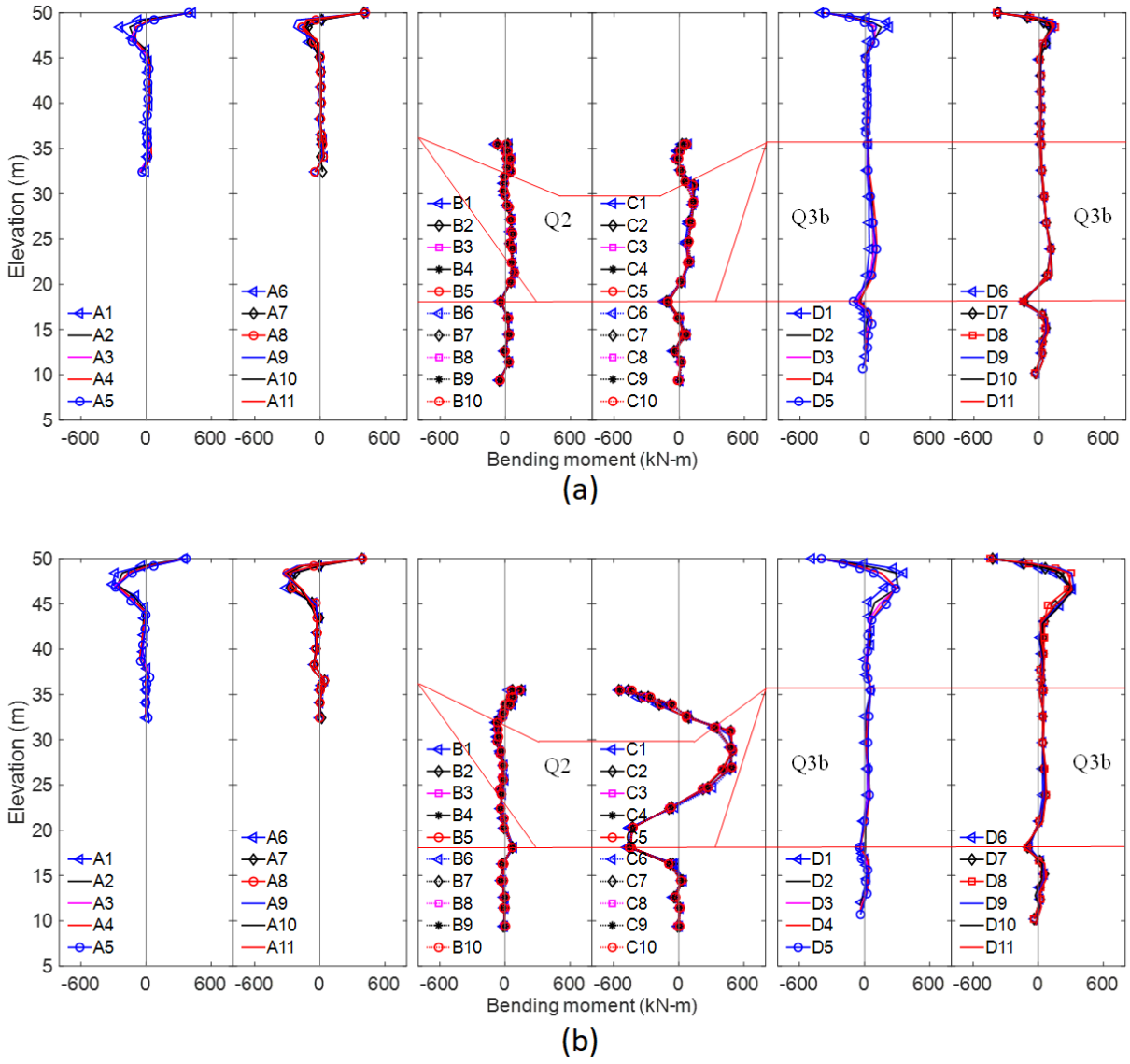

Figure 3-18. Bending moment (red line represents outline of medium dense sand Q2 and soft clay Q3b layers): (a) At maximum deck displacement; (b) At end of shaking.

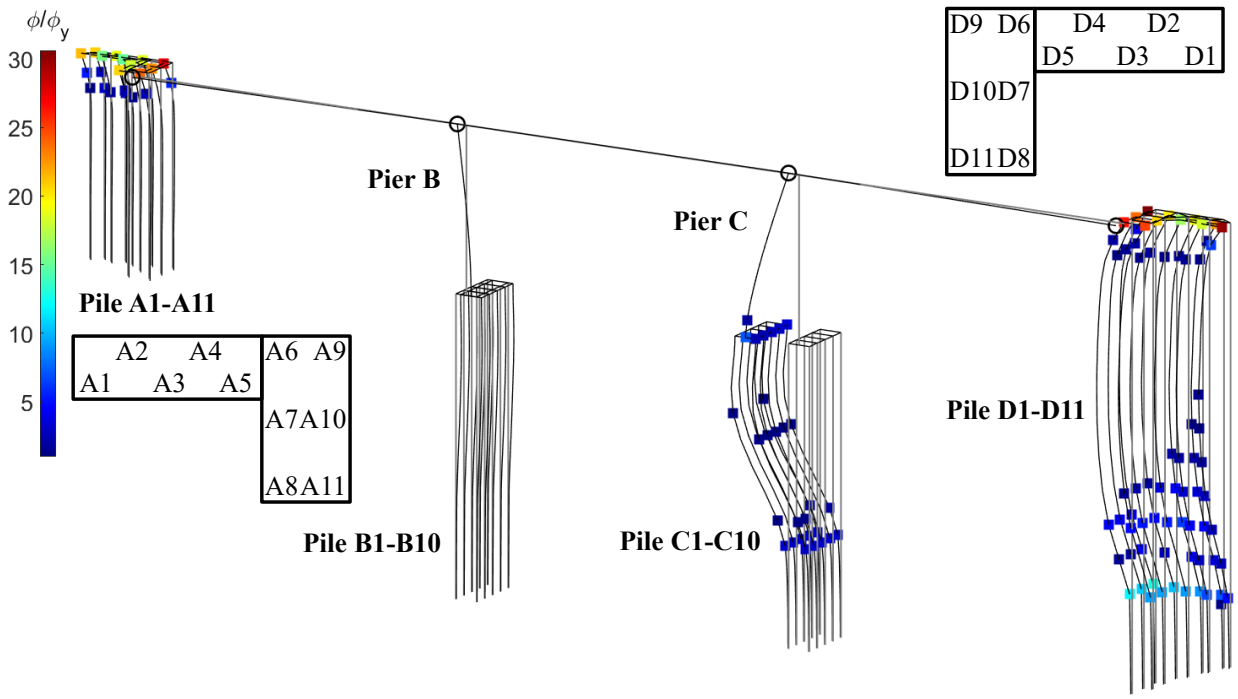

Figure 3-19. Ductility demand ratio ϕ/ϕ_y at end of shaking (grey represents original configuration; values < 1 are not shown for clarity; deformation factor = 10).

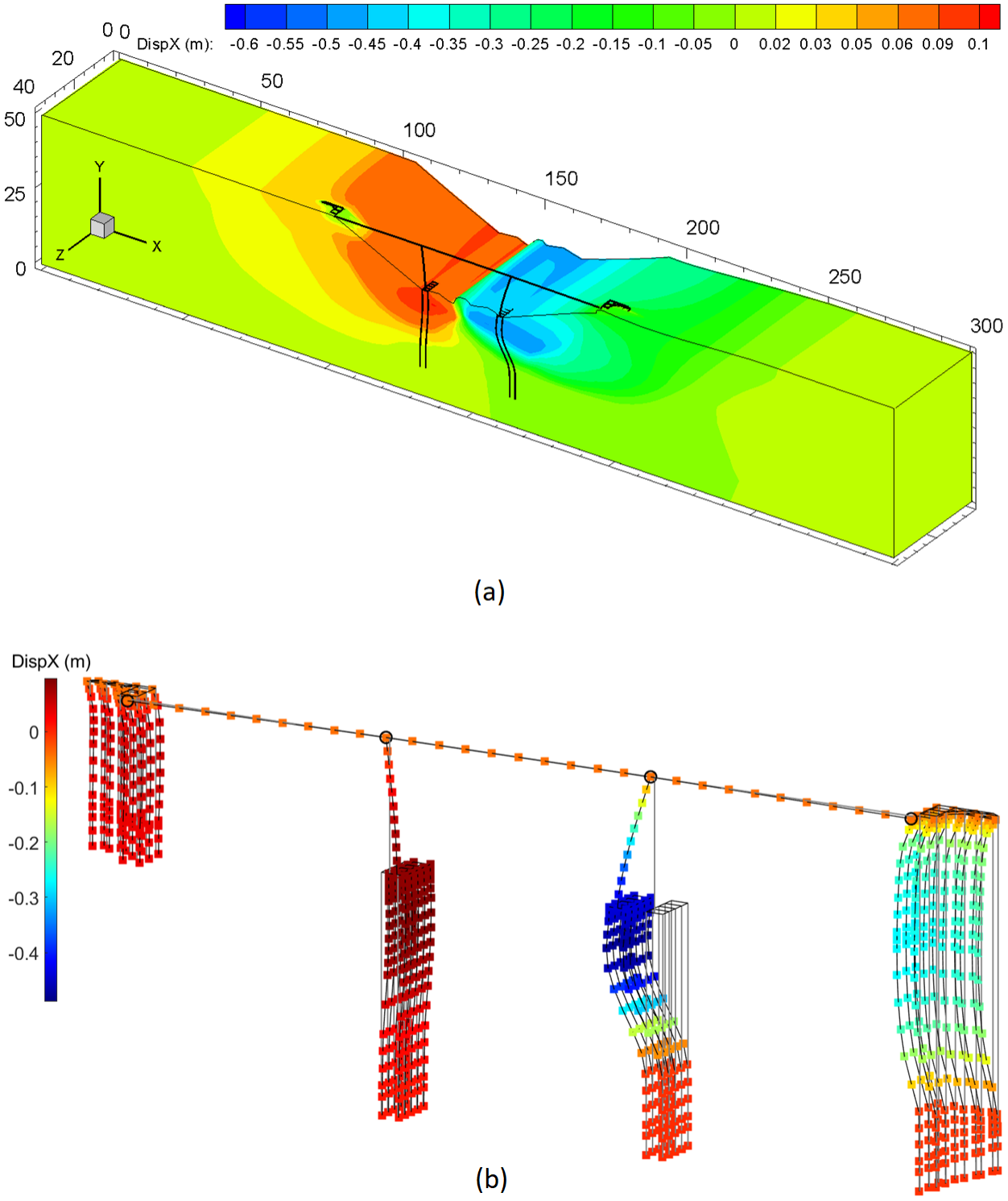

Figure 3-20. Deformed FE mesh of bridge under reversed input motion at end of shaking; (a) Contour; (b) Structure (factor = 10).

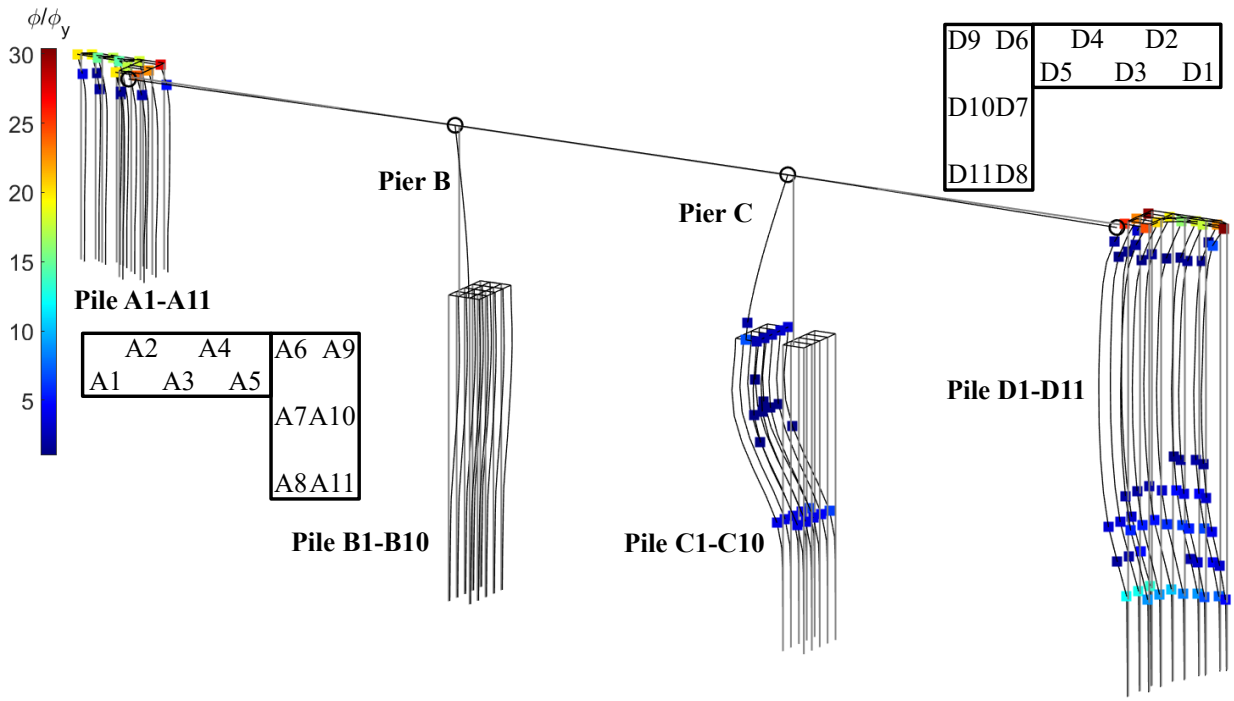

Figure 3-21. Ductility demand under reversed input motion at end of shaking: (a) Ratio ϕ/ϕ_y; (b) Profile (grey represents original configuration; values < 1 are not shown for clarity; factor = 10).

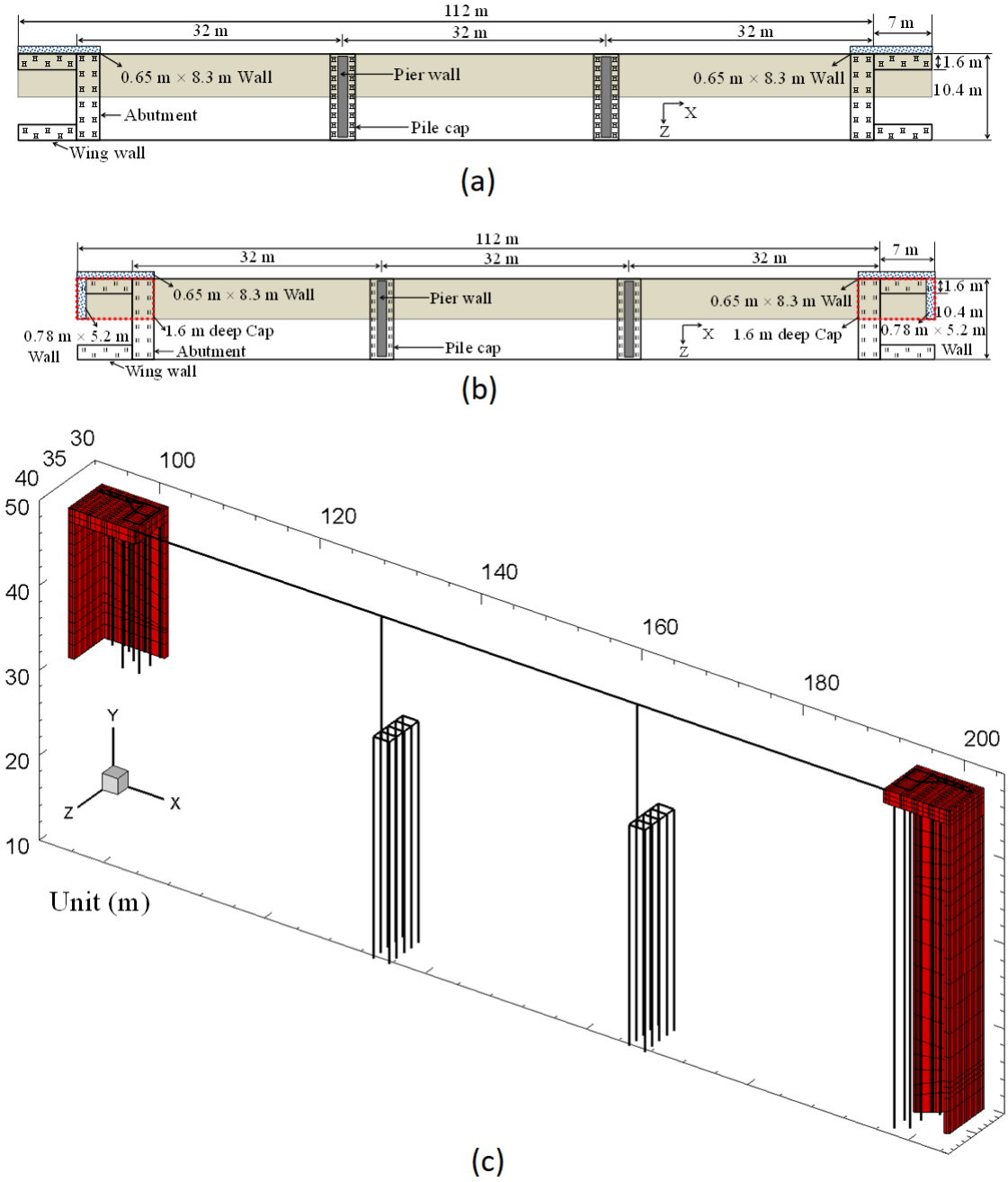

Figure 3-22. Retrofit analyses: (a) Scenario 1 by adding two 0.65 m × 8.3 m walls; (b) Scenario 2 by further adding two 0.78 m × 5.2 m walls along with 1.6 m deep caps; (c) Bridge structure of Scenario 2.

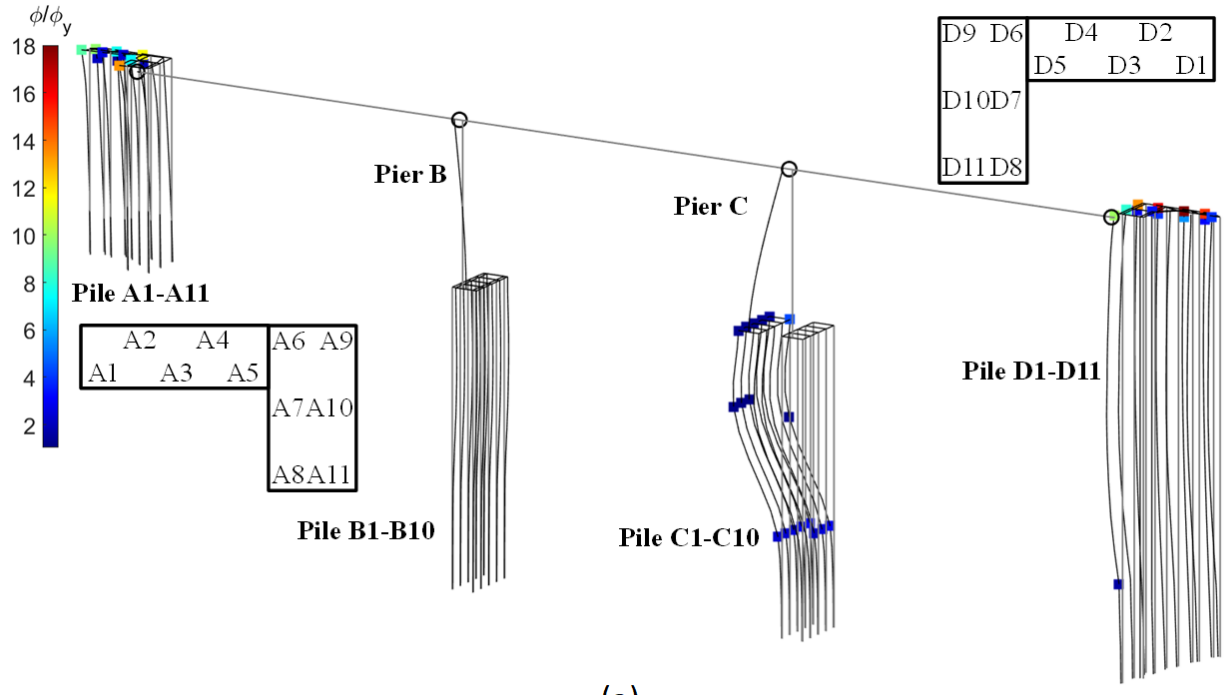

(a)

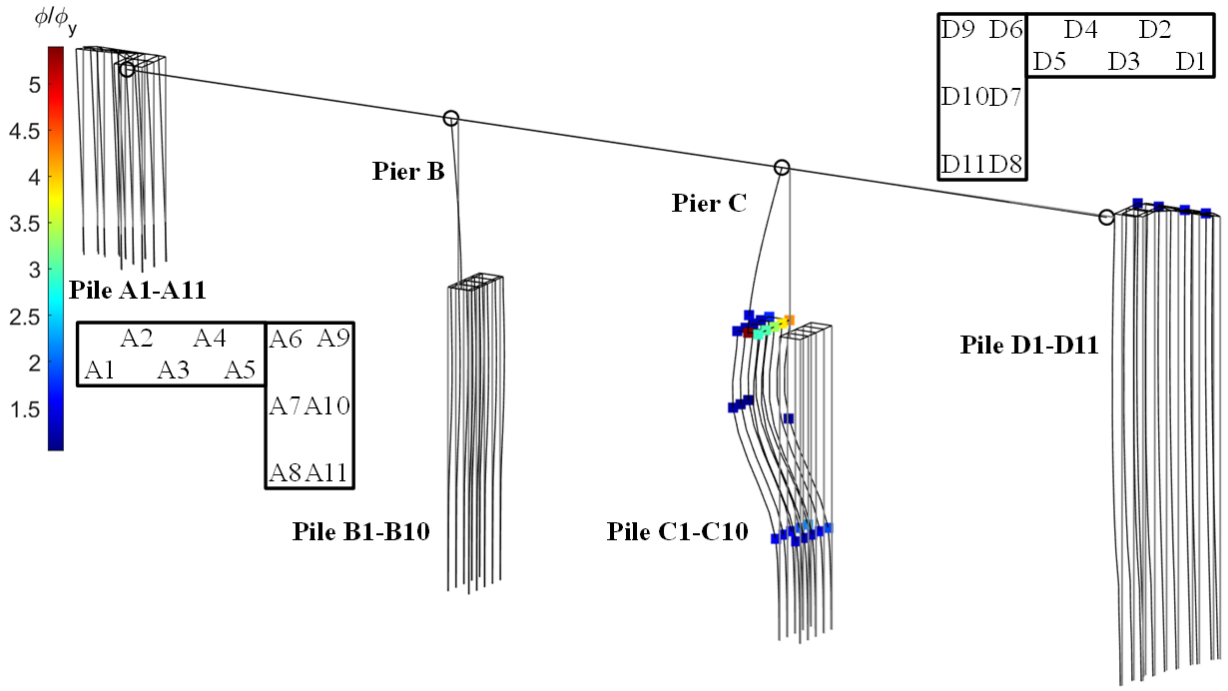

(b)

Figure 3-23. Ductility demand ratio ϕ/ϕ_y for retrofit analysis: (a) Scenario 1; (b) Scenario 2 (grey represents original configuration; values < 1 are not shown for clarity; factor = 10).

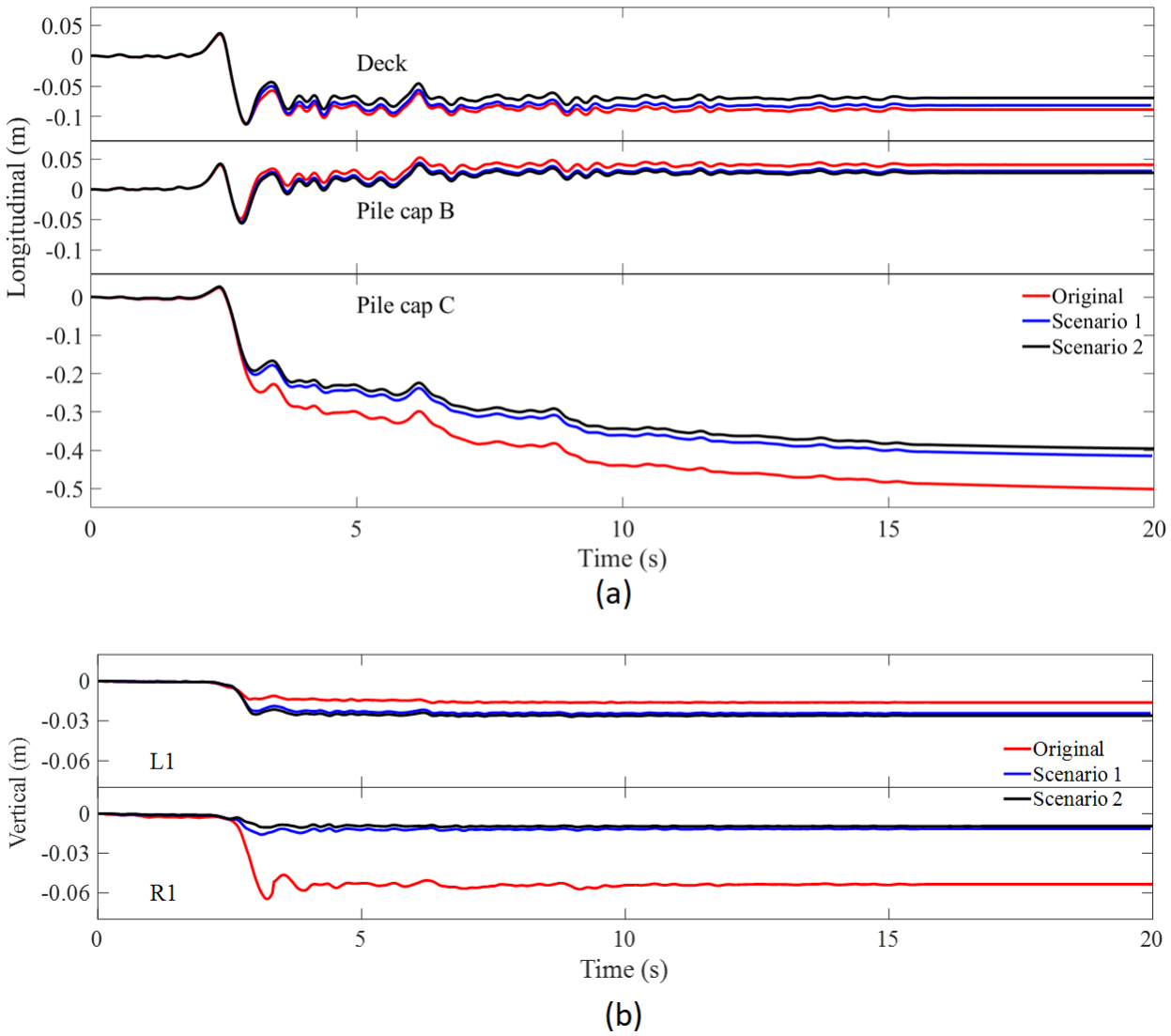

Figure 3-24. Bridge (Figure 3-4) relative displacement time histories: (a) Longitudinal (positive towards the right and negative towards the left); (b) Vertical (negative is settlement).

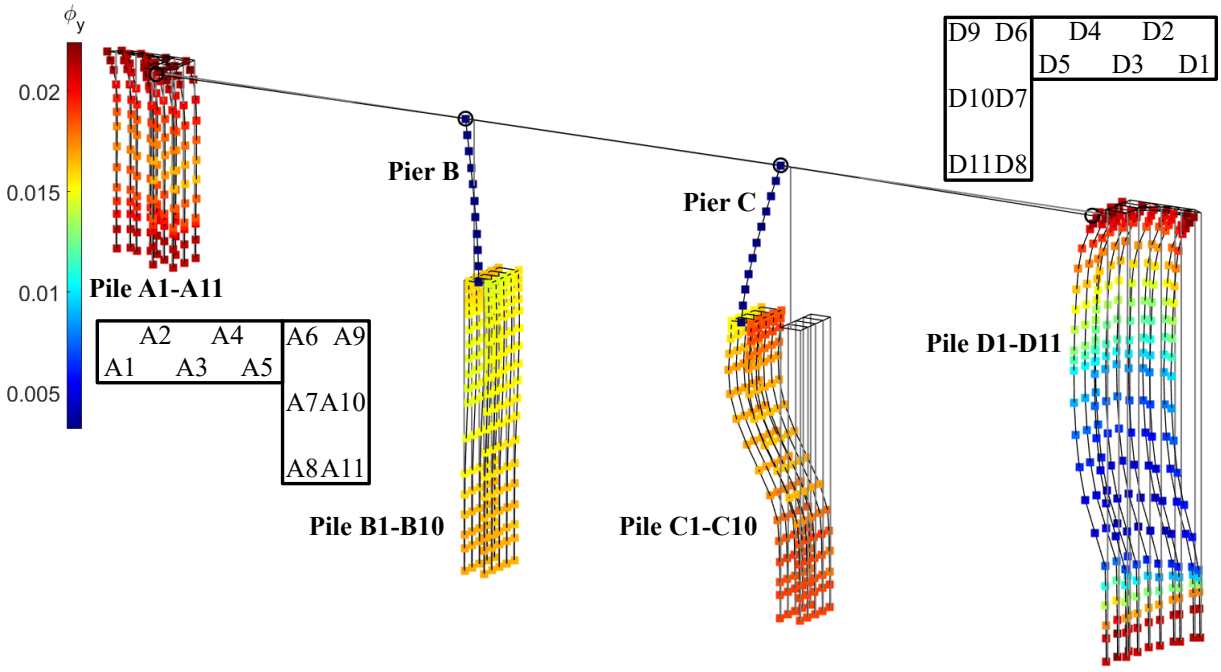

Figure 3-25. Yield curvature ϕ_y at end of shaking for calculation of ductility demand ratio.

4. DISTRIBUTION OF DEFORMATIONS AND STRAINS WITHIN A SLOPE SUPPORTED ON A LIQUEFIABLE STRATUM

Zhijian Qiu and Ahmed Elgamal

Abstract

Ground slopes with an underlying liquefiable layer are particularly prone to failure due to seismic excitation. For an embedded foundation, the extent of ground deformation at its specific location within the slope, will dictate the level of detrimental consequences. As such, knowledge about the spatial configuration of expected ground deformation along the slope's length and height will provide insights towards assessment and mitigation of the consequences. For that purpose, calibrated Finite element (FE) simulations of ground slopes are conducted, and derived insights from the seismic response analyses are gleaned, where properties of upper crust layer and thickness of the liquefiable layer are varied. Generally, lower levels of deformation are to be expected with distance away from the crest and toe of the sloping zone, and the study aims to quantify this effect. In addition, it is shown that properties of the upper crust may have a significant influence on the pattern and level of accumulated downslope permanent deformation.

4.1 Introduction

Liquefied soil layers may result in considerable accumulated permanent downslope deformations during earthquakes, causing severe damage to overlying structures and deep foundations. Recent earthquakes continue to demonstrate the detrimental effects of liquefaction on bridge abutments, supporting columns, and pile foundations. Key related references are provided in [1].

To gain more insights towards assessment and mitigation of the detrimental consequences, knowledge about the spatial configuration of ground deformation in the slope vicinity plays an important role. In general, lower levels of deformation are to be expected with distance away from the crest and toe of the sloping zone. As such, this study attempts to quantify such distribution of ground deformations within a slope supported on a liquefiable stratum. A total of 9 Finite Element (FE) slope simulations are conducted and the results are systematically discussed, where soil properties of an upper clay layer and thickness of the liquefiable layer are varied.

As such, the following sections of this paper present the: 1) computational framework, 2) specifics and model properties of the ground slope, and 3) computed response and insights derived from the study. Finally, a number of conclusions are presented and discussed.

4.2 Computational Framework

The Open System for Earthquake Engineering Simulation (OpenSees) framework [2] was employed to conduct the nonlinear slope analyses subjected to seismic excitation. OpenSees is developed by the Pacific Earthquake Engineering Research (PEER) Center and is widely used for simulation of geotechnical systems and soil-structure interaction applications [3-4]. The OpenSees elements and materials used in this FE model are briefly described below. Further details about the computational framework are discussed in reference [1].

1) Two-dimensional (2D) four-node quadrilateral elements (OpenSees quadUP) following the *u-p* formulation [5] were employed for simulating saturated soil response, where *u* is displacement of the soil skeleton and *p* is pore-water pressure.

2) The employed soil constitutive model was developed based on the multi-surface plasticity theory [6, 7]. In this model, the shear stress-strain backbone curve is represented by the hyperbolic relationship. As such, soil is simulated by the implemented OpenSees materials PDMY02 [6, 7] and PIMY [7, 8].

4.3 Finite Element Model

For illustration, a 2D Finite Element (FE) mesh (Figure 4-1) is created to represent the ground slope, comprising 5,334 nodes and 5,156 quadrilateral elements. This slope is approximately 300 m long, and the inclination angle is about 27^o (2 Horizontal: 1 Vertical). The subsurface conditions consist of (Table 4-1 and Table 4-2) clay (PIMY in OpenSees; [7, 8]), loose sand, and dense sand (PDMY02 in OpenSees; [6, 7]). The water table is prescribed at an elevation of 33 m, at the top of the loose sand layer (Figure 4-1). Along the left- and right-side mesh boundaries (Figure 4-1), 2D plane strain soil columns of large size (not shown) are included [1, 9]. These soil columns (away from the slope to minimize boundary effects), efficiently reproduce the desired shear beam free-field response at these locations (Figure 4-1).

For simplicity, nodes were fixed along the FE mesh base against longitudinal and vertical translation. The seismic motion (Figure 4-1) was taken as that of the 1940 Imperial Valley earthquake ground surface El Centro Station record (Component 180). Finally, dynamic analysis was conducted by applying this acceleration time history to the FE model base (elevation = 0.0 m). In this representation, free-field motion along both the left- and right-side side mesh boundaries is seamlessly generated by the included boundary soil columns mentioned above.

4.4 Computed Response

To study the spatial configuration of ground deformation along the slope's length and height, a total of 9 simulations were performed, where properties of upper clay layer and thickness of the liquefiable loose sand layer are varied. On this basis, the computed results are systematically presented and discussed below.

A. Longitudinal Deformation at End of Shaking

Figure 4-2 depicts the longitudinal relative displacement contours at end of shaking. It can be seen that the maximum ground displacement occurs near the crest and toe of the sloping zone, reaching as much as 2.2 m, 1.7 m and 0.7 m, respectively. With distance away from the slope, lower levels of lateral deformation are clearly observed (Figure 4-3). In the vicinity of the slope, the width of deformed zone and the amount of local downslope ground displacement are significantly affected by thickness of the liquefiable loose sand layer. With the increase of liquefiable layer thickness, permanent ground deformation and the deformed zone are larger. At both side boundaries, (X = 0 m and X = 300 m in Figure 4-3), the displacements were minimal, when compared to the large downslope deformation within the slope.

For illustration, the lateral displacement profile near location A Figure 4-1) at end of shaking is shown in Figure 4-1. It can be seen clearly that lateral displacement increased sharply within the loose sand layer. However, relative deformation within the overlying clay varies along depth (i.e., not behaving as a sliding rigid block as modeled by simplified methods [10]). As seen in Figure 4-3, the displacement starts decreasing in elevation (upward) and is not uniform near the top of loose sand layer and within the clay layer. In addition, properties of the upper clay layer (Table 4-2) and thickness of the liquefiable sand layer play a significant role in dictating the overall lateral ground deformation. With the decrease in cohesion (shear strength) and increase in loose sand layer thickness, lateral displacement is consistently higher.

B. Vertical Deformation at End of Shaking

In addition to lateral deformation, vertical displacement (Figure 4-5) is an important component, providing more insights towards assessment and mitigation of the detrimental consequences. As seen in Figure 4-5, peak settlement occurred near the slope crest and showed slumping of as much as 0.55 m, 0.29 m, 0.11 m for soft, medium, and stiff clay, respectively. Similar to the lateral counterpart, peak value of vertical displacement is greater, with decrease in the upper clay curst cohesion. In addition, the vertical displacement is affected by thickness of the liquefiable loose sand layer.

C. Liquefaction and Accumulated Shear Strains

Figure 4-6 shows time histories of effective confinement p' divided by the initial value p'_0 (before shaking) at loose sand layer base near location A (Figure 4-1). The ratio p'/p'_0 reaching 0.0 indicates loss of effective confinement due to liquefaction. As seen in Figure 4-6, the ratio p'/p'_0 gradually decreases towards 0.0 for all scenarios and this loose stratum attains its low specified residual shear strength of 2 kPa (Table 4-1). In accordance with the above-mentioned observed lateral deformations, peak shear strain within the loose sand layer becomes larger with decrease of the overlying clay crust cohesion (Figure 4-7).

4.5 Conclusions

This study aims to quantify the distribution of ground deformations within a slope supported on a liquefiable stratum. As such, a total of 9 Finite Element (FE) slope simulations are performed and the computed results are systematically presented and discussed, where soil properties of the upper clay layer and thickness of the liquefiable layer are varied. Specific observations and conclusions include:

1) With distance away from the crest and toe of the sloping zone, lower levels of resulting ground deformation are achieved as expected.

2) Knowledge about the spatial configuration of ground deformation within the slope provides more insight towards assessment and mitigation of the detrimental consequences due to liquefaction.

3) Peak strength of overlaying clay layer above the liquefied loose sand stratum plays an important role in overall deformation of the sloping ground. With the increase of upper clay layer cohesion,

permanent ground displacement was lower. Such a deformation mechanism differs from the simplified method of [10], in which the sliding mass is considered to be rigid.

4) Spatial distribution of deformations around the slope appears to be highly dependent on thickness of the liquefiable layer. It is shown that both the amount of permanent deformation and extent of the deformed zone are larger, with the increase of liquefiable layer thickness.

4.6 References

1. Qiu, Z., Ebeido, A., Almutairi, A., Lu, J., Elgamal, A., Shing, P.B. and Martin, G. (2020). "Aspects of bridge-ground seismic response and liquefaction-induced deformations." Earthquake Engineering & Structural Dynamics, 49(4), 375-393.
2. McKenna, F., Scott, M.H. and Fenves, G.L. (2010). "Nonlinear finite-element analysis software architecture using object composition." Journal of Computing in Civil Engineering, 24(1): 95-107.
3. Yang, Z. and Elgamal, A. (2002). "Influence of permeability on liquefaction-induced shear deformation." Journal of Engineering Mechanics, 128(7), 720-729.
4. Lu, J., Elgamal, A., Yan, L., Law, K.H. and Conte, J.P. (2011). "Large-scale numerical modeling in geotechnical earthquake engineering." International Journal of Geomechanics, 11(6), 490-503.
5. Chan A.H.C. (1988). "A unified finite element solution to static and dynamic problems in geomechanics." *PhD Thesis*, University College of Swansea.
6. Elgamal, A., Yang, Z. and Parra, E. (2003). "Modeling of cyclic mobility in saturated cohesionless soils." International Journal of Plasticity, 19(6), 883-905.
7. Yang, Z., Lu, J. and Elgamal, A. (2008). "OpenSees soil models and solid-fluid fully coupled elements." User's manual: Version 1. La Jolla, CA: Univ. of California, San Diego.
8. Elgamal, A., Yan, L. and Yang, Z. (2008). "Three-dimensional seismic response of Humboldt Bay bridge-foundation-ground system." Journal of Structural Engineering, 134(7), 1165-1176.
9. Qiu, Z. (2020). "Computational modeling of ground-bridge seismic response and liquefaction scenarios." PhD Thesis, UC San Diego.
10. Newmark, N. M. (1965). "Effects of earthquakes on dams and embankments." Geotechnique, 15(2), 139-160.

Table 4-1. Calibrated sand model parameters.

Model Parameters	Loose Sand	Dense Sand
Reference mean effective pressure, p'_r (kPa)	101.0	101.0
Mass density, ρ (t/m^3)	1.9	2.1
Maximum shear strain at reference pressure, $\gamma_{max,r}$	0.1	0.1
Shear modulus at reference pressure, Go (MPa)	60.0	200.0
Stiffness dependence coefficient d, $G = Go(\boldsymbol{P'/P'_r})^{\boldsymbol{d}}$	0.5	0.5
Poisson's ratio v (for dynamics)	0.4	0.4
Shear strength at zero confinement, c (kPa)	2.0	2.0
Friction angle and Phase transformation angle, ϕ/ϕ_{PT}	31°/31°	40°/26°
Contraction coefficients, $c_1/c_2/c_3$	0.087/5.0/3.0	0.001/5.0/3.0
Dilation coefficient, $d_1/d_2/d_3$	0.0/0.0/0.0	0.5/3.0/0.0
Damage parameter, y_1/y_2	1.0/0.0	1.0/0.0
Permeability (m/s)	1.0×10^{-5}	1.0×10^{-5}

Table 4-2. Clay model parameters.

Model Parameters	Soft Clay	Medium Clay	Stiff Clay
Mass density, ρ (t/m^3)	1.8	1.9	2.0
Low-strain shear modulus, Go (MPa)	20.0	60.0	150.0
Poisson's ratio v (for dynamics)	0.4	0.4	0.4
Maximum shear strain at reference pressure, $\gamma_{max,r}$	0.1	0.1	0.1
Shear strength, c (kPa)	20.0	40.0	80.0
Shear strain at maximum shear strength	0.1	0.1	0.1

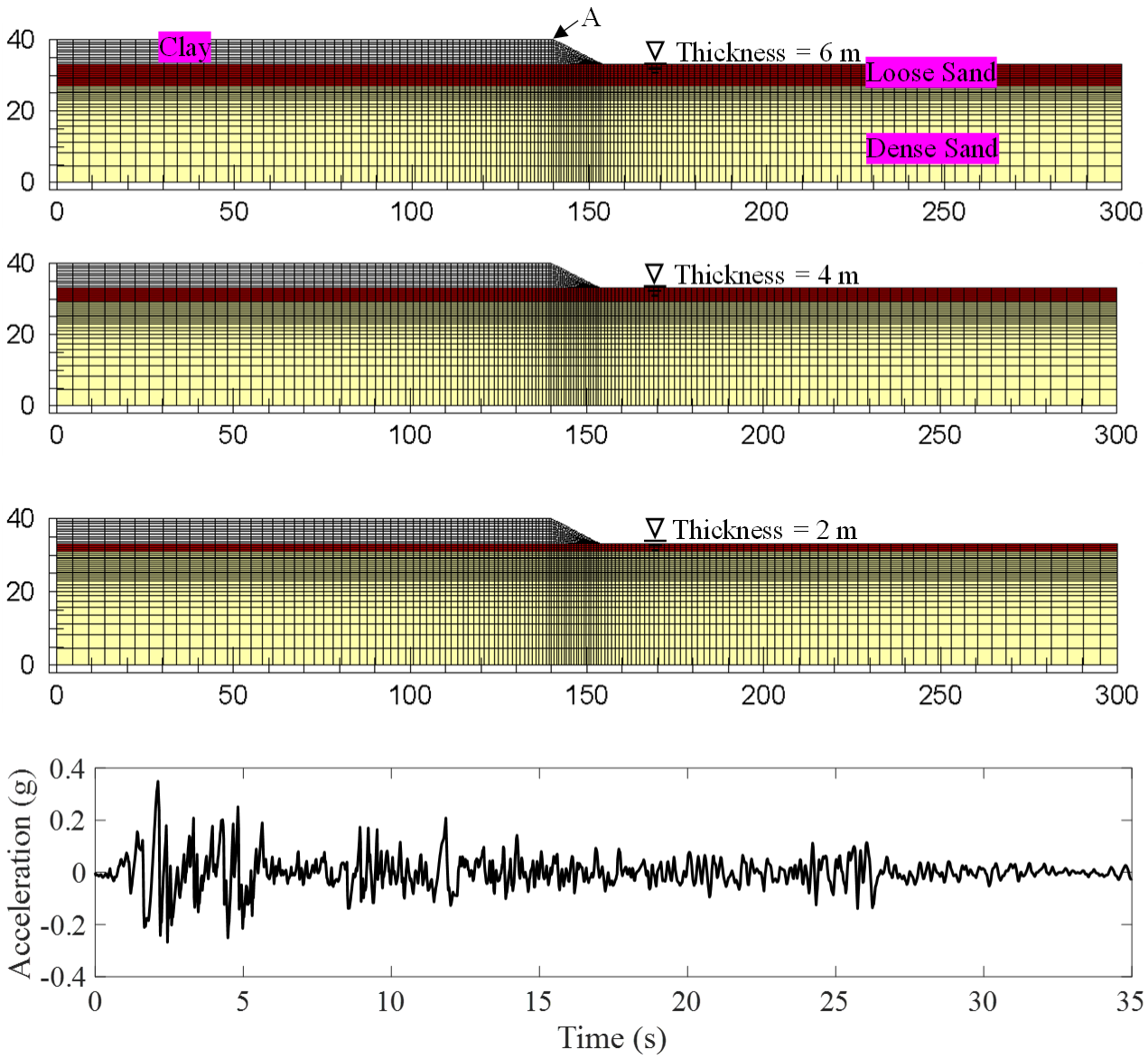

Figure 4-1. Two-dimensional FE model with different thickness of loose sand layer (i.e., 6m, 4m, 2m) subjected to a base input motion (1940 El Centro, Component 180).

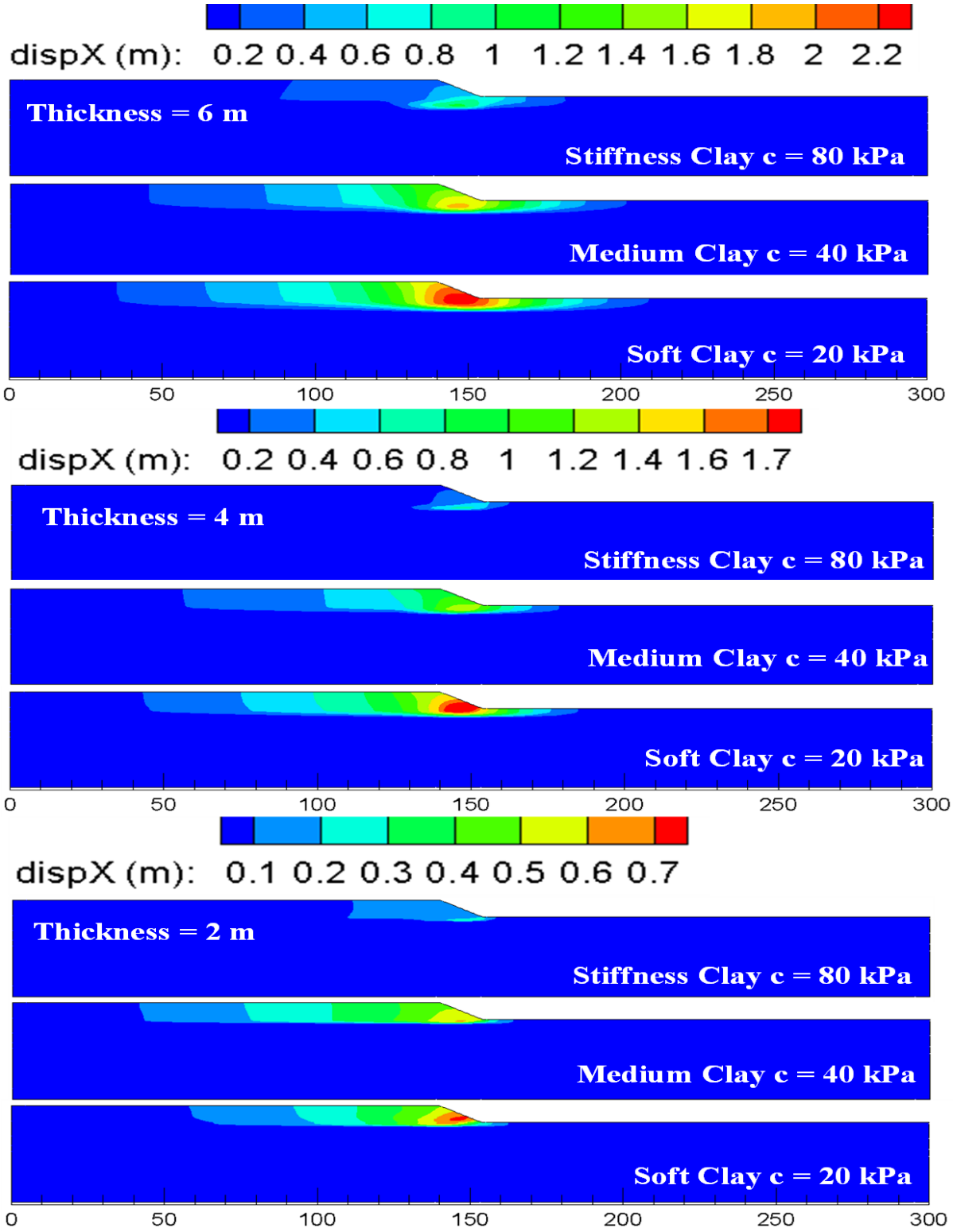

Figure 4-2. Lateral ground deformation at end of shaking with various properties of upper clay layer and thickness of the liquefiable loose sand layer.

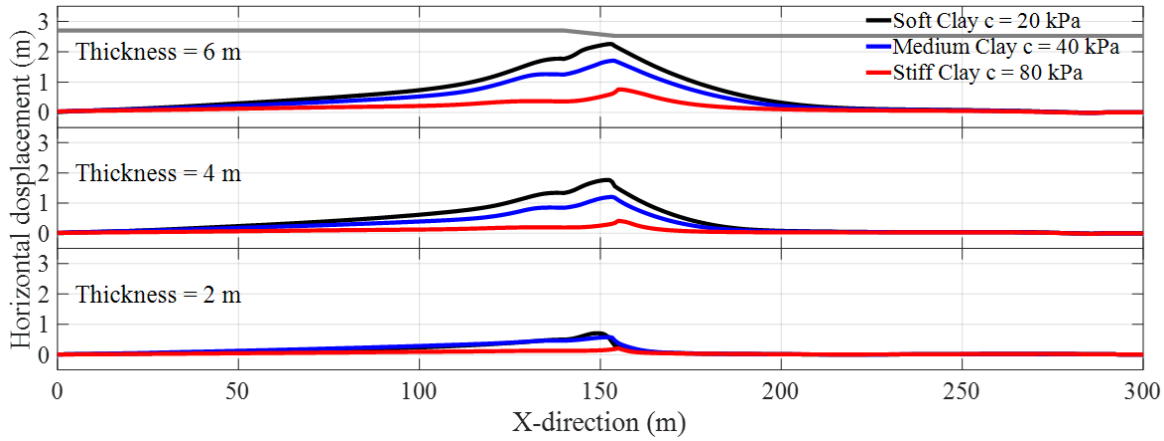

Figure 4-3 Lateral displacement along ground surface at end of shaking (grey line represents the outline of ground surface).

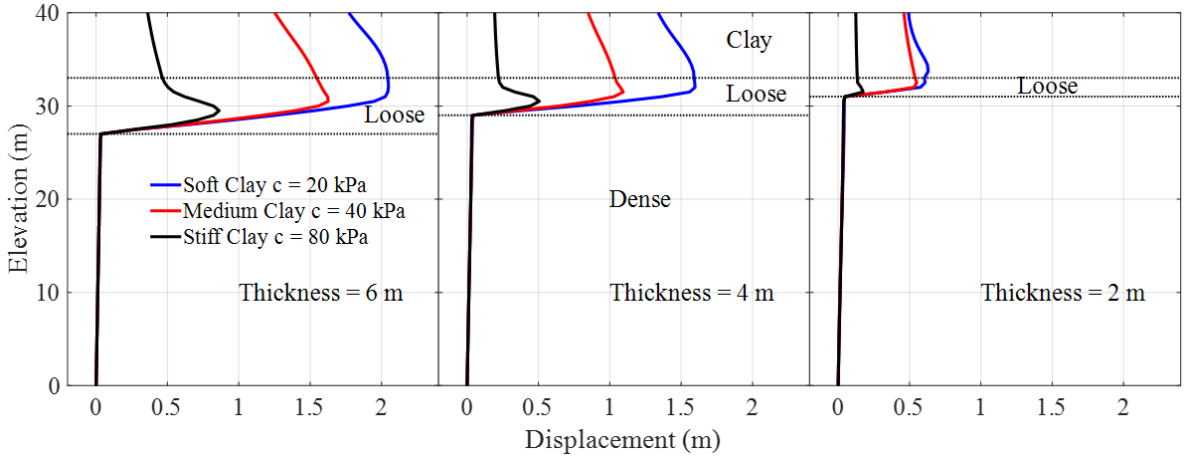

Figure 4-4 Lateral displacement profile near location A at end of shaking.

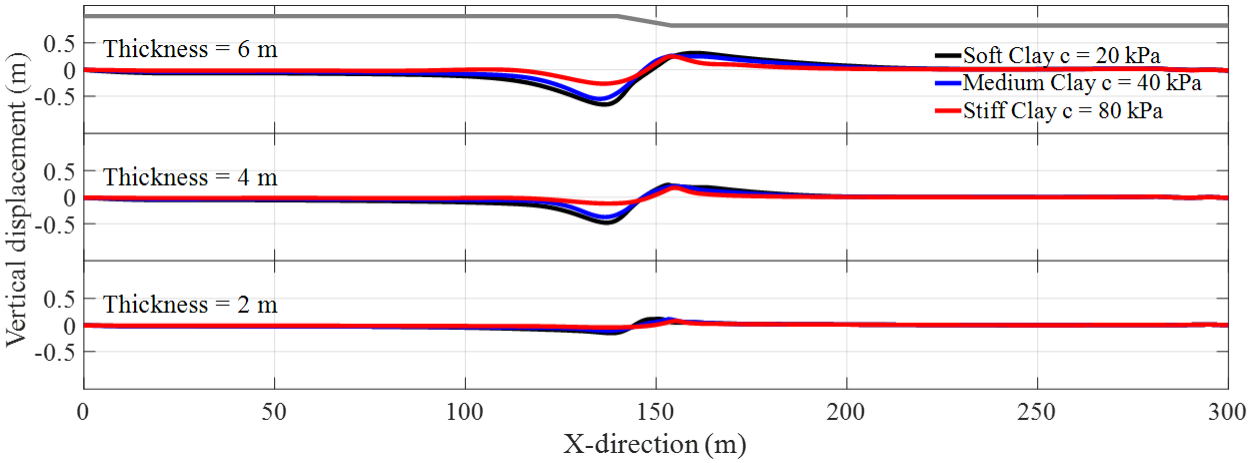

Figure 4-5. Vertical displacement along ground surface at end of shaking (grey line represents the outline of ground surface).

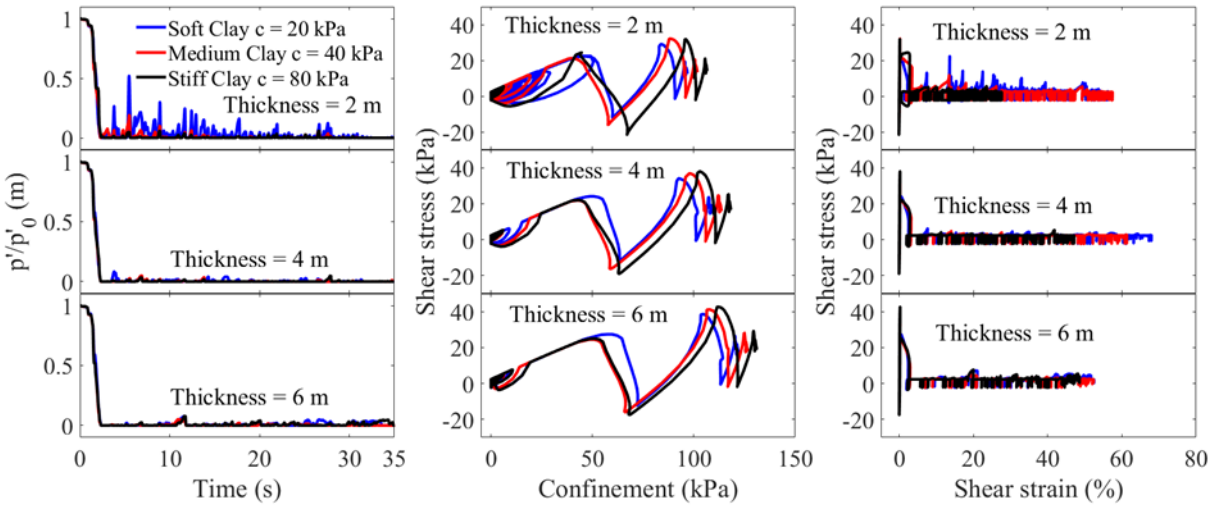

Figure 4-6. Soil response at the loose sand layer base near location A.

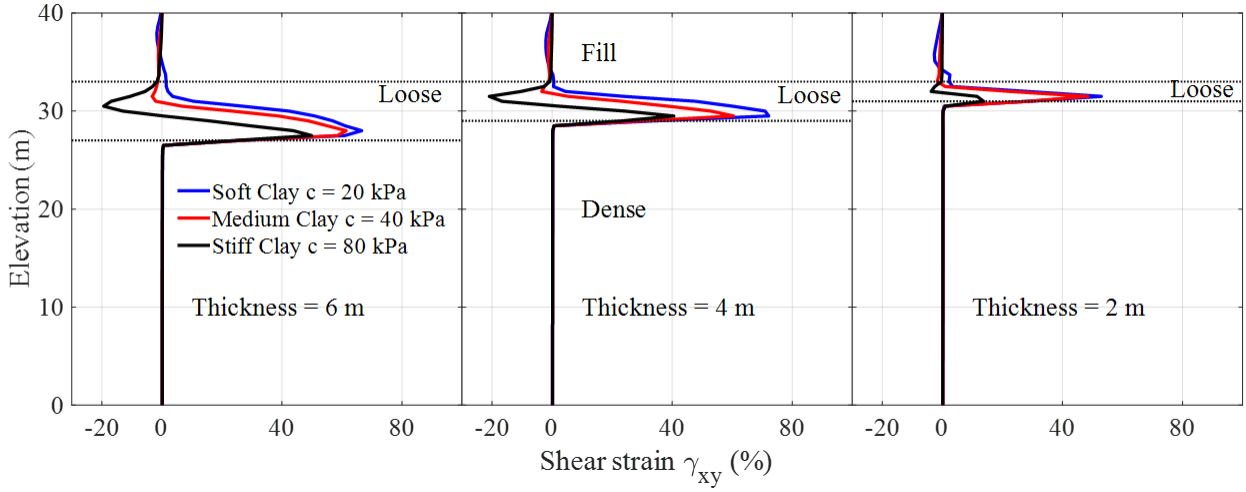

Figure 4-7. Shear strain profile near location A at end of shaking.

5. SEISMICALLY INDUCED GROUND DEFORMATION AND REDUCTION OF IMPACT ON BRIDGE SYSTEMS

Ahmed Elgamal and Zhijian Qiu

Abstract

Seismically induced ground deformations are observed to cause damage to the bridge superstructure and its foundation. Piles and pile groups may experience excessive lateral permanent displacements and loads, which translate into various mechanisms of potential damage to the bridge. In an attempt to reduce the detrimental consequences of such ground deformations, a number of bridge configurations are suggested, in which: i) the foundations are placed at locations of potentially lower lateral deformations, ii) a shallow foundation is employed, iii) the bridge deck is employed as a strut to shore the slopes on both sides of the canyon, and iv) the canyon slopes are braced using the bridge superstructure and its foundation. In this study, the characteristics of the involved lateral ground deformations are discussed. On this basis, schematics of the proposed bridge configurations are presented. Furthermore, illustrative idealized two-dimensional (2D) finite-element computational simulations are included, motivated by observations from post-earthquake reconnaissance data. The presented outcomes and conclusions provide insights for bridge retrofit efforts or for new construction.

5.1 Introduction

During earthquakes, liquefied soil layers may result in substantial accumulated permanent downslope deformations, causing severe damage to the bridge and its deep foundations (Youd 1993; Hamada et al. 1996; Tokimatsu and Asaka 1998; Berrill et al. 2001; Turner et al. 2013, 2016). Recent earthquakes (Arduino et al. 2010; Wotherspoon et al. 2011; Ledezma et al. 2012; Verdugo et al. 2012; Cubrinovski et al. 2011, 2014a, b) continue to demonstrate the detrimental effects of liquefaction-induced lateral spreading and loss of capacity in bridge abutments, supporting columns and pile foundations.

To reduce damage near the bridge abutments and at the supporting pile foundations, a number of bridge configurations are suggested in this paper, including: i) placing foundations at locations of potentially lower lateral deformations, ii) employing shallow foundations and/or concepts of base-isolation, iii) using the bridge deck as a strut to shore the slopes on both sides of the canyon, and iv) bracing the canyon slopes using the bridge superstructure and its foundation. In essence, such

bridge configurations can offer advantages stemming from: i) placing the bridge foundations at locations away from the zones of large downslope ground deformations, ii) adopting shallow foundations and/or the base isolation logic to reduce damage to the superstructure, iii) making the relatively rigid bridge superstructure (of high axial stiffness) act as a strut between both sloping sides of the underlying canyon, thus providing a self-reacting mechanism, with the resulting bridge deck axial compressive force providing a restoring influence. On this basis, after a strong earthquake, potential retrofit may be relatively fast and economical, as the bridge structure naturally conforms to the surrounding deformed ground configuration, with relatively minor grading or re-levelling work needed.

In order to conceptually illustrate these beneficial response mechanisms, a number of representative idealized two-dimensional (2D) Finite Element (FE) models were developed with interbedded liquefiable (saturated loose sand)/non-liquefiable (dry soils or saturated very dense sand) strata (Elgamal and Qiu 2022). As such, the following sections of this paper outline the: 1) specifics of the suggested bridge-ground configurations, 2) details of the employed FE model and analysis techniques, and 3) computed response and insights derived from the study. Finally, a number of conclusions are presented and discussed.

5.2 Finite Element Model

OpenSees is employed to conduct the simulations (McKenna et al. 2010). For illustration, the modeled reinforced concrete bridge (Figure 5-1b) is about 60 m long, and the ground FE mesh is comprised of 5,355 plane-strain quadrilateral elements. The subsurface conditions consist of Medium Clay (PIMY with tension cutoff; Yang et al. 2008; Lu et al. 2011), Loose Sand and Very Dense Sand (PDMY02; Yang 2000; Yang and Elgamal 2002; Elgamal et al. 2003; Yang et al. 2003, 2008). The medium clay and sand model parameters are listed in Yang et al. (2008). The water table is prescribed at an elevation of 25 m, at the top of the Loose Sand Layer (Figure 5-1). Along the left- and right-side mesh boundaries (Figure 5-1), 2D plane strain soil columns (not shown) of large size (width = 100 m and depth = 10^7 m) are included (Qiu et al. 2020; Qiu, 2020). These soil columns (away from the bridge structure to minimize boundary effects), efficiently reproduce the desired shear beam free-field response at these locations (Figure 5-1).

In view of the typical high stiffness and strength, the reinforced concrete deck is modeled by linear elastic beam-column elements, while the piles (Figure 5-1b-f) are modeled using nonlinear force-based beam-column elements with fiber-section (Figure 5-2). In order to represent the geometric space occupied by the pile in the soil domain, rigid beam-column links ($EI = 10^5$ times the linear EI of the pile) are used normal to the vertical axis of the pile (Qiu et al. 2020). The 2D quadrilateral elements representing the soil (taken with thickness of 2.44 m into the page as a transverse direction center to center pile-spacing) are connected to the pile geometric configuration at the outer rigid link nodes using the OpenSees equalDOF constraint command.

Lateral response of the soil strata below the model base was represented by a dashpot boundary in the longitudinal X-direction (Lysmer and Kuhlemeyer 1969), so as to avoid spurious wave reflections. On this basis, input seismic motion (Figure 5-1j) was simply taken as that of the 1940 Imperial Valley El Centro Station record (Component 180). As such, deconvolution was employed using Shake91 (Idriss and Sun 1993) to derive an incident earthquake motion, imparted (Zhang et al. 2008; Elgamal et al. 2008) along the base of the FE model (Vs = 600 m/s; elevation 0.0 in Figure 5-1). In this representation, free-field motion along both the left- and right-side mesh boundaries is seamlessly generated by the included soil columns mentioned above.

5.3 Computed Response

Liquefaction and accumulated shear strains

Figure 5-3a shows time histories of effective confinement p' divided by the initial value p'_0 (before shaking) at point A (Figure 5-1), near the base of the loose sand layer. The ratio p'/p'_0 reaching 0.0 indicates loss of effective confinement due to liquefaction. As seen in Figure 5-3a, the ratio p'/p'_0 gradually decreases towards 0.0, with scenario b displaying the restraining (pile-pinning) effect of the bridge foundation. As such, the scenario b accumulated shear strain at point A (close to the pile foundation) is lower than those of the other scenarios (Figure 5-3b).

Longitudinal deformation at end of shaking

Figure 5-4 depicts the longitudinal relative displacement contours at end of shaking. Without the bridge, significant local downslope deformation occurred at both sides between locations along the horizontal mesh dimension X = 120 m – 140 m, and X = 160 m - 180 m (Figure 5-1), reaching about 0.9 m (Figure 5-4j). As a result, the piles (at X = 130 m, 170 m) in scenario (b) experienced

relatively high permanent deformations (Figure 5-4b and Figure 5-5), and the ductility demand (ratio of ultimate curvature ϕ_u to yield curvature ϕ_y) reached about 1.8 (Figure 5-5). Generally, these attained peak values would be considered of concern.

To reduce deformation and ductility demand for the piles, scenarios (c) and (d) are suggested, placing the piles at locations of lower lateral deformations (i.e., at X = 110 m, 190 m and X= 100 m, X = 200 m as shown in Figure 5-1c, Figure 5-1d). From Figure 5-5 scenarios (c), and (d), it can be seen that the deformation was reduced significantly as the piles are now farther away from the large downslope ground deformation zone (Figure 5-4j); and the attained ductility demand values were lower than 1.0 throughout.

Since there was no considerable deformation at the center column of scenarios (c) and (d), two additional bridge configurations (i.e., scenarios e and f) are suggested, replacing the abutment piles on both sides by shallow foundations (stiff linear elastic zones with Young's modulus E = 30 GPa; Figure 5-1e and f). In scenario e (Figure 5-1e), the superstructure was connected to a shallow foundation by a pinned connection. In scenario (f), base-isolation (in the form of a roller) was employed at the connection between superstructure and shallow foundation (Figure 5-1f). Under these scenarios (Figure 5-4e and f), the pile displacements and attained ductility demand values were insignificant, when compared to those of scenario b.

Three additional bridge configurations (without center column) supported on the stiff shallow foundation are proposed as the structural system (Figure 5-1g-i). In scenarios g and h, the superstructure was connected to the shallow foundation by a pinned connection and a roller connection, respectively. Furthermore, in scenario i, an arch bridge configuration was placed on a shallow inclined bracing foundation covering the entire exposed slope surface. As such, own weight of the arch bridge exerts restoring lateral earth pressure forces that stabilize the canyon sloping ground and reduce the extent of potential lateral deformations. As seen in Figure 5-4g and Figure 5-4i, longitudinal displacements were significantly lower compared to scenario (a) due to the axially stiff bridge superstructure acting as a strut that exerts significant added restraint on the slope deformations at each end. Finally, as expected, scenario (h) with roller connection between superstructure and shallow foundation results in a similar outcome compared to the free-field scenario (Figure 5-4a and h).

Vertical ground deformation at end of shaking

Figure 5-6 displays the vertical displacement contours at end of shaking. Without the bridge, peak settlement occurred near the slope crest and showed slumping of as much as 0.2 m (Figure 5-6a). Compared to this free-field scenario, the vertical displacement of scenarios g and h is much higher reaching about 0.5 m and 0.55 m near the slope top, respectively, as the own weight of superstructure exerts additional surcharge load on the shallow foundations (Figure 5-6g and h).

Due to the pile restraining effect and the relatively rigid bridge deck acting as a strut between both sides (Figure 5-6b, e and i), the vertical settlement is seen to be significantly lower compared to the free-field scenario (Figure 5-6a). Moreover, the bridge settlement conforms seamlessly to that of the ground on both sides (e.g., scenarios b, e, i). As such, relatively minor grading work might be needed, with minimal to no damage sustained by the bridge structure.

5.4 Summary and Conclusions

In an attempt to reduce the extent of liquefaction-induced damage to the bridge pile-foundation/pier systems, a number of FE conceptual models are presented. As such, this pilot study aims to illustrate salient beneficial response features associated with a number of proposed bridge configurations, including: i) placing foundations at locations of potentially lower lateral displacements, ii) employing shallow foundations and/or base-isolation mechanisms, iii) employing the bridge deck as a strut to shore the slopes on both sides of the canyon, and iv) using own weight of the bridge to further brace the canyon slopes. In this paper, characteristics of the involved ground and structural responses were discussed. The presented outcomes provide insights for retrofit efforts and well as for construction of new bridges.

Specific observations and conclusions include:

1) Placing the bridge deep foundations at locations away from large downslope ground deformations, may greatly reduce the detrimental outcome.

2) Whenever possible, designs that employ no bridge columns and underlying deep foundations reduce the negative impacts of potential downslope ground deformations.

3) Using the bridge superstructure as a strut to shore, or further to brace the canyon slopes, can reduce overall deformations to the ground as well as the bridge structure.

4) After an earthquake: i) potential retrofit might be relatively economical with no need to address costly deep foundation damage challenges, and/or ii) the bridge structure naturally conforms to the surrounding deformed ground configuration, where relatively minor grading or re-levelling work might be needed, and with minimal to no damage to the bridge structure.

5.5 References

Arduino, P., Ashford, S., Assimaki, D., Bray, J., Eldridge, T., Frost, D., Hashash, Y., Hutchinson, T., Johnson, L., Kelson, K. and Kayen, R. (2010). "Geo-engineering reconnaissance of the 2010 Maule, Chile earthquake." GEER Association Report No. GEER-022, 1.

Berrill, J.B., Christensen, S.A., Keenan, R.P., Okada, W. and Pettinga, J.R. (2001). "Case study of lateral spreading forces on a piled foundation." Geotechnique, 51(6), 501-517.

Cubrinovski, M., Bradley, B., Wotherspoon, L., Green, R., Bray, J., Wood, C., Pender, M., Allen, J., Bradshaw, A., Rix, G. and Taylor, M. (2011). "Geotechnical aspects of the 22 February 2011 Christchurch earthquake." Bulletin of the New Zealand Society for Earthquake Engineering, 44(4), 205-226.

Cubrinovski, M., Winkley, A., Haskell, J., Palermo, A., Wotherspoon, L., Robinson, K., Bradley, B., Brabhaharan, P. and Hughes, M. (2014a). "Spreading-induced damage to short-span bridges in Christchurch, New Zealand." Earthquake Spectra, 30(1), 57-83.

Cubrinovski, M., Haskell, J., Winkley, A., Robinson, K. and Wotherspoon, L. (2014b). "Performance of bridges in liquefied deposits during the 2010-2011 Christchurch, New Zealand, earthquakes." Journal of Performance of Constructed Facilities, 28(1), 24-39.

Elgamal, A., Yang, Z. and Parra, E. (2003). "Modeling of cyclic mobility in saturated cohesionless soils." International Journal of Plasticity, 19(6), 883-905.

Elgamal, A., Yan, L. and Yang, Z. (2008). "Three-dimensional seismic response of Humboldt Bay bridge-foundation-ground system." Journal of Structural Engineering, 134(7), 1165-1176.

Elgamal, A., & Qiu, Z. (2022). "Seismically Induced Ground Deformation and Reduction of Impact on Bridge Systems." In Geo-Congress 2022, ASCE (pp. 291-299).

Hamada, M., Isoyama, R. and Wakamatsu, K. (1996). "Liquefaction-induced ground displacement and its related damage to lifeline facilities." Soils and foundations, 36(Special), 81-97.

Idriss, I.M. and Sun, J.I. (1993). "User's manual for SHAKE91: A computer program for conducting equivalent linear seismic response analyses of horizontally layered soil deposits." Center for Geotechnical Modeling, Dept. of Civil and Environmental Engineering, University of California Press, Davis, CA.

Lysmer, J. and Kuhlemeyer, R.L. (1969). “Finite Dynamic Model for Infinite Media.” Journal of Engineering Mechanics Division, 95, 859-878.

Ledezma, C., Hutchinson, T., Ashford, S.A., Moss, R., Arduino, P., Bray, J.D., Olson, S., Hashash, Y.M., Verdugo, R., Frost, D. and Kayen, R. (2012). “Effects of ground failure on bridges, roads, and railroads.” Earthquake Spectra, 28(S1), S119-S143.

Lu, J., Elgamal, A., Yan, L., Law, K.H. and Conte, J.P. (2011). “Large-scale numerical modeling in geotechnical earthquake engineering.” International Journal of Geomechanics, 11(6), 490-503.

McKenna, F., Scott, M. and Fenves, G. (2010). “Nonlinear finite-element analysis software architecture using object composition.” Journal of Computing in Civil Engineering, 24(1), 95-107.

Parra, E. (1996). “Numerical modeling of liquefaction and lateral ground deformation including cyclic mobility and dilation response in soil systems.” PhD Thesis, Rensselaer Polytechnic Institute.

Qiu, Z., Ebeido, A., Almutairi, A., Lu, J., Elgamal, A., Shing, P.B. and Martin, G. (2020). “Aspects of bridge-ground seismic response and liquefaction-induced deformations.” Earthquake Engineering & Structural Dynamics, 49(4), 375-393.

Qiu, Z. (2020). “Computational modeling of ground-bridge seismic response and liquefaction scenarios.” PhD Thesis, UC San Diego.

Tokimatsu, K. and Asaka, Y. (1998). “Effects of liquefaction-induced ground displacements on pile performance in the 1995 Hyogoken-Nambu earthquake.” Soils and Foundations, 38(Special), 163-177.

Turner, B., Brandenberg, S.J. and Stewart, J.P. (2013). “Evaluation of collapse and non-collapse of parallel bridges affected by liquefaction and lateral spreading,” Proc. 10th International Conf. on Urban Earthquake Engineering., Center for Urban Earthquake Engineering, March 1-2, 2013, Tokyo Institute of Technology, Tokyo, Japan.

Turner, B.J., Brandenberg, S.J. and Stewart, J.P. (2016). “Case study of parallel bridges affected by liquefaction and lateral spreading.” Journal of Geotechnical and Geoenvironmental Engineering, 142(7), 05016001.

Verdugo, R., Sitar, N., Frost, J.D., Bray, J.D., Candia, G., Eldridge, T., Hashash, Y., Olson, S.M. and Urzua, A. (2012) "Seismic performance of earth structures during the February 2010 Maule, Chile, earthquake: dams, levees, tailings dams, and retaining walls." Earthquake Spectra, 28(S1), S75-S96.

Wotherspoon, L., Bradshaw, A., Green, R., Wood, C., Palermo, A., Cubrinovski, M. and Bradley, B. (2011). "Performance of bridges during the 2010 Darfield and 2011 Christchurch earthquakes." Seismological Research Letters, 82(6), 950-964.

Yang, Z. (2000). "Numerical modeling of earthquake site response including dilation and liquefaction." PhD Thesis, Columbia University.

Yang, Z. and Elgamal, A. (2002). "Influence of permeability on liquefaction-induced shear deformation." Journal of Engineering Mechanics, 128(7), 720-729.

Yang, Z., Elgamal, A. and Parra, E. (2003). "Computational model for cyclic mobility and associated shear deformation." Journal of Geotechnical and Geoenvironmental Engineering, 129(12), 1119-1127.

Yang, Z., Lu, J. and Elgamal, A. (2008). "OpenSees soil models and solid-fluid fully coupled elements." User's manual: Version 1. La Jolla, CA: Univ. of California, San Diego.

Youd, T.L. (1993). "Liquefaction-induced damage to bridges." Transportation Research Record, 1411, 35-41.

Zhang, Y., Conte, J.P., Yang, Z., Elgamal, A., Bielak, J. and Acero, G. (2008). "Two-dimensional nonlinear earthquake response analysis of a bridge-foundation-ground system." Earthquake Spectra, 24(2), 343-386.

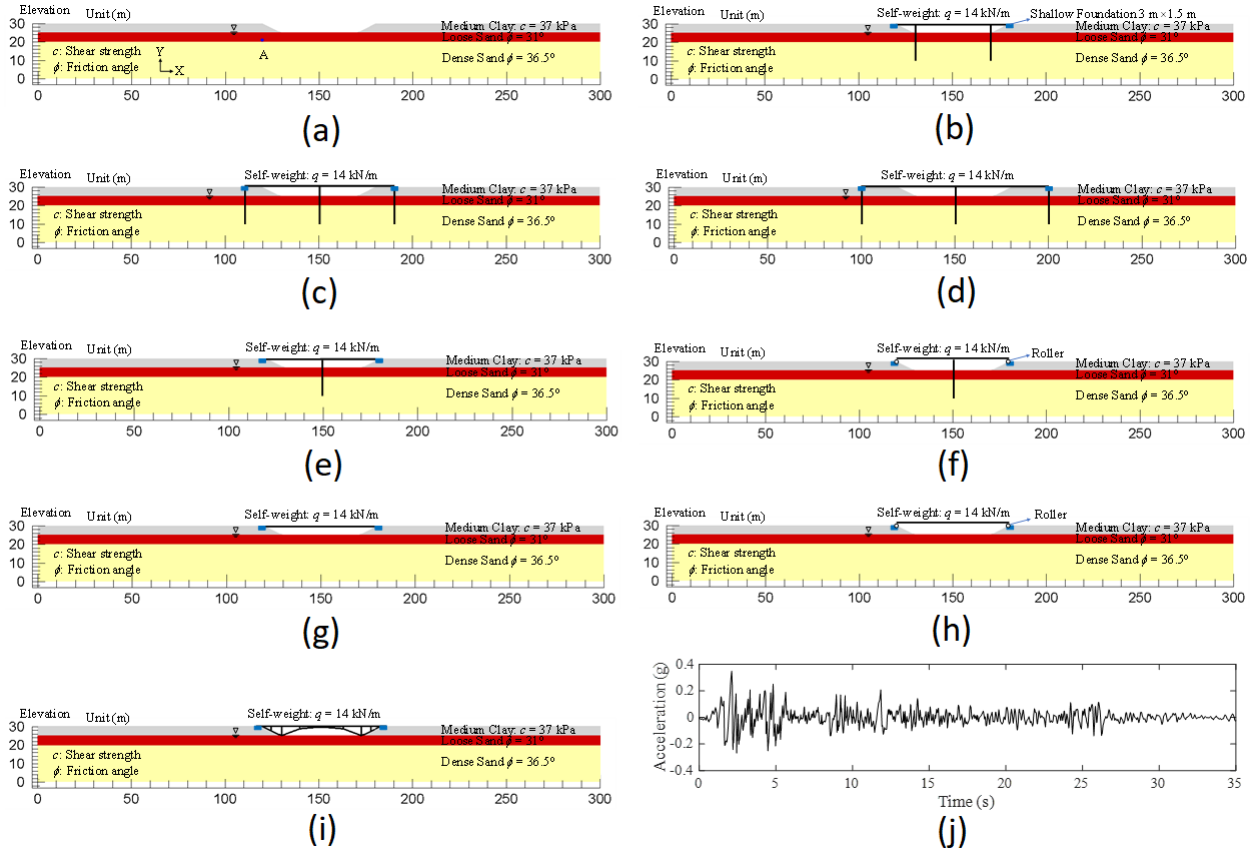

Figure 5-1. Bridge-ground configurations: (a) No bridge, to illustrate pattern of ground deformation, (b) Piles near slope toe, a location of high downslope ground deformations; (c), (d) Proposed alternatives where abutment piles are placed 10 m/20 m away from the slope crest; (e), (f) Proposed alternatives with a center column (away from the slope large deformations) with superstructure resting on a shallow foundation at the abutments with/without base isolation; (g), (h) Proposed configuration with superstructure resting on shallow foundations with/without base isolation, in order to avoid damage to a deep foundation system (i) Proposed configuration with bridge structure resting on an inclined bracing foundation; (j) Input motion at the FE model base.

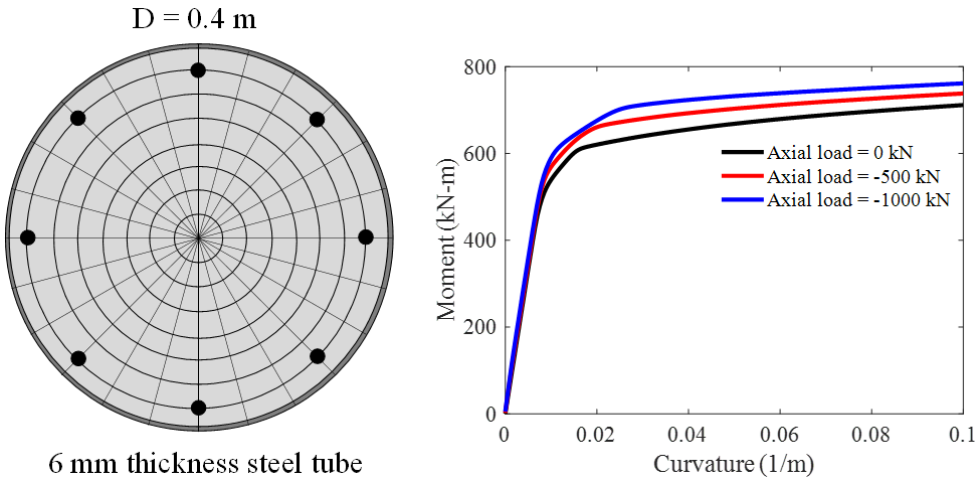

Figure 5-2 Pile fiber section and response.

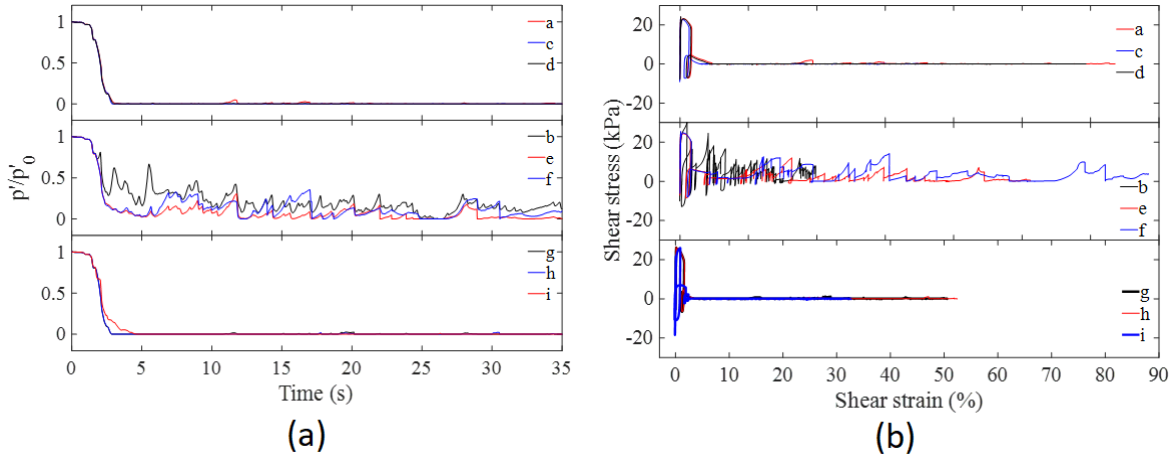

Figure 5-3. Soil response at point A: (a) Effective confinement ratio; (b) Shear stress-strain.

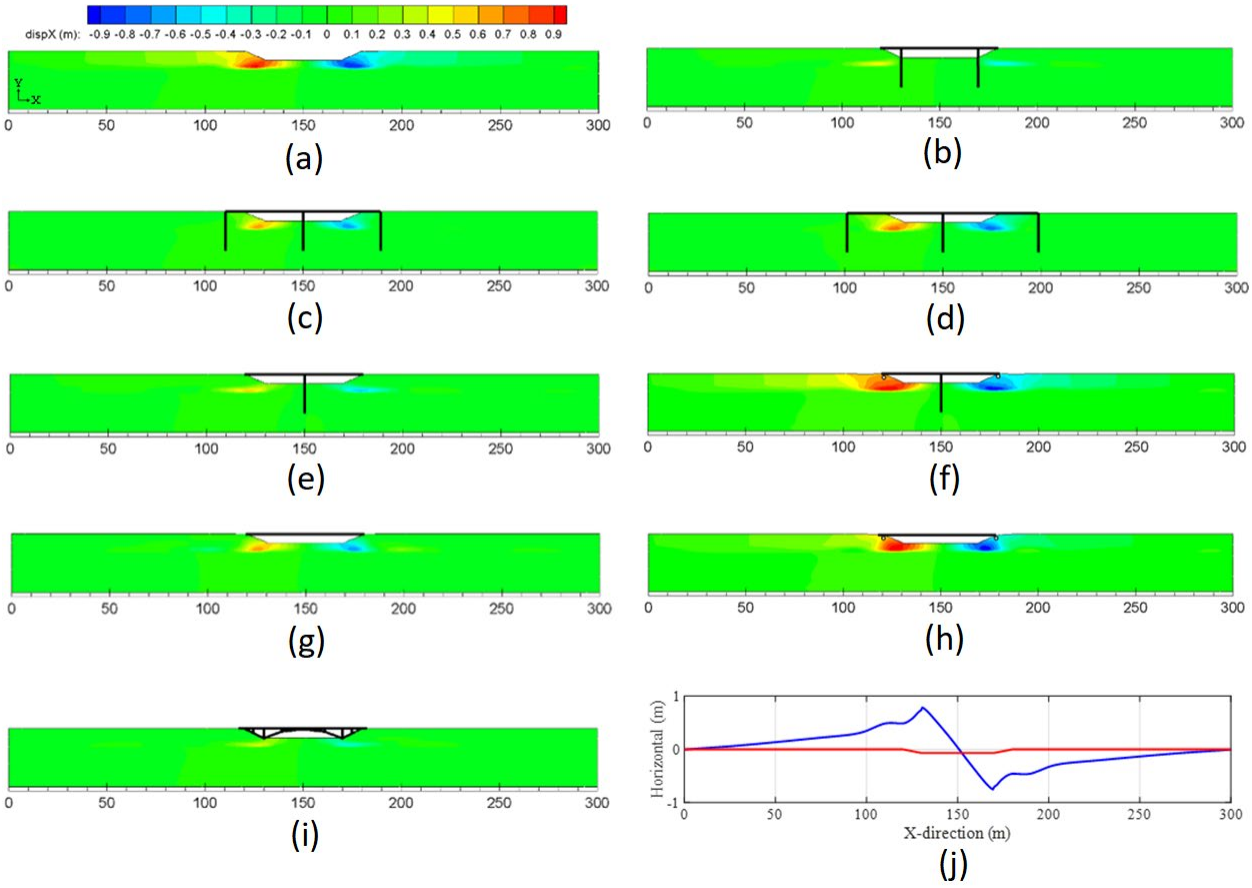

Figure 5-4. Longitudinal deformation at end of shaking: (a)-(i) Scenarios a-i; (j) Scenario a displacement (blue line) along the ground surface configuration (red line).

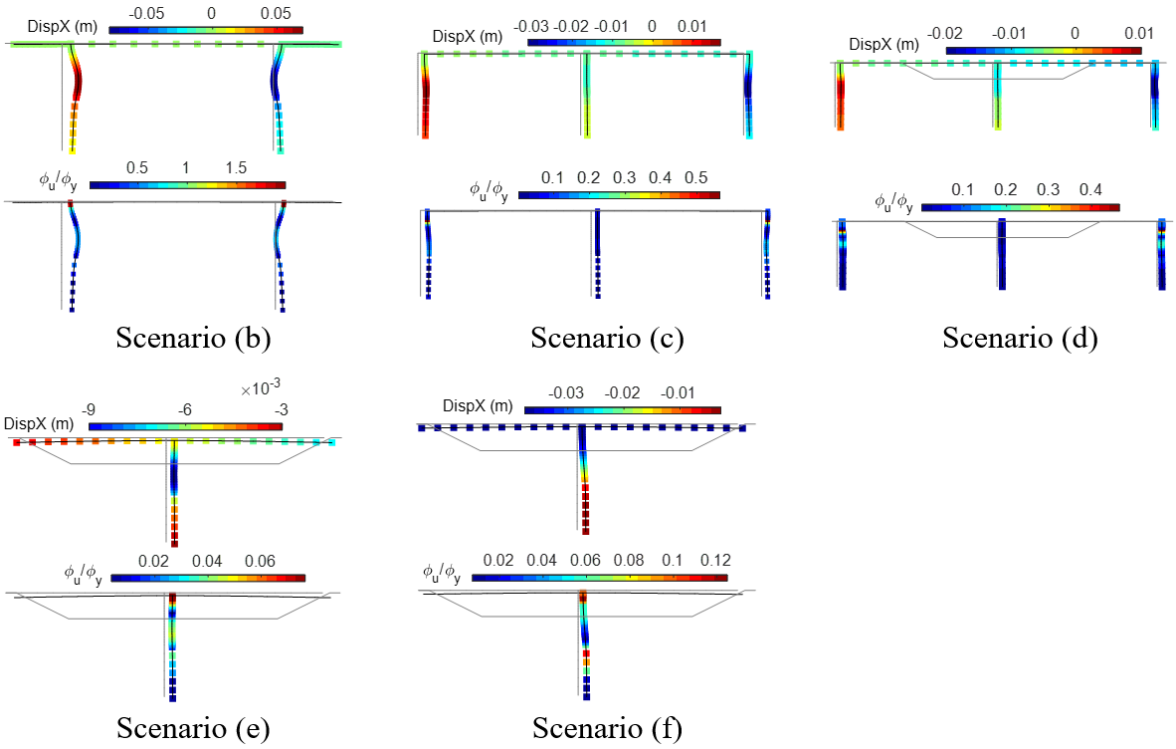

Figure 5-5. Bridge deformation (factor = 20) and ductility ratio (ϕ_u/ϕ_y) at end of shaking.

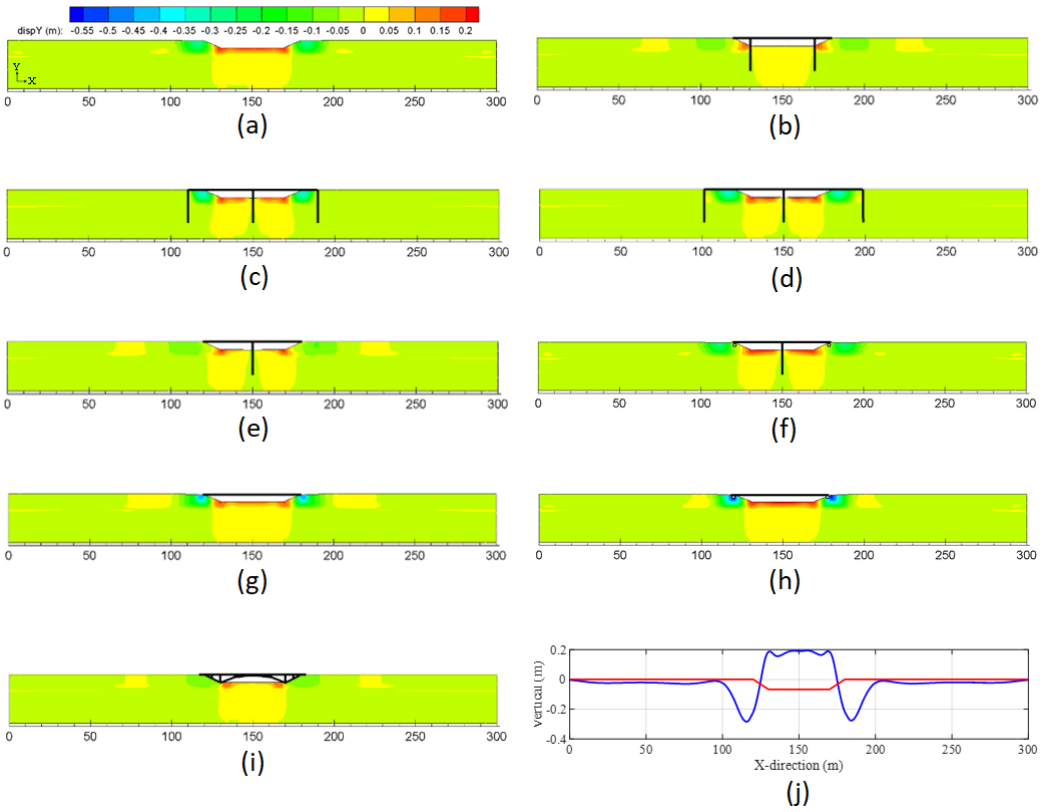

Figure 5-6. Vertical displacement at end of shaking: (a)-(i) Scenarios a-i; (j) Scenario a displacement (blue line) along the ground surface configuration (red line).

6. BRIDGE-SYSTEM AS A STRUT FOR MITIGATION OF NARROW WATERWAY DOWNSLOPE GROUND DEFORMATION

Zhijian Qiu, Ahmed Elgamal, Ahmed Ebeido, Fadel Alameddine, and Geoffrey Martin

Abstract

For narrow waterway scenarios, a shallow foundation integral-bridge configuration is proposed conceptually to mitigate the potential consequences of downslope ground deformations. Where applicable in terms of the underlying soil profile and waterway geometry, such an integral bridge-foundation system will counteract such ground deformation via; i) the bridge superstructure acting as a brace or strut that self-reacts against the sloping sides of the waterway, and ii) the bridge self-weight being employed as a potential additional stabilizing mechanism. In order to illustrate these beneficial effects, a three-dimensional (3D) Finite Element (FE) computational simulation is conducted. The restraining effect of the superstructure (acting as a strut) on the downslope ground deformation is illustrated. For additional stability, an additional ground improvement scenario is presented. In this proposed bridge configuration, absence of columns and deep foundations precludes the related detrimental consequences of lateral ground movement. With this study viewed as an illustrative pilot investigation, recommendations are included towards further investigations.

6.1 Introduction

Recent earthquakes (Arduino *et al*. 2010; Wotherspoon *et al.* 2011; Ledezma *et al.* 2012; Verdugo *et al.* 2012; Cubrinovski *et al.* 2011, 2014a, b) continue to demonstrate the detrimental effects of downslope deformations on bridge abutments, supporting columns, and pier foundations. A schematic illustration of such damage (Cubrinovski *et al.* 2014a, b) for pile-supported bridges is shown in Figure 6-1a. Due to seismic excitation, liquefied soil layers may result in substantial accumulated permanent downslope deformation near the abutments, causing severe damage to the pile foundations (Youd 1993; Hamada *et al.* 1996; Tokimatsu and Asaka 1998; Berrill *et al.* 2001; Arduino *et al.* 2010; Wotherspoon *et al.* 2011; Ledezma *et al.* 2012; Verdugo *et al.* 2012; Turner *et al.* 2013, 2016).

In order to avert such damage (Figure 6-1a), an integral-bridge shallow foundation configuration is proposed conceptually as the structural system (Figure 6-1b). In this configuration (Figure 6-1b),

the bridge deck is supported on an essentially rigid shallow foundation, precluding the possible damage to bridge columns and their underlying deep foundations (Figure 6-1a). In essence, such a configuration stands to offer the following advantages: i) the superstructure acts as a strut between both sides of the underlying waterway, providing a self-reacting mechanism with restoring lateral forces at both ends of the bridge, ii) as a potential additional mechanism, lateral earth pressure forces exerted by own weight of the bridge can be engaged to further stabilize the waterway slopes. In this regard: i) the bridge will only undergo minor detrimental consequence of potential lateral ground deformations, due to absence of conventional bridge columns and underlying foundations, and ii) after a strong earthquake, retrofit might be relatively fast and economical, as the bridge-foundation system naturally conforms to the surrounding deformed ground configuration, with minor grading or re-levelling work needed.

In order to illustrate these beneficial response mechanisms, a three-dimensional (3D) Finite Element (FE) model of a representative bridge-shallow foundation system is developed. On this basis, the following sections outline the: 1) computational framework, 2) specifics and model properties of the bridge-ground system, 3) details of the employed FE modeling techniques, 4) conducted numerical simulations and salient bridge-system response mechanisms, and 5) insights derived from the study. Finally, a number of conclusions are presented and discussed.

6.2 Conceptual Framework

For narrow waterways, two aspects of stabilization are discussed herein by employing the integral bridge-foundation system (Figure 6-1b) as:

i) a strut to brace the waterway side slopes against the accumulation of seismically-induced lateral spreading deformations, noting that the underlying basic mechanism is ubiquitously adopted as a technique for shoring excavations (Fang 2013). As such, lateral ground deformations are reduced by forces on one side of the waterway resisted by reactions on the other side, and

ii) with the abutment shallow foundation built in an inclined configuration, an additional gravity-driven bridge own-weight stabilizing force is generated. In this regard, the logic is somewhat analogous to that of the restoring force provided by own-weight of the structure in the friction pendulum base isolation mechanism (Zayas *et al.* 1987; Hamidi *et al.* 2003a, b; Hamidi and El Naggar 2007).

6.3 Computational Framework

The Open System for Earthquake Engineering Simulation (OpenSees, McKenna *et al.* 2010, http://opensees.berkeley.edu) framework is employed to conduct the nonlinear bridge-shallow foundation system analysis subjected to seismic excitation. OpenSees is developed by the Pacific Earthquake Engineering Research (PEER) Center, and it is widely used for simulation of geotechnical systems and soil-structure interaction applications (Yang and Elgamal 2002; Lu *et al.* 2011; Su *et al.* 2017). Further details concerning the employed computational framework are presented in Appendix 6-A.

6.4 Finite Element Model

Figure 6-2 depicts the representative bridge-shallow foundation model. The modeled reinforced concrete bridge is approximately 60 m long and 10 m wide. For the purpose of this study, seismic excitation is applied only in the longitudinal X-direction (i.e., no transverse Z-direction or vertical Y-direction shaking imparted). On this basis, a 3D bridge-shallow foundation FE mesh (half mesh due to symmetry, Figure 6-2) is generated comprising 45,474 nodes, representing 40,782 brick elements. Being much stiffer and stronger than the soil materials, the bridge-foundation system is idealized as essentially rigid beam-column elements. All structural components including the reinforced concrete deck (with a linear self-weight q as shown in Figure 6-3) are modeled using 3D linear elastic beam-column elements. Along the far-field soil mesh lateral boundaries (Figure 6-2), 2D plane strain soil columns of large size and depth (not shown) are included (Su *et al.* 2017; Qiu 2020). These soil columns, at an adequate distance away from the bridge structure (Figure 6-2) to minimize boundary effects (around 120 m, i.e., twice length of the bridge structure), efficiently reproduce the desired shear beam free-field response at these locations (Qiu *et al.* 2020, 2022). In the transverse Z-direction (Figure 6-2), 50 m of the soil domain is included in order to capture ground response away from the bridge structure.

6.4.1 Ground Configuration

Figure 6-3 shows the overall ground configuration with the site profile idealized as an upper clay layer, a middle loose sand layer, and a lower very dense sand layer. Table 6-1 and Table 6-2 list the sand and clay model parameters employed in the corresponding OpenSees PDMY03 and PIMY constitutive models (as discussed in Appendix 6-A). Water table is prescribed at an elevation of 23 m, at the top of the loose sand layer (Figure 6-3). The relatively low shear strength of the upper

clay and middle loose sand layers is depicted in Figure 6-4. As shown in Figure 6-4b (at a representative initial confinement of 100 kPa or 1 atmosphere), undrained shear strength of the loose sand mildly increases with applied shear strain, in accordance with the prescribed dilation coefficients (Table 6-1).

6.4.2 Boundary and Loading Conditions

As mentioned above, both lateral mesh boundaries (X = 0 m and X = 300 m) are located away from the bridge structure (Figs. 2 and 3). Along the 50 m apart ground longitudinal planes (Figure 6-2, Z = 0 m and Z = 50 m), no out-of-plane motion is allowed (to enforce the symmetry logic). Loading is implemented in a staged fashion as follows (Su *et al.* 2017; Qiu 2020; Qiu *et al.* 2020, 2022):

1) Gravity is applied to activate the initial static state for the soil domain only with: i) linear elastic properties (Poisson's ratio of 0.47 for all layers), ii) nodes on both lateral boundaries of the model fixed against longitudinal translation, iii) nodes fixed along the base in terms of vertical translation, iv) pore pressure degrees of freedom fixed at and above the 23 m elevation to specify the water table (Figure 6-2). At the end of this step, the static soil state is imposed and displacements under own-weight application are-set to zero using the OpenSees command InitialStateAnalysis.

2) Soil properties are switched from linear elastic to plastic (Table 6-1and Table 6-2).

3) The reinforced concrete deck and foundation 3D elastic beam-column elements are added. The foundation nodes are connected to the soil nodes using the OpenSees EqualDOF constraint (for the three translations). Thereafter, self-weight of the bridge structure is applied.

In this study, base of the computational soil domain is located at a depth of 30 m (Figure 6-3), about 23 m away from the bridge foundations. Lateral response of the soil strata below this 30 m depth is represented by the Lysmer-Kuhlemeyer (Lysmer and Kuhlemeyer 1969) dashpot boundary, applied along the FE model base so as to avoid spurious wave reflections (base shear wave velocity Vs = 600 m/s, in the range of soft rock, slightly higher than stiffness of the overlying stratum). As such, a dashpot is activated in the longitudinal X-direction at each node along the base, and the incident seismic wave excitation is defined by dynamic equivalent nodal forces (details of this process are presented earlier in Zhang *et al.* 2008 and Elgamal *et al.* 2008).

For the purpose of illustrating the salient seismic response mechanisms, shaking along the base (purely in the longitudinal X-direction) is imparted using the 1940 Imperial Valley earthquake El Centro Station record, Component 180 (Figure 6-5, Location MB). In this regard, deconvolution is employed as a simple approach (using Shake91 by Idriss and Sun 1993), to derive an incident earthquake motion, imparted thereafter along the base of the FE model (Elevation 0.0 in Figure 6-2). In this representation, free-field motion along the lateral mesh boundaries (X = 0 m and X = 300 m) is generated by the included soil columns mentioned above.

6.5 Computed Response

6.5.1 Acceleration

Figure 6-5 shows the free-field ground surface and bridge deck acceleration response. In general, ground surface acceleration amplitudes are slightly lower compared to those of the base input motion, due to the associated nonlinear soil response and liquefaction (discussed below). Motion of the bridge deck appears to be rather similar to that of the ground surface, and as such is very much driven by that of the surrounding ground response.

6.5.2 Longitudinal Ground Deformation

Figure 6-6 depicts the end of shaking permanent longitudinal relative displacements. At the left and right FE mesh boundaries, deformation of the free field (i.e., along the X = 0 m and 300 m planes) is minimal, only reaching about -0.005 m (Figure 6-6). Transversally, away from the bridge (Z = 0 m), much left (L) and right (R) downslope deformations are seen to occur within the waterway. These downslope deformations are substantially reduced at the bridge location (Z = 50 m plane). This is more clearly shown in Figure 6-7, where the bridge is seen to have acted as a strut within the foundation zone (Z = 45 m - 50 m), limiting the slope-crest permanent deformation to about 0.11 m leftwards. As such, resistance is mobilized through the left side, where downslope deformation is reversed from the L0 of about +1 m (downslope) to the L1 of -0.11 m (Figure 6-7). In essence, the entire bridge moved leftwards by about -0.11 m (Figure 6-7a), pushing against the left-side slope, resulting in this restraining mechanism.

6.5.3 Vertical Ground Deformation

In terms of vertical deformation, the corresponding picture is displayed in Figure 6-8 and Figure 6-9. The free-filed slope-crests are seen to settle by about 0.45 m. Due to presence of the bridge's structural system (Locations L1, R1 compared to L0, R0), slope deformation interaction results in a thrust that lifts the bridge upwards by as much as 0.2 m, with an essentially imperceptible inclination of the deck (0.2 m – 0.04 m = 0.16 m over the bridge length of 60 m). In addition, it may be noted that the bridge structure largely remains in conformance with the surrounding ground geometry, with minor earthwork required to restore its full functionality.

6.5.4 Liquefaction and Accumulated Shear Strain

Corresponding to the permanent ground deformations depicted in Figure 6-6, permanent shear strain γ_{xy} at end of shaking is shown in Figure 6-10, where it may be noted that:

1. At the left and right boundaries of the ground domain, permanent shear strain in the free field is relatively quite small.

2. At both side slopes (Locations L0, L1, R0 and R1), downslope shear strains are accumulated within the loose sand layer zone, reaching very high values in excess of 60 % near its base. At the bridge location (Z = 50 m), it may be observed that presence of the bridge has caused additional large strain zones to appear within the supporting underlying loose sand and upper clay layers. These large strain zones are indicative of the foundation-soil interface interaction stemming from the strut action of the bridge.

Figure 6-11 shows representative soil response. Within the upper clay layer (Elevation 23 m), accumulated shear strains are notably low (Locations L1 and R1) due to the bridge's restraining effect, compared to their free-field counterpart (Locations L0 and R0).

Within the loose sand layer (Elevation 17 m), effective confinement is gradually lost due to liquefaction. The resulting stress-strain response clearly shows the corresponding substantial reduction in shear strength and: i) cyclic straining with minimal accumulation within the central zone of the waterway (Location M), ii) accumulation of large shear strains due to the side slopes (Locations L0, L1, R0 and R1). Nevertheless, the overall shear strain at Locations L1 and R1 (Z = 50 m, under the bridge) is about 30 % less than that at Locations L0 and R0 (Z = 0 m, free-filed away from the bridge), due to restraining effect of the bridge's structural system.

6.6 Additional Ground Improvement Scenario

6.6.1 Finite Element Model with Two Improved Zones

In seismic areas, soil mixing as a ground improvement technique has been used for supporting bridge abutments on spread footings (Arora *et al.* 2012; Yamasaki *et. al.* 2015; Franke *et al.* 2019; Stuedlein *et al.* 2021). For added stability, the numerical model is employed herein to conduct a representative analyses. For that purpose, an additional numerical simulation is conducted by implementing a deep soil mixing scenario, to increase stiffness and strength of the sloping ground zone. As such, two soil mixing improved zones are considered (Figure 6-12), aiming to further stabilize the slope materials on both sides. In configuring this mitigation approach, attention is given to the option where retrofit is implemented at the abutments rather than within the waterway, where cost and effort would substantially increase. In this FE analysis, the wall is modeled by the OpenSees PIMY model (as discussed in Appendix 6-A) with the modeling parameters shown in Table 6-2.

6.6.2 Results

Figure 6-13 shows the longitudinal and vertical displacement contours at end of shaking. Within the waterway, ground deformation near the bridge is significantly reduced, due to the additional restraining effects provided by the soil mixing zones on both sides. As seen in Figure 6-14a, longitudinal deformation of these zones is small, only reaching about 0.05 m near the ground surface. The corresponding highest shear strains are seen to be about 7 % (Figure 6-14b).

Compared to the original scenario (Figure 6-10), shear strains near the base of the liquefied loose sand layer are substantially lower at Z = 50 m, reaching a peak value of about 10 % (Figure 6-15). In addition, the overall shear strains at Z = 50 m under the bridge are 50 % less than those of the free field (Z = 0 m away from the bridge).

Figure 6-16 depicts the longitudinal and vertical bridge displacements for this scenario. It can be seen that the longitudinal displacement at the end of shaking is considerably reduced from 0.11 m in the original configuration (Figure 6-7) to 0.03 m. Furthermore, the vertical displacement at locations L1 and R1 are small, reaching only about -0.024 m, mainly due to the increased bearing capacity provided by the soil mixing zones on both sides. Figure 6-16a shows the bridge deck acceleration response. Due to presence of the relatively stiff zones on both sides, somewhat higher bridge deck accelerations are noted (Figure 6-16a), compared to those of Figure 6-5.

As illustrated above, ground improvement, if needed, can offer an effective path towards realization of the proposed shallow foundation bridge-ground system. The extent of this improvement would be defined to meet the specified criteria of own-weight static stability and seismic performance.

6.7 Summary and Conclusions

In narrow waterway scenarios, an integral-bridge shallow foundation system is proposed conceptually as a bracing mechanism to counteract downslope ground deformation. For that purpose, 3D FE modeling is employed to illustrate the involved salient seismic response characteristics. Feasibility of this proposed conceptual bridge configuration is further illustrated by the possible deployment of ground improvement countermeasures. On this basis, specific observations and conclusions include:

1) The bridge superstructure is shown to provide significant restraining effects on lateral ground deformation. Such effects stem from: i) the bridge acting as a strut, self-reacting against the waterway side slopes, and ii) own weight of the bridge exerting additional restoring lateral earth pressure forces on these slopes.

2) Absence of bridge columns and underlying foundations cause potential lateral ground deformations to have minimal detrimental influence of the bridge superstructure.

3) After an earthquake: i) retrofit is relatively economical with no need to address costly deep foundation challenges, and ii) the bridge structure naturally conforms to the surrounding deformed ground configuration, where minor grading or re-levelling work might be needed; and with minimal to no damage of the bridge structure.

6.8 References

Arora, S., Shao, L. and Schultz, J.M. (2012). "Wet soil mixing for bearing capacity, liquefaction mitigation, and water cutoff for scour protection for a new bridge abutment." In *Grouting and Deep Mixing 2012* (575-584).

Arduino, P., Ashford, S., Assimaki, D., Bray, J., Eldridge, T., Frost, D., Hashash, Y., Hutchinson, T., Johnson, L., Kelson, K. and Kayen, R. (2010). "Geo-engineering reconnaissance of the 2010 Maule, Chile earthquake." *GEER Association Report* No. GEER-022, 1.

Berrill, J.B., Christensen, S.A., Keenan, R.P., Okada, W. and Pettinga, J.R. (2001). "Case study of lateral spreading forces on a piled foundation." *Geotechnique*, 51(6), 501-517.

Carlson N.N., Miller K. (1998). "Design and application of a gradient-weighted moving finite element code I: in one dimension." *SIAM Journal on Scientific Computing*, 19(3):728-765.

Chan A.H.C. (1988). "A unified finite element solution to static and dynamic problems in geomechanics." *PhD Thesis*, University College of Swansea, UK

Cubrinovski, M., Bradley, B., Wotherspoon, L., Green, R., Bray, J., Wood, C., Pender, M., Allen, J., Bradshaw, A., Rix, G. and Taylor, M. (2011). "Geotechnical aspects of the 22 February 2011 Christchurch earthquake." *Bulletin of the New Zealand Society for Earthquake Engineering*, 44(4), 205-226.

Cubrinovski, M., Winkley, A., Haskell, J., Palermo, A., Wotherspoon, L., Robinson, K., Bradley, B., Brabhaharan, P. and Hughes, M. (2014a). "Spreading-induced damage to short-span bridges in Christchurch, New Zealand." *Earthquake Spectra*, 30(1), 57-83.

Cubrinovski, M., Haskell, J., Winkley, A., Robinson, K. and Wotherspoon, L. (2014b). "Performance of bridges in liquefied deposits during the 2010-2011 Christchurch, New Zealand, earthquakes." *Journal of Performance of Constructed Facilities*, 28(1), 24-39.

Franke, K.W., Koehler, R.D., Beyzaei, C.Z., Cabas, A., Pierce, I., Stuedlein, A. and Yang, Z., (2019). "Geotechnical engineering reconnaissance of the 30 November 2018 Mw 7.0 Anchorage, Alaska earthquake." *GEER Report GEER-059*, 1-46.

Elgamal, A., Yang, Z. and Parra, E. (2003). "Modeling of cyclic mobility in saturated cohesionless soils." *International Journal of Plasticity*, 19(6), 883-905.

Elgamal, A., Yan, L. and Yang, Z. (2008). “Three-dimensional seismic response of Humboldt Bay bridge-foundation-ground system.” *Journal of Structural Engineering*, 134(7), 1165-1176.

Fang, H. Y. (2013). Foundation engineering handbook. Springer Science & Business Media.

Hamada, M., Isoyama, R. and Wakamatsu, K. (1996). “Liquefaction-induced ground displacement and its related damage to lifeline facilities.” *Soils and Foundations*, 36(Special), 81-97.

Hamidi, M., El Naggar, M.H., Vafai, A. and Ahmadi, G. (2003a). “Seismic isolation of buildings with sliding concave foundation (SCF).” *Earthquake Engineering & Structural Dynamics*, 32(1), 15-29.

Hamidi, M., El Naggar, M.H. and Vafai, A. (2003b). “Response of structures supported on SCF isolation systems.” *Earthquake Engineering & Structural Dynamics*, 32(10), 1555-1584.

Hamidi, M. and El Naggar, M.H. (2007). “On the performance of SCF in seismic isolation of the interior equipment of buildings.” *Earthquake Engineering & Structural Dynamics*, 36(11), 1581-1604.

Idriss, I.M. and Sun, J.I. (1993). “User’s manual for SHAKE91: A computer program for conducting equivalent linear seismic response analyses of horizontally layered soil deposits.” Center for Geotechnical Modeling, Dept. of Civil and Environmental Engineering, University of California Press, Davis, CA.

Idriss, I.M. and Boulanger, R.W. (2008). Soil liquefaction during earthquakes. Earthquake Engineering Research Institute.

Khosravifar, A., Elgamal, A., Lu, J. and Li, J. (2018). “A 3D model for earthquake-induced liquefaction triggering and post-liquefaction response.” *Soil Dynamics and Earthquake Engineering*, 110, 43-52.

Ledezma, C., Hutchinson, T., Ashford, S.A., Moss, R., Arduino, P., Bray, J.D., Olson, S., Hashash, Y.M., Verdugo, R., Frost, D. and Kayen, R. (2012). “Effects of ground failure on bridges, roads, and railroads.” *Earthquake Spectra*, 28(S1), S119-S143.

Lu, J., Elgamal, A., Yan, L., Law, K.H. and Conte, J.P. (2011). “Large-scale numerical modeling in geotechnical earthquake engineering.” *International Journal of Geomechanics*, 11(6), 490-503.

Lysmer, J. and Kuhlemeyer, R.L. (1969). “Finite Dynamic Model for Infinite Media.” *Journal of Engineering Mechanics Division*, 95, 859-878.

Mazzoni, S., McKenna, F., Scott, M.H. and Fenves, G.L. (2009). “Open System for Earthquake Engineering Simulation, User Command-Language Manual.” *Pacific Earthquake Engineering Research Center, University of California, Berkeley*, OpenSees version 2.0, May.

McKenna, F., Scott, M. and Fenves, G. (2010). “Nonlinear finite-element analysis software architecture using object composition.” *Journal of Computing in Civil Engineering*, 24(1), 95-107.

Parra, E. (1996). “Numerical modeling of liquefaction and lateral ground deformation including cyclic mobility and dilation response in soil systems.” *PhD Thesis*, Department of Civil Engineering, Rensselaer Polytechnic Institute, Troy, NY.

Qiu, Z., Ebeido, A., Almutairi, A., Lu, J., Elgamal, A., Shing, P.B. and Martin, G. (2020). “Aspects of bridge-ground seismic response and liquefaction-induced deformations.” *Earthquake Engineering & Structural Dynamics*, 49(4), 375-393.

Qiu, Z. (2020). “Computational modeling of ground-bridge seismic response and liquefaction scenarios.” *PhD Thesis*, Department of Structural Engineering, UC San Diego, La Jolla, CA.

Qiu, Z., Lu, J., Ebeido, A., Elgamal, A., Uang, C.M., Alameddine, F. and Martin, G. (2022). “Bridge in Narrow Waterway: Seismic Response and Liquefaction-Induced Deformations.” *Journal of Geotechnical and Geoenvironmental Engineering*, 148(8), 04022064.

Su, L., Lu, J., Elgamal, A. and Arulmoli, A.K. (2017). “Seismic performance of a pile-supported wharf: Three-dimensional finite element simulation.” *Soil Dynamics and Earthquake Engineering*, 95, 167-179.

Stuedlein, A.W., Gibson, M.D., Yamasaki, K., Hemstreet, D. and Shao, L. (2021). “Performance of the Wet Soil Mixing-Supported West Dowling Bridge during the 30 November 2018 Anchorage Earthquake.” In *IFCEE 2021* (414-429).

Tokimatsu, K. and Asaka, Y. (1998). “Effects of liquefaction-induced ground displacements on pile performance in the 1995 Hyogoken-Nambu earthquake.” *Soils and Foundations*, 38(Special), 163-177.

Turner, B., Brandenberg, S.J. and Stewart, J.P. (2013). "Evaluation of collapse and non-collapse of parallel bridges affected by liquefaction and lateral spreading," *Proc. 10th International Conf. on Urban Earthquake Engineering.*, Center for Urban Earthquake Engineering, March 1-2, 2013, Tokyo Institute of Technology, Tokyo, Japan.

Turner, B.J., Brandenberg, S.J. and Stewart, J.P. (2016). "Case study of parallel bridges affected by liquefaction and lateral spreading." *Journal of Geotechnical and Geoenvironmental Engineering*, 142(7), 05016001.

Verdugo, R., Sitar, N., Frost, J.D., Bray, J.D., Candia, G., Eldridge, T., Hashash, Y., Olson, S.M. and Urzua, A. (2012). "Seismic performance of earth structures during the February 2010 Maule, Chile, earthquake: dams, levees, tailings dams, and retaining walls." *Earthquake Spectra*, 28(S1), S75-S96.

Wotherspoon, L., Bradshaw, A., Green, R., Wood, C., Palermo, A., Cubrinovski, M. and Bradley, B. (2011). "Performance of bridges during the 2010 Darfield and 2011 Christchurch earthquakes." *Seismological Research Letters*, 82(6), 950-964.

Yamasaki, K., Hemstreet, D., Gerondale, A. and Shao, L. (2015). "Wet soil mixing for supporting bridge abutments on spread footings." *Deep mixing, 2015*, 395-404.

Yang, Z. (2000). "Numerical modeling of earthquake site response including dilation and liquefaction." *PhD Thesis*, Columbia University.

Yang, Z. and Elgamal, A. (2002). "Influence of permeability on liquefaction-induced shear deformation." *Journal of Engineering Mechanics*, 128(7), 720-729.

Yang, Z., Elgamal, A. and Parra, E. (2003). "Computational model for cyclic mobility and associated shear deformation." *Journal of Geotechnical and Geoenvironmental Engineering*, 129(12), 1119-1127.

Yang, Z., Lu, J. and Elgamal, A. (2008). "OpenSees soil models and solid-fluid fully coupled elements." User's manual: Version 1. La Jolla, CA: Univ. of California, San Diego.

Youd, T.L. (1993). "Liquefaction-induced damage to bridges." *Transportation Research Record*, 1411, 35-41.

Zayas, V., Low, S. S., and Mahin, S. A. (1987). “The FPS earthquake resisting system, experimental report.” *Report* No. UCB/EERC-87/01, Earthquake Engineering Research Center, Univ. of California, Berkeley, CA, June.

Zhang, Y., Conte, J.P., Yang, Z., Elgamal, A., Bielak, J. and Acero, G. (2008). “Two-dimensional nonlinear earthquake response analysis of a bridge-foundation-ground system.” *Earthquake Spectra*, 24(2), 343-386.

Appendix 6-A

OpenSees Formulation and Materials

Three-dimensional solid-fluid brick elements (bbarBrickUP in OpenSees) following the *u-p* formulation (Chan 1988) are employed for simulating saturated soil response, where *u* is displacement of the soil skeleton and *p* is pore-water pressure. Implementation of this *u-p* element is based on the following assumptions: 1) small deformation and rotation; 2) solid and fluid density remain constant in time and space; 3) porosity is locally homogeneous and constant with time; 4) soil grains are incompressible; 5) solid and fluid phases are accelerated equally. Hence, the soil layers represented by these effective stress fully coupled elements account for deformations and changes in pore-water pressure during seismic excitation.

For sand, the OpenSees material PDMY03 (Khosravifar *et al.* 2018) is employed to capture the liquefaction-induced shear strain accumulation mechanism (Yang and Elgamal 2002; Elgamal *et al.* 2003; Yang *et al.* 2003, 2008). For undrained-clay response, the OpenSees PIMY material (Elgamal 2008; Yang *et al.* 2008; Lu *et al.* 2011) is employed for simulating the elasto-plastic hysteresis shear response.

The FE matrix equation of the bridge-ground system is integrated in time using a single-step predictor multi-corrector scheme of the Newmark type (Chan 1988; Parra 1996) with integration parameters $\gamma = 0.6$ and $\beta = 0.3025$. The equation is solved using the modified Newton-Raphson approach with Krylov subspace acceleration (Carlson and Miller 1998; Mazzoni *et al.* 2009). A relatively low level of stiffness proportional viscous damping is used to enhance numerical stability (coefficient = 0.003), with the main damping emanating from the soil nonlinear shear stress-strain hysteresis response (Su *et al.* 2017; Qiu 2020; Qiu *et al.* 2020, 2022).

Table 6-1 Sand model parameters.

Model Parameters	Loose Sand ($N_{1,60}$ = 5)	Very Dense Sand ($N_{1,60}$ = 35)
Reference confinement, p'_r (kPa)	100	100
Mass density, ρ (t/m^3)	1.94	2.13
Friction angle, ϕ (degree)	30°	45°
Phase transformation angle, ϕ_{PT} (degree)	26°	28°
Shear modulus at p'_r, G_o (MPa)	46.9	180
Poisson's ratio, v	0.4	0.4
Stiffness dependence coefficient d	0.5	0.5
Maximum shear strain at reference pressure, $\gamma_{max,r}$	0.1	0.1
Contraction coefficients, c_1, c_2, c_3, c_4, c_5	0.03, 5, 0.2, 16, 2	0.001, 3, 0.2, 2, 0
Dilation coefficients, d_1, d_2, d_3	0.15, 3, 0.2	0.6, 3, 0.2
Damage parameters, y_1, y_2	1, 0	1, 0
Shear strength at zero confinement, c (kPa)	2	2
Permeability, k (m/s)	1.0×10^{-5}	1.0×10^{-5}

Table 6-2 Clay PIMY model parameters.

Model parameters	Clay	Improved
Mass density, ρ (t/m^3)	2.0	2.4
Shear modulus, G (MPa)	40.0	600.0
Poisson's ratio for dynamics, v	0.4	0.4
Cohesive strength, c (kPa)	40.0	300.0
Shear strain at which the maximum shear strength is reached, $\gamma_{max,r}$	0.1	0.1

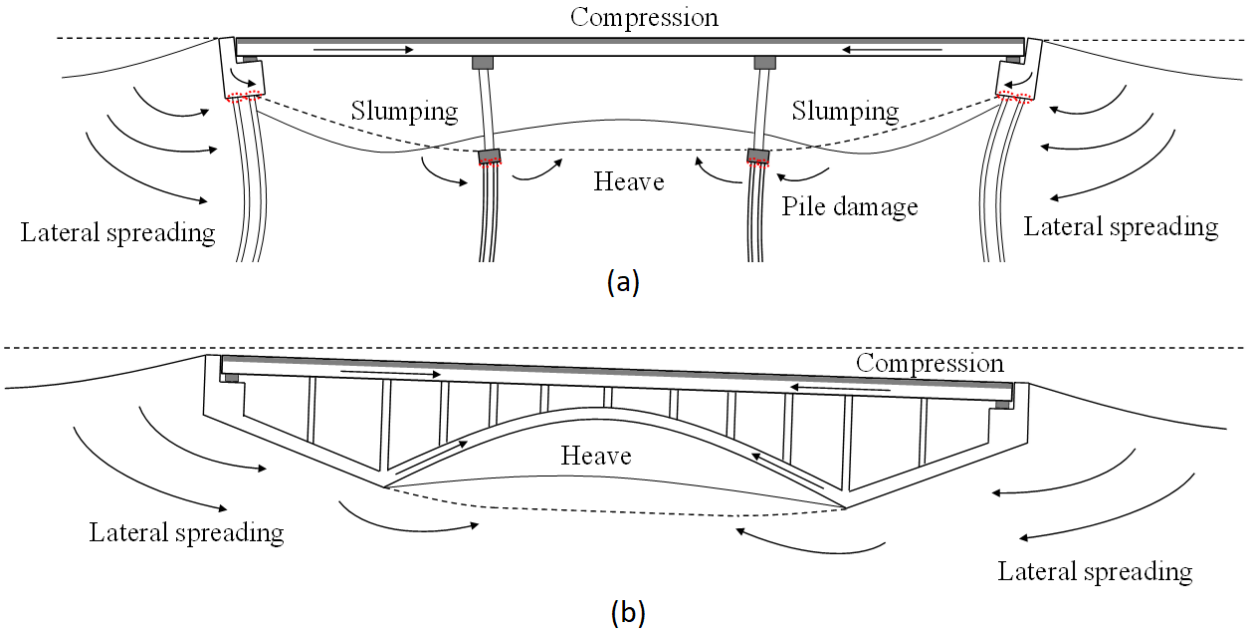

Figure 6-1. Schematic illustration of typical spreading-induced damage mechanism: (a) Pile-supported bridge; (b) Integral bridge-shallow foundation system.

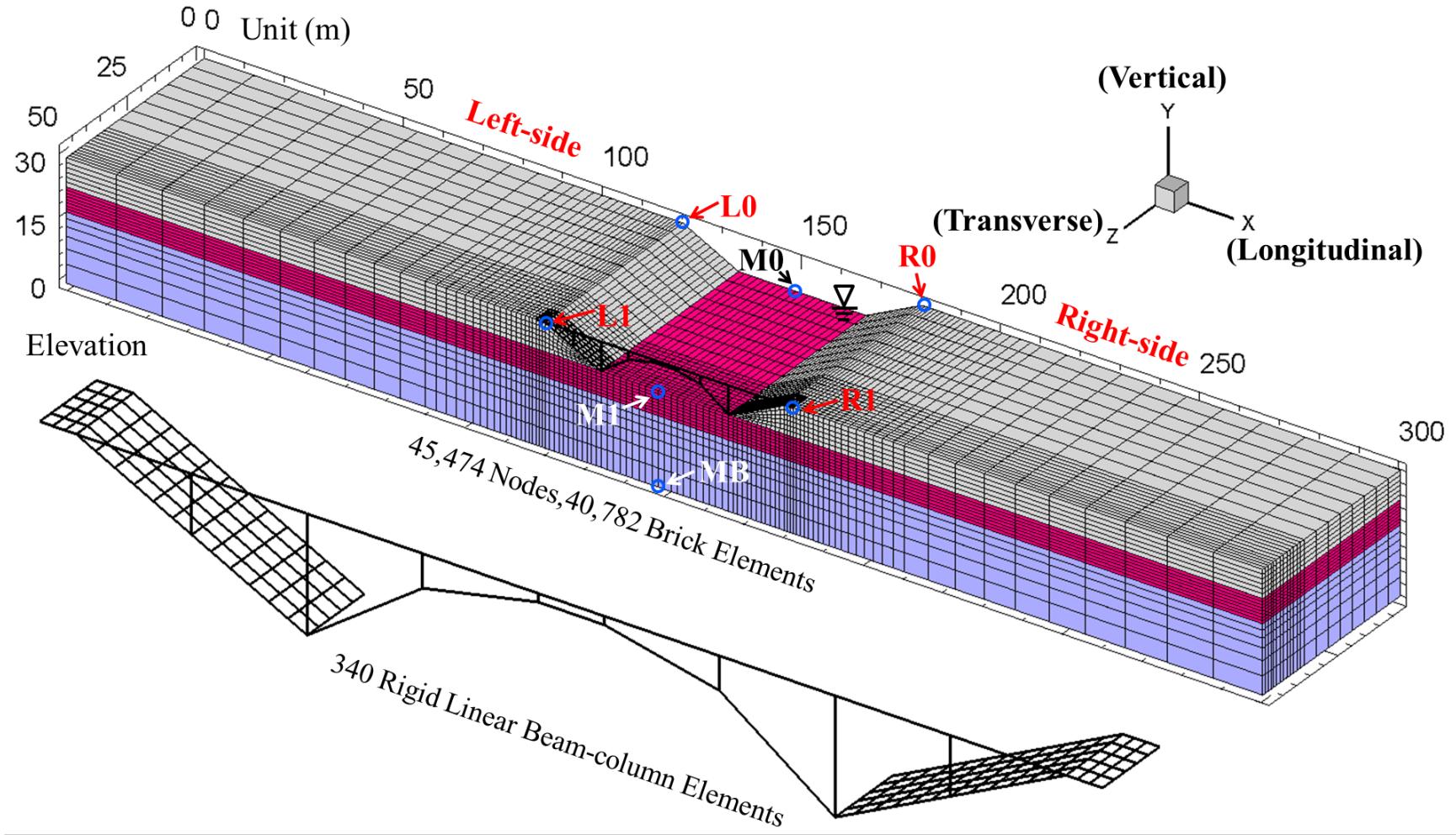

Figure 6-2. 3D FE model (half mesh due to symmetry).

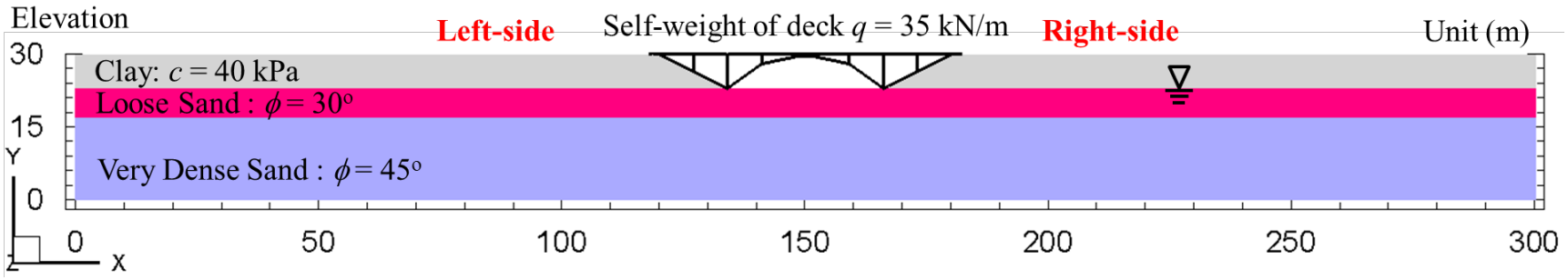

Figure 6-3. Groud configuration.

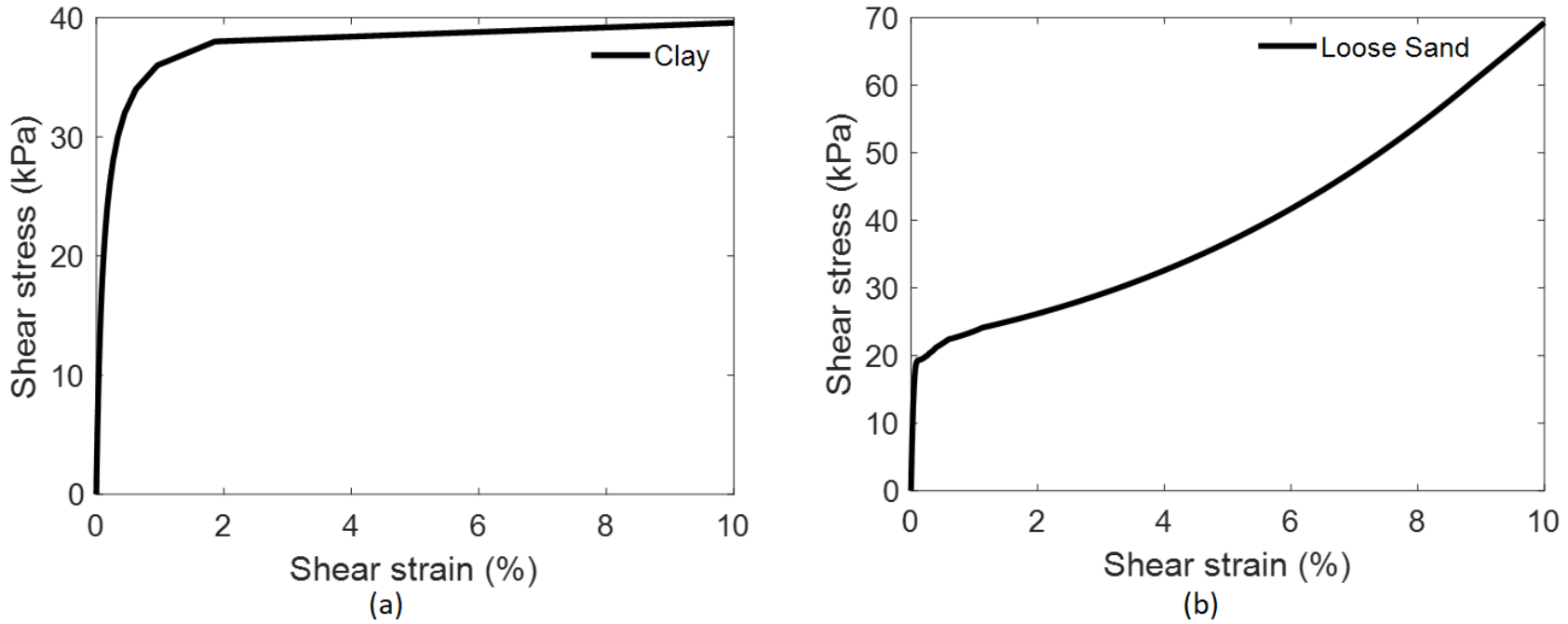

Figure 6-4. Illustrative soil behavior: (a) Clay PIMY model response; (b) Loose sand PDMY03 model undrained response.

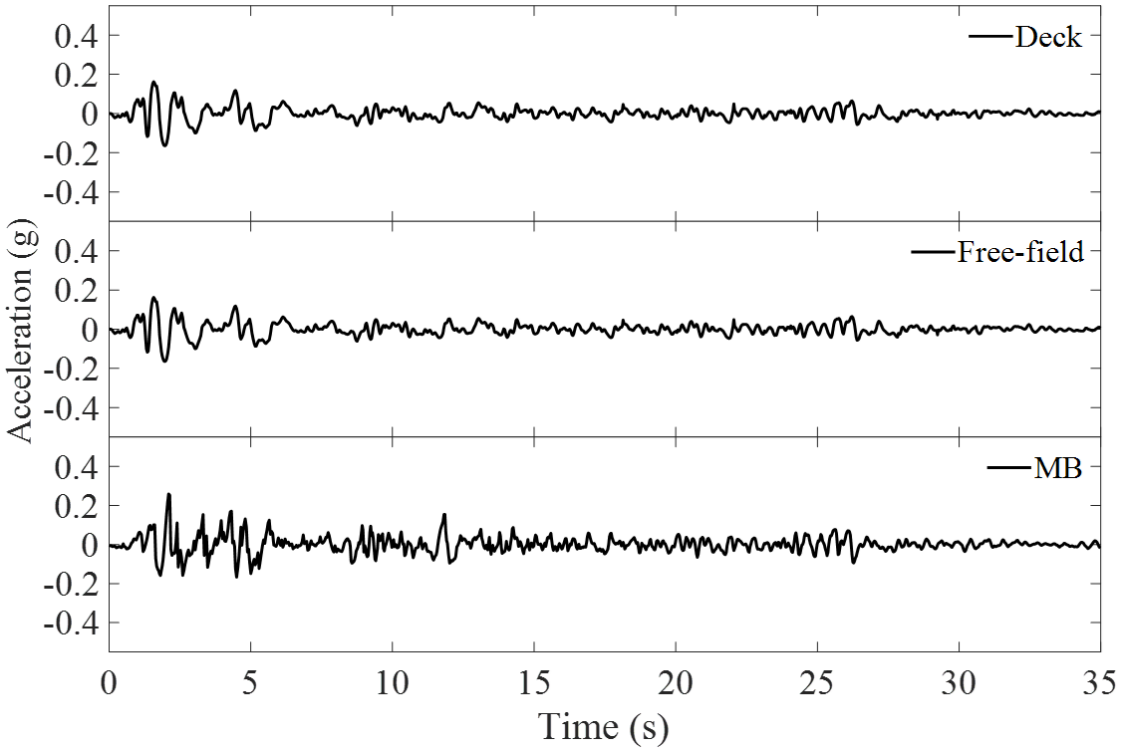

Figure 6-5. Acceleration time histories.

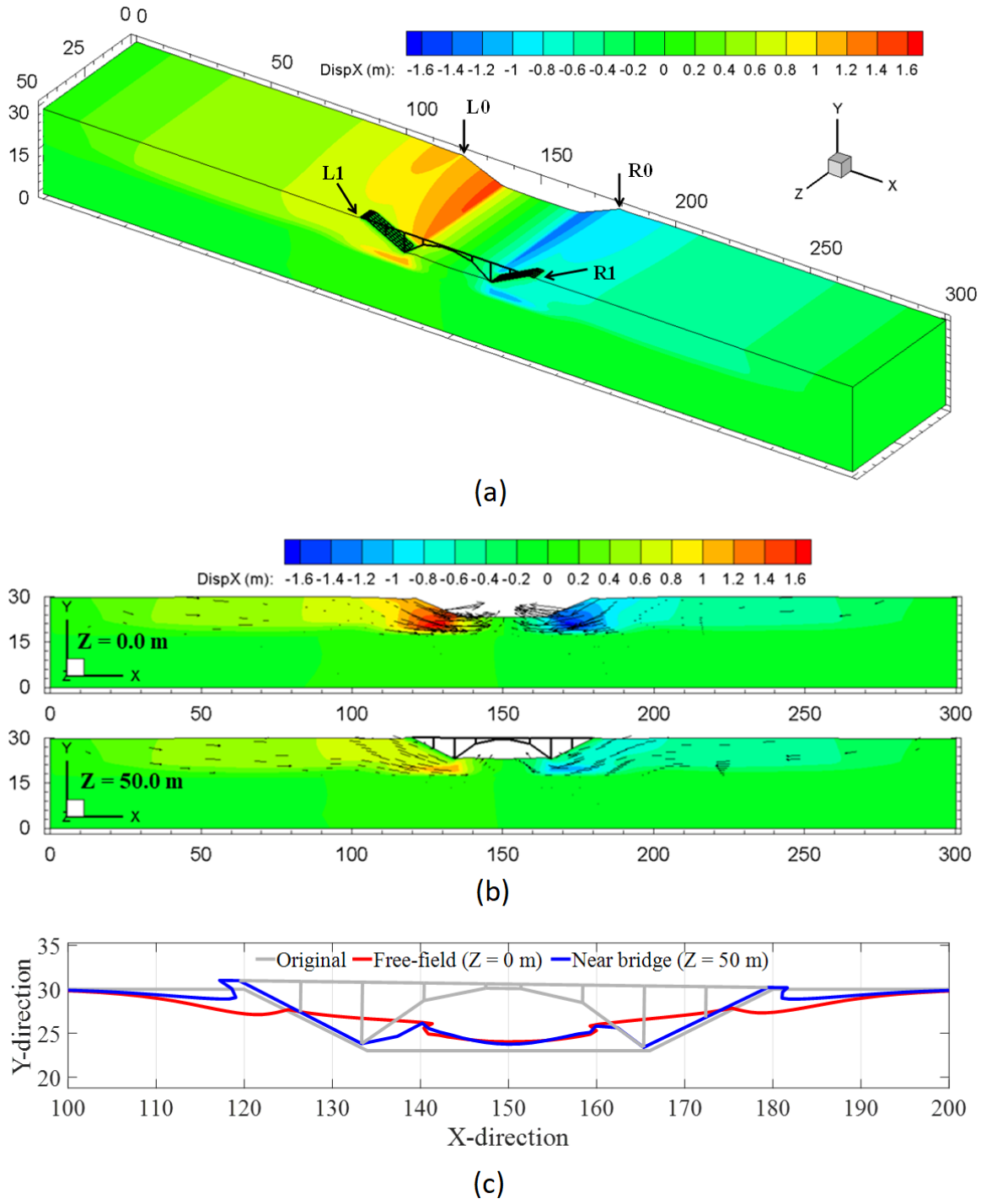

Figure 6-6. Longitudinal displacement contours at end of shaking: (a) Isometric view; (b) Side views at Z = 0 m and 50 m (arrows display direction of ground movement); (c) Deformation along ground surface (factor = 5).

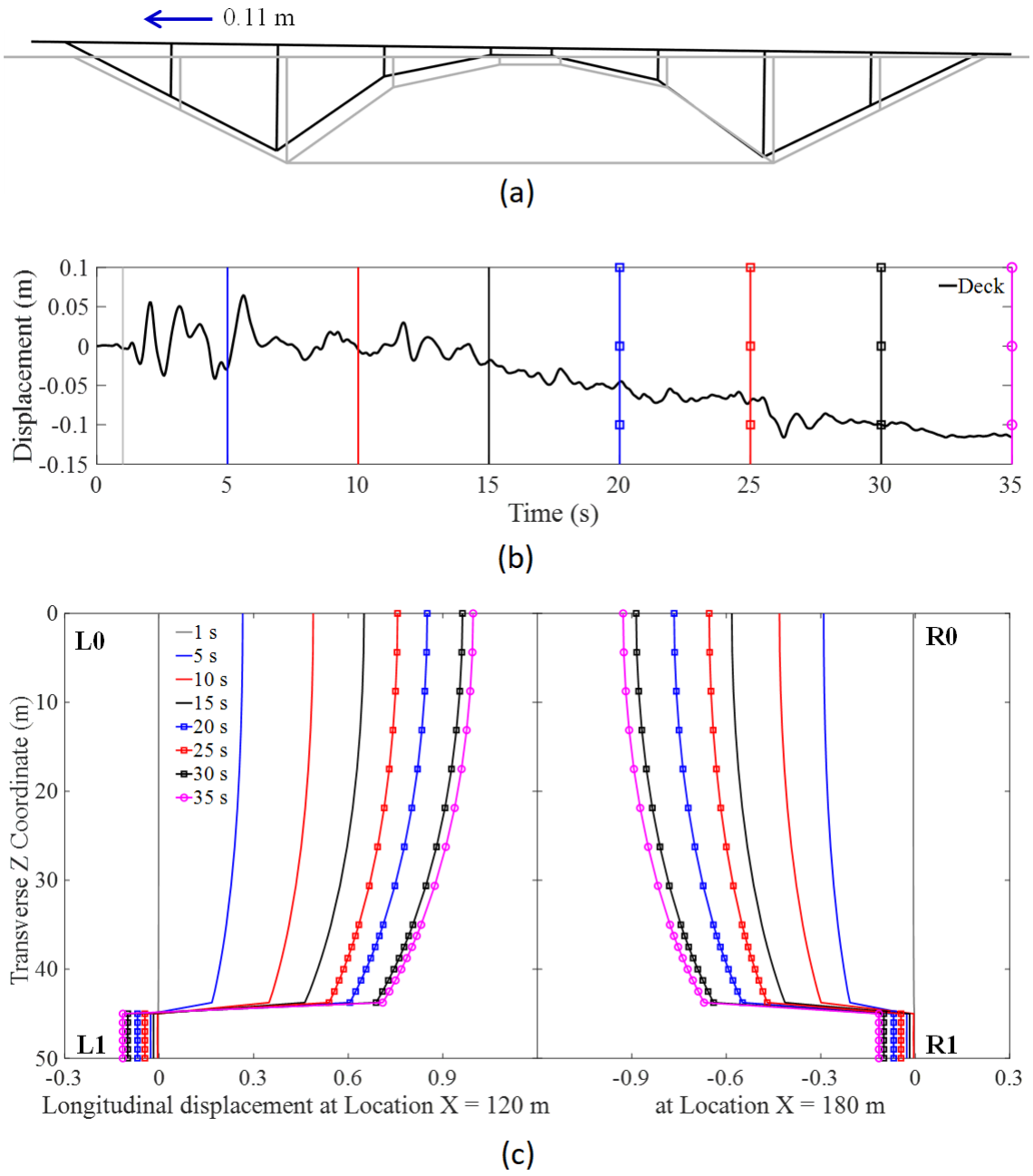

Figure 6-7. Longitudinal displacement: (a) Bridge configuration at end of shaking; (b) Time history of Deck displacement; (c) Profiles of slope-crest displacement (X = 120 m and X = 180 m).

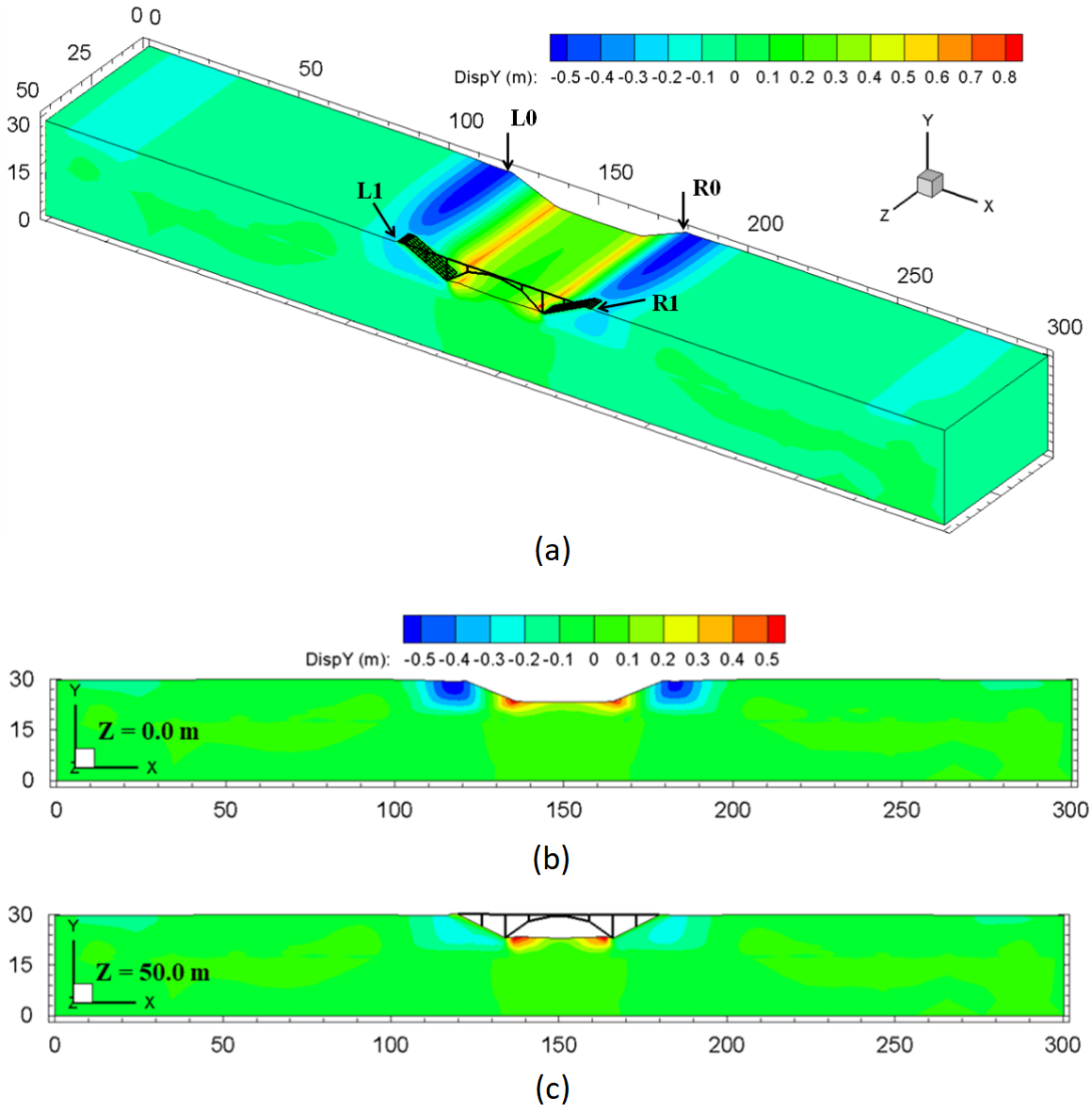

Figure 6-8. Vertical displacement contours at end of shaking: (a) Isometric view; (b) Side view at Z = 0, and (c) Side view at Z=50 m.

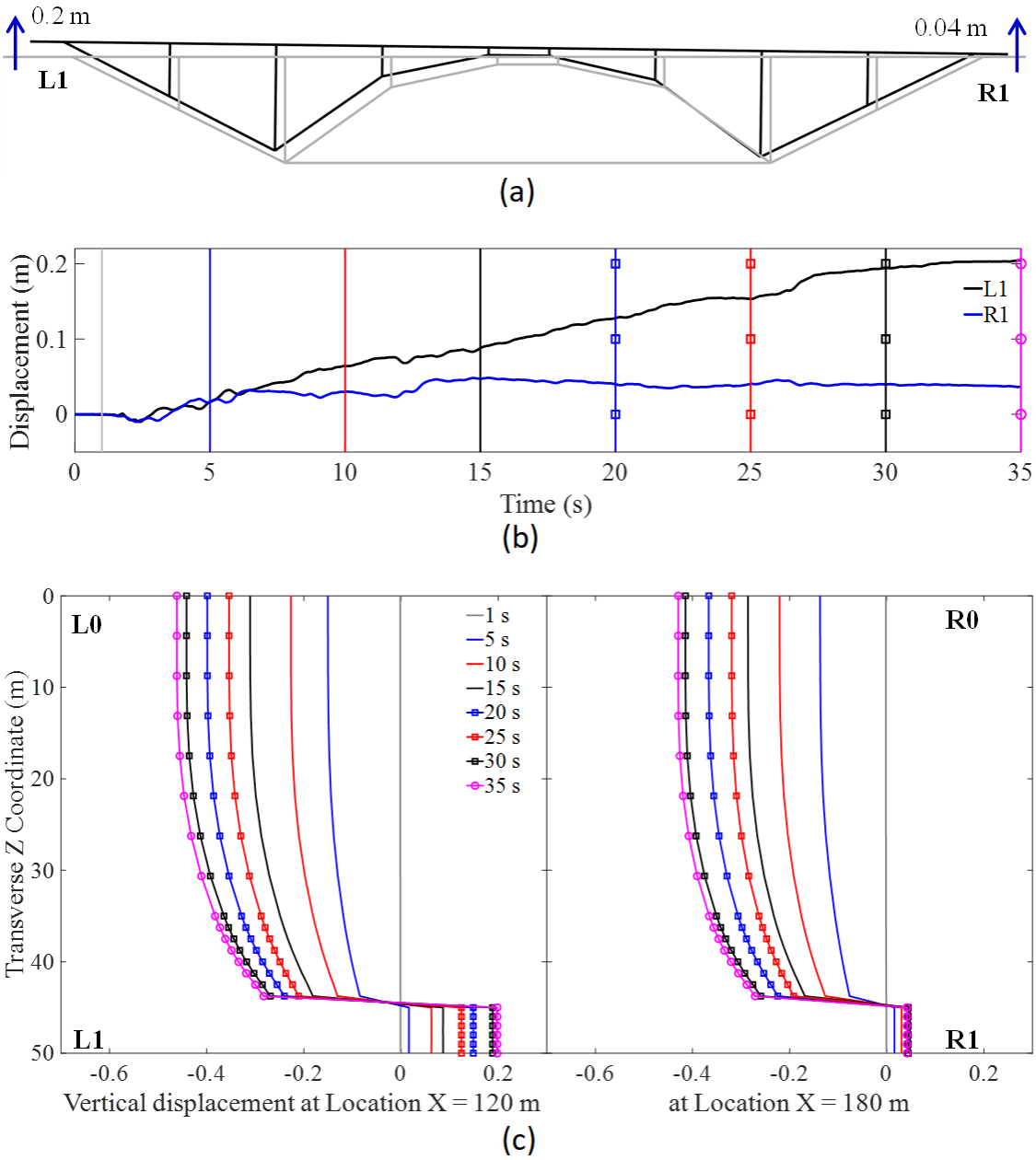

Figure 6-9. Vertical displacement: (a) Bridge configuration at end of shaking; (b) Time history of Deck displacement; (c) Profiles of slope-crest displacement (X = 120 m and X = 180 m).

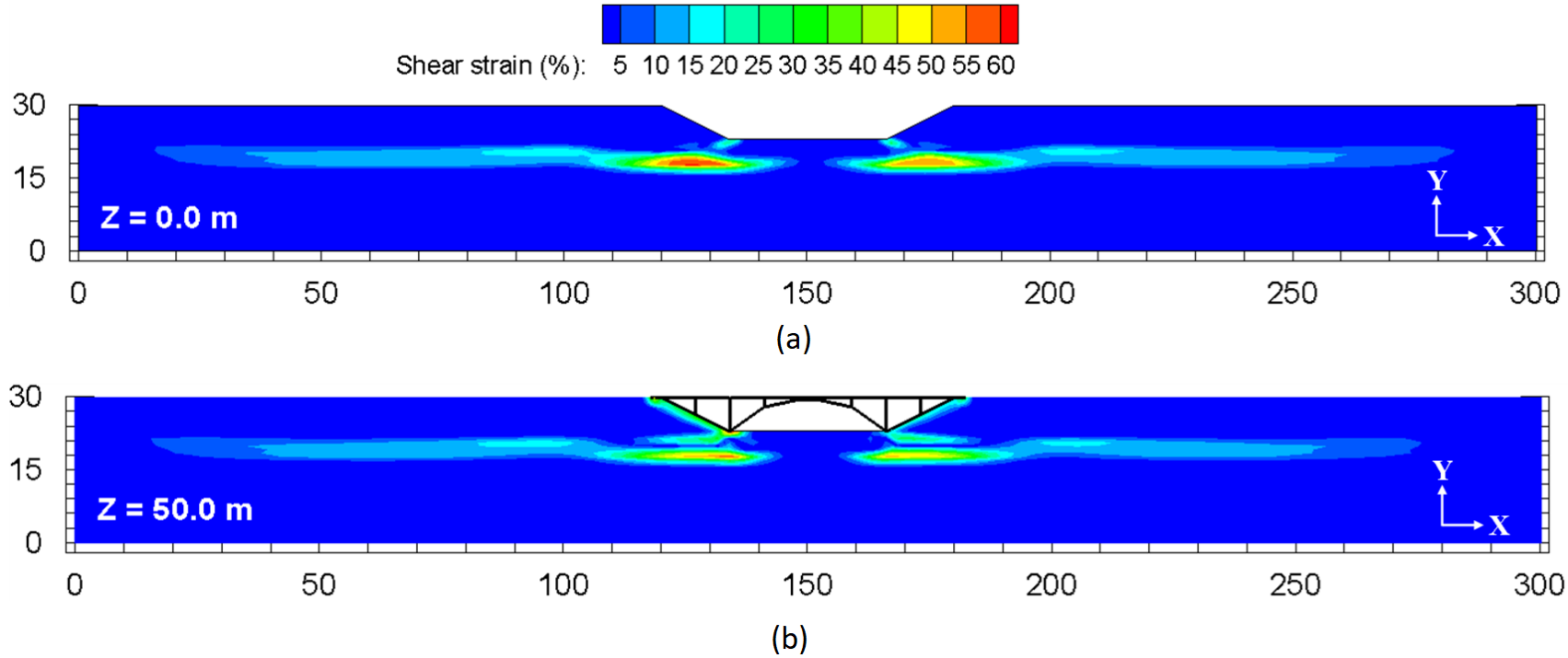

Figure 6-10. Shear strain γ_{xy} contours at end of shaking, (a) Z = 0 m, (b) Z = 50 m.

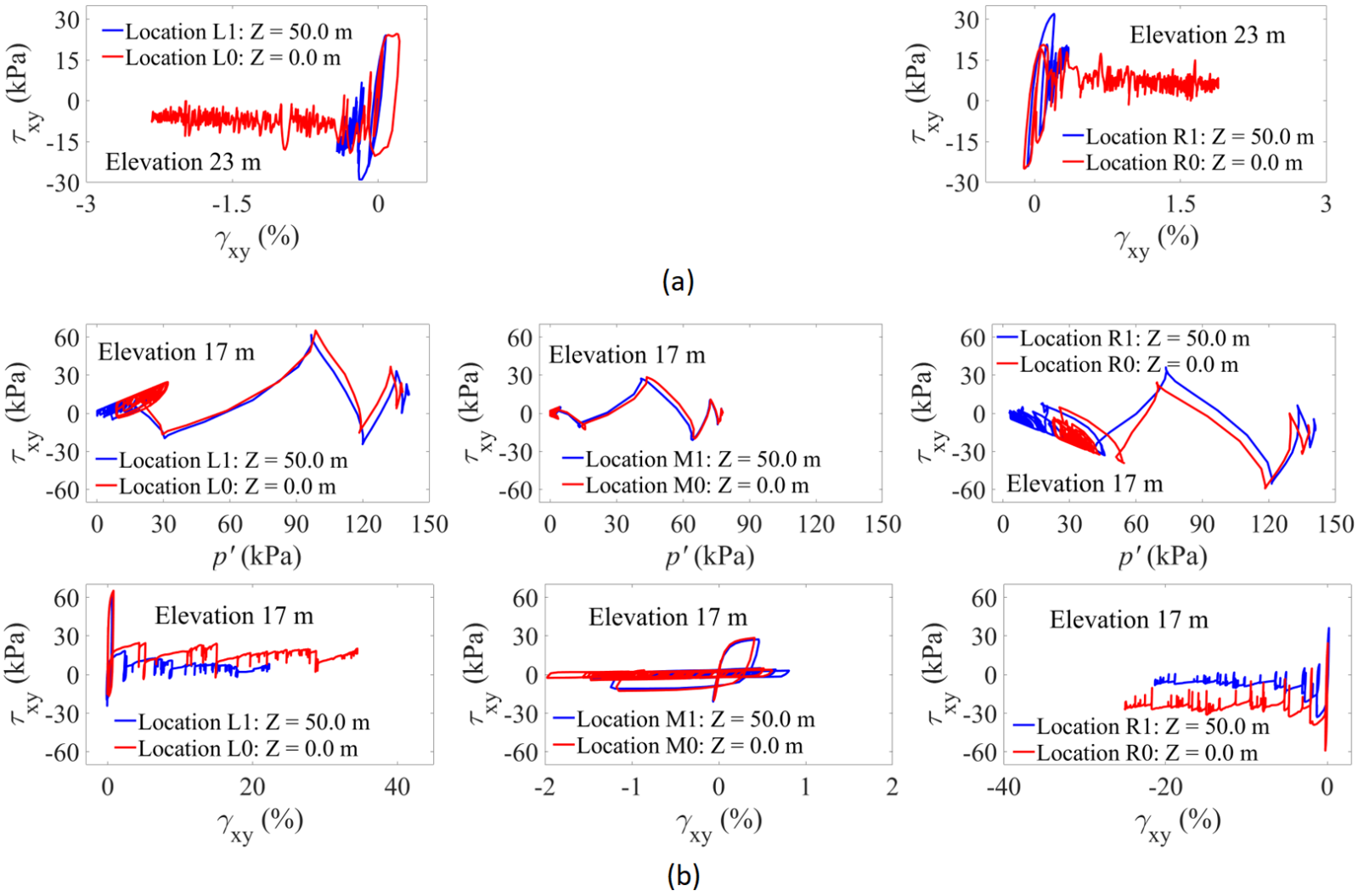

Figure 6-11. Soil response: (a) Upper clay layer at elevation = 23.0 m; (b) Loose sand layer at elevation = 17.0 m.

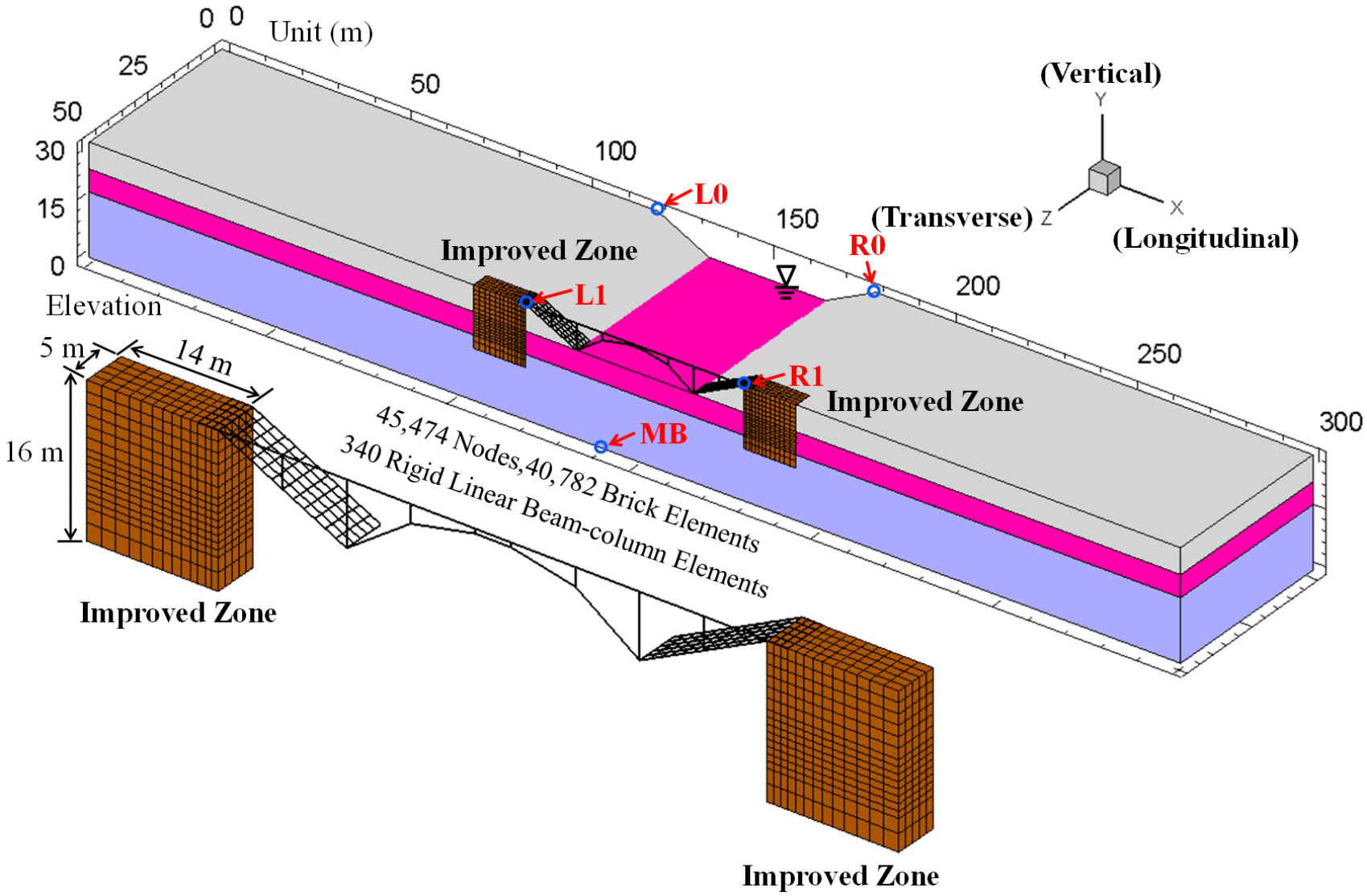

Figure 6-12. Retrofit analysis by adding two 14 m × 5 m × 16 m soil mixing walls.

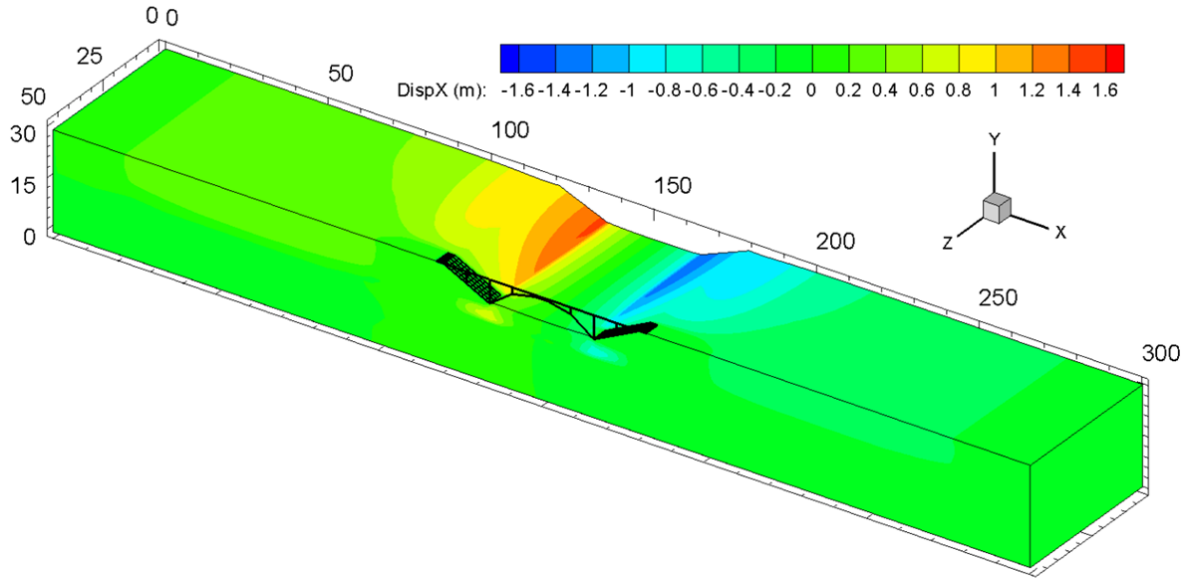

(a)

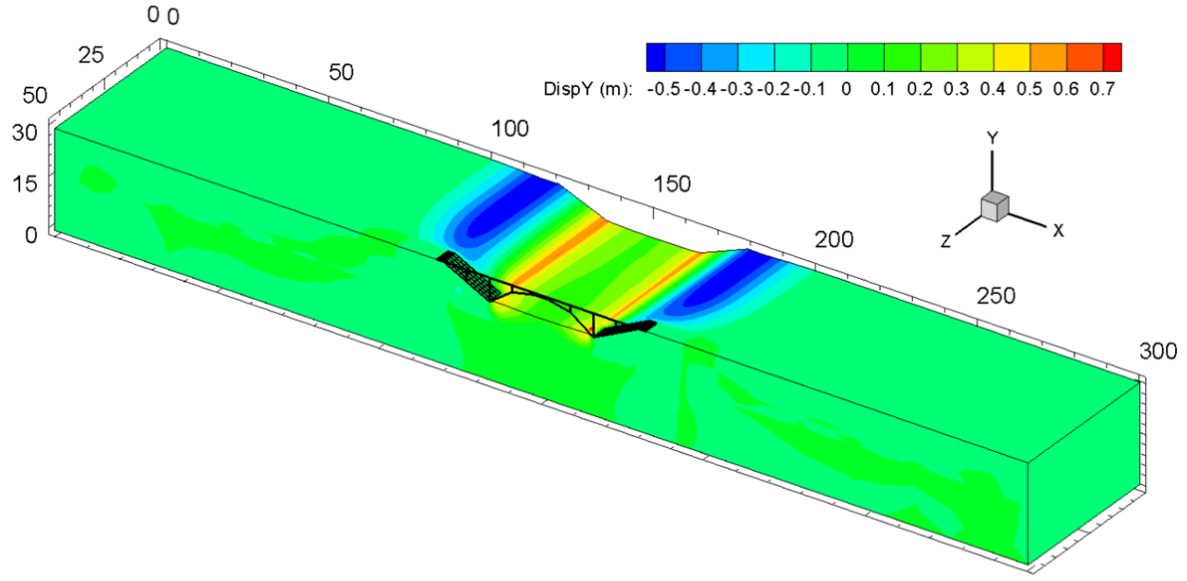

(b)

Figure 6-13. Displacement contours at end of shaking: (a) Longitudinal; (b) Vertical.

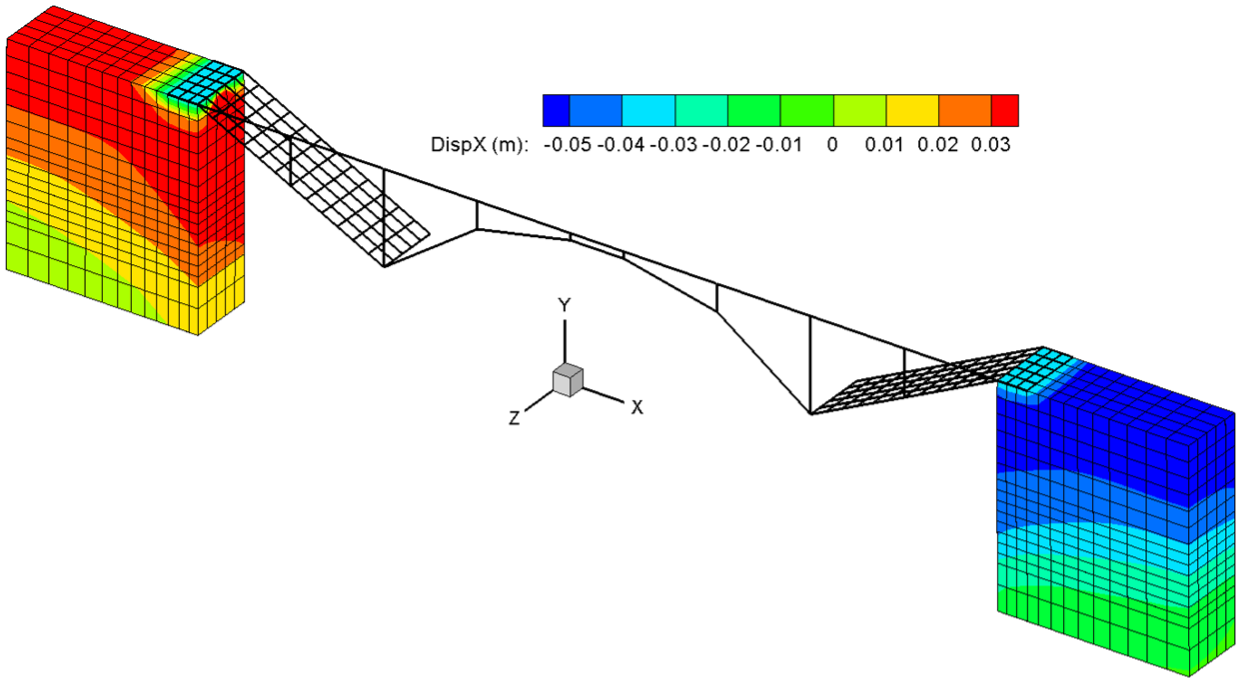

(a)

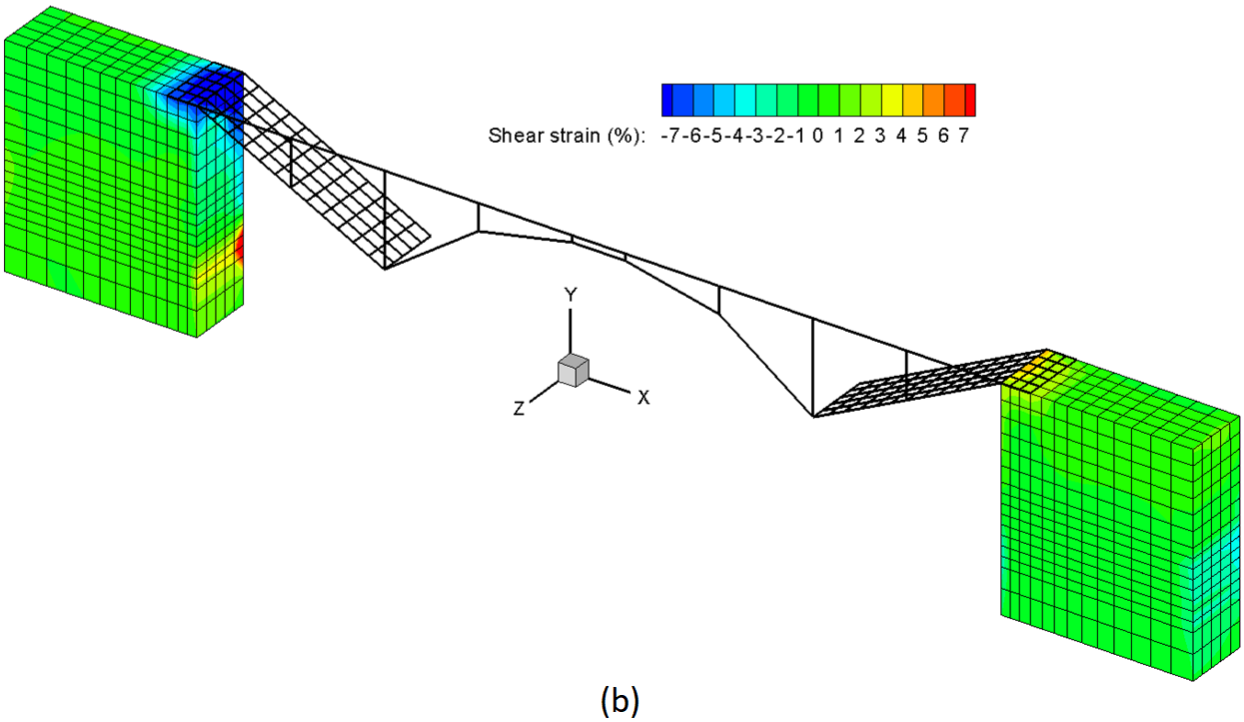

(b)

Figure 6-14. Deformation of soil mixing zones at end of shaking: (a) Longitudinal displacement; (b) Shear strain.

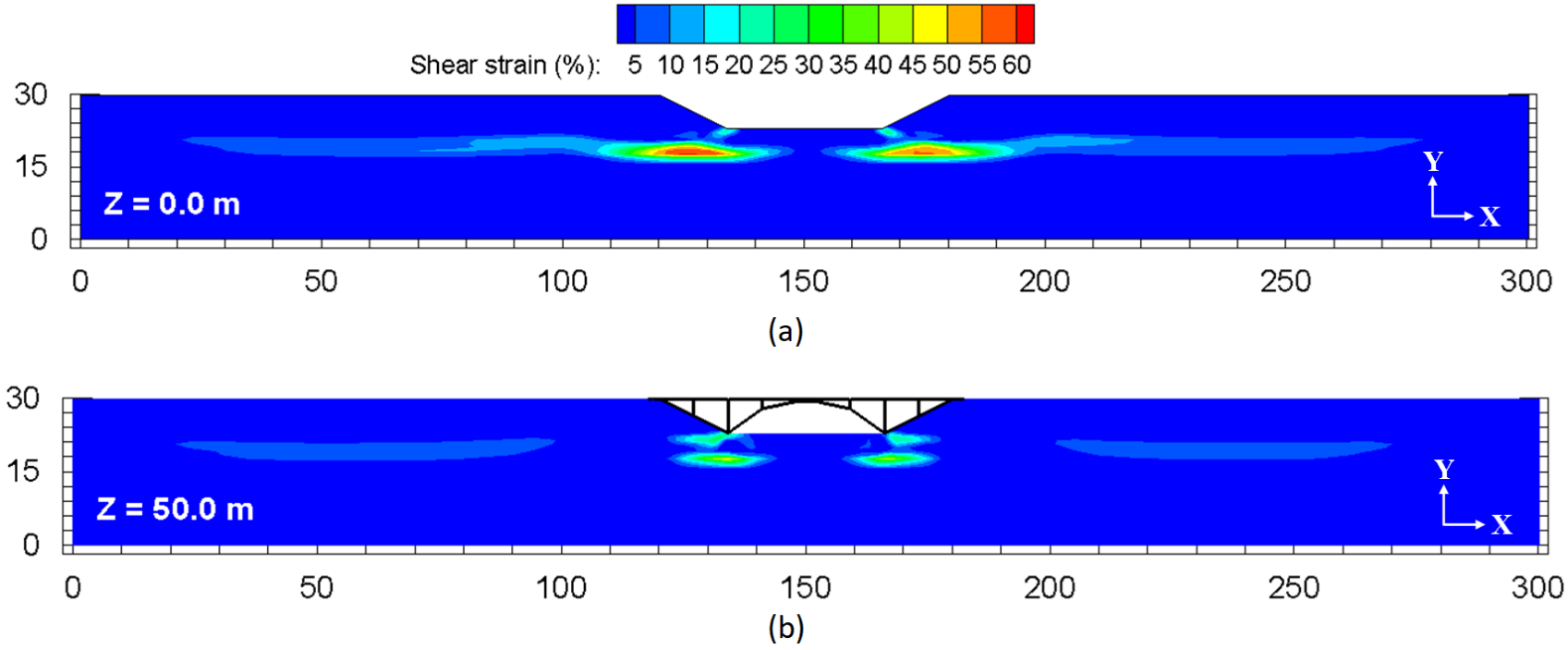

Figure 6-15. Shear strain γ_{xy} contours at end of shaking. (a) Z = 0 m, (b) Z = 50 m.

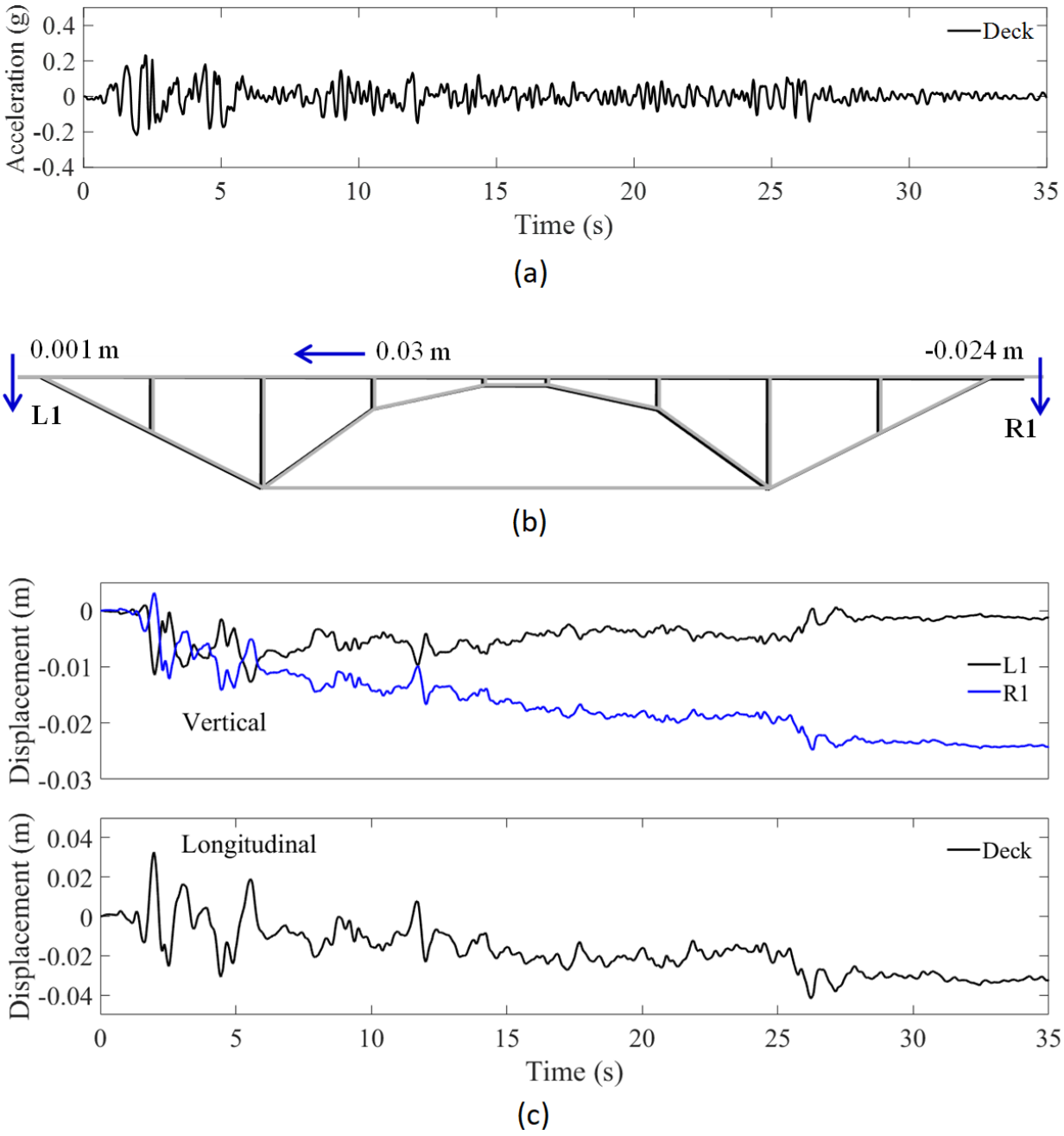

Figure 6-15. Bridge response: (a) Acceleration; (b) Displacement at end of shaking; (b) Time histories of displacement.

7. RESPONSE OF THE SAN FELIPITO BRIDGE-GROUND SYSTEM DURING THE 2010 EL MAYOR-CUCAPAH EARTHQUAKE: COMPUTATIONAL SIMULATION, INSIGHTS AND REMEDIATION

Athul Prabhakaran1, Zhijian Qiu, and Ahmed Elgamal

Abstract

A valuable bridge seismic response case history became available from the relatively nearby 2010 7.2 M_w El Mayor-Cucapah earthquake. In this regard, liquefaction-induced lateral spreading demands on a pair of adjacent parallel bridges, along with the bridge responses are well-documented. On this basis, this case history is studied herein. The salient ground and bridge behavior observations are highlighted, and a computational model is developed to capture the associated main response characteristics. During this earthquake, liquefaction and consequent loss of soil strength resulted in large accumulated ground displacements of as much as 5 m in the nearby free field. As such, a railroad bridge (RRB), built in 1962, experienced severe damage with unseating of a span, while the adjacent highway bridge (HWB), constructed in 1999, only displayed minor flexural column cracks. Data from the reconnaissance surveys and earlier related studies is employed to build an idealized computational model for each bridge, supported on an interbedded multilayered soil profile. Within the scope of available data and information, the modeling properties aimed to capture the salient deformation/damage features of the actual observed response. Using these models, additional studies were undertaken to address the railroad bridge-ground configuration shortcomings, with mechanisms such as extensions to the seat width, structural retrofit to enhance the deck-bent connectivity, and ground modification to mitigate the consequences of liquefaction.

7.1 Introduction

Lateral spreading induced damage to bridge foundations has been observed in many major earthquakes (Youd 1993; Hamada et al. 1996; Tokimatsu and Asaka 1998; Berrill et al. 2001; Ledezma and Bray 2010; Arduino et al. 2010; Wotherspoon et al. 2011; Ledezma et al. 2012; Verdugo et al. 2012; Cubrinovski et al. 2011, 2014, and Turner et al. 2013, 2016). Reconnaissance surveys from these events have demonstrated that consideration of the global bridge-ground

system, as an integral entity, highly influenced the observed response. As such, global analysis is paramount in realistically evaluating the performance of bridge-ground systems due to lateral spreading. As such, idealized 3D finite element (FE) models were developed, motivated by the performance of two adjacent parallel bridges during the 2010 El Mayor Cucapah earthquake (Turner, 2016, Stewart and Brandenberg 2010, EERI 2010). Attention is paid to the consequences of liquefaction-induced ground deformation on the salient observed structural response deformation/damage mechanisms.

The following sections outline the: 1) seismological aspects of the 2010 El Mayor Cucapah earthquake, 2) specifics and model properties of each bridge-ground system, 3) simplified limit equilibrium-based assessment of the free field soil deformation, 4) finite element model development, 5) conducted computations and salient bridge system response mechanisms, and 6) discussion of computed response and analysis methods. Finally, conclusions are presented and discussed.

7.2 The 2010 El Mayor Cucapah Earthquake

The 7.2 M_w El Mayor-Cucapah earthquake occurred on the 4th of April 2010 near the Imperial County-Baja California border at a focal depth of about 10 km. It emanated from a previously unknown strike-slip fault, parallel to the main San Andreas fault system (Stewart and Brandenberg 2010, EERI 2010). Historically, this region is seismically active, and the epicenter was in close proximity to that of the 1934, 1940 El Centro, and 1979 Imperial Valley earthquakes. Both sides of the US-Mexico border experienced strong shaking, and the main event was recorded by the relatively dense instrumentation along the Baja California region.

The Imperial County/Baja California sedimentary basin includes large areas of prime agricultural land, with soft alluvium, characterized by upper 30 m averaged shear wave velocities (V_{s30}) of less than 250 m/s, and shallow groundwater. Coupled with the proximity to faults, this region is particularly vulnerable to soil liquefaction. Associated soil liquefaction in the alluvial planes of Mexicali valley (along the Rio-Colorado) caused severe damage to agricultural/water infrastructure systems, including irrigation systems, earth dams, water, and wastewater treatment facilities, canals, and levees. Further, transportation infrastructure systems, including bridges, roadways, and railroad lines experienced severe damage and loss of functionality post the earthquake. Overall, direct losses of about 520 mission USD were reported in the region. Further

details are thoroughly documented by Stewart and Brandenberg (2010) and EERI (2010). The location of the earthquake epicenter and the two bridges under investigation is presented in Figure 7-1.

7.3 Configuration of the Bridges

Full details regarding the bridge configurations and observed seismic response are presented in EERI (2010), Turner et al. (2014), Turner et al. (2016), and Turner (2016). Located about 25 km west of the epicenter, the two parallel bridges span the Rio Colorado, with a center-to-center distance (between decks) of about 12 m. The river crossing consists of a highway bridge (HWB) built in 1999 and a railroad bridge (RRB) built in 1962. The bridges were built such that the columns of the highway bridge were aligned to match piers of the railroad bridge. The section below briefly discusses the stratigraphy, configuration, and observed damage patterns for both bridges and the surrounding free field.

7.3.1 Strong Motion

The main event of the 2010 El Mayor-Cucapah earthquake generated over 490 strong motion records in Baja California and Mexico. The maximum recorded peak ground acceleration was about 0.56 g near El Centro, California. Herein, we employ the closest available recording station to the bridges (PEER NGAWest2) ground motion records from the Riito strong-motion station (station RII) maintained by the Mexican Northwest Accelerometer Network (RANM), with a rupture distance of 13.6 km. The strong motion and 5% damped acceleration response spectra for the recorded fault normal and fault parallel components is presented in Figure 7-2, along with a prediction by the Boore et al. (2014) attenuation relationship.

Following estimates of H/V spectral ratios, Liao and Meneses (2013) estimated a V_{s30} of approximately 210 m/s for this station. For simplicity, the fault parallel component of the input motion recorded at the Riito station, scaled by 0.5, was used as the input motion to the bridge site, imparted at at a depth of 40 m (please see more details below).

7.3.2 Soil Stratigraphy at River Crossing

Figure 7-3 presents the two parallel bridges and a configuration of the river channel and soil profile layering following Turner *et al.* (2014). About 200 m in length, both bridges traverse the 180 m channel across the Rio Colorado. The active river channel is about 50 m wide throughout

the year, and the two abutments (A1 and A2) raise the grade of the deck, providing an average 10 m clearance. Within the active channel, the western slope is approximately 1.5H:1V, whereas the eastern slope is about 4H:1V at this location. The water table at the site was estimated based on Turner et al. (2016), following the river surface elevation.

Towards the abutments, the site consists of a 1.5-2 m loose upper fill, composed primarily of silty sand, above the groundwater table. Within the active channel, a loose sand layer extends from below the ground water table to a depth of about 6 m. Below this layer, the stratigraphy consists of interbedded silty-sand layers up to a depth of about 17 m.

The cross-section presented by Turner et al. (2016) was used along with CPT data from Turner (2016) to generate the representative stratigraphy in Figure 7-3. Further, simplified liquefaction triggering analysis was performed following Robertson and Wride (1998) to identify liquefiable layers within the interbedded strata. CPT 1, CPT 2, and CPT 3 represent three CPT soundings within the channel from west to east. The PGA at the Riito strong-motion station was used along with estimates of the groundwater table to estimate the Cyclic Stress Ratio (CSR) at the river crossing. The triggering analysis shown in Figure 7-4 identifies interbedded liquefiable and nonliquefiable layers, which were used in addition to the cross-section mentioned above to generate the soil profile at the site. Below the liquefiable layers (at about 15 m near the center of the active channel), the soil domain is assumed dense and not susceptible to liquefaction.

Figure 7-5 presents the observed performance of the east and west slopes of the active channel GEER (2010) in the free field (about 60 m north of the bridge site). About 4-5 m of liquefaction induced lateral spreading deformations on the eastern slope and about 1-2 m on the western slope, were observed (Turner et al. 2014). It is also noted that the out-of-plane extent of the lateral spread is much larger compared to the footprint of the bridge. Therefore, though reduced deformations were observed near the vicinity of the bridge, this reduction is not due to conventional pile pinning where the width of the abutment embankment has an influence (Turner and Brandenberg 2015).

7.4 Simplified Limit Equilibrium Assessment

Slope stability analyses were performed to identify regions of strain localization and obtain estimates of the yield coefficient (k_y) using the simplified soil profile shown in Figure 7-3. Estimates of liquefied soil shear strength ($s_{u,liq}$) using the provided CPT data were employed

following Robertson et al. (2010). Figure 7-6 presents results of the slope stability analysis on the western and eastern slopes of the active river channel, respectively. In general, the analyses identified regions of observed strain localization with reasonable accuracy on both (east and west) slopes of the active river channel.

Coupled with a Newmark-type sliding block analysis, estimates of k_y for each slope in the active channel were used to obtain a simplified assessment (Bray and Macedo 2019) of the free field soil displacement (Figure 7-7). The fundamental period of the sliding mass was obtained through the measured shear wave velocity (V_s) at the site, and the acceleration demand was obtained through the response spectrum of the fault parallel motion at the Riito station.

$$T_{n,east} = 4H/V_s = 4(8)/120 = 0.27s$$

$$PS_{a,east}(1.3T_{n,east}) \approx 1g$$

The simplified limit equilibrium analysis coupled with Newmark sliding block analyses from Bray and Macedo (2019) reasonably predicted the expected levels of free field deformations that occurred (1.4 - 6.1m). However, the analyses are sensitive to the choice of residual shear strength ($s_{u,liq}$), the intensity of ground shaking, and the estimated period of the sliding mass. Therefore, the selection of the input parameters in Bray and Macedo (2019) requires caution, and consideration should be made of uncertainty in the predicted free field displacement from such sliding block models.

7.5 Bridge Configurations and Observed Performance

The two parallel bridges are constructed such that their corresponding piers are aligned. The structural configuration of both bridges is summarized along with their observed performance in the following section. Readers are referred to Turner et al. (2014) for full details of both bridge configurations.

7.5.1 Highway Bridge

The highway bridge (HWB) was constructed in 1998 and consists of ten 20 m long spans, each with seven 1.15 m deep I-section girders. The deck slab was cast-in-place with a width of about 11 m. Laminated elastomeric bearings transferred deck loads to the 1.6 m wide bent cap from the girders. The bent cap was supported by four extended shaft columns, each 1.2 m in diameter, which continued to four drilled shaft foundations with the same reinforcement detailing.

Figure 7-8 presents salient structural features of the HWB. Elastomeric bearings transfer deck loads to the bent cap in all bents except spans between B3-B4, B7-B8, and abutment ends (Turner *et al.* 2014). At all other bents, anchorage by rectangular shear tabs restricts longitudinal and transverse movement to prevent unseating. The deck-pier condition for all ten spans is considered as fixed. Full details can be found in Turner et al. (2016).

The HWB remained in operation following the earthquake and suffered low-moderate damage, including flexural cracking of columns near the active river channel and settlement of bent B6 due to liquefaction-induced end-bearing failure.

7.5.2 Railroad Bridge

The single-track railroad bridge (RRB) was constructed in 1962 and is currently operated by a private rail consortium. Similar to the HWB, the RRB consisted of ten 20 m long spans (Figure 7-9), each with three 1.2 m deep I-section girders. All spans are considered simply supported and transfer loads to oblong sectioned reinforced concrete piers through plain elastomeric bearings. It is noted that no anchorage exists between the deck and piers to prevent unseating. Construction drawings and foundation details are not available for the RRB.

Unlike the HWB, the RRB experienced severe damage. Columns closer to the active river channel translated due to lateral spreading induced soil movement on the riverbanks. The span between bents B5-B6 unseated at B5 (Figure 7-9) and collapsed into the river. Similarly, the translation of bents B1-B2 led to the near collapse of the deck between these bents.

Figure 7-10a presents the displaced pier at B5 (pier closest to the active river channel on the east bank), indicating that B5 had displaced further towards the river than B6 leading to the deck collapse. Inadequate anchorage from the deck to bents B5 and B6 resulted in reduced lateral stiffness of the individual piers without axial resistance from the deck. Therefore, each pier performed as an individual unrestrained (at top) column at these two bents. Figure 7-10b presents the nearly unseated span at bent B2. Similar to B5, the inadequate anchorage led to the pier sliding beneath the deck, nearly unseating the span between B1-B2. Temporary steel shoring (connected to bent B2) to support the deck is also visible in this figure. The displaced pier at bent B6 indicates that the relatively stiff column did not deform, and the plastic hinge developed below the pile cap.

7.6 Finite Element Modeling

The models were developed using the mixed, fully coupled *u-p* formulation (Chan 1988) based on Biot (1962). The saturated soil domain was modeled using 8-noded hexahedral elements with the mean dilatational formation ($\bar{B}$ method) as per (Hughes 2008) to remove numerical issues associated with the incompressible fluid phase. Implementation of this u-p element is based on the following assumptions: 1) small deformation and rotation; 2) solid and fluid density is constant in time and space; 3) porosity is locally homogeneous and constant; 4) soil grains are incompressible; 5) solid and fluid phases are accelerated equally. Hence, soil represented by these fully coupled elements accounts for deformations and changes in pore-water pressure during seismic excitation. In this study, a 3.6 m slice of the bridge canyon system is considered for analyzing the longitudinal response of the bridge-ground system (Figure 7-11). This slice encompasses 1 column per bent of the HWB, and the entire width of the RRB. At the boundary, response is dictated by tying nodes to a large extent shear beam to enforce free field response.

The loading was performed in 3 stages, including:

1. Application of gravity using linear elastic soil properties with a Poisson's ratio of 0.4. This stage ensures the static soil self-weight is imposed (to obtain confinement, static stresses). For that purpose, a large permeability (1 m/s) is set to the soil domain to ensure a drained response.
2. The soil properties are switched to plastic to obtain compatible strain levels to match the static stresses imposed in stage 1.
3. The permeability is switched to the actual soil permeability, and the time history is imposed at the base of the model.

The FE matrix equation of the bridge-ground system is integrated in time using a single-step predictor multi-corrector scheme of the Newmark type with integration parameters $\gamma = 0.6$ and $\beta = 0.3025$. The resulting system of equations is solved using a modified Newton Raphson incremental, iterative procedure with a Krylov subspace accelerator (Scott and Fenves 2009) for faster convergence. A relatively low level of stiffness proportional viscous damping was used to enhance numerical stability (coefficient = 0.003), with the main damping emanating from the soil's nonlinear shear stress-strain hysteresis response.

7.6.1 Piers, Pile and Soil-Pile Interface

Three-dimensional nonlinear force-based beam-column elements with fiber sections were employed to represent the piers, deck, and piles for the purpose of this liquefaction-induced lateral spreading investigation. Figure 7-12 presents the employed cross-sections and the corresponding moment-curvature response of the reinforced concrete piers for the HWB and RRB, respectively.

The piers of the HWB extend below the ground and perform as a Type 1 Shaft (Caltrans). Therefore, the same moment-curvature relationship presented in Figure 7-12a is used for the piles in the HWB. Due to the lack of structural drawings of the foundation system of the RRB, this study employed the following moment-curvature relationship (Figure 7-13) for a "superpile" representation based on the most likely configuration reported in Turner et al. (2016). In order to represent the geometric space occupied by the pile in the soil domain, rigid beam-column links (EI = 10^4 times the linear EI of the pile) are used normal to the vertical axis of the pile, effectively defining its surface for friction along its length and end bearing at its base. The 3D brick elements representing the soil are connected to the pile geometric configuration at the outer nodes of these rigid links by using zerolength elements, zerolengthSection elements, and the OpenSees equalDOF translation constraint. The zerolength and zerolengthSection elements are employed to axially connect the rigid links to adjacent soil nodes and provide yield shear force in each link according to the soil-pile interface friction angle and adhesion. As such, the yield shear force is limited by $F = [c_A + k\sigma' \tan(\phi)] \cdot l \cdot h / N$, where l is the perimeter of the pile, h is center to center contributing height (according to the adjacent soil element heights), c_A is the soil-pile adhesion, ϕ is the soil-pile friction angle, $k\sigma'$ is the effective lateral stress and N is the number of zeroLengthSection elements along the pile perimeter.

7.6.2 Deck to Bent Interface

The anchorage in the HWB is modeled by transferring moments at the top of the bents to the deck. Since no anchorage exists in the RRB, the deck is connected to the top of the pier wall using an elastic-perfectly plastic spring in the longitudinal direction, with a stiffness corresponding to frictional resistance (coefficient of 0.15) offered by the vertical load from the deck to the girders. In addition, deck-to-deck separation and pounding were modeled with an elastic-no tension spring (Figure 7-14). After convergence (at every time step), the elongation of each friction spring (Figure 7-14) was checked against the current seat width (about 0.85m for a single deck at a bent). If the

seat width is exceeded, the updateMaterials command was employed in OpenSees to reduce the stiffness and strength of the corresponding friction element to phenomenologically model unseating, with the analysis continued thereafter.

7.6.3 Employed Soil Constitutive Models

State-of-the-art multi-surface plasticity-based stress-strain constitutive models termed PressureDependMultiYield03 (PDMY03), and PressureIndependentMultiyield (PIMY) were used to reproduce the liquefiable and non-liquefiable soil. The hyperbolic relationship represents the shear stress-strain backbone curve in these models. It is noted that PressureDependMultiYield03 has been calibrated in earlier studies (Khosravifar et al. 2018) and includes recent modifications to capture more closely the established guidelines for liquefaction triggering. Further model parameters specific to PDMY03 are presented in Table 7-1. The fill is modeled using the PIMY model with a V_s of 210 m/s, Poisson's ratio of 0.4, and cohesion of 40 kPa. Monotonic undrained response of each soil layer at a confinement of 1 atm is presented in Figure 7-15. Additionally, stress controlled simple shear responses of each cohesionless layer (LS, MS, SS and DS) at varying cyclic stress ratio levels (at a vertical stress of 1 atm) are presented in Figure 7-16.

7.6.4 Limitations of the Employed Models

The limitations of the employed models are briefly discussed below:

1. Soil properties and layering are based on the available limited CPT data.
2. Ground motion derived from a station 15 km away from the bridges is employed in the analysis.
3. A 3.6 m slice is used for both bridges, with the HWB modeled with a single column per bent, and the RRB modeled in full (with limited free field soil around the bridge)
4. Shadowing effects of the much stiffer HWB to the RRB are not explicitly accounted for. Each bridge is studied in isolation.
5. RRB pile configuration is not known, and a "superpile" is used to model the RRB foundations with a representative moment curvature behavior (on stronger side of what was assumed by Turner et al. 2014).
6. Connections between RRB bent and deck are represented by a friction spring (coefficient of 0.15). In this regard, results are rather sensitive to the choice of this friction yield coefficient.
7. Connection of deck to abutments is similar to that at bents (only through friction).

8. Deck-deck interaction for the RRB is modeled using a compression only element of very high stiffness.

Considering all the above-mentioned limitations, we aimed to employ realistic parameters that capture the essential features of observed deformations.

7.7 Computed Response

This section presents the computed response from FE analysis of the free field, HWB, and RRB, with attention paid to mechanisms contributing to the observed response.

7.7.1. Accelerations

Figure 7-17 presents the computed acceleration along the east and west boundaries of the FE model for the free field, HWB, and RRB. The massive shear beam on either boundary enforces a 1D site response condition for all three models. In the first mode period range of both bridge bridges (1.7 - 2.3 s), based on Turner (2016), the computed motion at the soil surface shows good agreement with the recorded motion.

7.7.2 Shear Strain Demands

Figure 7-18 presents the change in soil confinement (normalized to the initial confinement) and shear stress-strain (normalized with the vertical effective stress) demands within different locations of the canyon for the RRB, HWB, and free field models. a-c presents shear strain contours of the ground at the free field, vicinity of HWB, and vicinity of RRB.

Free field

Loss in soil confinement (due to excess pore pressure buildup) and development of large shear strains (order of >1%) are evident from a. In the free field, the eastern side of the active river channel experiences a greater loss in confinement attributed to thicker liquefiable layers. In the free field (a), localized shear bands can be seen, generally agreeing with the observed slip planes on either side of the active river channel. Further away from the channel, much lower shear strains are distributed over a larger area. The soil at the center of the river channel undergoes a slumping-like deformation pattern. On the eastern bank of the river channel (Location C), shear strains of about 20 % are observed.

Highway Bridge

Much reduced shear strains are observed (b) compared to the free field in the vicinity of the HWB. The presence of the HWB system pins the soil at either end of the active river channel and effectively reduces localized slip. In addition, soil in the middle of the active river channel is not observed to slump and deform due to the presence of the bridge bent. On the eastern riverbank (Location C), shear strains of about 3 % are observed due to the restraining effect offered by the HWB.

Railroad Bridge

The RRB (c) is not able to arrest localized shear strains along the active river channel as effectively as the HWB. Further, the shear strains are distributed over a larger area than soil in the vicinity of the HWB. On the eastern bank (Location C), the RRB is able to reduce free field deformations (with shear strains of about 10 %), to a lesser degree as compared to the HWB.

7.7.3 Structural Demands

Computed demands on the foundation systems of the HWB and RRB are presented in this section (Figure 7-20). Attention is paid to foundations supporting Bent 2 and Bent 5 for both bridges, *i.e.*, bents near either side of the active river channel and local slope faces. In addition. time histories of the computed deck displacements are presented (Figure 7-21).

Highway Bridge

Typical moment-curvature response of HWB foundations at Bent 2 and 5 are shown in Figure 7-20a. In addition, the structural drawings of the HWB foundation estimates of ϕ_y (curvature where extreme steel fiber starts to yield) are presented. The moment-curvature responses indicate cracking for both bent 2 and bent 5 foundations (on the side of columns facing the river) and slight yielding of the extreme rebar fiber. Further, deck displacements (Figure 7-21) indicate low deformations, suggesting the overall good performance of the HWB.

Railroad Bridge

Typical moment-curvature response of RRB foundations at Bent 2 and 5 are shown in Figure 7-20b. Compared to the HWB foundation system (Figure 7-21), computed curvatures suggest likely failure of timber piles in the pile group. Compared to the HWB, each bent of the RRB acts in isolation (due to inadequate anchorage) and undergoes much larger deck

displacements. Further, the span would have collapsed around 46 s into the shaking when the seat width of 0.85m is surpassed.

7.7.4 Deformations

Free field

Soil displacement histories in the free field (60 m north of the bridges, *i.e.,* without the bridges) are presented in Figure 7-22. The geometry of the canyon and thicker liquefiable layers on the eastern slope of the active river channel resulted in about 3-4 m of lateral downslope soil displacement. About 1-2 m of soil downslope displacement towards the river is observed on the western bank. In general, these simulation results reasonably agree with the observations (*i.e.,* about 3-4.5 m and 1-2 m on the east and west riverbanks, respectively).

Highway Bridge

The deformed configuration for the HWB structural system is presented in Figure 7-23. The figure shows that anchoring bents into the bridge deck leads to increased lateral resistance from the individual bents and reduced deformations compared to the RRB. The analysis predicts distress in bents B2 and B5 and having a double curvature type deformed shape (as observed in reconnaissance surveys) contributed to the significant restraint offered by the bridge deck. In return, flexural cracking might be expected on the inward face of the columns (away from the river) in bents B2 and B5 towards the interface of layers SS (silty sand) and MS (medium sand) and continuing to the LS layer (upper loose sand).

Figure 7-24 presents the deformed profile of soil in the free field, soil near bridge, and bents B5 and B6 at the end of shaking. The figure is indicative of the large shear strains developed in the LS layer (loose sand) near the ground surface for bent B5. It is noted that this bent is located near the toe of a local slope (near failure surface) within the active river channel and, therefore, experiences much larger free field soil influence than soil near bent B6 (at free field). The bridge offers substantial lateral stiffness and reduces the free field soil displacements to about 50%. Continuity of the deck further supports the top of the bents, leading to the double curvature type deflected shape as seen in this figure.

Railroad Bridge

Figure 7-25 presents the deformed configuration of the soil in the free field, soil near the bridge, and bents B5 and B6 of the RRB. Absence in the anchorage of pier walls to the deck leads to inadequate frame action and, subsequently, softer lateral resistance in each bent. Therefore, each bent essentially performs in isolation.

Prior to unseating on the eastern bank, it is shown that bents B5 and B6 displaced 1 m and about 0.5 m, respectively, towards the river. This difference in deformation of the individual piers during lateral spreading led to the collapse of the span at bent B5. On the western bank, bents B2 and B1 displaced about 0.7 m and 0.3 m towards the river, nearly leading to the collapse of the span between B1-B2.

The presence of the bridge is clearly shown to reduce soil displacement within the active river channel, as seen in the figure. An almost 50% reduction is observed in the free field soil displacements near bents B5 and B6 attributed to pile pinning effects from the bridge structure.

7.8 Discussion

Figure 7-26a-c presents the free field response of the channel, HWB-ground system, and RRB-ground system at the end of shaking. Post lateral spreading, free field geometry of the canyon is observed to slump and deform towards the rive center at both riverbanks (Figure 7-26a). In this particular channel, the geometry and layering resulted in about 3-4 m of lateral spreading induced soil displacement on the eastern riverbank and about 1-2 m on the western riverbank in the nearby free field. The deformation patterns observed generally indicate presence of local (concentrated) failures over the global lateral spreading deformations on either side of the active river channel.

In general, limit equilibrium-based (LE) methods coupled with Newmark sliding block analyses reasonably agree with the FE analysis and the observed deformation patterns from reconnaissance surveys in the free field. However, the limit equilibrium method predicts a distinct failure surface on the east and west riverbanks, rather than the observed lateral spreading deformation configuration (where slumping and strain redistribution over a larger areal extent is observed).

Estimates for the free-field slope displacements were computed using slope stability analysis (with liquefied residual shear strength) coupled with a sliding block model. The current equations in literature for estimating $s_{u,liq}$ (Robertson 2010; Idriss and Boulanger 2015; Kramer and Wang 2015) are based on flow-type failure mechanisms and are not intended for lateral spreading (Kramer and Wang 2015). Herein, a deterministic normalized residual strength model (Robertson 2010) is employed based on the provided CPT data. However, the LE analyses show sensitivity in yield acceleration (k_y) to the choice of the liquefied residual shear strength ($s_{u,liq}$). Further, given a value of k_y (corresponding to a given choice of $s_{u,liq}$), employing the sliding block model of Bray and Macedo (2019) leads to significant uncertainty in the predicted displacement of the slope due to the natural variability of employed ground motions. Therefore, practicing engineers must be aware of the uncertainty involved in the predicted free field slope displacement (16^{th}-84^{th} percentile corresponding to 1-6 m) from such methods, particularly for sites governed by a distributed lateral spreading type mechanism.

Both bridges reduce the free field soil deformations, including the local (flow type) and distributed (lateral spreading type) failure mechanisms. In the HWB, significant restraint is offered by the continuity of the deck and deformations closer to 1 m are observed on either side of the river channel at the end of shaking. In contrast, each pier of the RRB essentially acts as an individual system, leading to large deformations and unseating (around 46 s into strong shaking).

Of interest as well are the deformation patterns in the RRB- ground system at the end of shaking. Due to the overall reduced RRB stiffness, strain redistribution was observed over a much larger region on the eastern riverbank (as far as east of bent B6) compared to the HWB-ground system. Therefore, strengthening individual piers of a weaker bridge and performing a bent-by-bent analysis may warrant further investigation at adjacent locations.

7.9 Structural Retrofit Measures

Several structural retrofit measures were explored to prevent unseating of the railroad bridge span, including: 1) increasing friction at the deck to bent interfaces, and 2) increasing the seat width.

7.9.1 Increasing Friction at Deck-Bent Interfaces

FFigure 7-27 presents the effect of friction at the deck-bent connection on the displacement response (at the top) of bents B2 and B5. The displacement at the top of bents B2 and B5 (normalized to the available seat width, i.e., 0.85 m) at the end of shaking is presented. The coefficient of friction is varied from 25 % - 400 % of the reported value in Turner (2016). A strong nonlinear relationship is observed, where increasing the coefficient of friction by about 110% (from 0.15 to 0.33), using appropriate bearing pads prevents unseating of the span at bent B5. In the existing railroad bridge, the concrete deck was directly placed on each bent. The resistance to soil movement, after liquefaction, is capacity limited by the degree of friction at the bent-deck interface. Therefore, increasing the frictional resistance at the deck-bent connection directly affects the extent of deformations, due to liquefaction. Figure 7-28 presents the displacement of the railroad bridge-ground system, at the end of shaking, for a coefficient of friction of 7.5%, 15%, 30% and 60%. As seen in the figure, a greater degree of friction reduces the magnitude and spatial extent of ground deformations, highlighting the need to adequately model connections between the deck and bents to characterize lateral resistance of the overall structural system**.**

7.9.2 Seat width widening

To compute the necessary width to avoid unseating of the railroad bridge span between bents B5 and B6, an additional simulation was performed so as to preclude the collapse of the B5-B6 span (Figure 7-29). As noted in the figure, increasing the seat width (at bent B5) by about 45 % could have prevented unseating of the span.

7.10 Insitu Ground Remediation

In addition to the structural retrofit measures presented above, in-situ ground remediation measures were explored to restrict lateral soil deformations. In this regard, the polymer injection technique was employed.

Due to its ease of deployment in dense urban environments, the polymer injection remediation measure is commonly used for re-leveling of roadways and foundations (Naudts 2003; Buzzi et al. 2010; Xiao et al. 2014; Xiao et al. 2018; Saleh et al. 2019). Geotechnical applications polymers are usually deployed using a two-component chemically blown foam consisting of a curative phase (poly-isocyanate) and a resin phase (polyol). Upon mixing, rapid polymerization

occurs forming polyurethane, which expands (due to released CO_2 as a by-product), and cures into a hardened foam. A summary of polymer-sand composite properties is discussed below.

7.10.1 Polymer sand composite properties

Post injection and subsequent expansion, the resulting improvement in mechanical properties of the remediated ground might be attributed to the combined effects of: *i)* soil replacement and cementation by the created expanding composite inclusions, *ii)* soil densification, and increase in confinement around these inclusions. The shear strength characteristics of the polymer-sand composite are based unconfined compression test results (Parayancode 2023), where a cohesion intercept of 300 kPa is introduced to the insitu soil (with the friction angle of the insitu sand left unchanged). It is noted that unconfied compression tests of the pure polymer (Figure 7-30) indicate similar responses. As such, the monotonic shear stress-strain curves employed in the computational simulations are presented in Figure 7-31. Stiffness of the composite is varied with confinement and is presented in Figure 7-32 (alongside the in situ soil's shear wave velocity).

Three strategies of soil improvement were adopted including 1) Improvement of the LS layer, through polymer injection and resulting cementation to improve soil shear strength, 2) improvement of the LS and MS layers, through polymer injection, and 3) addition of polymer-sand composite inclusions that pin the slopes along the active river channel. Schematics of the proposed remediation layout are presented in Figure 7-33 (and Figure 7-34 for the polymer-sand composite inclusions).

The above injection techniques address various mechanisms that contribute to the extent of ground improvement. The first two approaches primarily focus on remediation of a spatial zone through densification. The third strategy employs structural inclusions, where the polymer-sand composite effectively pins the ground to reduce the extent lateral spreading ground.

The railroad bridge-ground mesh presented in Figure 7-11 is modified to increase the slice width (out-of-plane width) to 20 m. The modified mesh is presented in Figure 7-35. The proposed remediation strategies along the full railroad bridge-ground system are presented in Figure 7-36.

7.10.2 Remediation of Layer LS

In this approach (Figure 7-36a), polymer injection is performed in the LS layer (Loose Sand) along the bridge footprint (based on an out of plane width of 3.6 m). Injection is performed such that the $(N_1)_{60}$ (normalized standard penetration blow count), of remediated zone is increased from about 9 to about 29 using the methodology presented in Prabhakaran et al. (2020). As such, about 8% volume of liquid polymer to soil was employed (Figure 7-37) resulting in the injection of about 120 tons of polymer into the sand. As such, it is noted that remediation is primarily attributed to densification of the sand around the composite inclusions.

Figure 7-38(a) and (b) present the response of the railroad bridge-ground system in the absence of any remediation measure and following remediation of the LS Layer, respectively. As seen in the figures, deformations of the bridge structure are reduced significantly. Of interest as well, is the displacement of the B5-B6 span at bent B5, reducing from about 1.8 m (prior to improvement) to about 0.7 m post remediation. Consequently, this remediation measure would effectively prevent unseating, albeit with presence of substantial deformations.

7.10.3 Remediation of Layers LS and MS

In this scenario (Figure 7-36b), both liquefiable layers LS (Loose Sand) and MS (Medium Sand) layers are improved along the footprint of the bridge. About 8% volume of the liquid polymer to soil was employed, similar to the previous case, such that the $(N_1)_{60}$ (of remediated zone is increased from about 9 to about 29. As such, about 440 tons of liquid polymer is injected for this illustrative scenario.

Figure 7-38c presents the response of the system after remediation of both liquefaction susceptible layers (LS and MS Layers). As seen in the figure, the deformations of the bridge structure are further reduced. In this illustrative scenario, the displacement of the B5-B6 span at bent B5, reduces from about 1.8 m (without improvement) to about 0.35 m after remediation, effectively precluding any possible unseating of the span.

7.10.4 Remediation Using Grout Inclusions

In the third illustrative scenario (Figure 7-36c), the polymer is injected to form structural inclusions to effectively pin the ground against liquefaction induced lateral spreading. As such about 60 tons of the polymer is injected (based on the layout presented in Figure 7-34) along the active river channel.

Figure 7-38d presents the response of the system after the addition of the composite inclusions. As seen in the figure, deformations of the bridge structure are reduced as compared to the case without remediation. In this case, displacement of the B5-B6 span at Bent B5, reduces from about 1.8 m (without improvement) to about 0.8 m after remediation (i.e., unseating of the B5-B6 span at bent B5 would not have occurred). However, significant distortion of the bridge occurs due to the large deformations.

7.11 Conclusions

The longitudinal response of the San Felipito bridges spanning the Rio Colorado during the 7.2 M_w 2010 El Mayor Cucapah earthquake is explored in this study. The bridge-ground systems were analyzed with simplified limit equilibrium type analyses, followed by detailed finite element simulations. The analyses aimed to replicate the observed global deformation patterns and reasonably predict salient features of the observed performance of both bridges.

Specific conclusions and observations include:

1. The structural system of the bridge (piles, piers, and deck) is shown to reduce free-field soil deformations significantly. In this regard, continuity of the deck (through adequate deck-pier connectivity) increases the lateral resistance of individual piers, enforcing a frame-like response, and emphasizing the strut action of the bridge deck. As such, attention must be paid to connections between the bridge pier and deck to adequately characterize the lateral resistance afforded by the piers.

2. Deformation patterns consisting of local soil failure mechanisms overlain on a more distributed lateral spreading-type mechanism are shown to influence the overall system response. Both bridge structures resulted in reductions to the free field deformations. However, the much overall stiffer HWB was able to pin the ground and effectively reduce the formation of localized shear bands.

3. The employed FE 3D slice-based back analysis can capture salient response mechanisms in the longitudinal direction. These FE analyses reasonably accounted for unseating of the RRB span between B5-B6 and near failure of the deck between bents B1-B2.

4. Computed structural demands on the bridges indicate flexural cracking (on the side of columns facing the active river channel) and slight yielding of the HWB foundations and suggest likely

failure of the RRB foundation system. Further, the analysis indicates that unseating of the RRB span between bents B5-B6 could have been precluded if the seat width was increased by about 45 % or if friction at the deck-pier interface was increased. In such a case, the increased demands on the RRB foundation system warrant further inspection.

5. Limit equilibrium-based methods coupled with Newmark sliding block models can bound estimates of local slope deformations. However, attention must be paid to their sensitivity to the choice of k_y (given an $s_{u,liq}$) and the aleatory uncertainty associated with the ground motions. Further work is needed to assess sensitivity of the computed results to the choice of input parameters in both the FE and LE-based analyses.

6. As noted earlier by Turner and Brandenberg (2015), proximity of the much stiffer HWB has possibly led to reduced ground deformations near the RRB. In this regard, efforts are suggested toward full 3D FE analysis with both the HWB and RRB represented in the simulation.

7. Following the comprehensive calibration of the railroad bridge-ground system, various structural and geotechnical retrofit options were proposed. These included enhancing deck-bent friction, expanding seat width, and injecting an expansive polymer along the footprint of the bridge. To emphasize the potential of the polymer injection technique in mitigating liquefaction-induced lateral deformations, three representative scenarios were explored, and system response was discussed.

7.12 Acknowledgement

The authors are grateful for the detailed post-earthquake surveys conducted by the Geotechnical Extreme Events Reconnaissance (GEER) and EERI teams following the 2010 El Mayor Cucapah earthquake. In addition, the authors are grateful to the Pacific Earthquake Engineering Research Center (PEER) NGAWest2 team for providing the recorded strong motions used in this study. Finally, the authors would also like to thank Professor Scott Brandenberg and Dr. Benjamin Turner for their input, provided photographs, and excellent documentation of this case history.

7.13 References

Biot, M. A. (1962). “Mechanics of deformation and acoustic propagation in porous media.” *Journal of Applied Physics*, American Institute of Physics(AIP), 33(4), 1482–1498.

Boore, D. M., Stewart, J. P., Seyhan, E., and Atkinson, G. M. (2014). “NGA-West2 Equations for Predicting PGA, PGV, and 5% Damped PSA for Shallow Crustal Earthquakes:” *Earthquake Spectra*, SAGE Publications, Sage UK: London, England, 30(3), 1057–1085.

Bray, J. D., and Macedo, J. (2019). “Procedure for Estimating Shear-Induced Seismic Slope Displacement for Shallow Crustal Earthquakes.” *Journal of Geotechnical and Geoenvironmental Engineering*, American Society of Civil Engineers, 145(12), 04019106.

Buzzi, O., Fityus, S., and Sloan, S. W. (2010). “Use of expanding polyurethane resin to remediate expansive soil foundations.” *Canadian Geotechnical Journal*, 47(6), 623–634.

Chan, A. (1988). “A unified Finite Element Solution to Static and Dynamic Geomechanics problems.”, *PhD Dissertation*, Department of Civil Engineering, University College of Swansea, Swansea.

EERI (Earthquake Engineering Research Institute). (2010). “The El Mayor Cucapah, Baja California earthquake, April 4, 2010.” EERI Reconnaissance Rep. 2010-02, Oakland, CA.

Esri Inc. (2020). *ArcGIS Pro* (Version 2.9). Esri Inc. https://www.esri.com/en-us/arcgis/products/arcgis-pro/overview.

GEER (Geotechnical Extreme Event Reconnaissance). (2010). “Preliminary report on seismological and geotechnical engineering aspects of the April 4, 2010, Mw 7.2 El Mayor-Cucapah (Mexico) earthquake.” Rep. No. GEER-023, Oakland, CA

Hughes, T. J. R. (2008). “The Finite Element Method: Linear Static and Dynamic Finite Element Analysis: Thomas J. R. Hughes.” *Computer-Aided Civil and Infrastructure Engineering*, Prentice-Hall, 4(3), 245–246.

Idriss, I. M., and Boulanger, R. W. (2015). “2nd Ishihara Lecture: SPT- and CPT-based relationships for the residual shear strength of liquefied soils.” *Soil Dynamics and Earthquake Engineering*, Elsevier, 68, 57–68.

Kramer, S. L., and Wang, C.-H. (2015). “Empirical Model for Estimation of the Residual Strength

of Liquefied Soil." *Journal of Geotechnical and Geoenvironmental Engineering*, American Society of Civil Engineers, 141(9), 04015038.

Khosravifar, A., Elgamal, A., Lu, J., and Li, J. (2018). "A 3D model for earthquake-induced liquefaction triggering and post-liquefaction response." *Soil Dynamics and Earthquake Engineering*, Elsevier, 110, 43–52

Liao, Y., and Meneses, J. (2013). "Engineering Characteristics of Ground Motion Records from the 2010 Mw 7.2 El Mayor–Cucapah Earthquake in Mexico", SAGE Publications, Sage UK: London, England, 29(1), 177–205.

McKenna, F., Scott, M. H., and Fenves, G. L. (2010). "Nonlinear Finite-Element Analysis Software Architecture Using Object Composition." *Journal of Computing in Civil Engineering*, American Society of Civil Engineers, 24(1), 95–107.

Naudts, A. (2003). "Irreversible Changes in the Grouting Industry Caused by Polyurethane Grouting: An Overview of 30 Years of Polyurethane Grouting." American Society of Civil Engineers, 1266–1280.

Olson, S. M., and Johnson, C. I. (2008). "Analyzing Liquefaction-Induced Lateral Spreads Using Strength Ratios." *Journal of Geotechnical and Geoenvironmental Engineering*, American Society of Civil Engineers, 134(8), 1035–1049.

PEER (Pacific Earthquake Engineering Research Center). (2013). "NGAWest2 database" ⟨https://peer.berkeley.edu/ngawest2⟩ (Feb. 24, 2022).

Parayancode, A. P. (2023). "Polymer Injection for Mitigating Ground Liquefaction and Associated Deformations," Ph.D. Dissertation, University of California, Ssn Diego, La Jolla, CA, USA.

Prabhakaran, A., Kyungtae, K., Ebeido, A., Jahed Orang, M., Motamed, R., Elgamal, A., and Frazao, C. (2021). "Polymer injection and associated site liquefaction remediation mechanisms." *17th World Conference on Earthquake Engineering*, Sendai, Japan.

Robertson, P. K. (2010). "Evaluation of Flow Liquefaction and Liquefied Strength Using the Cone Penetration Test." *Journal of Geotechnical and Geoenvironmental Engineering*, American Society of Civil Engineers, 136(6), 842–853.

Robertson, P. K., and Wride, C. E. (1998). "Evaluating cyclic liquefaction potential using the cone

penetration test." *Canadian Geotechnical Journal*, NRC Research Press Ottawa, Canada, 35(3), 442–459.

Saleh, S., Yunus, N. Z. M., Ahmad, K., and Ali, N. (2019). "Improving the strength of weak soil using polyurethane grouts: A review." *Construction and Building Materials*, Elsevier, 202, 738–752.

Scott, M. H., and Fenves, G. L. (2009). "Krylov Subspace Accelerated Newton Algorithm: Application to Dynamic Progressive Collapse Simulation of Frames." *Journal of Structural Engineering*, American Society of Civil Engineers, 136(5), 473–480.

Turner, B., Brandenberg, S. J., and Stewart, J. P. (2014). "Evaluation of collapse and non-collapse of parallel bridges affected by liquefaction and lateral spreading." PEER Rep. 2014/10, Pacific Earthquake Engineering Research Center, Univ. of California, Berkeley, CA, 122.

Turner, B. J. (2016). "Kinematic Pile-Soil Interaction in Liquefied and Nonliquefied Ground.", *PhD Dissertation*, University of California Los Angeles.

Turner, B. J., and Brandenberg, S. J. (2015). "Pile pinning and interaction of adjacent foundations during lateral spreading.", *DFI-Journal, Deep Foundations Institute*, Taylor & Francis, 9(2), 92–102.

Turner, B. J., Brandenberg, S. J., and Stewart, J. P. (2016). "Case Study of Parallel Bridges Affected by Liquefaction and Lateral Spreading." *Journal of Geotechnical and Geoenvironmental Engineering*, American Society of Civil Engineers, 142(7), 05016001.

Xiao, Y., Liu, H., and Desai, C. S. (2015). "New Method for Improvement of Rockfill Material with Polyurethane Foam Adhesive." *Journal of Geotechnical and Geoenvironmental Engineering*, American Society of Civil Engineers (ASCE), 141(2), 02814003.

Xiao, Y., Stuedlein, A. W., Chen, Q., Liu, H., and Liu, P. (2018). "Stress-Strain-Strength Response and Ductility of Gravels Improved by Polyurethane Foam Adhesive." *Journal of Geotechnical and Geoenvironmental Engineering*, American Society of Civil Engineers (ASCE), 144(2), 04017108.

Zhang, G., Robertson, P. K., and Brachman, R. W. I. (2011). "Estimating liquefaction-induced ground settlements from CPT for level ground.", *Canadian Geotechnical Journal*, NRC Research Press Ottawa, Canada , 39(5), 1168–1180.

Table 7-1. Properties of the PDMY03 constitutive model employed in the analysis.

Model Parameters	**LS** D_r = 45%	**MS** D_r = 55%	**SS** D_r = 75%	**DS** D_r = 85%
Reference mean effective pressure, p'_r (kPa)	170	180	210	270
Mass density, ρ (t/m^3)	1.8	1.9	2.1	2.2
Maximum shear strain at reference pressure, $\gamma_{max,r}$	0.10	0.10	0.10	0.10
Shear modulus at reference pressure, G_r (MPa)	80	95	120	160
Stiffness dependence coefficient d	0.5	0.5	0.5	0.5
Poisson's ratio v for dynamics	0.40	0.40	0.40	0.40
Shear strength at zero confinement, c (kPa)	1.73	1.73	1.73	1.73
Friction angle ϕ, with resulting strength defined as $p' \sin\phi$	24	25	27	30
Phase transformation angle, ϕ_{PT}	24	25	25	27
Contraction coefficient, c_1	0.1	0.1	0.035	0.015
Contraction coefficient, c_2	5	5	3	1
Contraction coefficient, c_3	0.05	0.1	0.2	0.45
Dilation coefficient, d_1	0.10	0.12	0.15	0.2
Dilation coefficient, d_3	0.05	0.1	0.2	0.45
Permeability (m/s)	10^{-5}	10^{-5}	10^{-5}	10^{-5}
Initial stiffness damping coefficient	0.003	0.003	0.003	0.003
Convergence criteria based on norm of energy increment	10^{-4}	10^{-4}	10^{-4}	10^{-4}

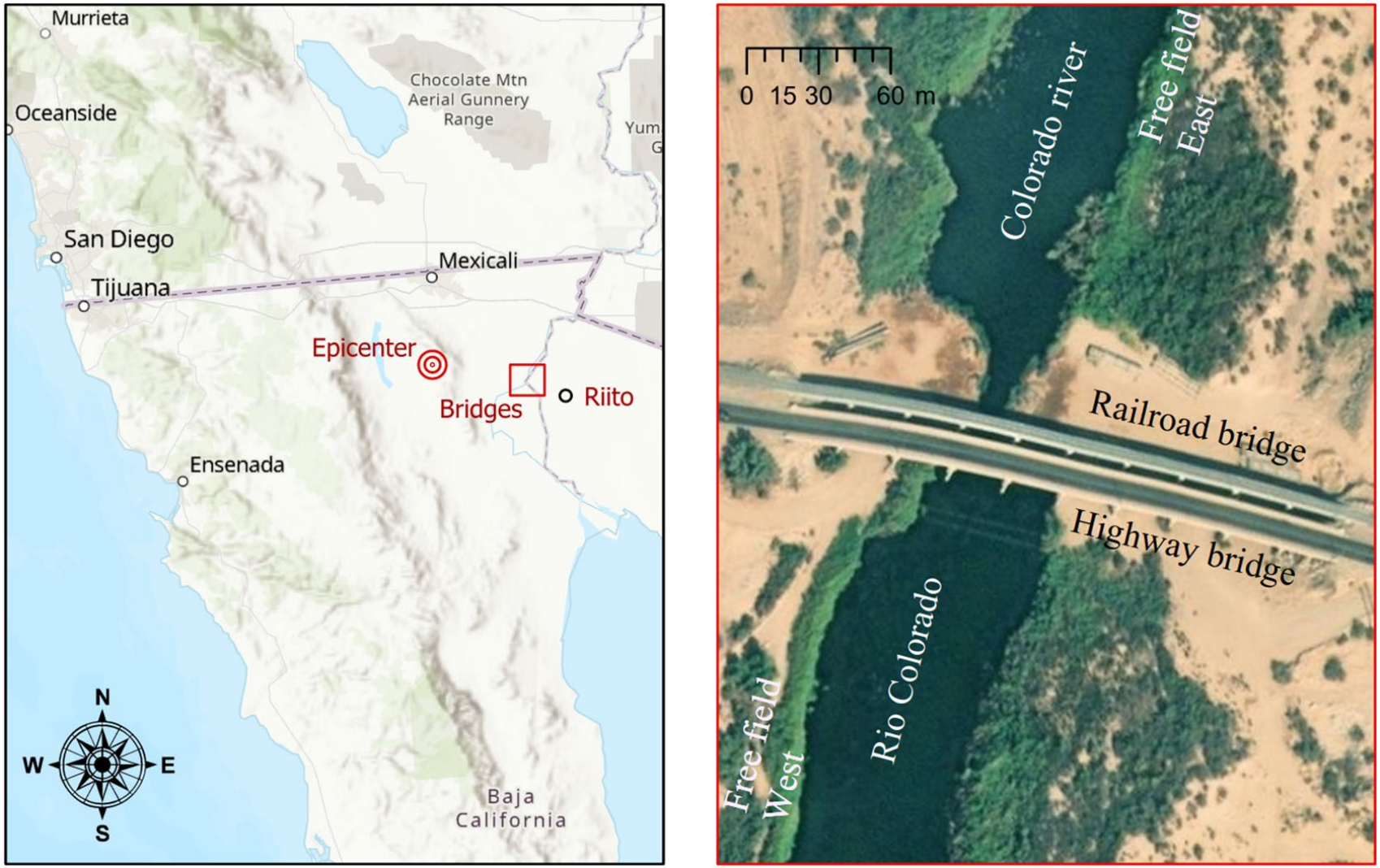

Figure 7-1. Location and layout of the San Felipito bridges (Esri Inc., 2020). The map also shows the location of the closest available strong motion recording station (Riito, about 14 km away from the bridge) employed in the analysis.

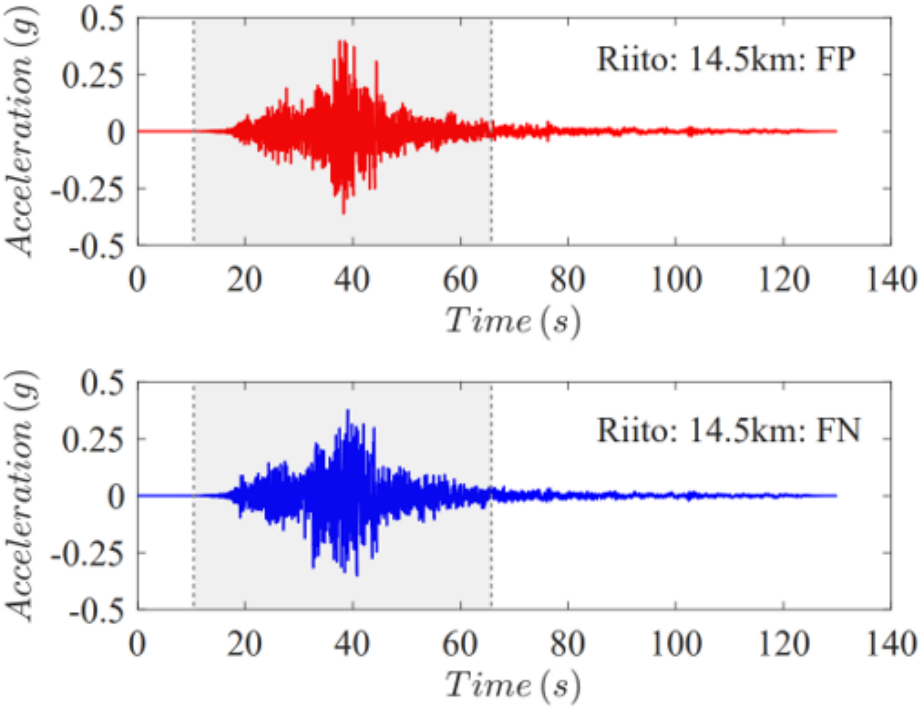

(a) Recorded motion at Riito station (dashed lines represent analysis duration based on 5% to 95% Arias Intensity). The fault parallel (FP) component was employed in the analysis presented herein.

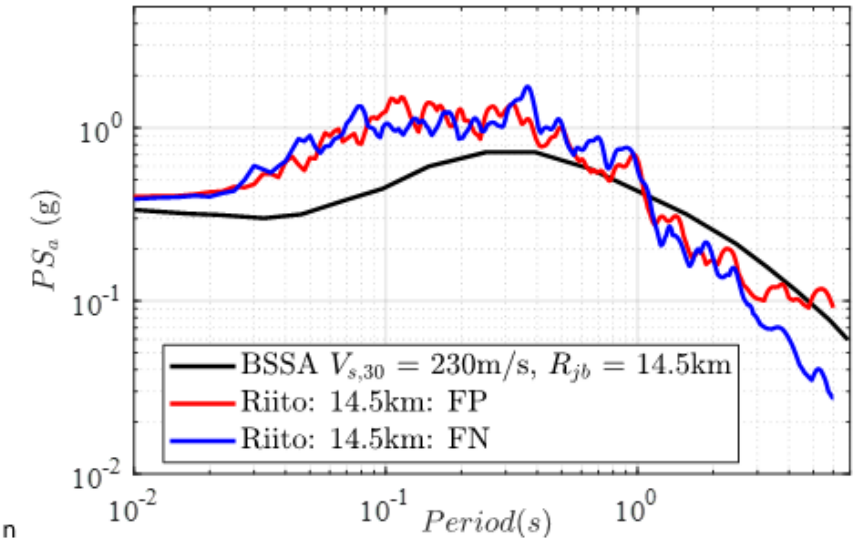

n

(b) Recorded and estimated 5% damped acceleration response spectra

Figure 7-2. (a) Recorded time history (b) Recorded response spectra and estimated 5% damped acceleration response spectra at the Riito station (PEER NGAWest2)

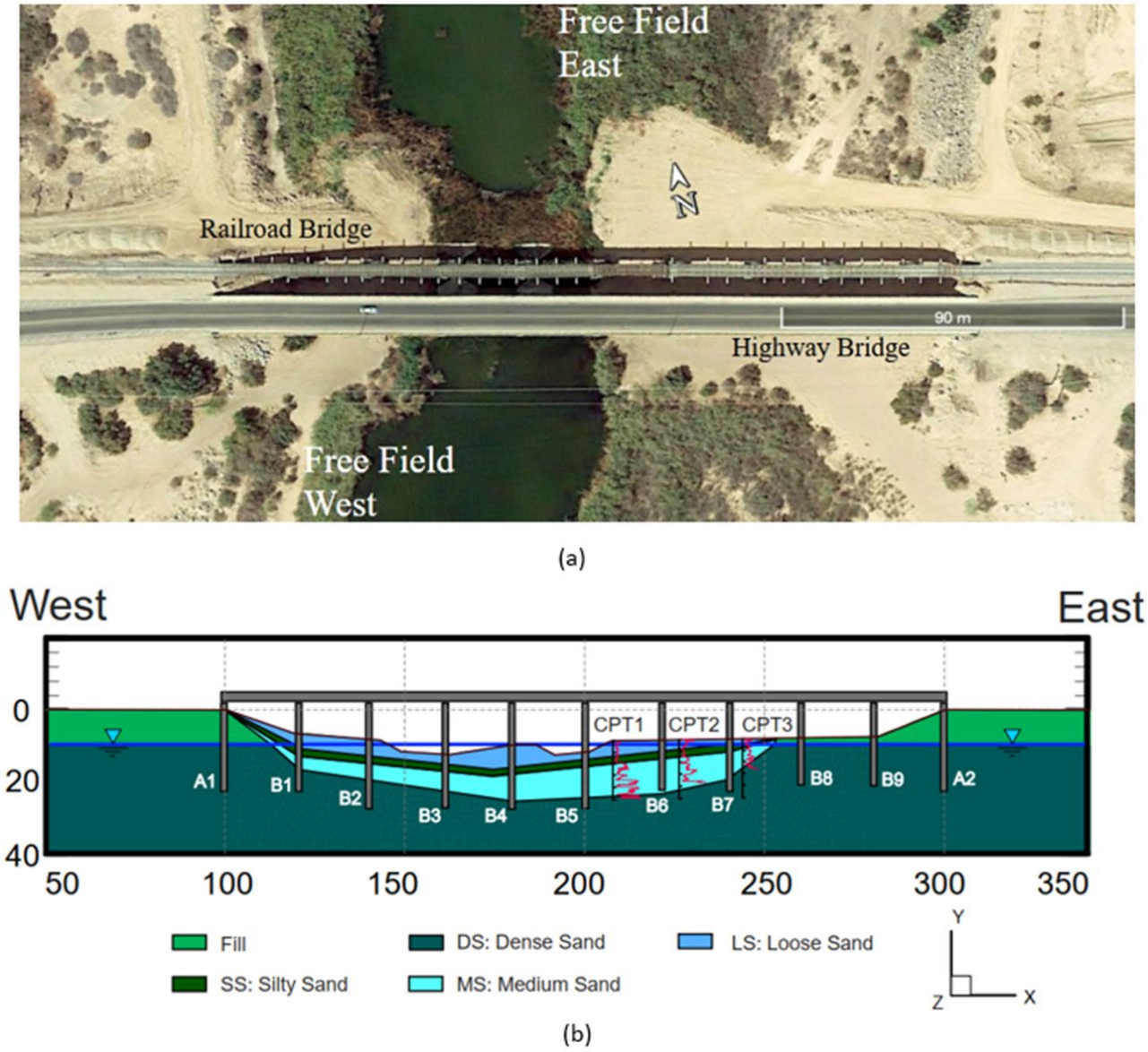

Figure 7-3. (a) Satellite view and (b) simplified layering of the soil profile at the river channel. (Dimensions are in m)

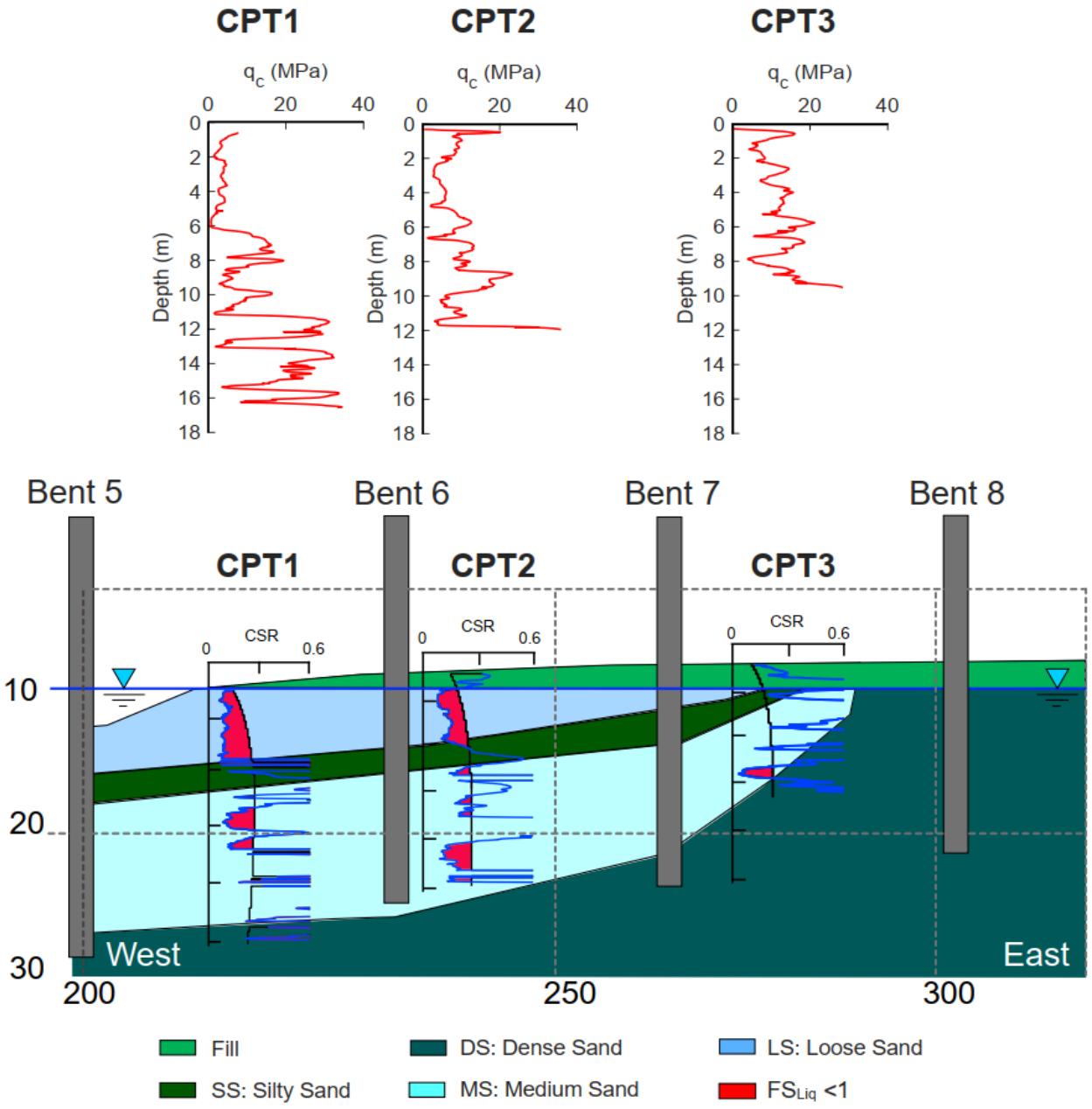

Figure 7-4. Observed cone tip resistance (q_c) and Simplified liquefaction triggering assessment with the cyclic stress ratio (CSR) of the eastern bank of the active river channel following Robertson and Wride (1998) (all dimensions are in m)

(a)

(b)

Figure 7-5. Observed lateral spreading induced deformations at (a) free field east bank (photograph by Scott Brandenberg) and (b) free field west bank of the active river channel at the free field (photograph by James Gingery) (GEER 2010)

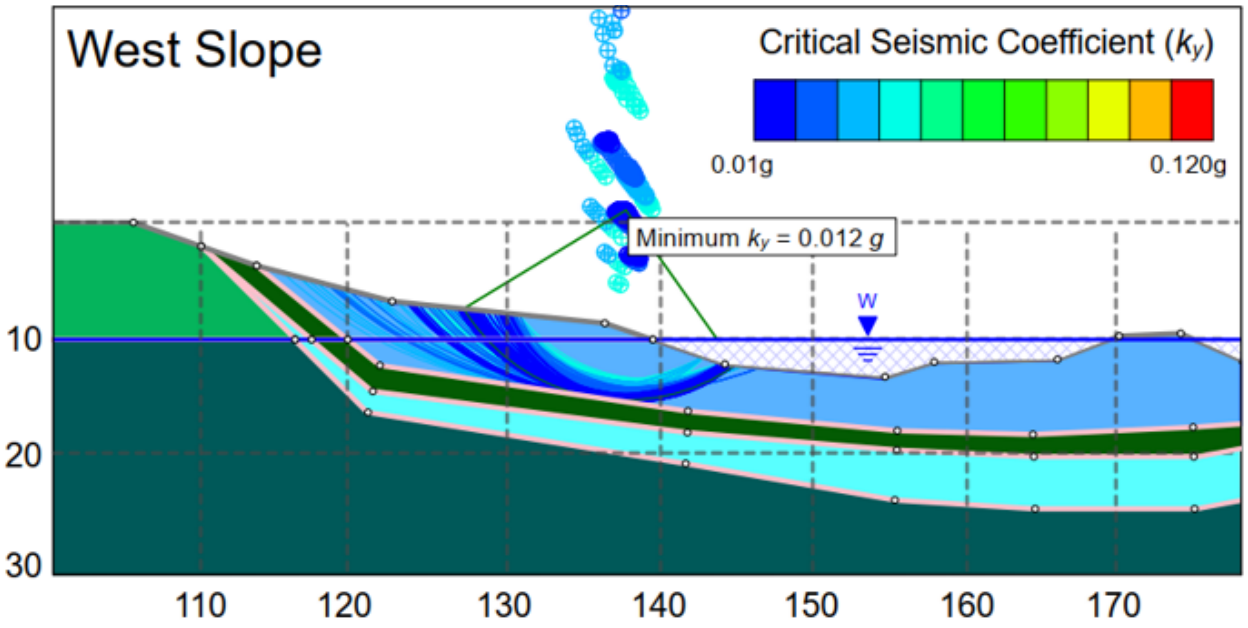

(a)

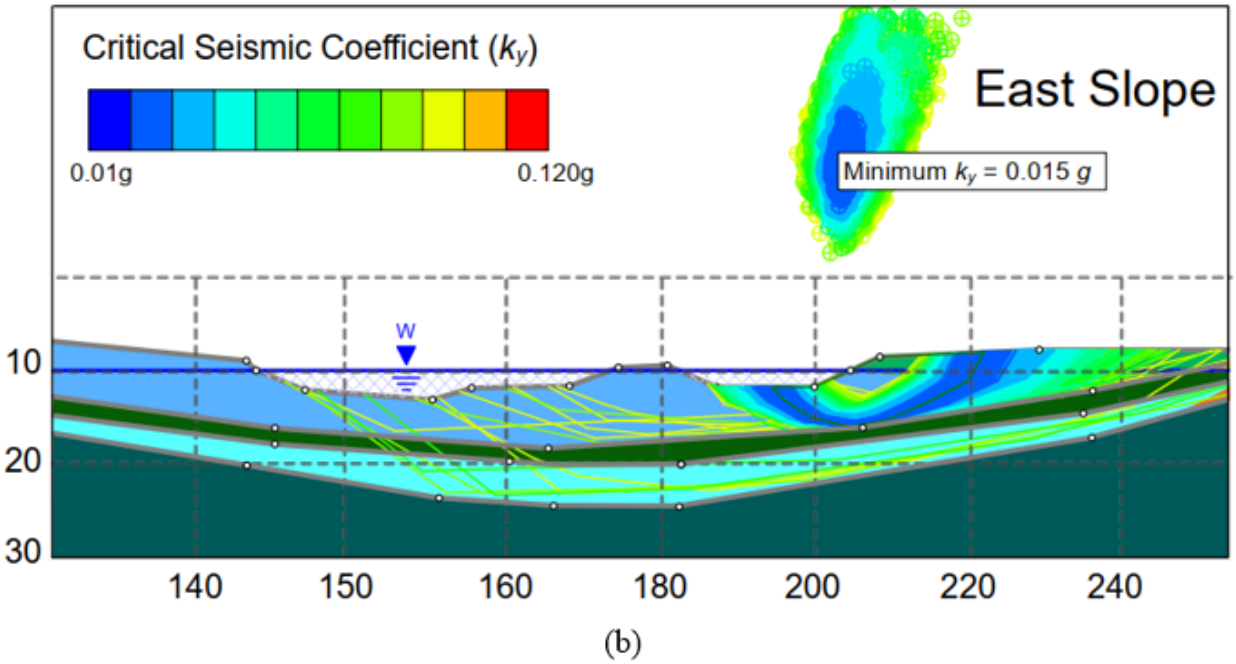

(b)

Figure 7-6. Slope stability analysis of the (a) western slope and (b) eastern slope in the active river channel (all dimensions are in m)

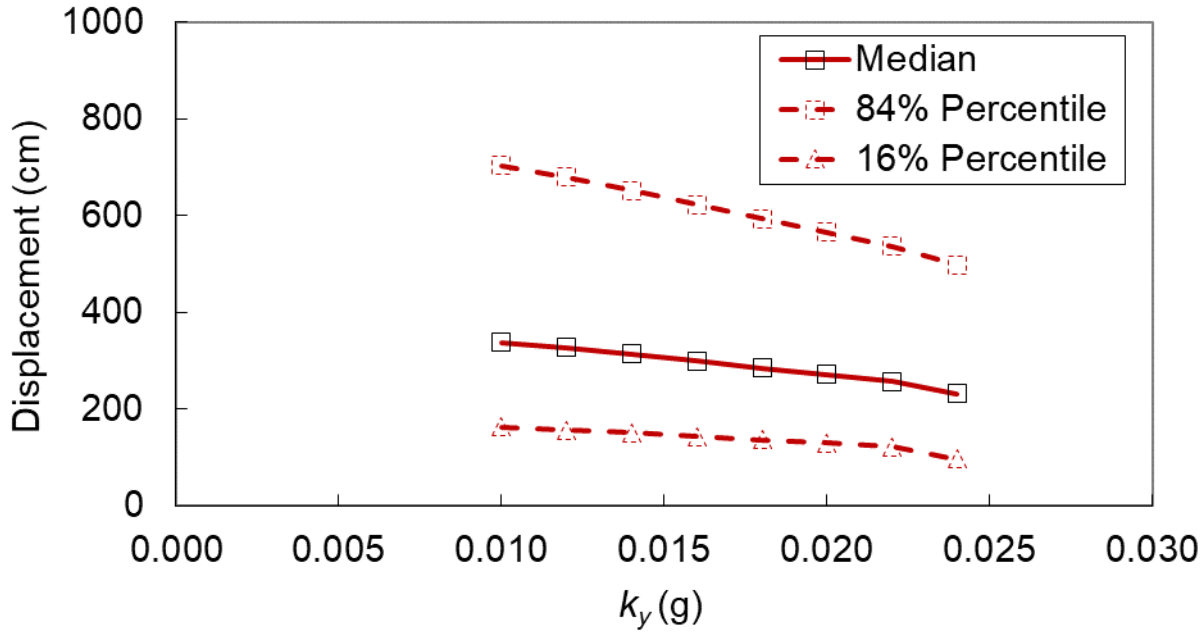

Figure 7-7. Estimates of slope displacement for the eastern slope of active river channel following Bray and Macedo (2019)

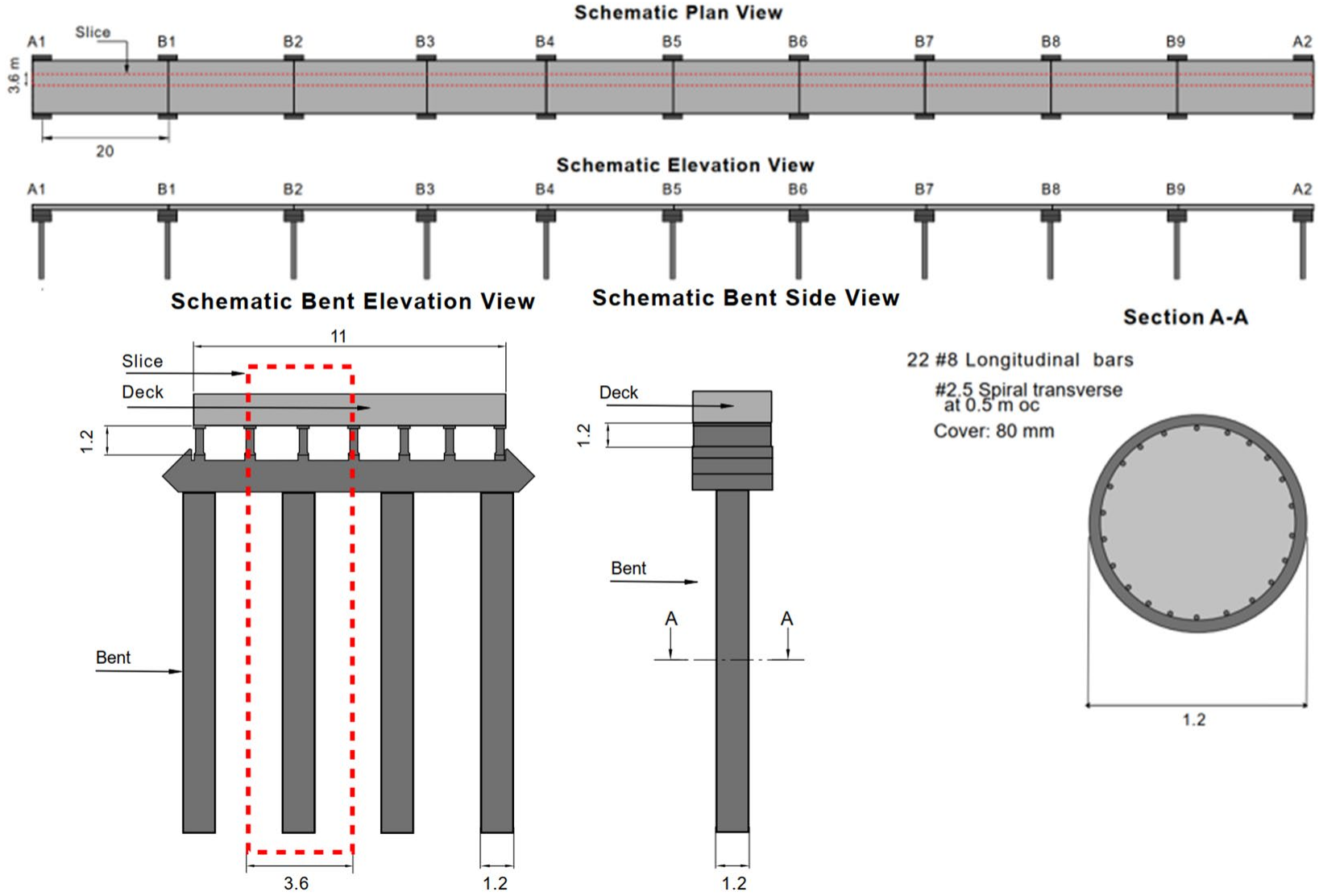

Figure 7-8. Salient structural features of the highway bridge (all dimensions are in m)

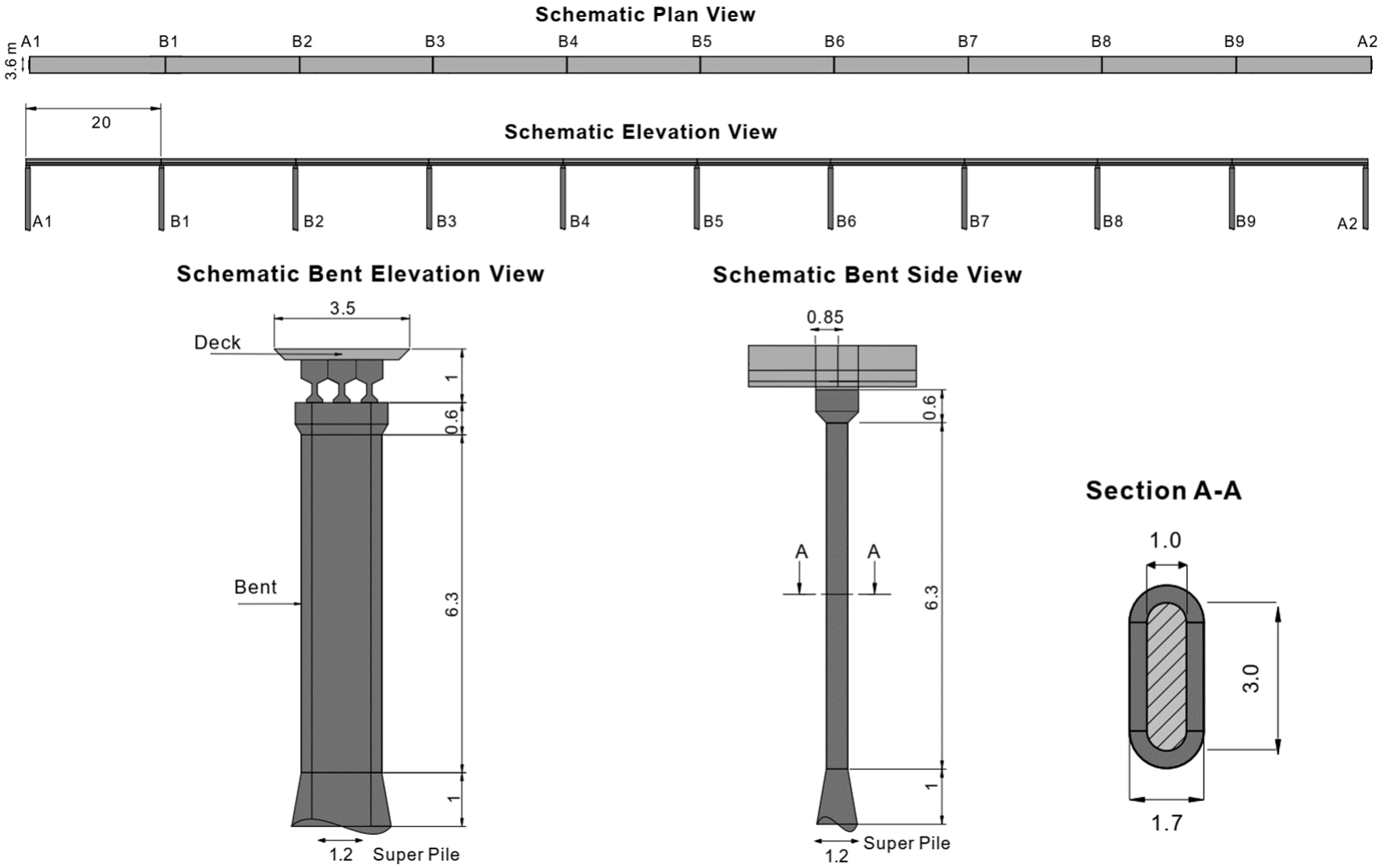

Figure 7-9. Salient structural features of the railroad bridge (all dimensions are in m)

(a) Nearly unseated Span at Bent B2 of Railroad bridge

(b) Unseated Span at Bent B5 of Railroad bridge

Figure 7-10. Unseated span at (a) nearly unseated B1-B2 span at Bent B2, and (b) unseated B5-B6 span of the railroad bridge at Bent B5 (Photos by Scott Brandenberg)

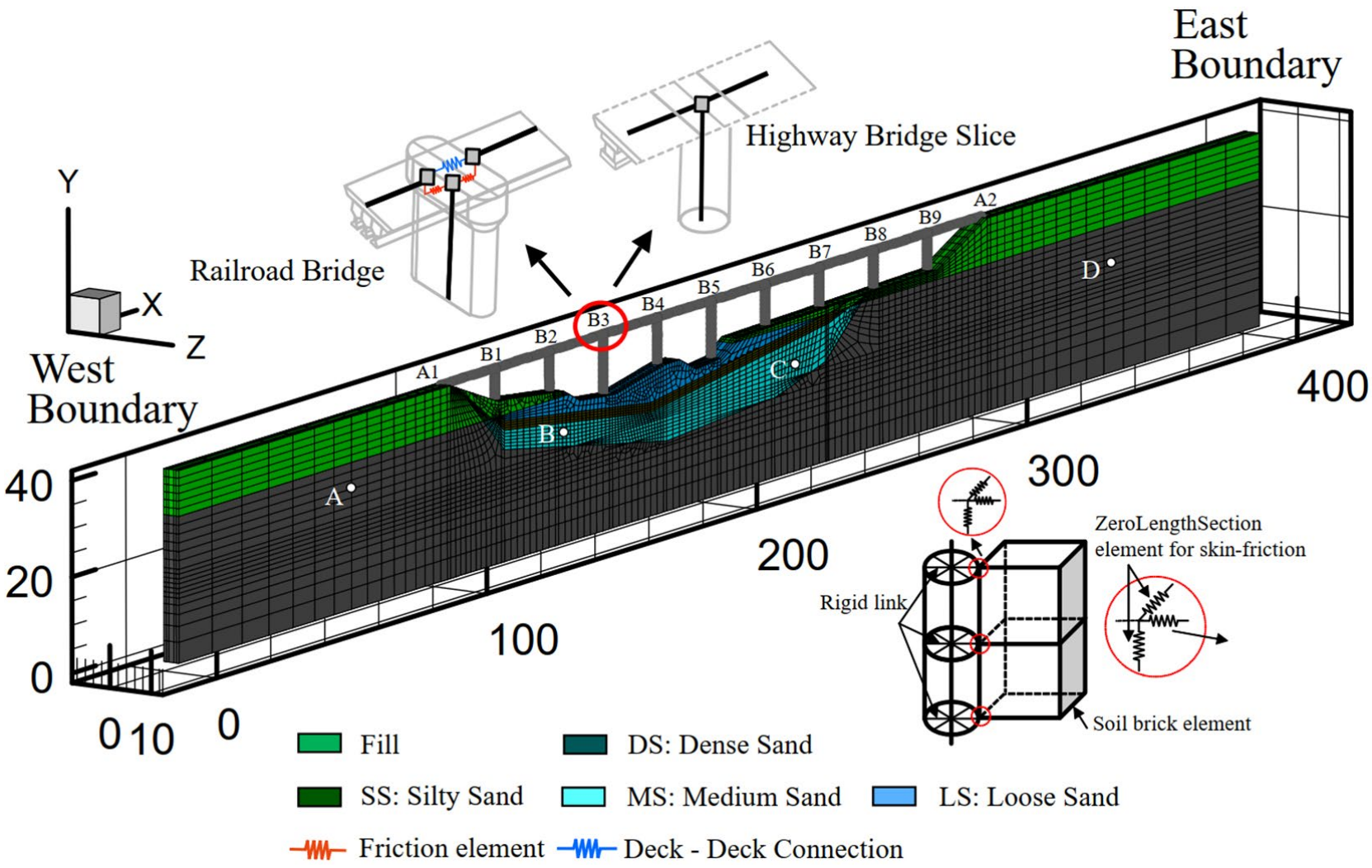

Figure 7-11. Mesh of the bridge ground system used in the analysis (colors represent soil layers)

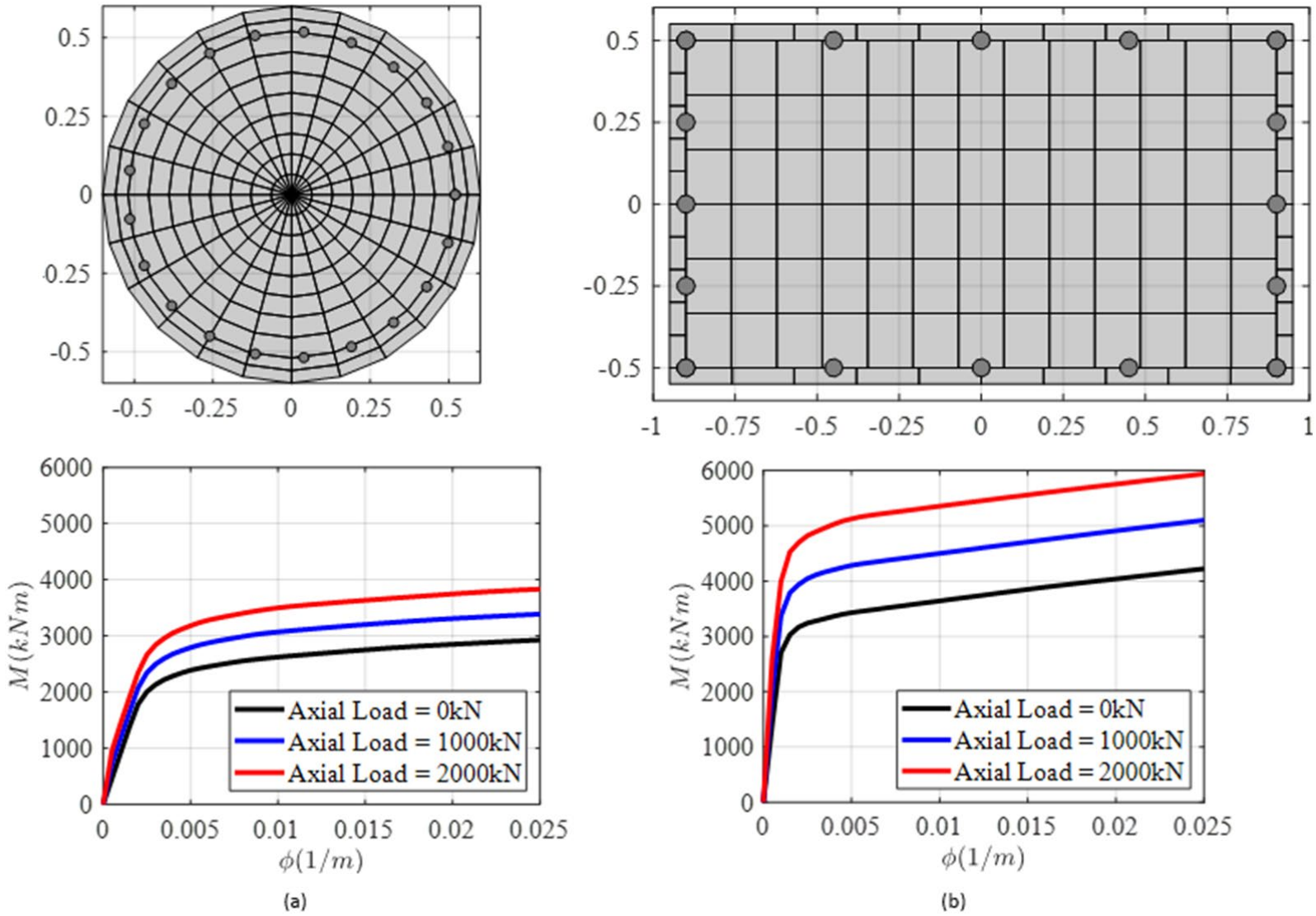

Figure 7-12. Section and the moment-curvature response of the piers of the (a) HWB and (b) RRB

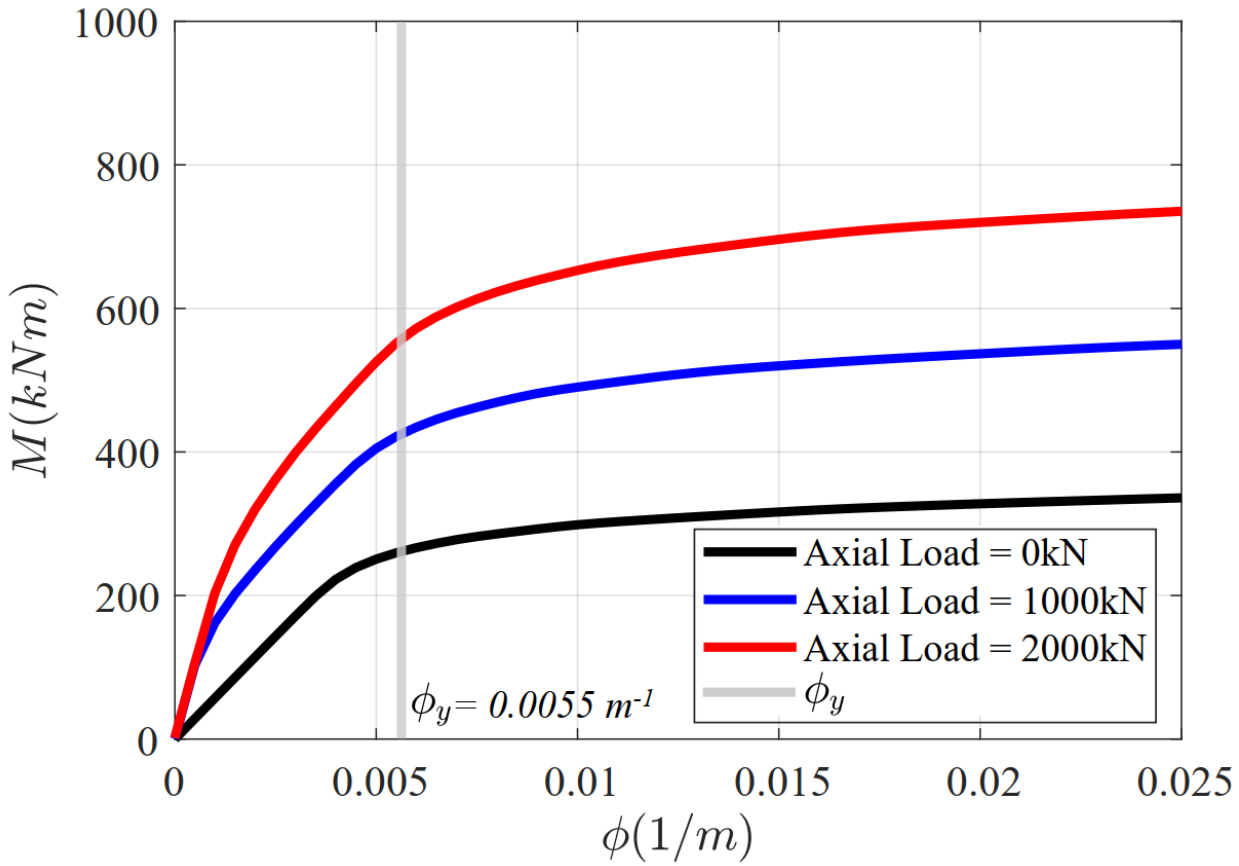

Figure 7-13. Employed moment-curvature relationship for the railroad bridge super pile.

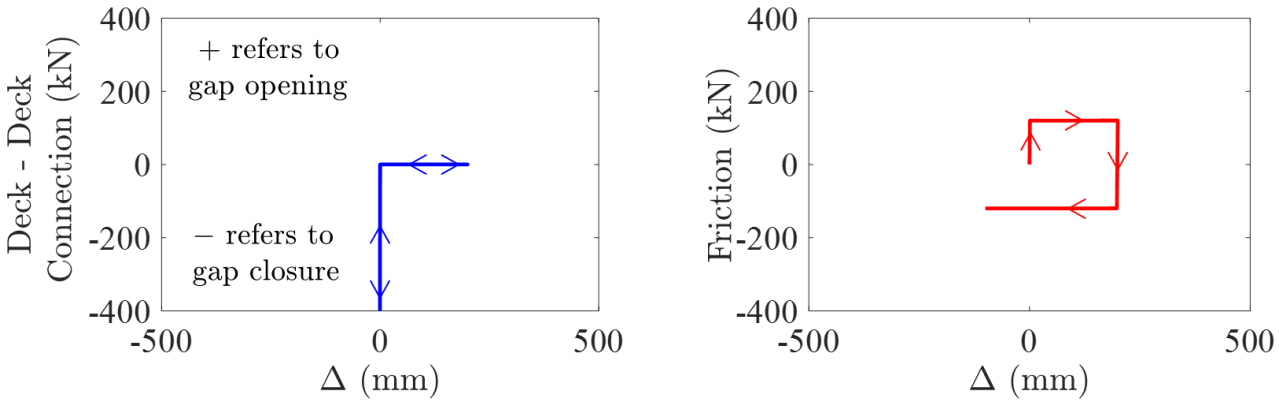

Figure 7-14. Interface elements between bent and deck of railroad bridge (a) deck-deck connection and (b) friction element

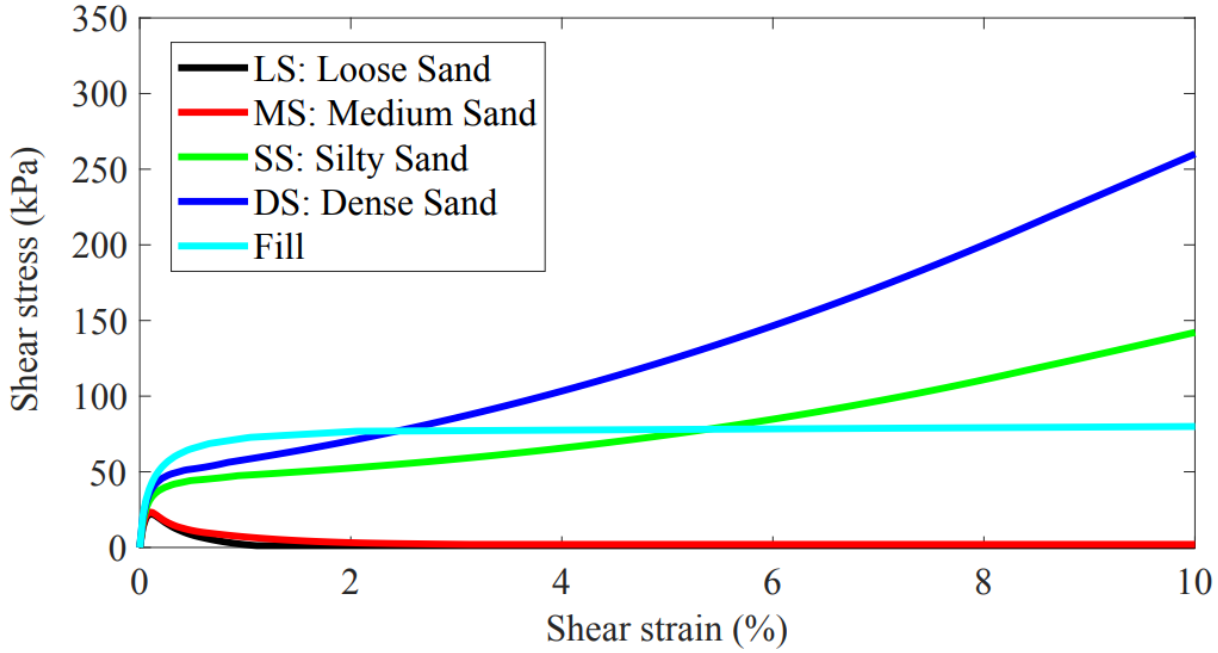

Figure 7-15. Monotonic undrained shear stress strain curves for each layer at a vertical stress of 1 atm

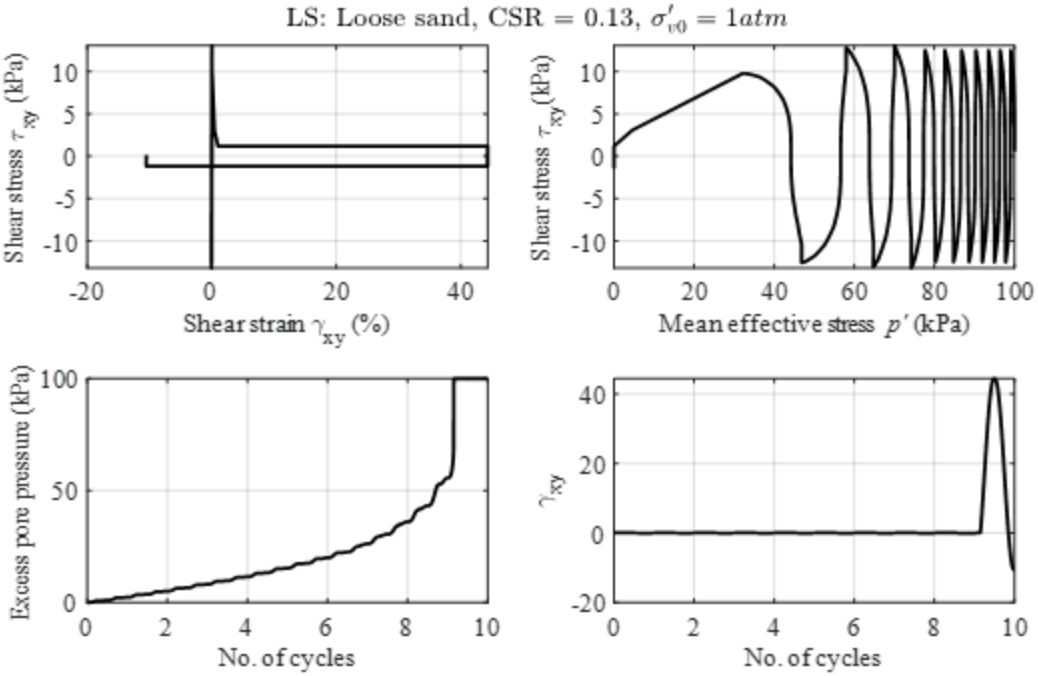

(a) LS (at a CSR of 0.13)

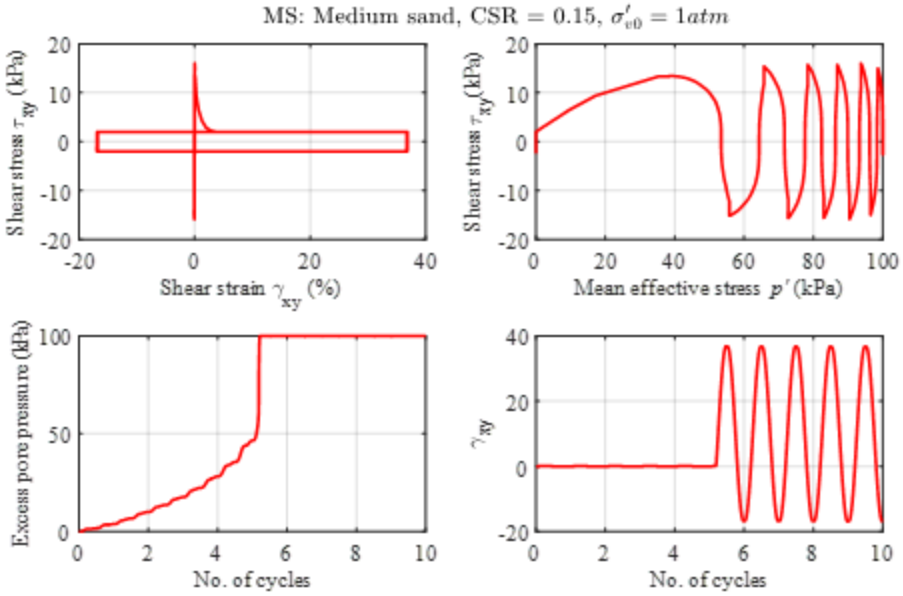

(b) MS (at a CSR of 0.15)

Figure 7-16. Cyclic stress controlled simple shear element simulations for (a) LS (at a CSR of 0.13), (b) MS (at a CSR of 0.15)

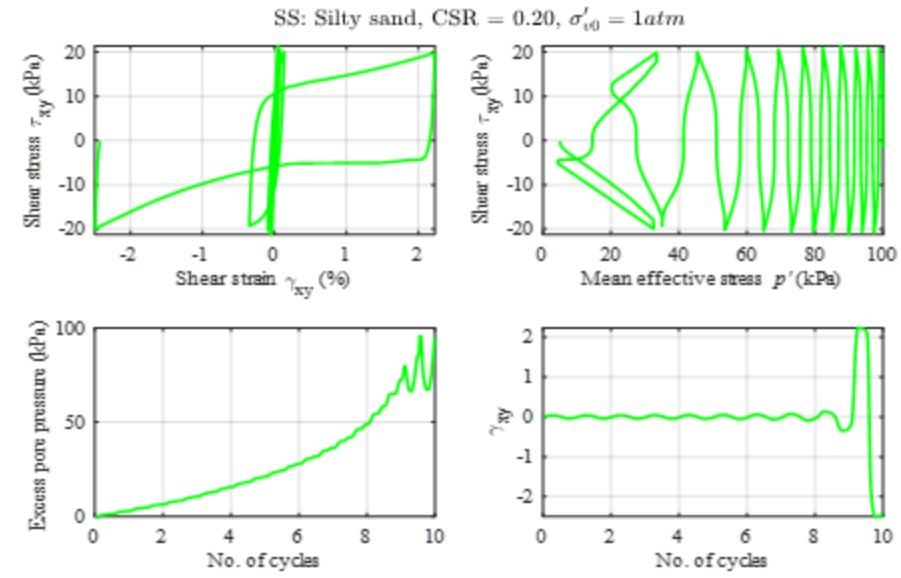

(a) SS (at a CSR of 0.2)

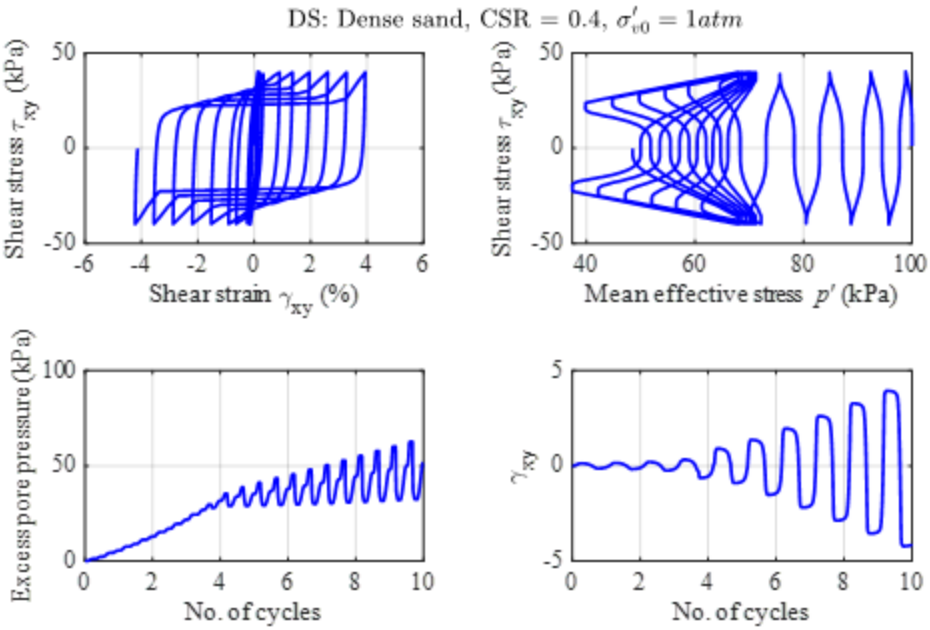

(d) DS (at a CSR of 0.4)

Figure 7-16. Cyclic stress controlled simple shear element simulations for (b) MS (at a CSR of 0.15), (c) SS (at a CSR of 0.2), and (d) DS (at a CSR of 0.4)

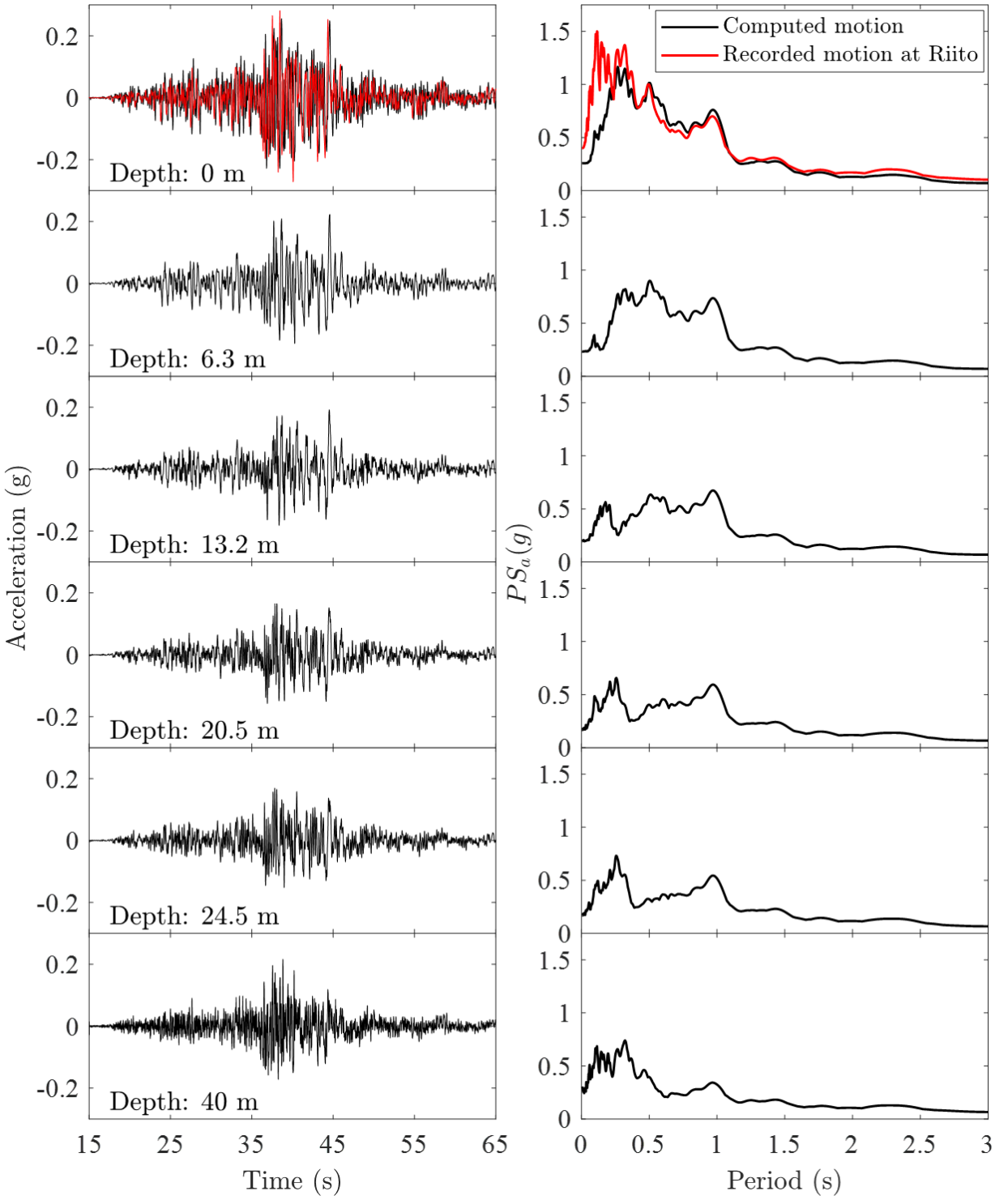

Figure 7-17. Computed acceleration at east and west boundaries of the model along shear beam (recorded motion at top is lowpass filtered at 20 Hz)

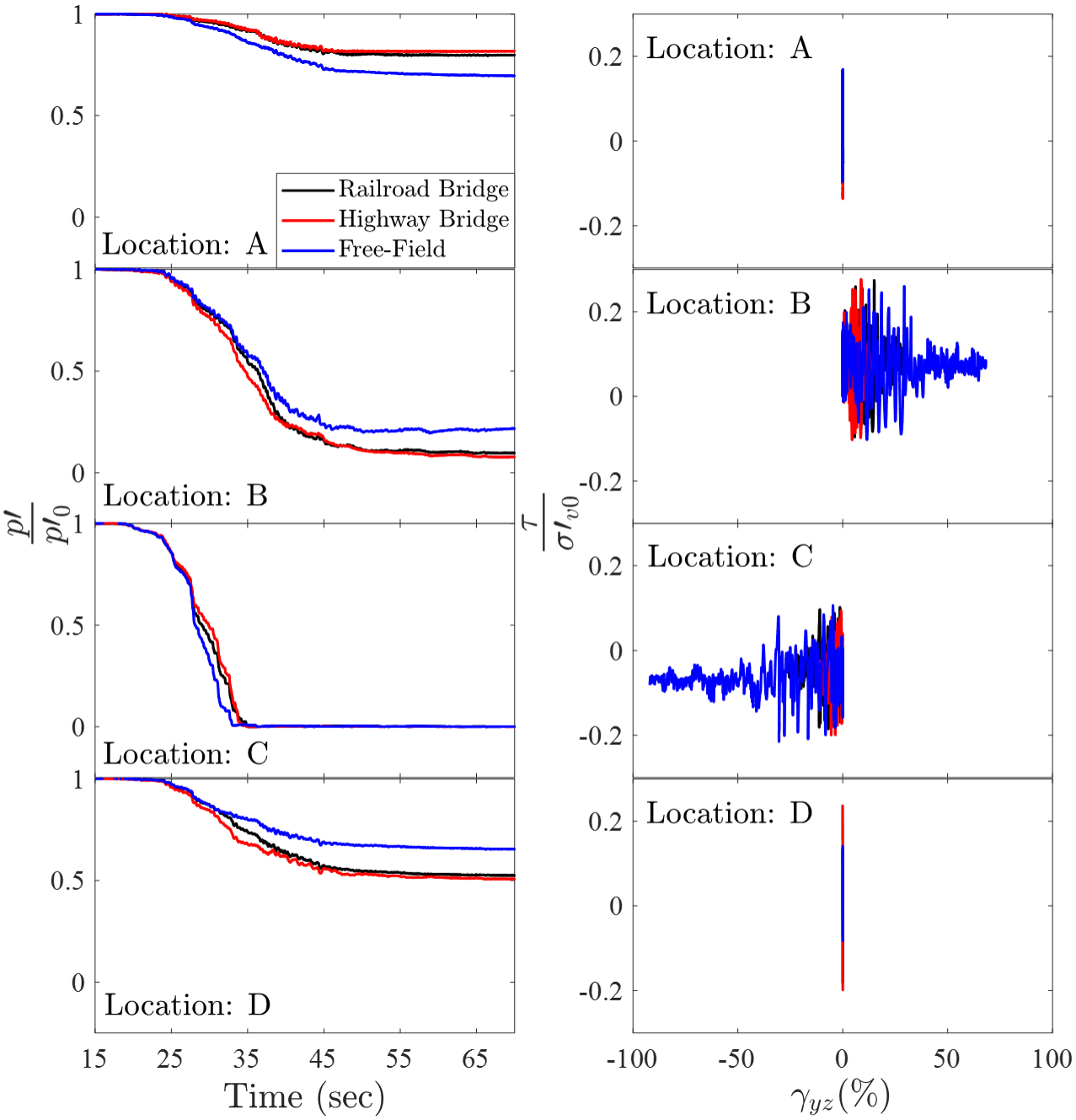

Figure 7-18. Computed soil confinement histories and shear stress-strain response for the Railroad bridge, Highway bridge, and free field at different locations within the canyon.

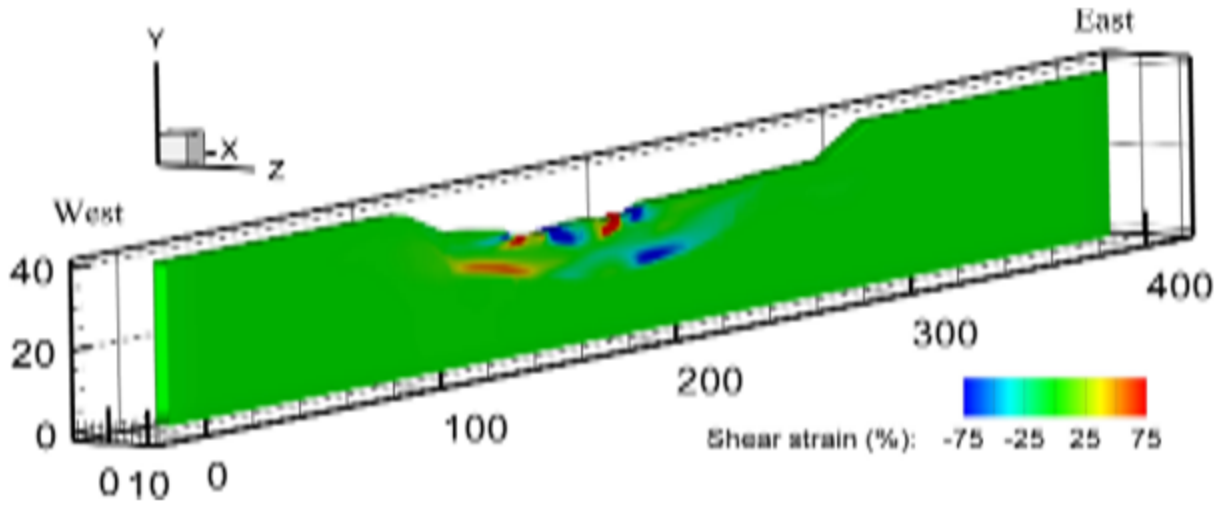

(a) Free-field Shear strains at the end of shaking.

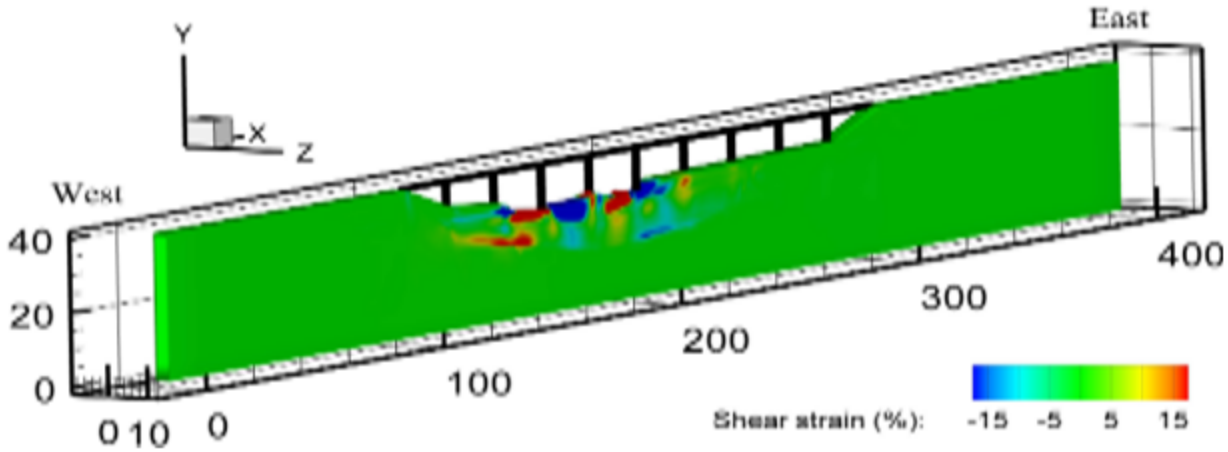

(b) Highway bridge-canyon system Shear strains at end of shaking

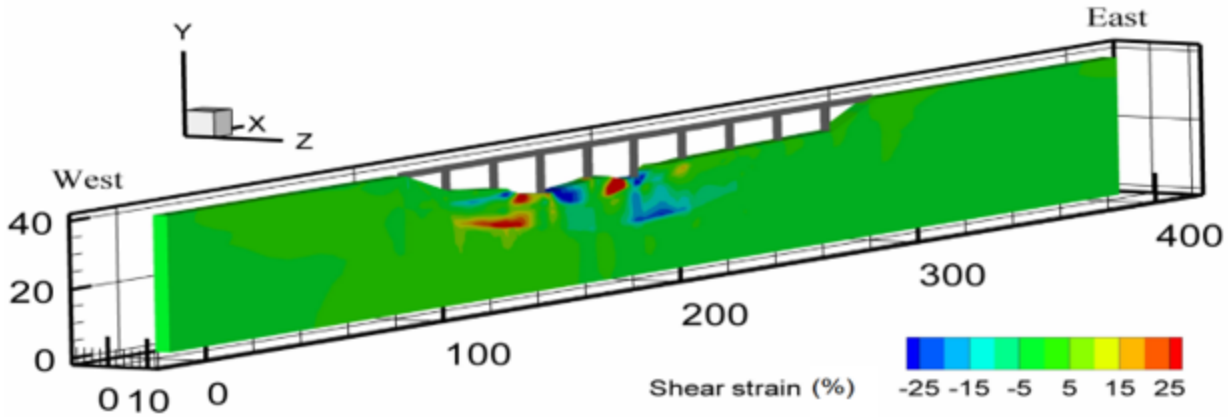

(c) Railroad bridge-canyon system Shear strains at at end of shaking

Figure 7-19. Shear strain profiles at (a) free field (without influence of bridge), (b) highway bridge-canyon system at end of shaking, and (c) railroad bridge at end of shaking

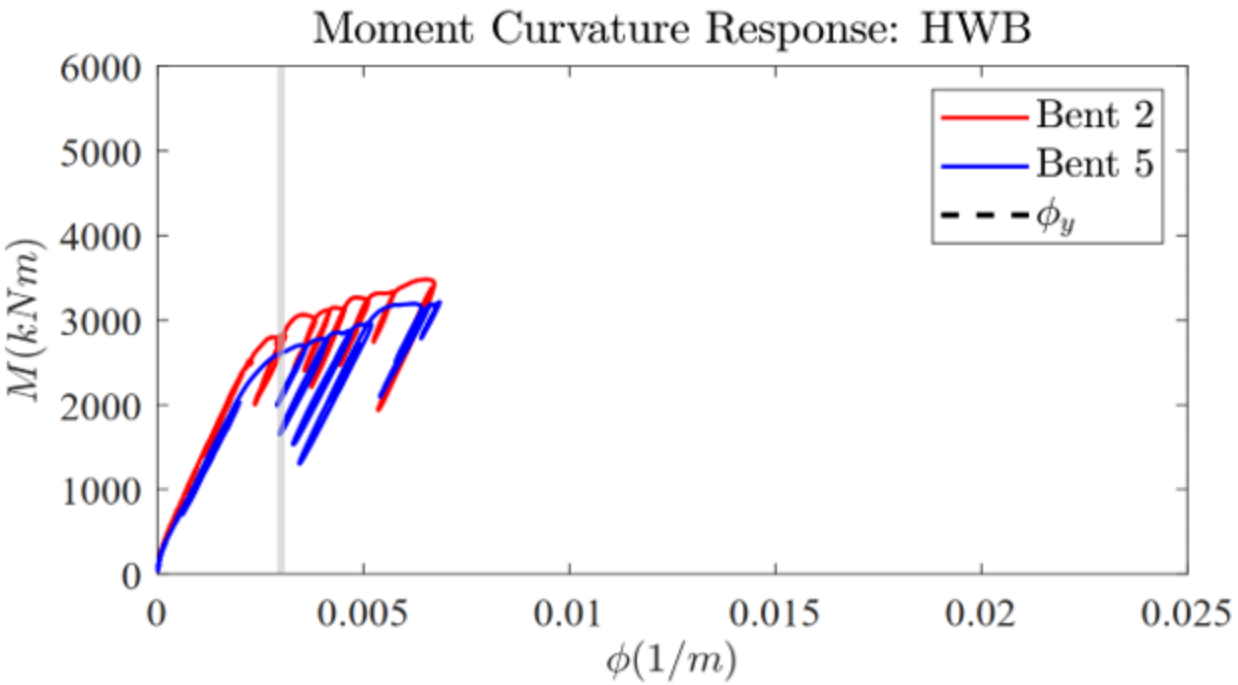

(a) Moment curvature demands on foundation of highway bridge

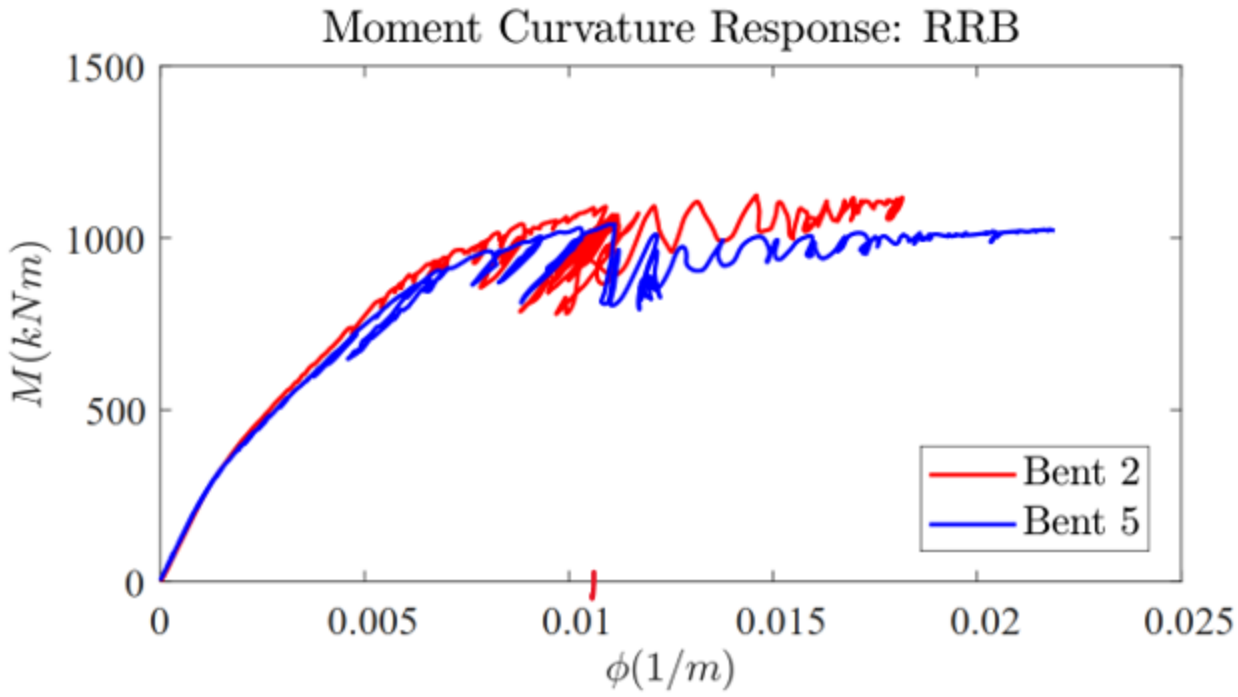

(b) Moment curvature demands of railroad bridge piles (at the location of peak moment)

Figure 7-20. Moment curvature demands on foundations of (a) highway bridge and (b) railroad bridge.

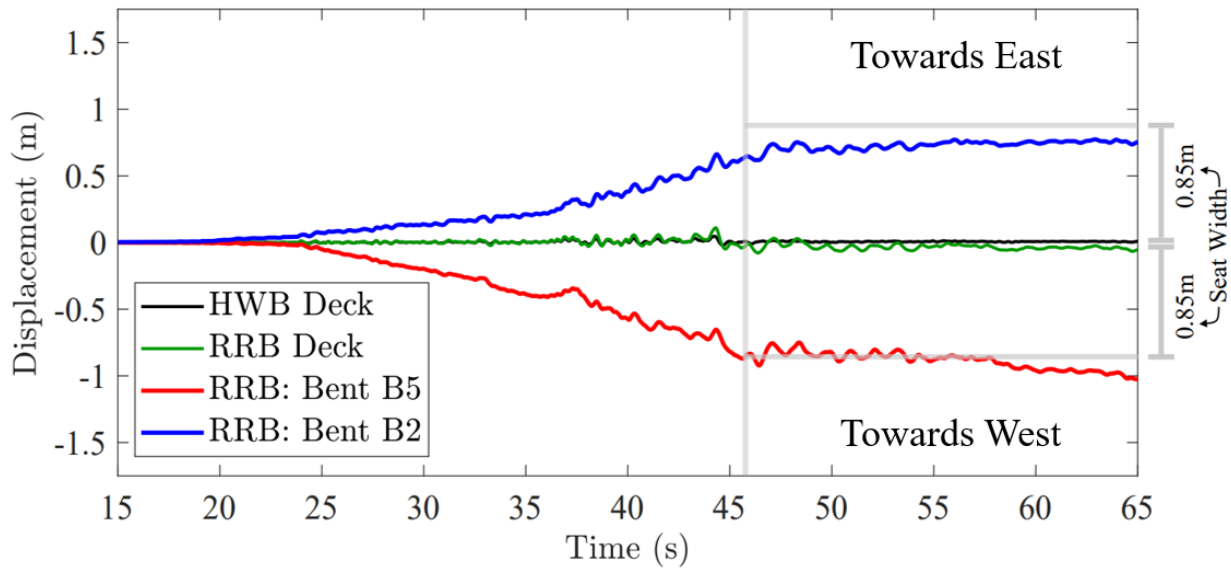

Figure 7-21. Computed deck displacements for the HWB, RRB and top of RRB bents B2 and B5 towards river channel.

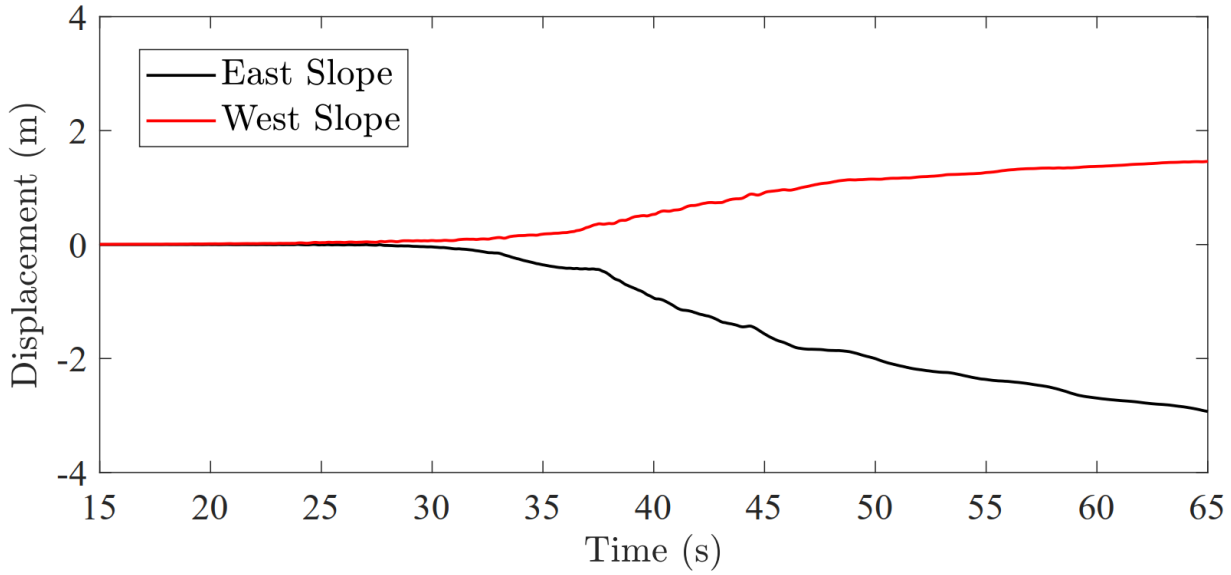

Figure 7-22. Computed soil displacement histories on east and west slopes of the active river channel

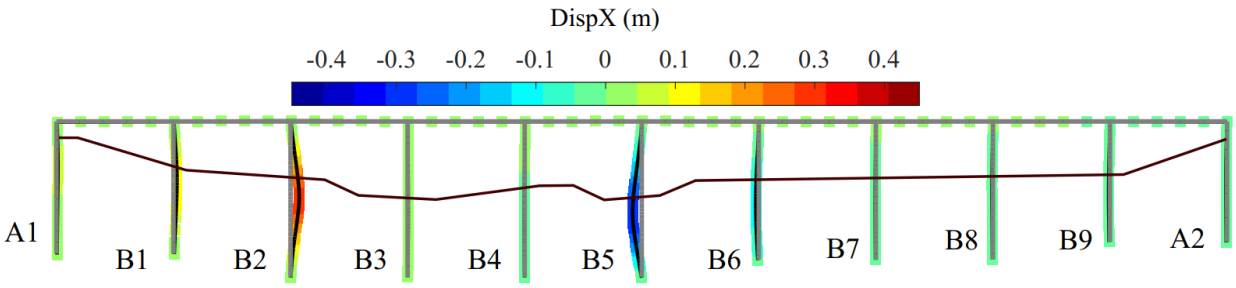

Figure 7-23. Deformed configuration of the highway bridge at the end of shaking. (Deformations scaled by a factor of 5 in figure)

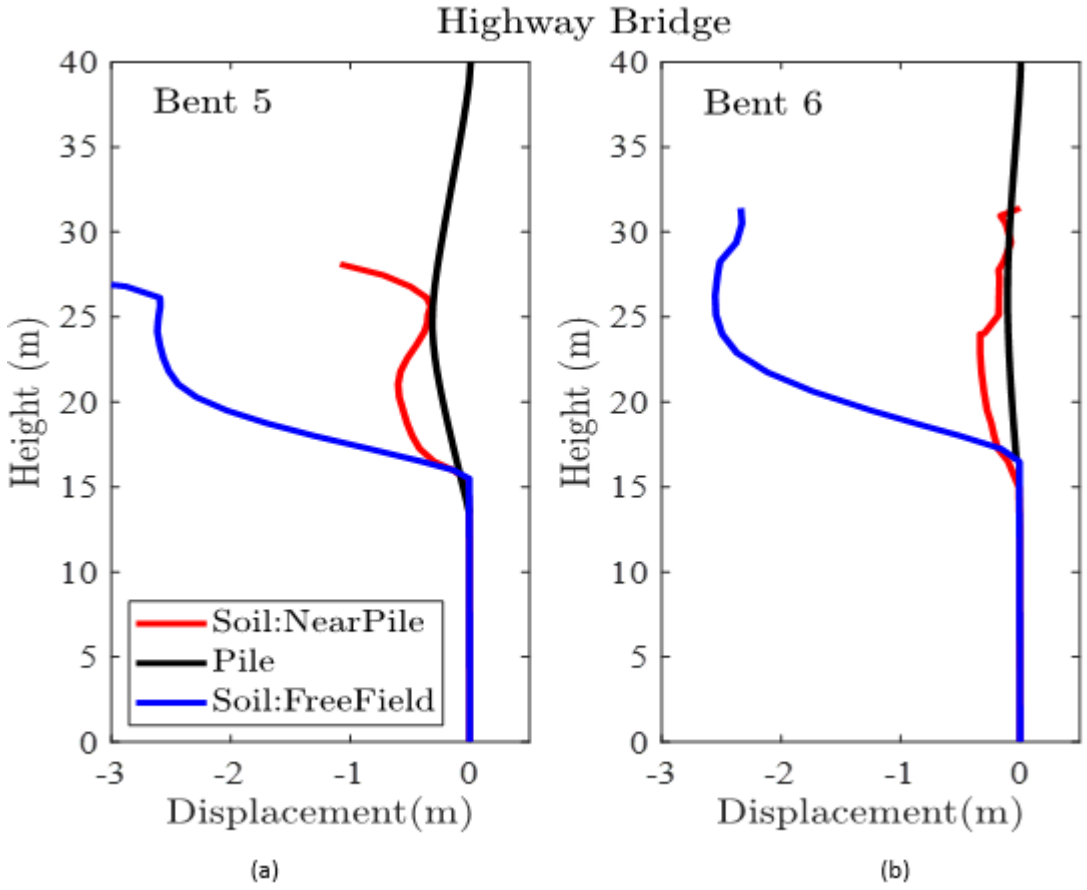

Figure 7-24. Configuration of deformed soil in free field, near pile and piers for bents (a) B5 and (b) B6 in the highway bridge at the end of shaking for the highway bridge

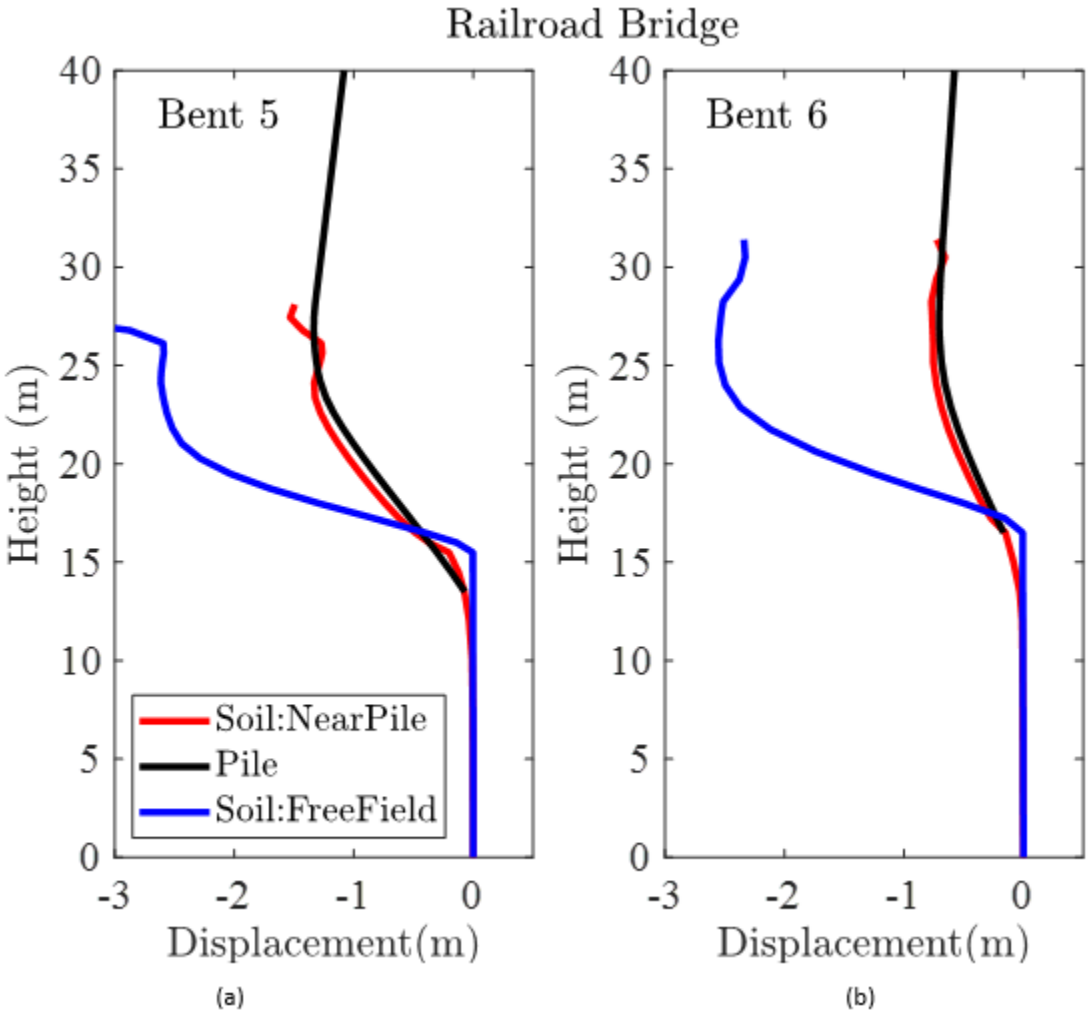

Figure 7-25. Configuration of deformed soil in free field, near pile and piers for bents (a) B5 and (b) B6 in the railroad bridge at end of shaking for the railroad bridge.

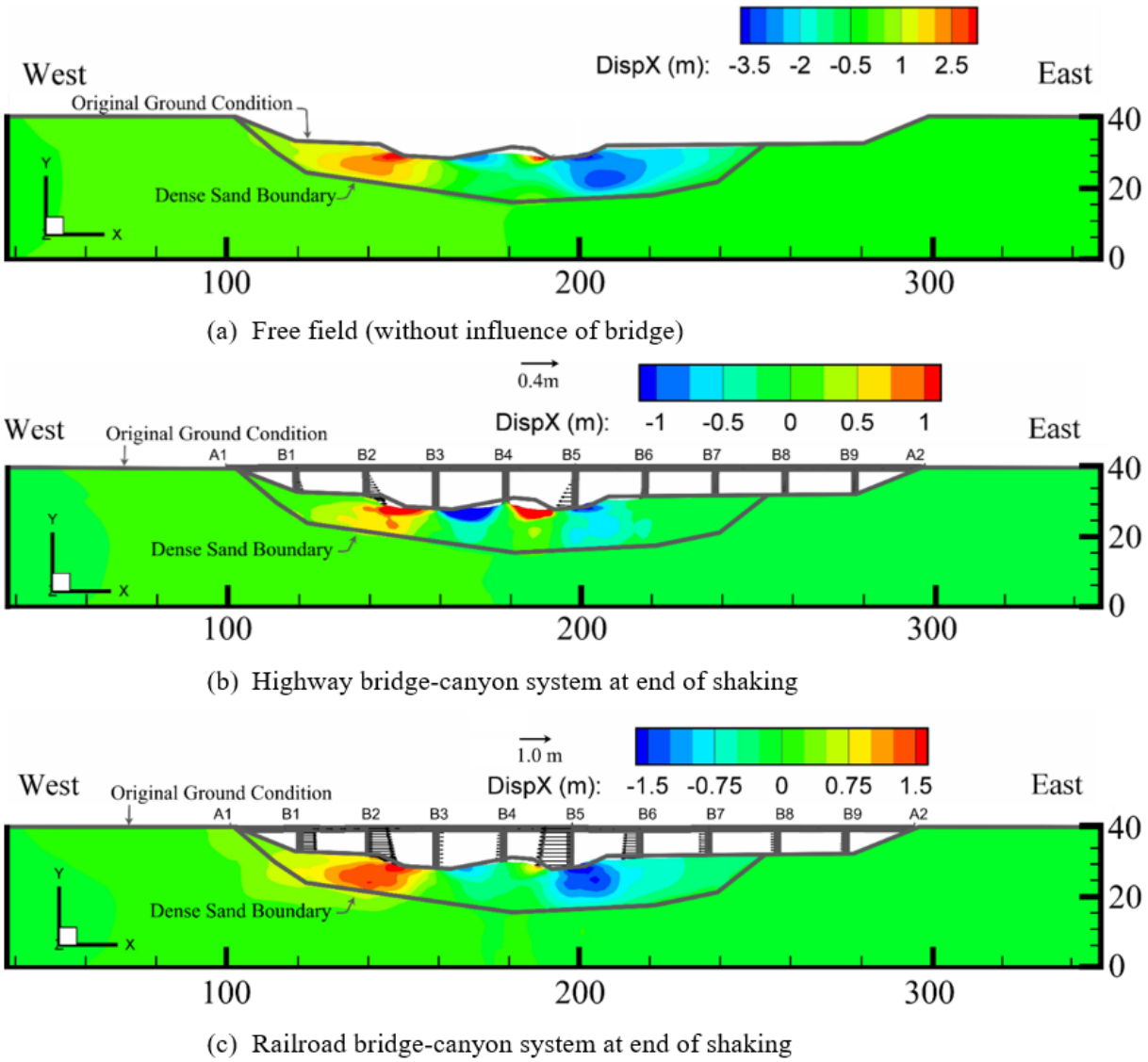

Figure 7-26. Displaced Configurations at (a) free field (without influence of bridge), (b) highway bridge-canyon system at end of shaking, and (c) railroad bridge at end of shaking.

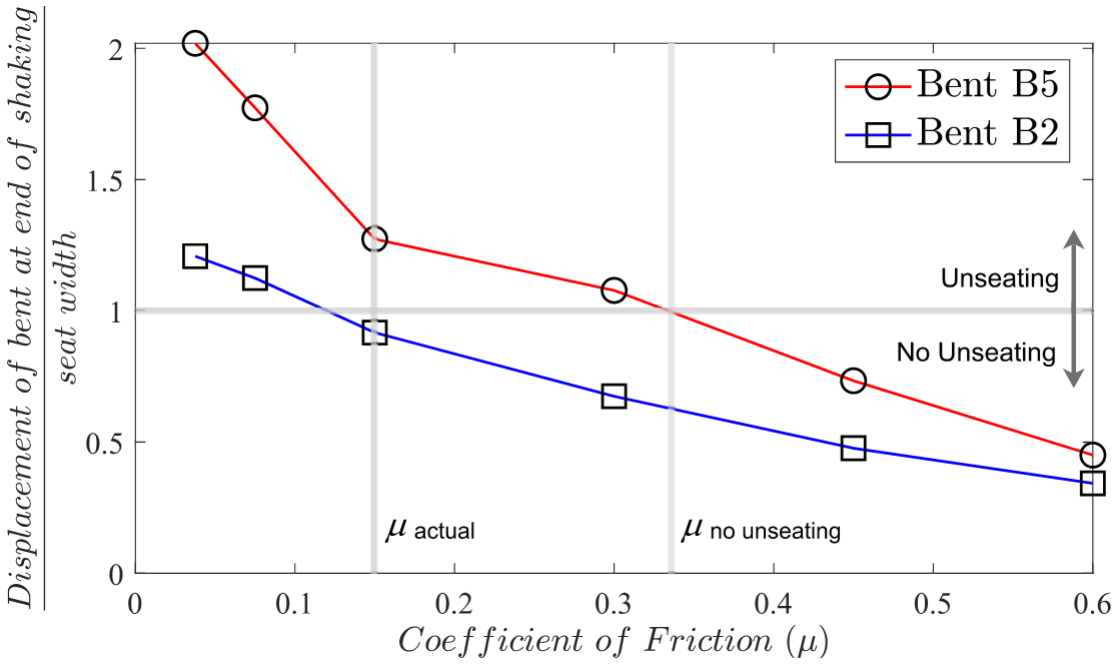

Figure 7-27. Displacement at the top of Bents 2 and 5 of the railroad bridge with different degrees of friction.

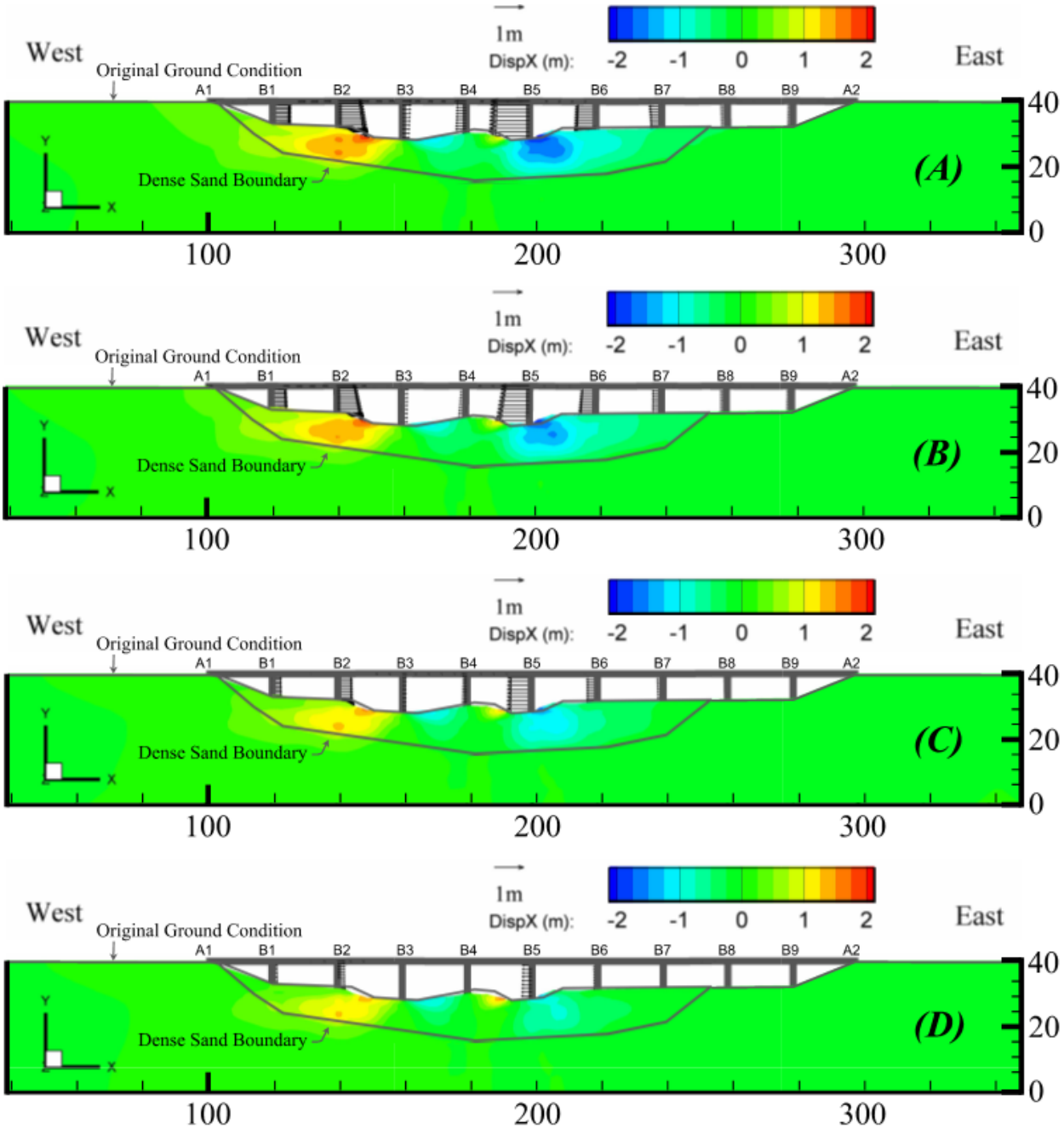

Figure 7-28. Deformed profiles of the railroad bridge-canyon system at end of shaking for a deck-bent friction coefficient of (A) 7.5%, (B) 15%, (C) 30%, and (D) 60%. (all dimensions are in m)

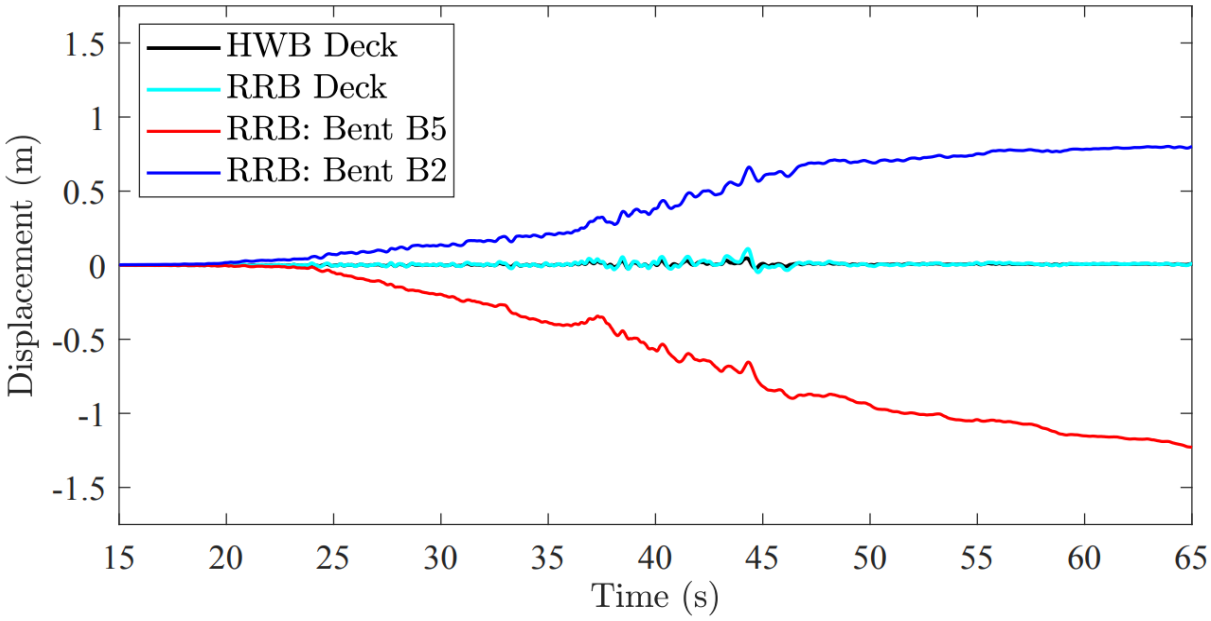

Figure 7-29. Computed deck displacements for the HWB, RRB and top of RRB bents B2 and B5 towards river channel (precluding unseating of span B5-B6).

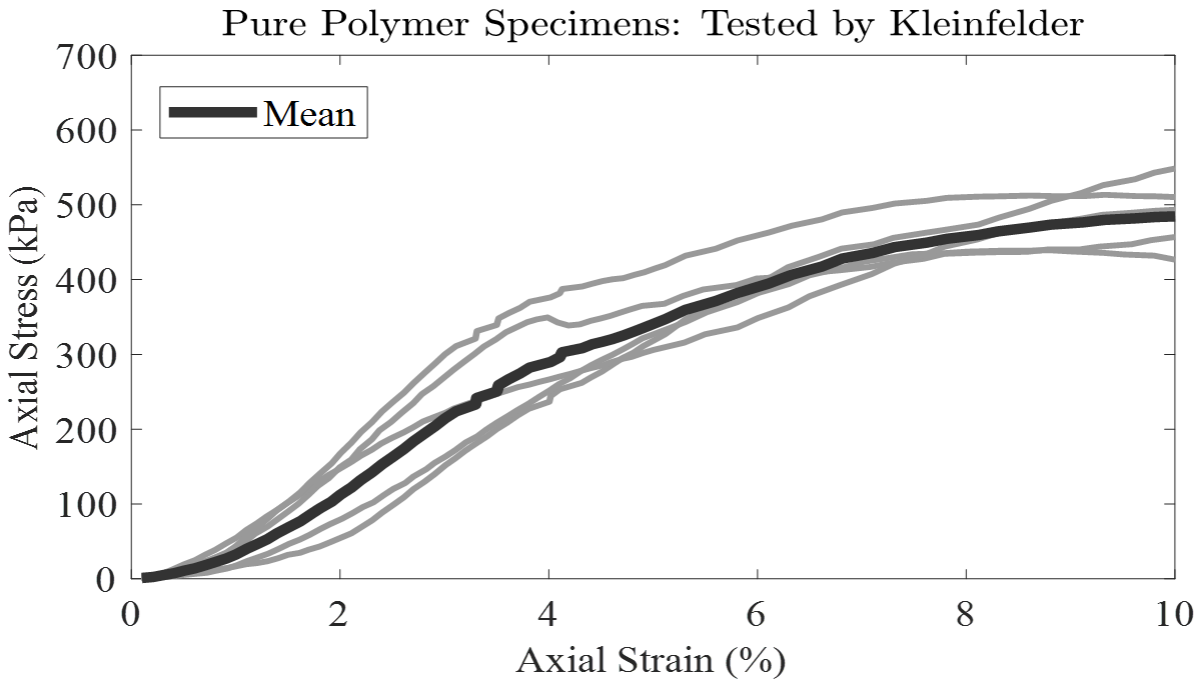

Figure 7-30. Stress strain response of pure polymer specimens (From Kleinfelder, 2019)

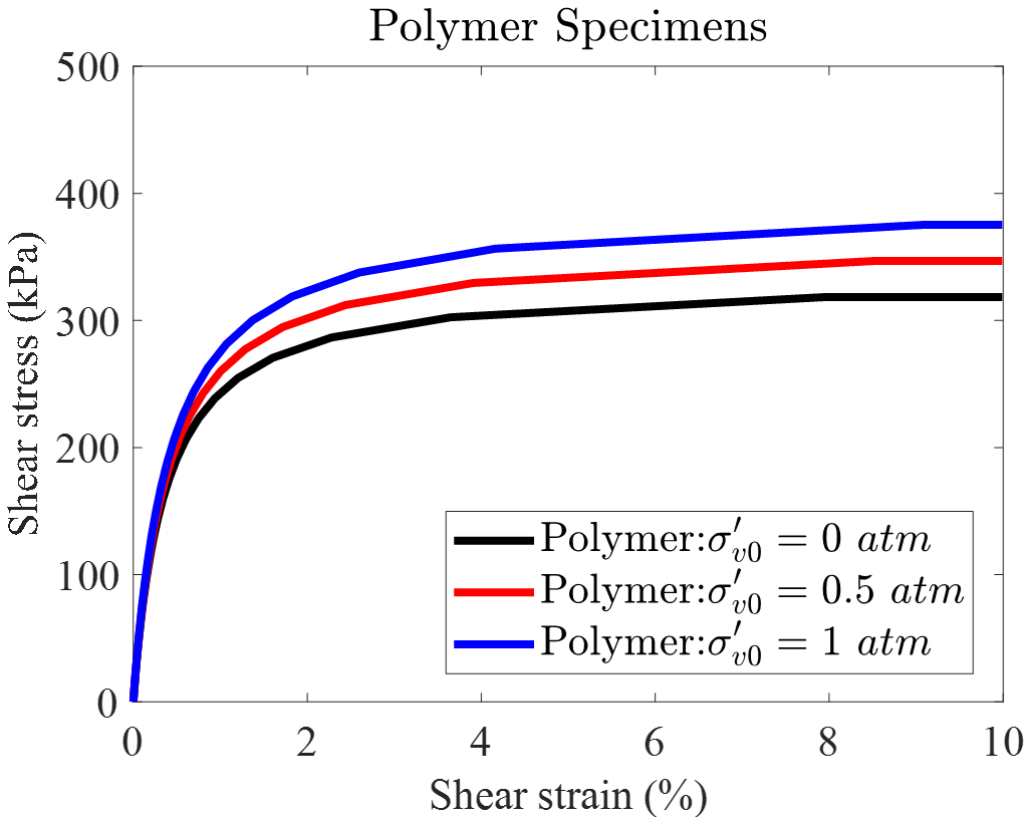

Figure 7-31. Monotonic shear stress-strain curves for the polymer-sand composite

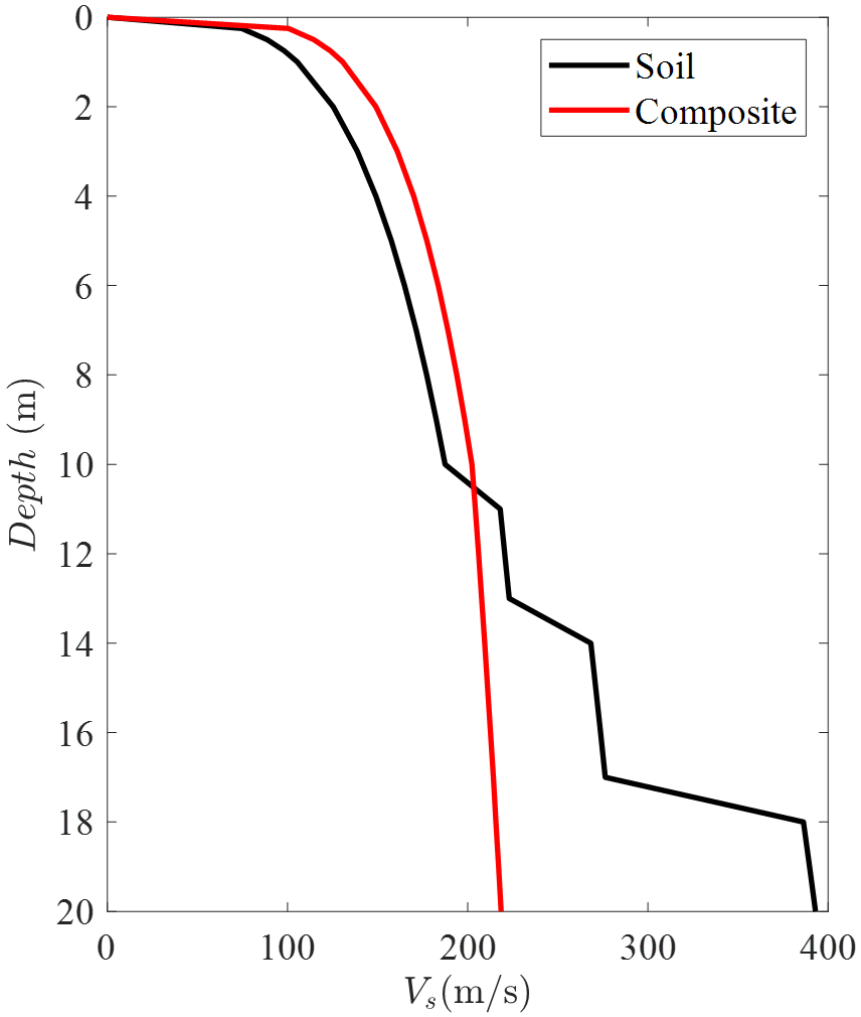

Figure 7-32. Shear wave velocity (V_s) of deposit and polymer-sand composite.

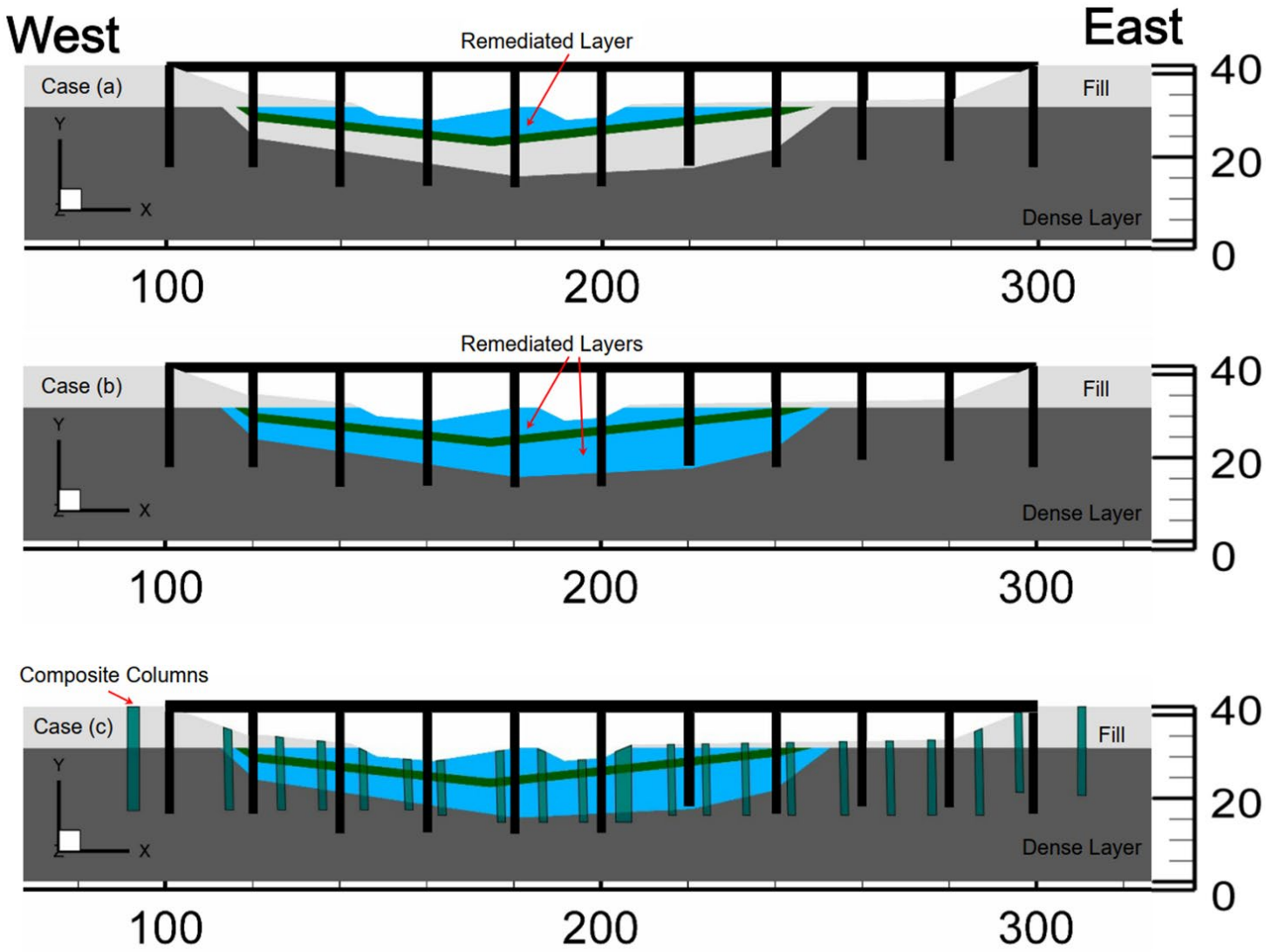

Figure 7-33. Insitu ground modification measures for the railroad bridge: remediation of (a) Layer LS (shallow liquefiable layer) along bridge footprint, (b) Layers LS, SS, and MS (along bridge footprint (c) grout inclusions.

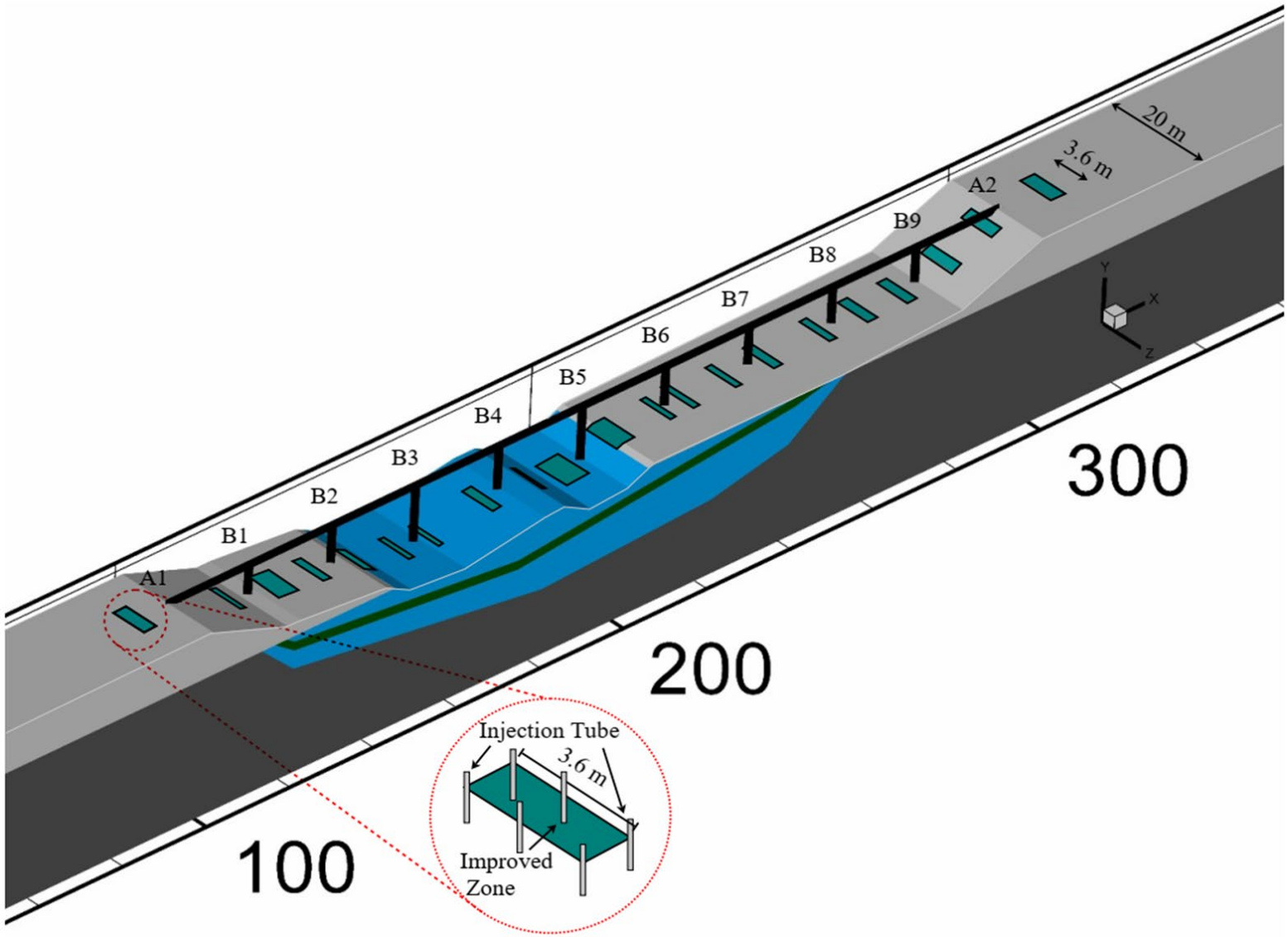

Figure 7-34. In-situ ground modification using grout inclusions (layout of injection is presented)

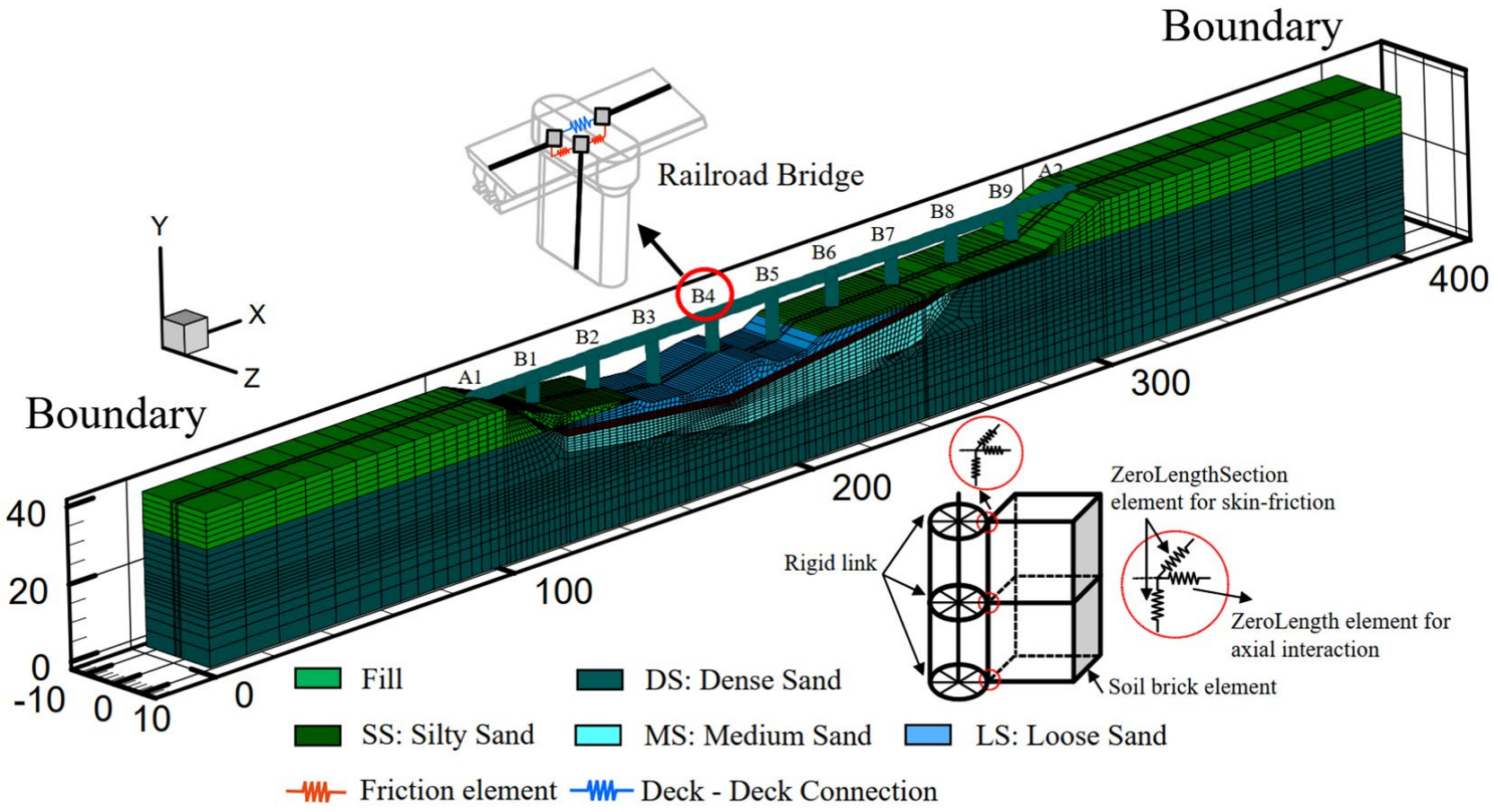

Figure 7-35. Expanded mesh of the railroad bridge -ground system employed in the simulations with ground remediation.

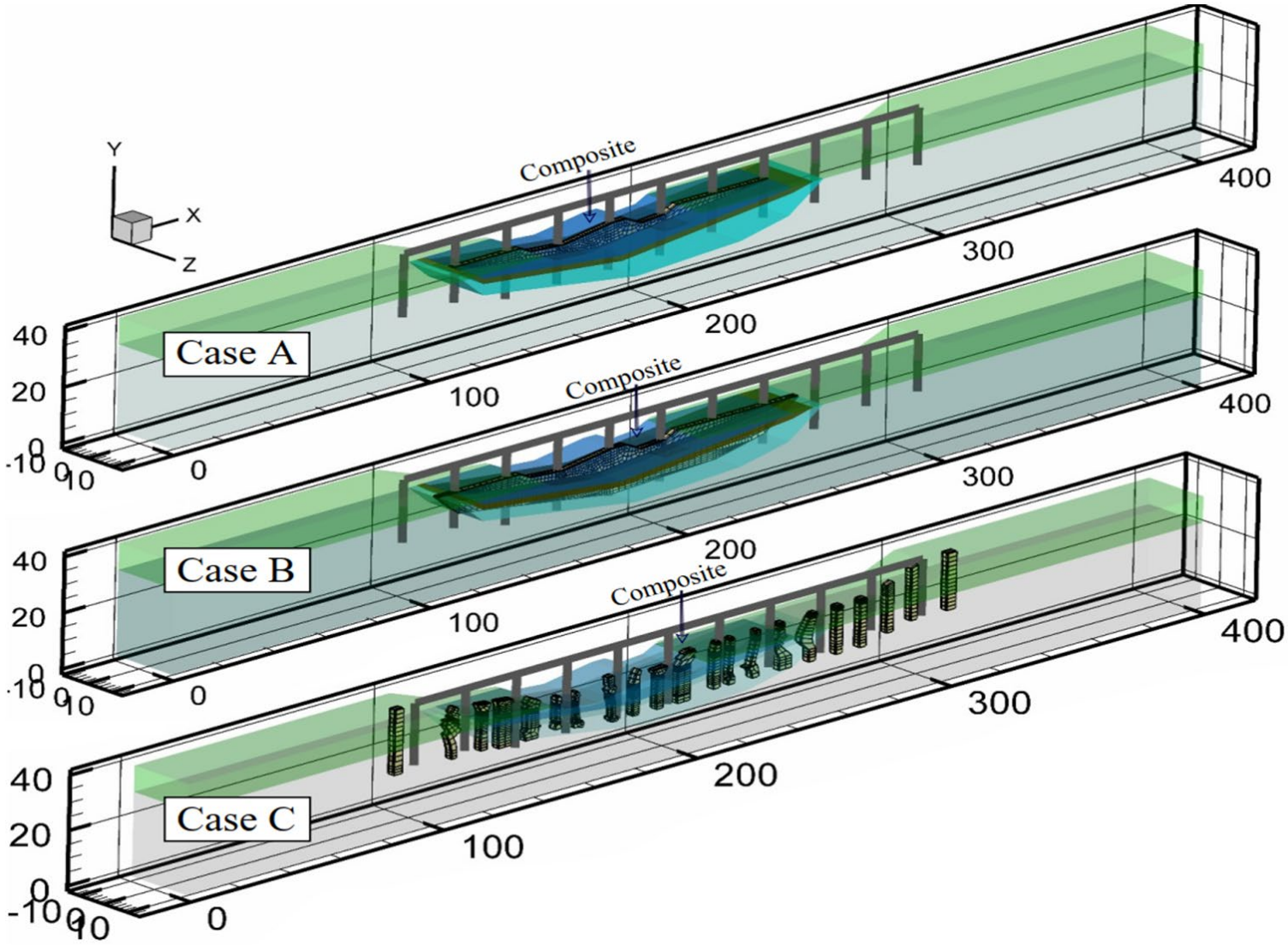

Figure 7-36. Employed remediation measures for the railroad bridge: remediation of (a) Layer LS (shallow liquefiable layer) along bridge footprint, (b)Layers LS, SS, and MS (along bridge footprint (c) grout inclusions.

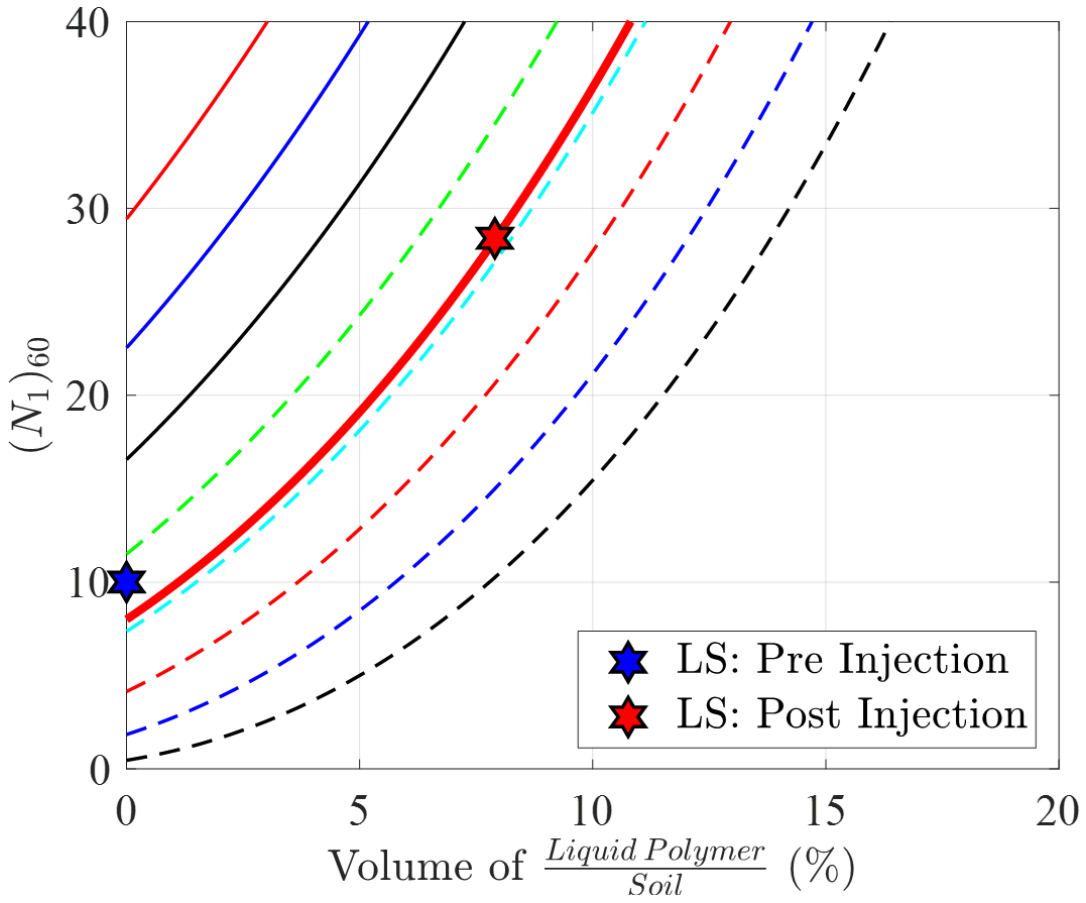

Figure 7-37. Degree of soil improvement pre- and post-injection into the LS (Loose Sand) layer

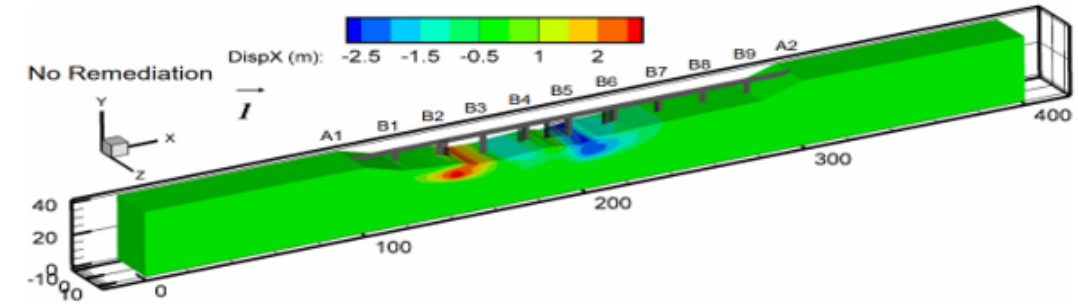

(a) Railroad bridge-ground system without remediation

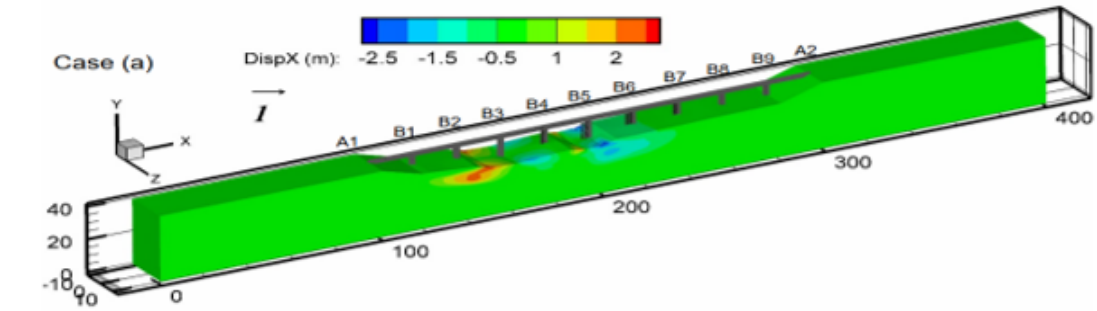

(b) Railroad bridge-ground system after remediation of the LS Layer

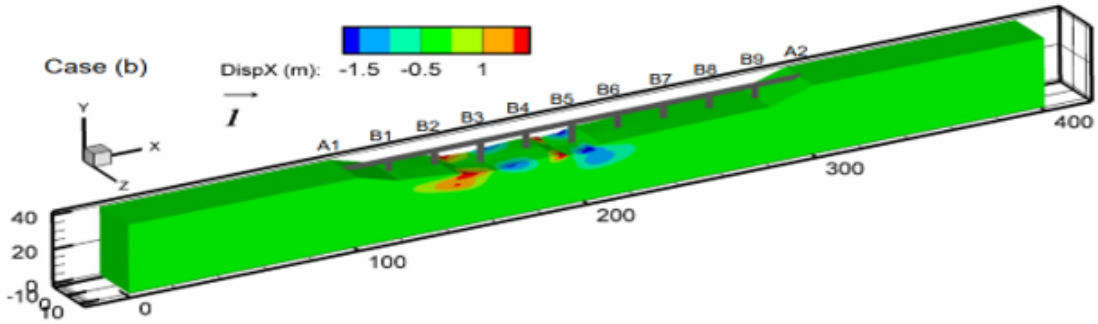

(c) Railroad bridge-ground system after remediation of the LS and MS layers

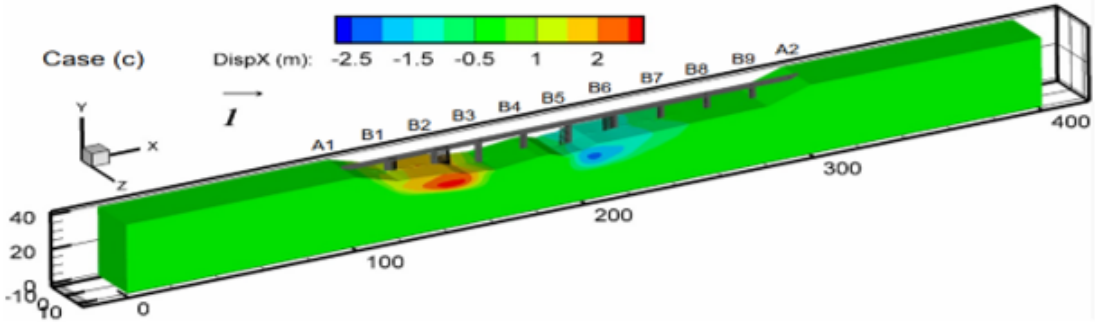

(d) Railroad bridge-ground system after remediation using composite inclusions

Figure 7-38. Deformed configuration of the railroad bridge -ground system at end of shaking: (a) without remediation, (b) improving LS Layer, (c) improving LS and MS layers, and (d) adding composite inclusions.

8. INSIGHTS FOR SIMPLIFIED ANALYSIS PROCEDURES

Ahmed Elgamal and Ahmed Ebeido

8.1 Abstract

Simplified procedures attempt to strike a balance between quality and quantity of available data, complexity of the employed analysis technique, and resulting accuracy of the outcomes. As such, based on judicious reasoning and sound engineering judgement, the Caltrans MTD 20-15 (2017) was developed. In view of the presented research outcomes, a number of elements are outlines herein, for consideration towards future updates.

8.2 Introduction

Efforts were undertaken (Ledezma and Bray 2008, Ashford *et al.* 2009, 2011) to document and critically assess the challenge of loading on bridge systems due to seismically induced lateral ground deformation. Based on this thorough background work, the outcomes were distilled in the form of a simplified analysis procedure MTD 2015 (2017) as shown schematically in Figure 8-1. For the purpose of the subsequent discussions below, an outline of the main involved elements and analysis steps is included below:

1. A single bridge bent is analyzed (Figure 8-1) with influence of the overall bridge-ground structural resistance imposed as a lateral resisting force along the bride deck elevation. A substantial challenge lies in definition of this imposed resisting force that represents the overall bridge-foundation-ground configuration. In this regard, recent bridge-foundation-ground system analyses (e.g., Qiu *et al.* 2020, 2022) indicate that deck-level lateral resistance at any bent location is an outcome of the overall system response as dictated by:

i) The entire bridge geometry and structural details,

ii) The underlying waterway topography along the bridge spatial extent (o this end, interaction between downslope ground deformations at both sides of the waterway can be of critical importance), and

iii) The soil profile and its potential significant spatial variability along the bridge's longitudinal direction.

2. A liquefied soil residual shear Strength (S_r) is estimated based on SPT blow counts following the latest published findings (e.g., Kramer and Wang 2015).

3. Based on the slope geometry and soil profile around the bridge bent (and in particular the value of S_r), a slope stability analysis is conducted to find the lateral yield coefficient (ky) for a factor of safety (FS) of 1.0. In turn, this yield coefficient (ky) is used to estimate expected lateral displacement of the slope (e.g., based on Bray and Travasarou 2007).

4. Through an iterative procedure, the restraining action due to presence of the deep foundation (so called, pile-pinning effects) is estimated to finally determine a lateral soil displacement magnitude (Δ) that will act on the foundation system (Figure 8-1b). This lateral displacement magnitude is used with an assumed lateral displacement profile that acts along the height of the foundation system.

5. Using the *p-y* curve analysis approach, this displacement profile is then applied to the foundation system (Figure 8-1b) and the resulting forces, moments and lateral deformations are assessed.

While the simplification afforded by the MTD 20-15 (2017) approach cannot be overstated, implementation of the procedure might result in a wide range of assessment outcomes in view of challenges such as:

i) the estimated shear strength S_r of the liquefied soil, and the current wide variability range in its empirical range (Kramer and Wang 2015),

ii) dependence of the results on the employed slope-stability method (e.g., Bishop, Spencer, ...etc.), and configuration of the assumed failure surface (Figure 8-1a),

iii) the assumptions associated with pile-pinning effects and the possible equally viable alternative ways to assess this mechanism (Figure 8-2),

iv) the assumed ground deformation profile to be applied to the pile foundation, and imposition of lateral pile load via *p-y* curve response representations that stem from logics such as those of soft clay (Matlock 1970) response.

In view of such considerations, and motivated by the research (e.g., Qiu and Elgamal 2020, Qiu *et al.* 2020, 2022, and Elgamal and Qiu 2022) presented in the earlier chapters of this report, a

somewhat different simplified analysis framework is proposed herein. This framework, which requires further research to refine and calibrate, attempts to:

i) Employ a structural model that represents the entire bridge structure from end-to-end, and

ii) Formally account for the topography and soil profile variability along the bridge structure,

iii) Further simplify the MTD 20-15 (2017) step-by-step analysis framework, by a more direct definition of lateral loads to be imposed simultaneously on all impacted bents of the bridge.

In the following sections, elements of this proposed approach are described. Each of these elements can be further modified to provide additional assessment accuracy, as permitted by the extent and quality of available information/data and sophistication of the available analysis tool.

8.3 Proposed Simplified Procedure Framework

The logics presented below should be viewed as a framework towards future updates of simplified procedure analyses. As such, it constitutes a basis for development of a formal step-by-step procedure that can be further calibrated based on more rigorous analysis, experimentation, and data from related earthquake reconnaissance efforts. With that in mind, the main involved elements are:

1. Represent bridge and foundation by an appropriate simple Finite Element (FE) stick model (Figure 8-3), or similar frame-analysis approach (e.g., using CSiBridge https://www.csiamerica.com/products/csibridge , or OpenSees MSBridge http://www.soilquake.net/msbridge/).

2. Conduct a classical liquefaction Simplified Procedure Analysis (e.g., Idriss and Boulanger 2008) on the site profile(s) of interest, or the spatial location(s) where liquefaction might occur (Figure 8-4). Estimate factor of safety against liquefaction for each location (FS_{liq}).

3. Where liquefaction is noted, estimate spatial distribution of lateral loads based on waterway topography and soil profile variability (Figure 8-4). If liquefaction is expected to occur on both sides of the bridge, we define a neutral axis where no lateral deformation takes place. This neutral axis location can be decided upon based on the slope stability safety factor considerations on either side of the waterway, as dictated by the bridge and soil profile variability along the waterway (Figure 8-4 and Figure 8-5). As such, for a perfectly symmetric bridge-foundation-ground configuration (in the longitudinal direction), this neutral axis would fall along the central cross-

section of the bridge. Otherwise, insights from system stability considerations on each side of the bridge must be invoked. Finally, if needed, more than one scenario of defromations can be considered, to address issues such as onset of such defromations along the longitudinal ground profile.

4. Based on the neutral axis logic (Figure 8-5), we can reduce lateral loads on the bent deep foundations according to proximity to this neutral axis (for instance, start zero displacement logic at a location that is 2x or 3x height of the slope away from the slope crest, and end with zero displacement along the neutral axis).

5. Via the overall bridge stick model, apply these lateral loads locally to each bent/abutment (Figure 8-6). This can be done based on:

i) The displacement (Δ) and *p-y* curve logics of MTD 20-15 (Figure 8-1, or similar updated guidelines), with Δ modulated by the waterway topography and soil profile displacement distribution shown schematically in Figure 8-5. Further insights into this displacement may be also inferred from the reconnaissance (Figure 8-7), experimentation, and analysis literature (Haskell *et al.* 2013, Cubrinovski *et al.* 2014a, b, c, Ishihara and Cubrinovski 2020, Little and Rathje 2021, Qui and Elgamal 2022). Among other related options to be considered,

ii) Since peak liquefied soil load (Figure 8-8) occurs at small deformations (Ebeido 2019, Ebeido and Elgamal 2019, Ebeido *et al.* 2019) and peak crust loads occur at larger deformations (Turner *et al.* 2016, Ebeido 2019), we can assess either scenario separately and take the worst case outcome. Load from the liquefied stratum can be taken as its peak value (MTD 20-15 2017, Turner *et al.* 2016, Ebeido 2019), and load from crust taken according to FS_{liq} value (e.g., conceptually, pending further refinement and research, full passive for FS_{liq} less than 0.3, and 0.3 for FS_{liq} greater than 0.6, where these values can be also adjusted based on reconnaissance observations). Slope angle can be also included as a factor in determining level of the crust passive load.

6. Asses the overall response of the bridge (Figure 8-9). In this regard, below the liquefied soil strata, the foundations can be laterally supported on stiff soil *p-y* curves (to be selected based on SPT N-value for instance, or even assumed essentially rigid at some user-defined depth).

8.4 Other Possible Considerations

As mentioned above, MTD 20-15 (2017) is a procedure to estimate lateral displacement demand and the resulting bridge foundation behavior and response. Above, it was already highlighted that use of a global bridge-foundation-ground model offers a number of important advantages. Nevertheless, within the current scope of the single bent model (Figure 8-1), some insights are included below for consideration towards future research and updates.

1. Reconnaissance (e.g., Haskell *et al.* 2013, Cubrinovski *et al.* 2014a, b, c, Robinson *et al.* 2014, Ishihara and Cubrinovski 2020) and related recent studies clearly show that slope deformations vary significantly within the sliding zone domain (e.g., Little and Rathje 2021, Qiu and Elgamal 2022). As such, location of the bent within the sliding mass can have a significant influence on the lateral displacement magnitude estimate (Figure 8-7), an issue that might be of significance in certain cases.
2. Schematic of the lateral imposed displacement profile might be defined to more closely mimic experimental observations (Figure 8-8). This profile might start from the upper crust through the liquefiable layer and into the underlying layer as affected by the liquefaction process. The smear zone of the underlying layer might need to be included depending on the soil type (Ebeido 2019, Ebeido and Elgamal 2019).
3. Each pile should be modelled as accurately as possible. Most piles have different cross-sections with depth. Pipe piles maybe be hollow, filled with soil, filled with concrete, and/or contain rebar. The variation of the pile cross-section will affect the locations of maximum moment and shear force (Ebeido 2019).
4. The current procedure might underestimate residual strength of the liquefied soil and thus over predict the soil displacement (which is subject to significant uncertainty). As such, correlations using SPT or preferably CPT need to be more carefully examined (Ebeido 2019).
5. Residual strength of liquefied soil modeled by soft clay *p-y* curves might not provide an adequate tool for lateral pile-load analysis. A different set of *p-y* curves might be a better representation particularly depicting the gradual loss of soil strength with cyclic loading (such as the one proposed in Figure 8-8b).
6. Use of site-specific earthquake motions in conducting sliding block displacement analysis might be helpful. Conversely, an empirical relationship, dependent on peak velocity and peak acceleration, instead of Newmark's sliding block analysis that is only PGA dependent, might

be of value to consider (e.g., Martin and Qiu 1994, NCHRP 2008).

7. For Slope Stability analysis, it is recommended to use Spencer's Method (NCHRP 2008).

8.5 References

Almutairi, A., Lu, J., Elgamal, A. and Mackie, K. (2019). MSBridge: OpenSees Pushover and Earthquake Analysis of Multi-Span Bridges – User Manual, Report No. SSRP-16-05, Department of Structural Engineering, University of California, San Diego, La Jolla, CA.

Ashford, S.A., Boulanger, R.W., Brandenberg, S.J., Shantz, T.: Overview of recommended analysis procedures for pile foundations in laterally spreading ground. In: TCLEE 2009: Lifeline Earthquake Engineering in a Multihazard Environment, pp. 1–8 (2009).

Ashford, S.A., Boulanger, R.W., Brandenberg, S.J.: Recommended design practice for pile foundations in laterally spreading ground. Pacific Earthquake Engineering Research Center. University of California, Berkeley, Calif. PEER Rep, (2011/04) (2011).

Bray, J., and Ledezma, C. (2007). Evaluating seismic displacements and damage for pile foundations undergoing liquefaction-induced lateral spreading. In Proceedings, 4th International Conference on Earthquake Geotechnical Engineering, paper No. 1460.

Bray, J. D., & Travasarou, T. (2007). Simplified procedure for estimating earthquake-induced deviatoric slope displacements. Journal of geotechnical and geoenvironmental engineering, 133(4), 381-392.

Cubrinovski, M., Winkley, A., Haskell, J., Robinson, K., & Wotherspoon, L. (2014a). Effects of lateral spreading on bridges in the 2010–2011 Christchurch earthquakes. Soil Liquefaction during Recent Large-Scale Earthquakes, Orense, Towhata & Chouw (Eds.), Taylor and Francis Group, London, ISNN, 978-1-138-02643-8. p. 119.

Cubrinovski, M., Haskell, J., Winkley, A., Robinson, K., & Wotherspoon, L. (2014b). Performance of bridges in liquefied deposits during the 2010–2011 Christchurch, New Zealand, earthquakes. Journal of Performance of Constructed Facilities, 28(1), 24-39.

Cubrinovski, M., Winkley, A., Haskell, J., Palermo, A., Wotherspoon, L., Robinson, K., ... & Hughes, M. (2014c). Spreading-induced damage to short-span bridges in Christchurch, New Zealand. Earthquake Spectra, 30(1), 57-83.

Ebeido, A. A. (2019). Lateral-Spreading Effects on Pile Foundations: Large-scale Testing and Analysis, PhD Thesis, Department of Structural Engineering, University of California, San Diego, La Jolla, CA.

Ebeido, A., & Elgamal, A. (2019). Assessment of seismic behavior of deep foundations from large‐scale liquefaction shake table experiments. In Earthquake Geotechnical Engineering for Protection and Development of Environment and Constructions (pp. 353-368). CRC Press.

Ebeido, A. (2019). Lateral-Spreading Effects on Pile Foundations: Large-scale Testing and Analysis. PhD Thesis. Department of Structural Engineering, University of California San Diego, La Jolla, CA.

Ebeido, A. & Elgamal, A. (2019). Assessment of seismic behavior of deep foundations from large‐scale liquefaction shake table experiments. In Earthquake Geotechnical Engineering for Protection and Development of Environment and Constructions (pp. 353-368). CRC Press.

Ebeido, A., Elgamal, A., Tokimatsu, K., & Abe, A. (2019). Pile and pile-group response to liquefaction-induced lateral spreading in four large-scale shake-table experiments. Journal of Geotechnical and Geoenvironmental Engineering, 145(10), 04019080.

Elgamal, A., & Qiu, Z. (2022). "Seismically Induced Ground Deformation and Reduction of Impact on Bridge Systems." In Geo-Congress 2022, ASCE (pp. 291-299).

Haskell, J. J. M., Madabhushi, S. P. G., Cubrinovski, M., & Winkley, A. (2013). Lateral spreading-induced abutment rotation in the 2011 Christchurch earthquake: Observations and analysis. Géotechnique, 63(15), 1310-1327.

Idriss, I.M., and Boulanger R.W. (2008). Soil Liquefaction during Earthquakes, EERI Monograph, 2nd Edition.

Ishihara, K., & Cubrinovski, M. (2020). Soil-pile interaction in liquefied deposits undergoing lateral spreading. In Geotechnical hazards (pp. 51-64). CRC Press.

Ledezma, C. A., & Bray, J. D. (2008). Performance-Based Earthquake Engineering Design Evaluation Procedure for Bridge Foundations Undergoing Liquefaction-Induced Lateral Ground Displacement, PEER Report 2008-05. Pacific Earthquake Engineering Research Center, University of California, Berkeley, CA.

Little, M., & Rathje, E. (2021). Key trends regarding the effects of site geometry on lateral spreading displacements. Journal of Geotechnical and Geoenvironmental Engineering, 147(12), 04021142. https://ascelibrary.org/doi/full/10.1061/%28ASCE%29GT.1943-5606.0002690

Martin, G. R., & Qiu, P. (1994). A comparative study of predictive methods for liquefaction induced embankment displacements. In Proceedings from the fifth US-Japan workshop on earthquake resistant design of lifeline facilities and countermeasures against soil liquefaction, T.D. O'Rourke and M. Hamada, Eds., NCEER-94-0026 (pp. 233-47).

Matlock, H. (1970). Correlations of Design of Laterally loaded Piles in Soft Clay, Proc. Offshore Tech. Conference, Houston Texas, 1(1204):577-594.

MTD 20-15 (2017): https://dot.ca.gov/-/media/dot-media/programs/engineering/documents/memotodesigner/20-15-a11y.pdf

NCHRP (2008). Report 611, "Seismic Analysis and Design of Retaining Walls,, Buried Structures, Slopes, and Embankments", Transportation Research Board of the national Academies.

Qiu, Z., Ebeido, A., Almutairi, A., Lu, J., Elgamal, A., Shing, P. B., & Martin, G. (2020). Aspects of bridge‐ground seismic response and liquefaction‐induced deformations. Earthquake Engineering & Structural Dynamics, 49(4), 375-393.

Qiu, Z., Lu, J., Ebeido, A., Elgamal, A., Uang, C. M., Alameddine, F., & Martin, G. (2022). Bridge in narrow waterway: seismic response and liquefaction-induced deformations. Journal of Geotechnical and Geoenvironmental Engineering, 148(8), 04022064.

Qiu, Z. & Elgamal, A. (2022). Distribution of Deformations and Strains within a Slope Supported on a Liquefiable Stratum. In Conference on Performance-based Design in Earthquake. Geotechnical Engineering. Cham: Springer International Publishing. (pp. 1340-1347).

https://link.springer.com/chapter/10.1007/978-3-031-11898-2_115

Robinson, K., Cubrinovski, M., & Bradley, B. A. (2014). Lateral spreading displacements from the 2010 Darfield and 2011 Christchurch earthquakes. International Journal of Geotechnical Engineering, 8(4), 441-448.

Turner, B. J., Brandenberg, S. J., & Stewart, J. P. (2016). Case study of parallel bridges affected by liquefaction and lateral spreading. Journal of Geotechnical and Geoenvironmental Engineering, 142(7), 05016001.

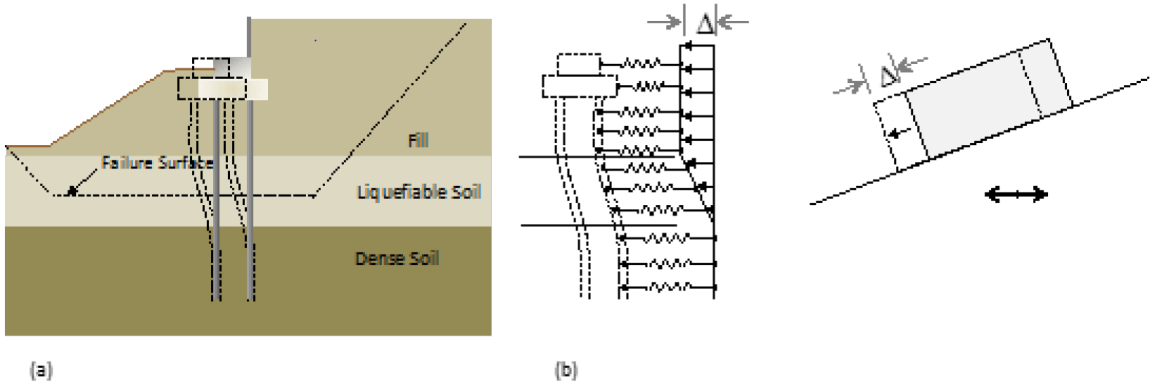

Figure 1 (a) Single bent idealization of the lateral spread-foundation interaction problem. (b) The analytical model relies on a soil displacement profile imposed on a Winkler spring foundation model. The displacement profile is estimated by a sliding block procedure that uses the yield coefficient determined from a slope stability analysis.

Figure 8-1. Schematic of the MTD 20-15 (2017) simplified analysis procedure framework

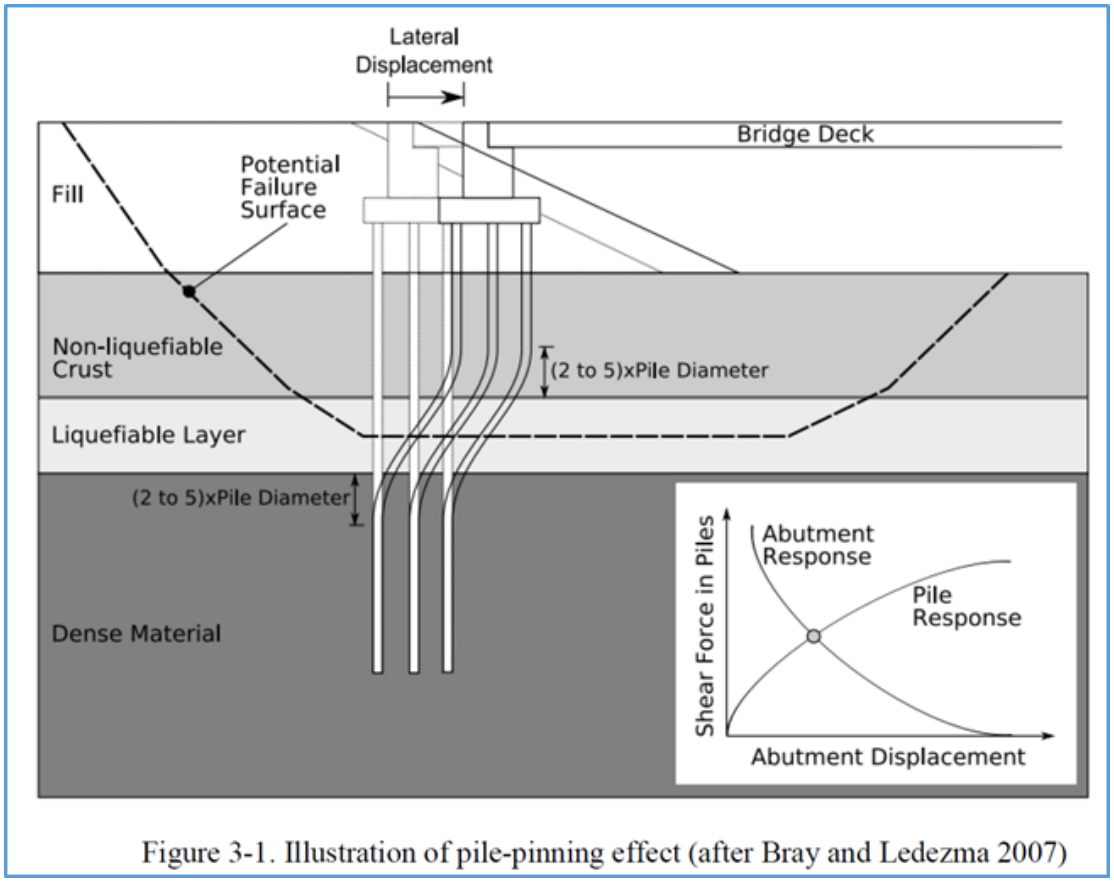

Figure 8-2. Illustration of Pile-pinning effect (Bray and Ledezma 2007).

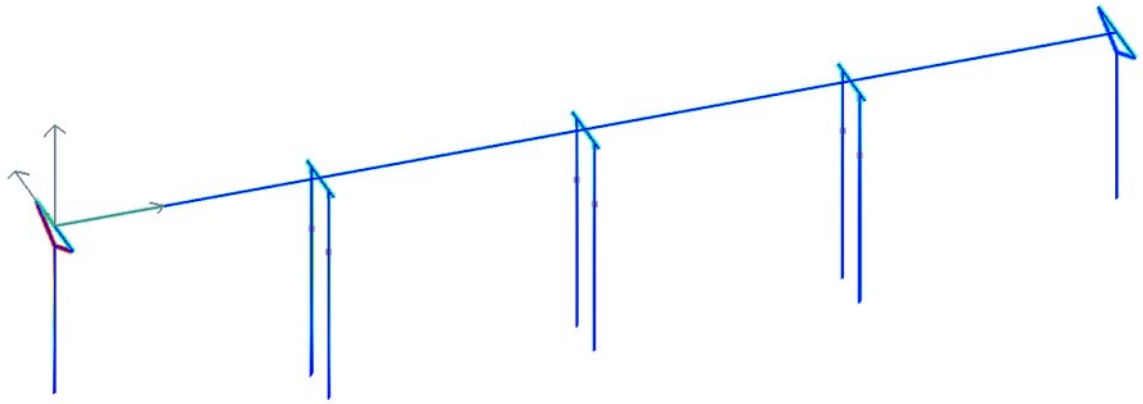

Figure 8-3. OpenSees Bridge Model generated via MSBridge (http://www.soilquake.net/msbridge/)

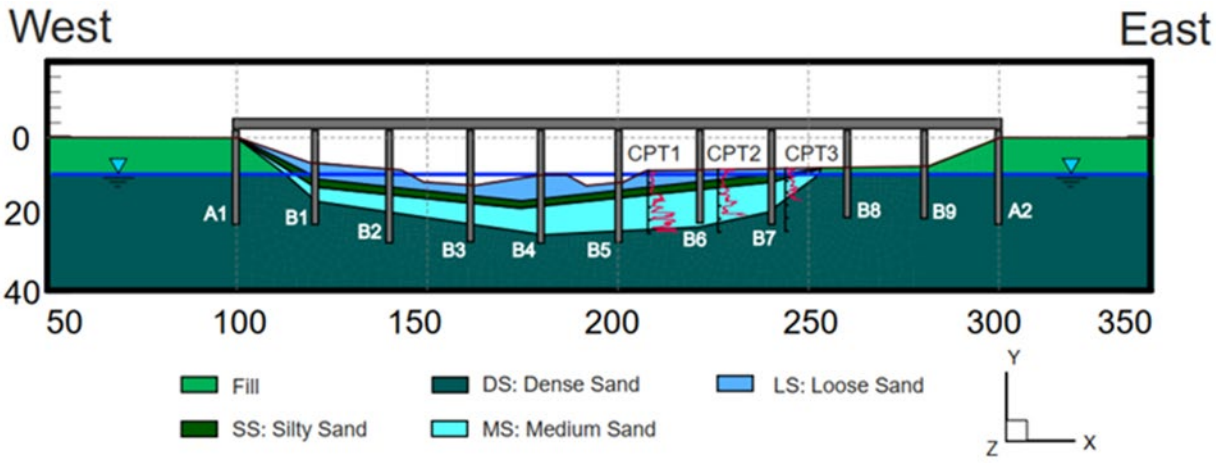

Figure 8-4. Schematic of Waterway topography and soil profile (liquefiable soils: LS and MS)

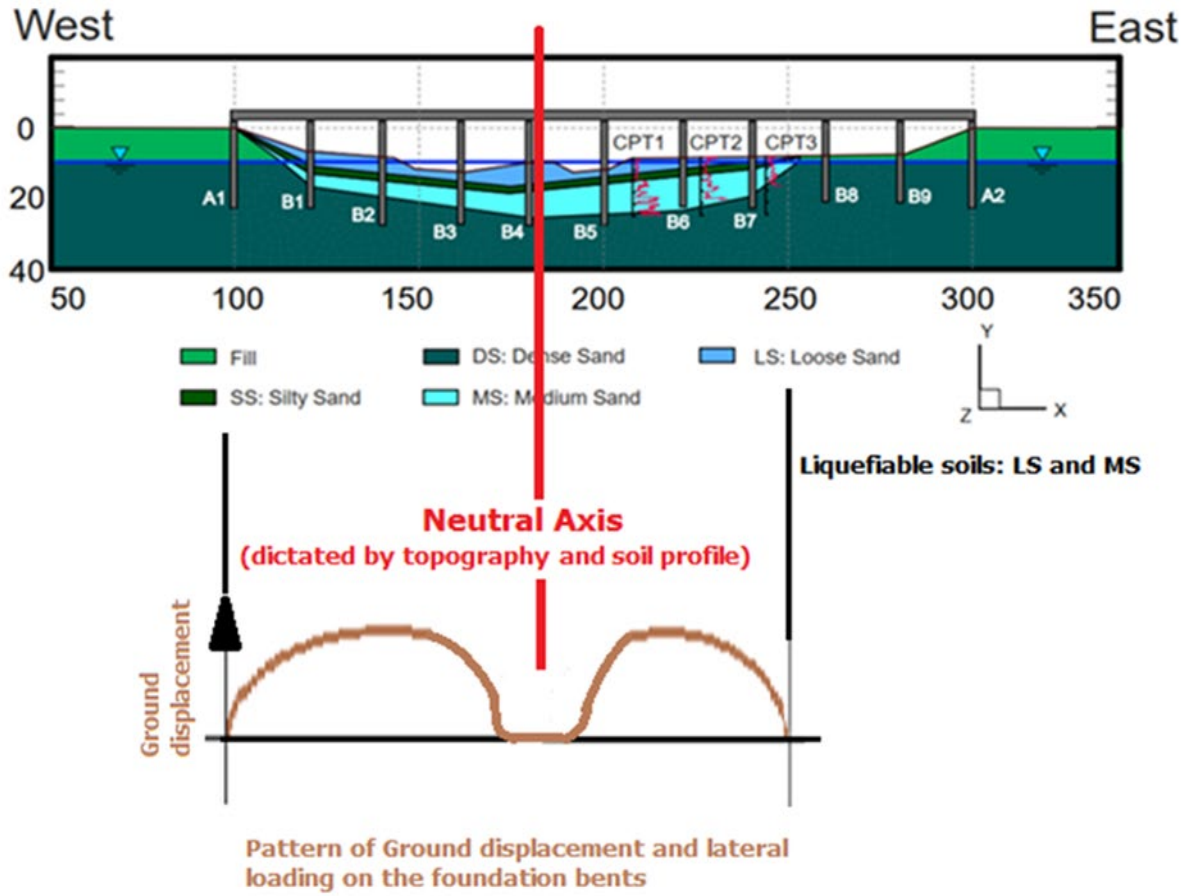

Figure 8-5. Schematic soil profile and distribution of lateral loads for a scenario of non-uniform soil profile and/or asymmetric waterway geometry.

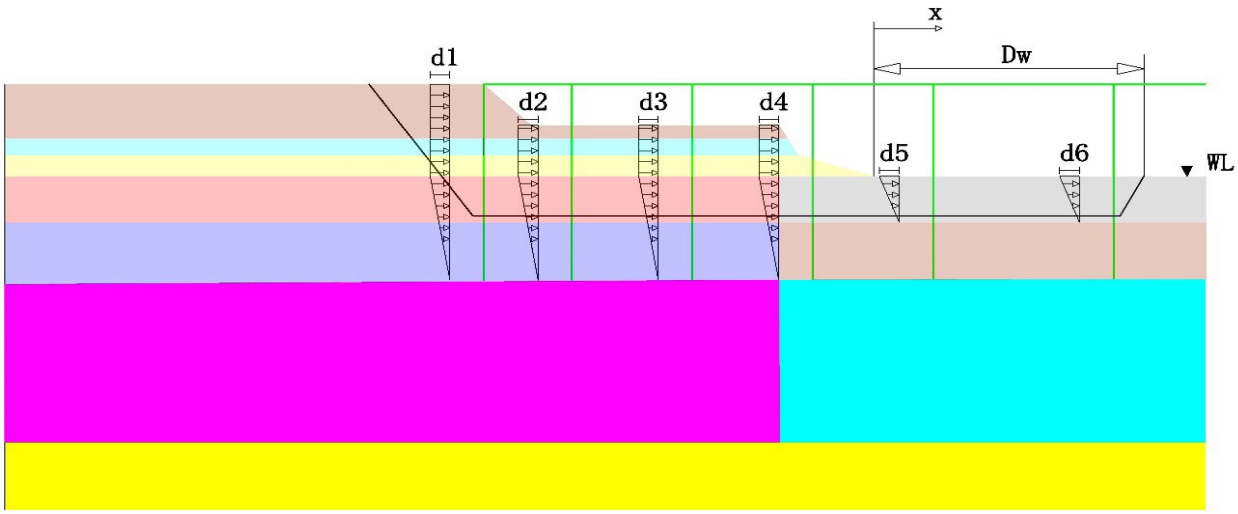

Figure 8-6.Schematic of soil lateral displacement profile for global bridge analysis

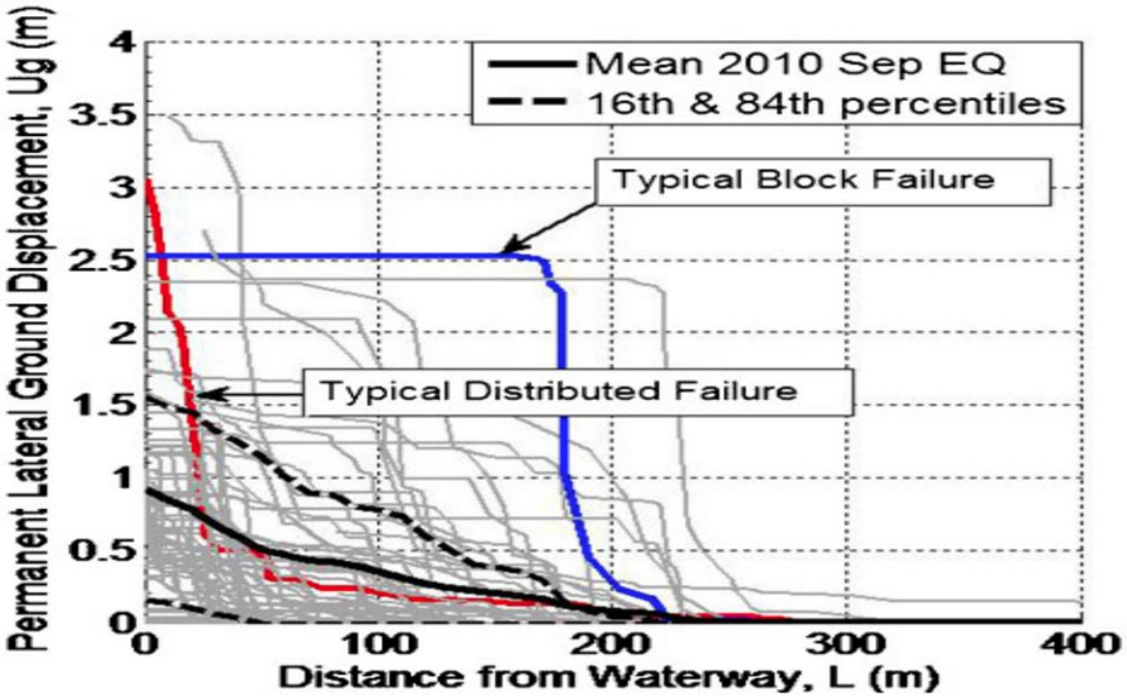

Figure 8-7. Lateral Spreading Reconnaissance results (after Cubrinovski *et al*. 2014a)

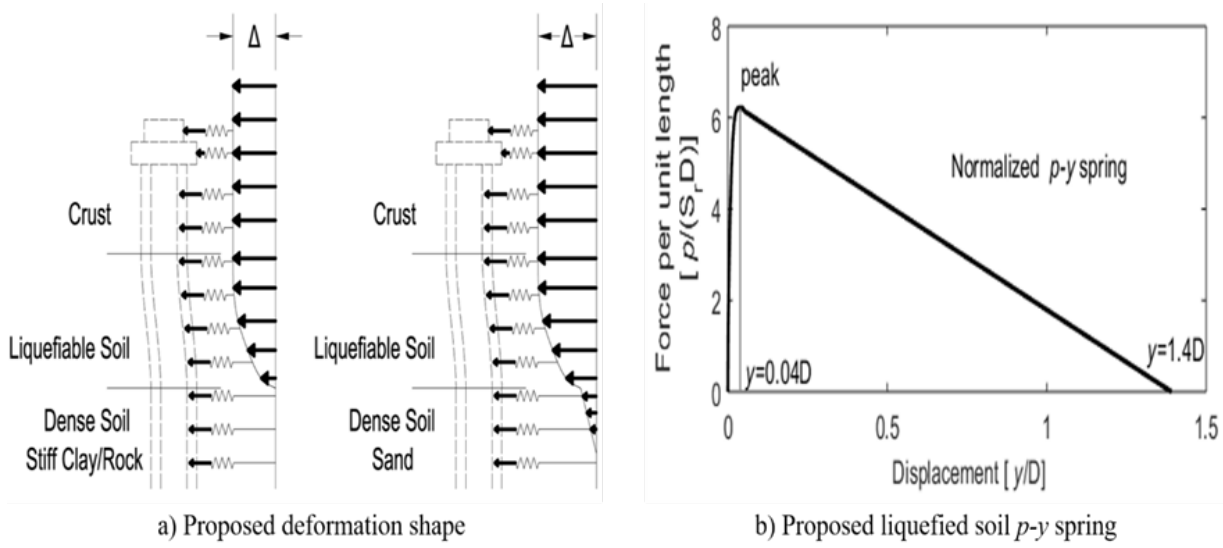

a) Proposed deformation shape

b) Proposed liquefied soil *p-y* spring

Figure 8-8. (a) Proposed soil-imposed lateral displacement profiles for different cases (Ebeido 2019), and (b) Proposed liquefied soil *p-y* curve (Ebeido 2019)

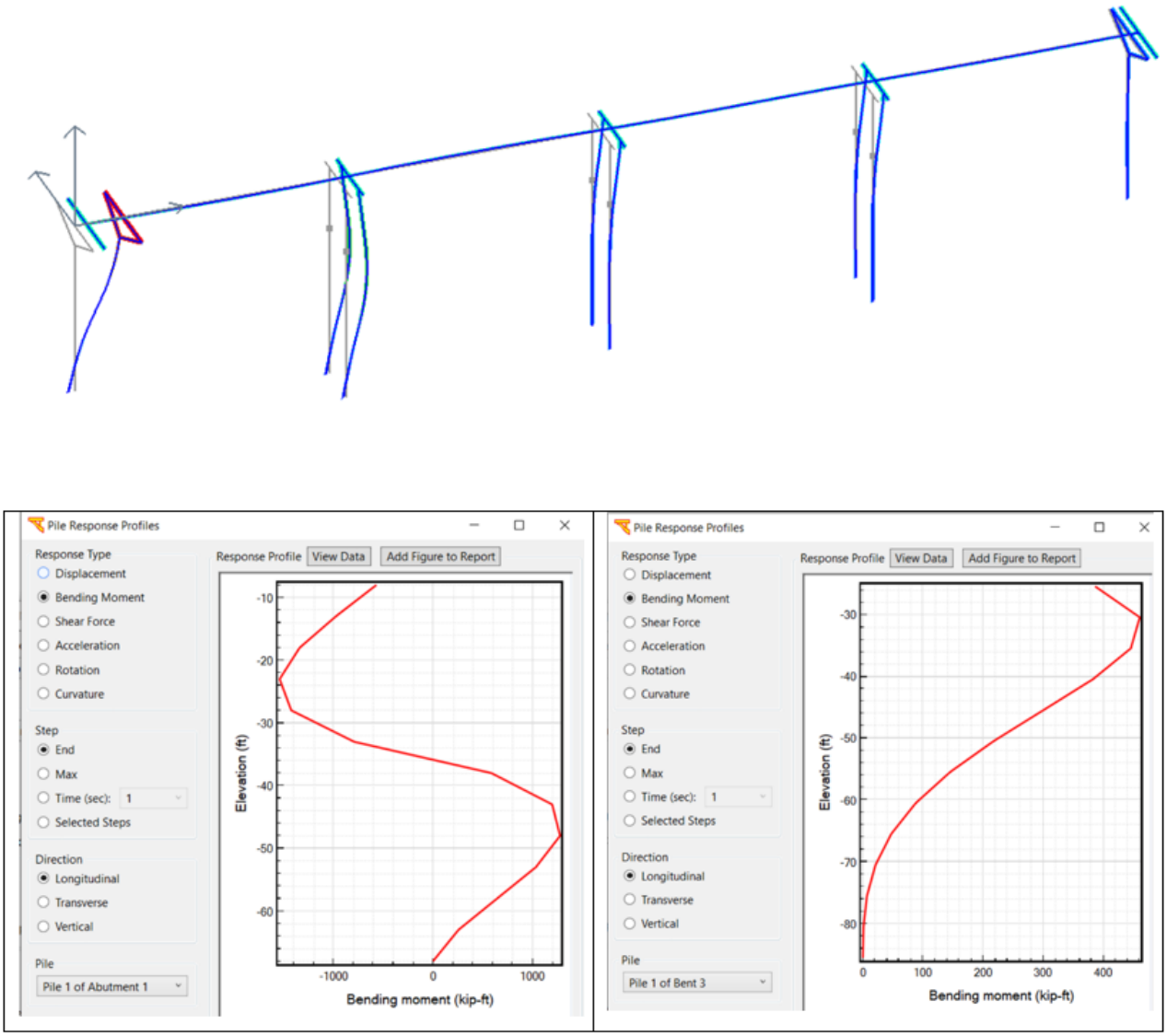

Figure 8-9. MSBridge (Almutairi *et al.* 2019) bridge global model representative response.

APPENDIX I

CALIFORNIA DEPARTMENT OF TRANSPORTATION

Engineering Assessment Report

ANALYSIS OF LATERAL SPREADING EFFECTS ON BRIDGE FOUNDATIONS

Report B: Mitigation of Liquefaction-Induced Lateral Spreading Effects on Bridge Piles using Tire Derived Aggregate

September 2024

Prepared by
Axel Arnold Yarahuaman Chamorro, M.S.
Sara Walston, B.S.
Jason Melara, B.S.
Xiao Tan, M.S.
Ahmed Elgamal, Ph.D.
John S. McCartney, Ph.D., P.E.

University of California San Diego (UCSD)
Department of Structural Engineering

Caltrans Agreement No. 65A0548

TABLE OF CONTENTS

EXECUTIVE SUMMARY

This research is directed towards developing a new approach for mitigating the effects of liquefaction induced lateral spreading on bridge foundation systems. Specifically, this study focuses on evaluating the feasibility of using a layer of tire derived aggregate (TDA) placed upslope from a bridge foundation system to absorb downslope lateral spreading deformations with the goal of reducing stresses imposed on piles to prevent their yielding. TDA is a lightweight recycled material that has high compressibility that may be suitable for accommodating and redistributing deformations and stresses from the lateral spreading event on the bridge foundation system. This research is experimental in nature and involves a series of four quasi-static lateral compression tests to simulate the effects of lateral spreading on the deformation response of steel and concrete piles within a layer of TDA. Horizontal displacements were applied to the TDA layer to simulate the effects of lateral spreading, and the deformation response of the pile was monitored. The results from this research demonstrate that the layer of TDA installed next to a fixed-base pile will absorb significant horizontal displacements at the pile head location up to nearly 2 pile diameters for the steel pile and the concrete pile without causing yielding, with shear forces induced in the pile being only up to 25% of the applied forces. In addition to presenting information on the pile deformation response for different widths of the compressible TDA layer, *P-y* curves for the steel and concrete piles in TDA were defined so that the results from this study could be extended to field design cases for piles with different geometries and end boundary conditions. Insights are provided on selection of the TDA layer thickness that should be used to mitigate the effects of lateral spreading in the field. Overall, this research demonstrates the feasibility of installing a layer of TDA upslope from a bridge foundation system to mitigate the effects of lateral spreading and provides data that can be used in the future for performance-based earthquake response analyses of bridge foundations in liquefiable soil deposits.

CHAPTER 1 INTRODUCTION

Liquefaction-induced lateral spreading during earthquakes is a major damage mechanism for piles supporting bridges. Down-slope movements of a non-liquefiable crust overlying a liquefiable soil layer may induce significant lateral stresses on piles as shown in Figure 1.1(a), which may cause yielding of the pile in a location that may be difficult to repair or cause damage at the pile's connection to the bridge superstructure. Although the underlying liquefied soil deposit is expected to move downslope as well as the overlying non-liquefiable crust, the stresses imposed by the non-liquefiable crust at the head of the pile are expected to have a greater effect on the pile response due to the position of this layer near the head of the pile and because the non-liquefied crust cannot flow as easily around the pile as the liquefied soil. This study investigates a new technique for mitigating the effects of liquefaction-induced lateral spreading on bridge piles. This technique does not attempt to restrain the down-slope movement of the non-liquefiable crust atop the liquefiable soil layer, but instead aims to create a flexible, compressible buffer between the piles and the non-liquefiable crust as shown in Figure 1.1(b). The compressible buffer may extend only through the non-liquefiable crust as shown in this figure or can be installed to the base of the liquefied soil layer. In the latter option the compressible layer may also provide drainage.

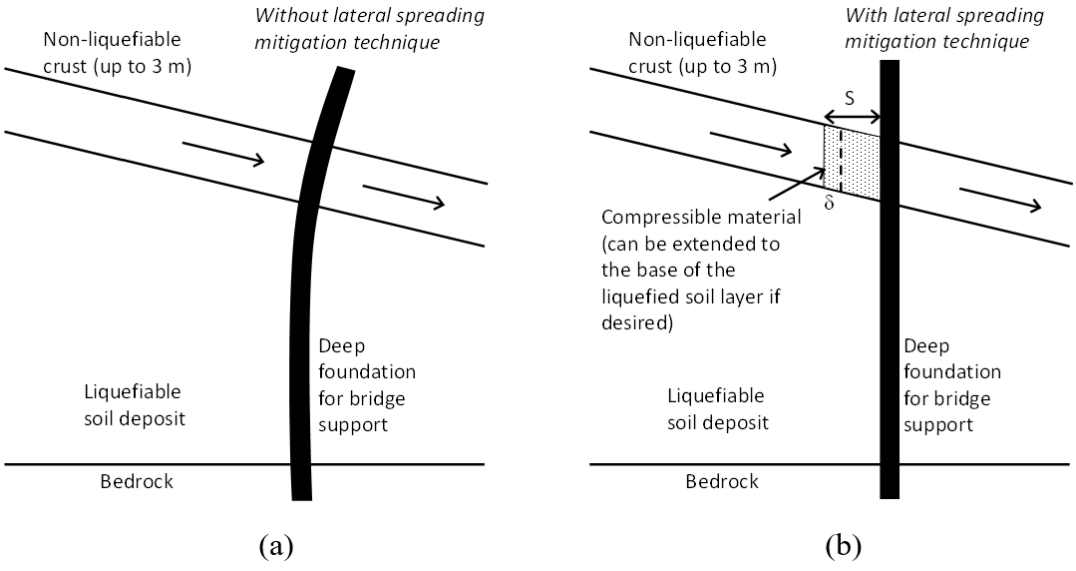

Figure 1.1: Lateral spreading effects on bridge piles and possible mitigation approach: (a) No mitigation; (b) With TDA compressible layer.

Although many flexible materials are available in engineering practice, this study investigates the placement of a layer of tire-derived aggregate (TDA) within a trench upslope from

the piles. In addition to being a low-cost, abundantly available, recycled material, TDA is lightweight and is nearly 7 times more compressible than granular soils (Yarahuaman and McCartney 2023). TDA has a comparable shear strength to soil backfills (Ghaaowd et al. 2017) but has a lower shear modulus and higher damping ratio (McCartney et al. 2017). TDA has been shown to have high energy dissipation during earthquake loading of footings (Yarahuaman and McCartney 2024). Acceleration amplification of the softer TDA during earthquake shaking is a topic that needs to be further studied in the future, but the thin compressible buffer installed within a trench proposed in Figure 1.1(b) is not expected to have a major effect on the seismic response of the overlying bridge especially as the bridge will not rest on the TDA. The approach in Figure 1.1(b) could be used in new bridge construction or as a retrofit option for existing bridges.

The costs of installing and placing the TDA are expected to be lower than the costs of a conventional structural solution near the ground surface (which may not be able to mitigate the effects of lateral spreading), and the TDA will be protected below the ground without the need for maintenance. TDA layers are typically wrapped with a nonwoven geotextile that serves to separate the TDA from the surrounding soils and acts as a filtration layer when the TDA is employed below the water table. Although TDA is most often used as a lightweight fill in applications above the water table, it can also be installed below the water table as its specific gravity is 1.15 with minimal environmental effects. Cheng et al. (2021) summarized the results from Toxicity Characterization Leaching Procedure (TCLP) experiments on TDA in different fluids. The TCLP tests measured the levels of heavy metals, key volatile organic compounds and semi-volatile organic compounds of concern in groundwater pollution. Negligible concentrations of these contaminants were recorded in the leachate for neutral pH groundwater. Higher aqueous concentrations of metals formed when leaching in acidic conditions while higher aqueous concentrations of organics formed when leaching in basic conditions. Even then, the metal and organic component concentrations were well below standards set by the USEPA. TDA is highly permeable so it may also provide a drainage pathway for dissipation of excess pore water pressures from the liquefied soil layer in the case that the compressible layer is extended to the bottom of the liquefied layer.

This report presents results from a testing program formulated to provide information necessary for the design of this new lateral spreading mitigation technique, including the deformation response of the TDA layer, the bending response of steel and concrete piles surrounded by TDA, and *P-y* curves necessary for lateral loading analysis of piles in TDA. The

testing program was performed in a large container at UC San Diego that contains a 3 m-thick layer of TDA and fixed-base piles, shown schematically in Figures 1.2(a) and 1.2(b). Quasi-static tests were performed where a hydraulic actuator was used to apply horizontal forces on a movable vertical wall to compress the TDA and evaluate impacts on the pile bending response.

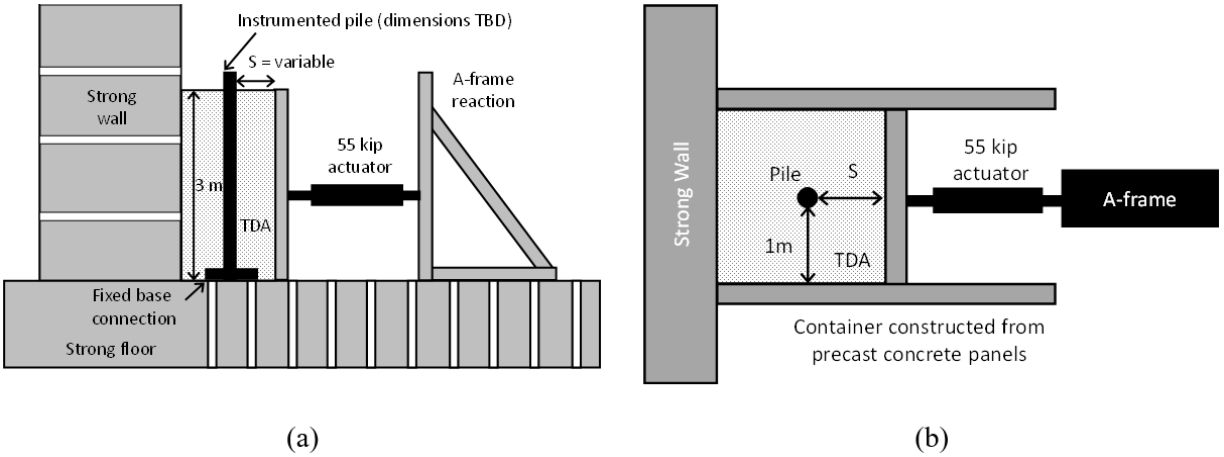

Figure 1.2: General schematic of the testing concept: (a): Elevation view; (b) Plan view.

The piles evaluated in this study have a fixed bottom boundary condition for simplicity and were instrumented with strain gages along their lengths and displacement sensors at the heads. For the steel pile, three tests were performed with different values of the TDA width *S* from Figure 1.1(b) to evaluate the impacts of the TDA layer geometry on the pile, while a single TDA width *S* was used for the concrete pile. The tests performed in this study demonstrate the feasibility of using TDA as a compressible material to mitigate the effects of lateral spreading and provide useful data that can be used to validate numerical models for lateral spreading analyses. This study is the first to provide information on *P-y* spring relationships that can be used in lateral loading analyses on piles surrounded by TDA. The liquefaction mitigation strategy with TDA can be applied for both existing bridges as part of seismic retrofits as well as for new bridges.

This report is comprised of 6 chapters following this introduction. Chapter 2 provides a discussion on the background related to this topic, including a discussion on lateral spreading and associated effects of bridges, details on the properties of TDA, and past studies on the development of *P-y* curves for lateral loading analysis. Chapter 3 describes the TDA materials used in this study. Chapter 4 presents the details of the testing program, and the details of the pile foundations tested. Chapter 5 presents the key results from the testing program including key load-deformation measurements. Chapter 6 presents an analysis of the data in the testing program including the pile

bending response and the *P-y* curves. Chapter 7 provides the conclusions drawn from this study and a summary of future opportunities enabled by this research.

Chapter 2 LITERATURE REVIEW

Effects of lateral spreading on bridge foundations

Liquefaction and related damage to large bridges have been observed in past earthquakes (Seed et al. 1990Youd 1993; Hamada et al. 1996; Tokimatsu and Asaka 1998; Berrill et al. 2001; Aygün et al. 2010) as well as in recent earthquakes including the 2010 Maule earthquake (Arduino et al. 2010; Ledezma and Bray 2010; Ledezma et al. 2012; Verdugo et al. 2012), the 2011 Christchurch earthquake (Cubrinovski et al. 2011, 2014; Wotherspoon et al. 2011), and the El Mayor-Cucapah events (Turner et al. 2013, 2016). In these earthquakes, the observed responses of bridges were influenced by the global bridge-ground characteristics as an integral system. Accordingly, several studies have advocated considering the entire bridge and the surrounding ground response within an integrated framework (Boulanger et al. 2007; Shin et al. 2008; Zhang et al. 2008; Ashford et al. 2009, 2011). Results of these studies show that consideration of the entire bridge-ground system provides a more realistic distribution of force and displacement demands and indicated that global analysis is needed in realistically evaluating the performance of liquefaction-induced lateral spreading and its consequences. McGann and Arduino (2014) conducted quasi static analysis of the Mataquito River Bridge abutment and foundation system subjected to liquefaction-induced lateral spreading, and McGann and Arduino (2015) and McGann (2020) conducted parametric studies to investigate the influence of 3D site geometry on seismic response of the bridge piles and abutments. Recently, Qiu et al. (2020) and Qiu et al. (2023) developed a three-dimensional (3D) finite element (FE) bridge-ground model to capture salient characteristics of the involved response mechanisms for a realistic bridge geometric layout and ground stratification profile. These numerical tools provide a useful way to predict the amount of lateral spreading that can be expected for a given ground stratification profile under a given earthquake shaking event.

With the results from 3D FE analyses, designs can be developed to help mitigate the effects of liquefaction-induced lateral spreading. In particular, *P-y* lateral loading analyses can be used to estimate the stress-strain response of the pile during lateral loading in different ground conditions. Development of *P-y* curves is challenging and is material-specific, but one advantage of this approach is that TDA is relatively uniform in nature so *P-y* curves developed between piles and TDA can be applied to different projects that use this approach. Kim et al. (2004), Guo et al.

(2014), Choo and Kim (2016) and Khati et al. (2020) developed *P-y* curves based on lateral loading of piles in soils. This study is different from these previous studies as the lateral loads are induced on the pile through down-slope movement of the ground. Nonetheless, these studies provide useful information on the development of *P-y* curves that will be adopted in this study.

Use of TDA in civil engineering applications

There is an urgent need for sustainable reuse options for waste tires due to the large number of tires being generated by society and the lack of environmentally friendly disposal options. USTMA (2020) reported that 263 million passenger tire equivalents were generated in 2019, while CalRecycle (2020) reported that 51.8 million were generated in California in 2019. The number of waste tires generated each year in the U*S* has increased steadily by approximately 18% over the past decade (USTMA 2020). Historically, these waste tires would be sent to stockpiles as they are not accepted by most landfills. However, stockpiles are not a sustainable disposal approach due to risks associated with tire fires and creating a breeding ground for disease spreading insects and rodents. Tires are combustible and can be used as fuel source when mixed with coal. Approximately 14% of the tires discarded in California in 2019 were burned at permitted facilities in the state as an alternate fuel source and an additional 22% was exported out of state to be used as fuel (CalRecycle 2020). However, this is not an environmentally friendly fuel source as burning tires release toxic air pollutants including acetaldehyde, benzene, dioxins, formaldehyde, furans, hexavalent chromium, several heavy metals, and PAHs (Cheng et al. 2021). Because of the concerns with stockpiling and burning waste tires, California has the goal of recycling and reusing 75% of waste tires (CalRecycle 2017).

An effective and environmentally friendly approach for reducing tire stockpiles and reusing waste tires has been the incorporation of waste tires as an alternative backfill material in civil engineering applications (Geisler et al. 1989; Ahmed and Lovell 1993; Bosscher et al. 1993; Bosscher et al. 1997; Hoppe 1998; Dickson et al. 2001; Tandon et al. 2007; Finney and Maeda 2016; Mahgoub and El Naggar 2019) and retaining walls (Humphrey et al. 1992, 1993, 1998; Humphrey 2008; Tweedie et al. 1998a, 1998b; Xiao et al. 2012). Specific civil engineering applications include use as a lightweight embankment fill, in landslide repair/slope stabilization, as insulation layers for landfill clay liners, as alternative drainage layers in landfills, as a retaining wall backfill, as stress reduction backfill over pipes, as storm water infiltration gallery media, and

as vibration mitigation layers for foundations and railroads. Through the reuse of waste tires in civil engineering applications, the quantity of stockpiled waste tires has reduced from approximately 800 million in the mid-1990's to 200 million today (Cheng et al. 2021). Approximately 5.1% of waste tires were reused in civil engineering applications in the U*S* (USTMA 2020), while 3.0% were reused in civil engineering applications in California (CalRecycle 2020). Based on data from CalRecycle (2019), the amount of waste tires reused in civil engineering applications in California increased by 2% from 2018 to 2019, which indicates that this reuse option is growing in popularity.

Waste tires have been used in civil engineering applications in the form of shreds, bales, and strips. An advantage of reusing waste tires in civil engineering applications is that both older tires from stockpiles and freshly recycled tires are suitable. In many civil engineering applications tire shreds are mixed with soils, but the cost associated with mixing and the reduction in the volume of tires reused affects the economic practicality of this approach. Accordingly, the most common form of waste tires reused in civil engineering applications is as a monolithic layer of shredded tires. In this case the shredded tires are referred to as tire-derived aggregate (TDA) to emphasize that they are similar to a granular aggregate. Due to the growing popularity of reusing waste tires in the form of TDA, ASTM D6270-20 was initially developed in 1998 to provide guidance on the classification of TDA and how it should be used in different civil engineering applications. This standard has been updated on a regular basis with new information on TDA performance. The cost of TDA is associated with the shredding process and the transport of the TDA from the recycling facility to the project and is significantly lower than other backfill materials (Wright 2015).

The use of TDA as backfill in civil engineering applications not only helps reduce stockpiles and reuse waste tires, TDA also has favorable engineering properties. For example, the total unit weight of TDA is 5 to 9 kN/m^3 (32 to 57 pcf), which is about one-third to one-half that of most granular backfill soils. Despite this low total unit weight that is less than that of water (9.8 kN/m^3 or 62.4 pcf), tire shreds are heavier than water (specific gravity of approximately 1.15) and will not float when submerged. The low total unit weight of TDA makes it favorable for use as a fill above deformable subgrade soil or on soils with global stability issues. In addition to the lower unit weight, TDA has shear strengths that are comparable to soils (Ghaaowd et al. 2017), a hydraulic conductivity of 0.01 m/s (on the same order of magnitude to gravel), a thermal conductivity of approximately 0.17 W/mK, which is approximately 8 times smaller than most

soils, and a high damping ratio that provide TDA with favorable vibration properties (McCartney et al. 2017). Differences between TDA and granular backfills are that TDA may deform more than soils upon external loading, and that the displacement at peak shear strength is greater than in dense backfill soils. These differences in deformation response require careful consideration in the construction of civil engineering infrastructure to accommodate the more flexible response of TDA to external loading. In this particular study, the flexible response of TDA is an asset that can be used to mitigate the effects of lateral spreading on piles.

The creation of TDA from waste tires requires specialized cutting equipment to minimize the amount of exposed steel in the tire particles. Exposed steel may corrode (or oxidize) which may result in exothermic reactions (Finney 2018). The sources of steel in tires are derived from the bead wire used to reinforce the tire/rim connection and cord wire embedded in the driving surface of the tire, both of which imply that iron will be present in all types of TDA. Humphrey (1996) studied the occurrence of exothermic reactions in TDA used as backfill for two road embankments in Washington and in a gravity-type retaining wall in Colorado. The fills evaluated had heights up to 60 m, free access to both air and water, and did not have careful quality control on the amount of exposed steel. While Humphrey (1996) noted that self-heating may occur due to oxidation of both the exposed steel and wires as well as microbial activity, Finney (2018) summarized several following studies that concluded that oxidation of the steel was the primary source of exothermic reactions. The rate of exothermic reactions due to steel oxidation increases with the presence of water as well as the cation or salt concentration in the water. To address the risks of exothermic reactions, ASTM D6270-20 provides guidance on the different categories of TDA suitable for use in civil engineering applications, as well as limitations on TDA fill heights and encapsulation requirements to minimize risks of exothermic reactions. Two categories of TDA are permitted in ASTM D6270 and are defined based on their particle size distributions: Type A TDA, with particle sizes ranging from 75 to 100 mm, and Type B TDA, with particle sizes ranging from 150 to 300 mm (ASTM D6270). Both types of TDA have limits on the amount of sidewall tire pieces and the quantity of particles having different lengths of exposed steel wire. However, Type B TDA requires less processing than Type A TDA and is therefore more cost effective for earth fill applications. Type B TDA also has less exposed steel due to the larger particle sizes. ASTM D6270 20 limits the height of fills constructed using Type B TDA to 3 m (approximately 10 ft), while it limits the height of fills constructed using Type A TDA to 1 m (3 ft). Further, ASTM

D6270 20 requires that monolithic layers of TDA be encapsulated with inorganic mineral soil to help dissipate heat and isolate the TDA.

Cheng et al. (2021) reviewed several studies that assessed the environmental impacts of using TDA in civil engineering applications and concluded that it has minimal effects on the environment. They summarized the results from Toxicity Characterization Leaching Procedure (TCLP) experiments on TDA in different types of fluids. The TCLP metals analyzed by the TCLP include arsenic, barium, cadmium, chromium, copper, lead, mercury, selenium, and silver, and key volatile organic compounds and semi-volatile organic compounds that are of concern in groundwater pollution. Cheng et al. (2021) noted that for neutral pH groundwater negligible concentrations of these metals and contaminants were recorded in the leachate. Higher aqueous concentrations of metals formed when leaching in acidic conditions while higher aqueous concentrations of organics formed when leaching in basic conditions. Even then, the metal and organic component concentrations were well below the TCLP standards set by the USEPA. While all laboratory testing performed to date indicates that TDA leachate does not exhibit toxic characteristics, most of the civil engineering applications where TDA is used are above the groundwater table and regular exposure to water is limited.

TDA has been widely used as a backfill in traditional gravity-type, reinforced concrete retaining walls (Tweedie et al. 1998a, 1998b; Humphrey et al. 1998). These include a gravity-type retaining wall constructed on California Route 91 reported by Humphrey et al. (2008). These walls generally had good performance in terms of lateral earth pressures exerted on the retaining wall. Recent civil engineering applications in California have also explored the approach of creating internally reinforced TDA walls that are similar to Mechanically Stabilized Earth (MSE) walls, referred to as Mechanically Stabilized TDA (MSTDA) walls (McCartney 2021). Internally reinforced retaining walls have lower material costs and faster construction times as they do not incorporate significant amounts of reinforced concrete. Like MSE walls, MSTDA walls are fill-type retaining walls that are used when there is a change in grade, lane widening, or for repair of slope instability issues. MSTDA walls have a unique feature over gravity-type reinforced concrete retaining walls in that the weight of the TDA backfill will not induce as large of a stress on the underlying subgrade material. This can be advantageous in areas with subgrade soils having high compressibility or when there is global instability influenced by the weight of the retaining wall.

Chapter 3 MATERIALS

Basic properties of TDA

Type B TDA is recommended for use in civil engineering applications because its larger maximum particle size requires less processing and therefore has lower costs associated with reusing a given number of tires and a lower exposure of steel wires. ASTM D6270 describes the limits on the particle size distribution of Type B TDA, which are shown in Figure 3.1. An example of an actual Type B TDA obtained from a California processing plant and characterized by Ghaaowd et al. (2020) is shown in this figure as well. The particles are flat and irregular with one plan dimension being greater than the other. ASTM D6270-20 notes that the maximum dimension in any direction of a tire shred in Type B TDA is 450 mm (18 inches), and that only 16% by weight can be greater in dimension in any direction than 300 mm (12 inches). There is also a restriction on the smallest particle size, with only 1% smaller than 4.75 mm (0.187 inches). The reasons behind the particle size range are to encourage the use of larger tire shreds in TDA as they are less susceptible to self-heating due to the fewer exposed steel wires, but to still provide a well graded particle size distribution to promote interlocking and easy of spreading the TDA into flat compaction lifts.

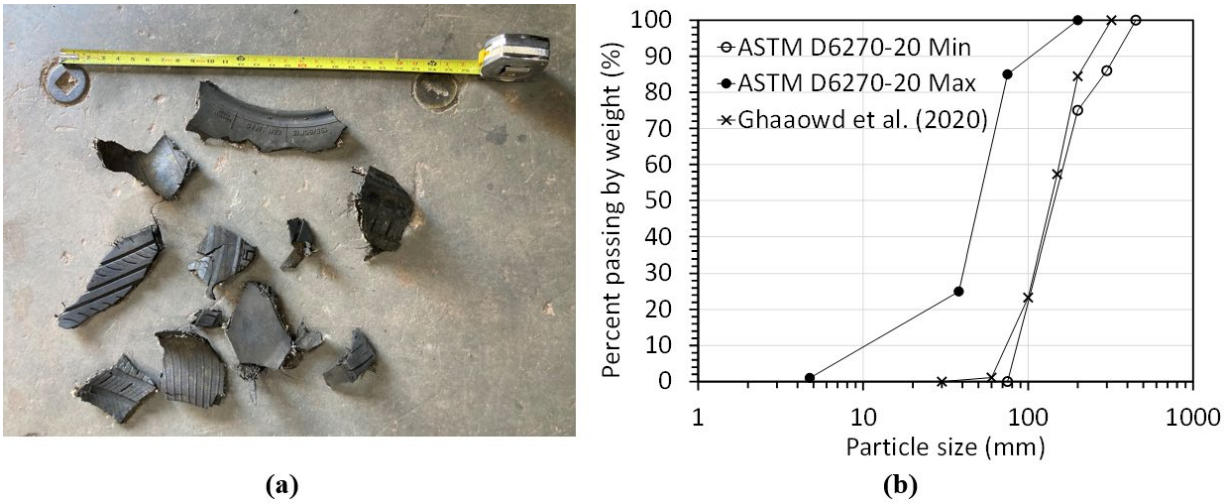

Figure 3.1 Type B TDA particle size characteristics: (a) Example of Type B TDA particle shapes; (b) Particle size distribution.

ASTM D6270-20 also states that the tire shreds should not include pieces that have a tread connected to sidewall pieces on either side (i.e., pieces having a horseshoe shape). These horseshoe-shaped pieces will not lie flat during compaction, so ASTM D6270-20 states that shreds can only have tread pieces connected to a sidewall on one side. Finally, ASTM D6270-20 limits the length of exposed steel in the tire shred pieces to minimize risks of corrosion and self-heating but also for handling purposes, with less than 10% of the shreds having exposed steel wires with lengths of 50 mm (2 inches) and less than 25% of the shreds having exposed steel wires with lengths of 25 mm (1 inch). When determining the particle size distribution of Type B TDA, ASTM

D6270-20 recommends using a similar approach to ASTM C136/C136M but with a larger sample size of Type B TDA ranging from 16 to 23 kg. Due to the relatively flat particles with large planar dimensions, the particle size distribution can also be determined by manual identification and sorting of particles by size as demonstrated by Ghaaowd et al. (2018). The requirements on the particle size distribution, particle shape, and steel wire exposed are typically achieved by a TDA manufacturer by using a shearing device instead of a tearing device and passing larger shreds through the shearing device twice.

In addition to guidance on the particle size distribution and exposed steel, ASTM D6270-20 provides guidance on the condition of the Type B TDA used in backfill applications to minimize risks of self-heating encountered in early TDA embankments. First, the TDA should be free from flammable contaminants like oil or fuel, the TDA should never have been subjected to a fire, and the TDA should be free from fibrous organic materials. There should be no direct contact between TDA and soil containing organic materials like topsoil. Finally, the TDA should be separated from surrounding soils using a geotextile. Finney (2018) noted that there have been no cases of exothermic reactions in TDA fills constructed according to ASTM D6270-20, and that the requirements in the standard may be overconservative. Finney performed experiments on TDA layers with a height up to 6 m and found that negligible self-heating was observed in dry TDA layers. TDA fills with heights of 3 m (10 ft) experienced an increase in temperature 13 °C when wetted with freshwater and 35 °C when wetted with saltwater, both of which are not sufficient to result in combustion. Both woven and nonwoven geotextiles have been used to provide separation, although nonwoven geotextiles have an advantage of providing filtration and lateral drainage capabilities. As mentioned, TDA has high permeability, so water that does enter the TDA layer during extreme events can be drained if the granular backfill in the gabion facing elements does not contain an appreciable fines content (less than 12% fines is recommended).

Another important variable in characterizing the deformation response of TDA is the specific gravity of the particles G_s (defined as the unit weight of the particles divided by the unit weight of water). The specific gravity of crumb rubber ranges from 1.10 to 1.20 (FHWA 1998), although studies on tire shreds have reported values ranging from 1.02 to 1.27 (Bressette 1984; Humphrey et al. 1992; Humphrey and Manion 1992; Ahmed 1993). It would be expected that the specific gravity of tire shreds should be larger than that of crumb rubber due to the presence of steel wire within the shreds. Ghaaowd et al. (2017) estimated the average specific gravity of

Type B TDA pieces having a variety of sizes by placing them within a porous plastic bag, then weighing the bag of TDA in air and after being submerged in water. They reported a specific gravity of 1.15, which is greater than the minimum specific gravity of crumb rubber.

Compaction and compression response of TDA

While TDA is often compacted when used as an alternative backfill material, this study proposes the placement of loose TDA to form a layer with the highest possible compressibility. Nonetheless, it is relevant to discuss the compaction and unit weight of TDA as these variables will have a significant effect on the compression response and strength and stiffness parameters of TDA layers. TDA is typically placed in lifts with a maximum thickness of 300 mm (1 ft). During compaction of TDA, voids will close, and tire shreds will rearrange and align so that their flat dimension is close to horizontal. Humphrey and Manion (1992) characterized the compaction response of Type A TDA with a maximum particle size of 75 mm (3 inches) using impact compaction and were able to reach initial dry unit weights after compaction of 6 to 6.8 kN/m^3 (38 to 43 pcf). They also found that the water content of the TDA has negligible effect on the unit weight achieved through compaction, and that when using impact compaction varying the compaction effort (number of blows or weight of the hammer) does not necessarily lead to a significant increase in unit weight. Despite the lack of trend in unit weight with compaction effort observed by Humphrey and Manion (1992), anecdotal evidence from contractors indicates that heavier compactors, use of vibration, and the lateral restraint conditions may lead to greater initial unit weights of TDA in the field. In the application evaluated in this research, the TDA is expected to be placed in loose conditions by dumping straight from a delivery truck.

Humphrey (1998) noted that TDA in the field may contain some water due to environmental interactions and recommended that if the amount of water is not measured, that a gravimetric water content of w=4% be assumed. The total unit weight γ_t is related to the gravimetric water content and dry unit weight γ_d as follows:

$$\gamma_t = \frac{\gamma_d}{1 + w} \tag{3.1}$$

Similar to soils, deformation of TDA is expected to follow the effective stress principle. Skempton (1961) derived the following relationship for the effective stress in porous materials:

$$\Delta p' = \Delta p - \left(1 - \frac{C_s}{C}\right)\Delta u_w \tag{3.2}$$

where Δp' is the increment in mean effective stress, Δp is the increment in mean total stress, Δu_w is the increment in pore water pressure, C_s is the compressibility of solid particles, and C is the compressibility of the "skeleton" of the porous material. Like soils, the compressibility of the TDA "skeleton" can be assumed to be much greater than the compressibility of the individual tire shred particles due to the void space in the TDA. In this case, the ratio C_s/C is close to zero, and Equation 3.2 reduces to Terzaghi's effective stress definition:

$$\Delta p' = \Delta p - \Delta u_w \tag{3.3}$$

The application of external stresses to compacted TDA will result in further densification, including from the self-weight stresses associated with overlying lifts of TDA and granular backfill. For example, the dry Type B TDA characterized by Ghaaowd et al. (2017) in large-scale direct shear tests was compacted to a total unit weight of approximately 5 kN/m^3 (31.8 pcf) using a small-scale vibratory compactor but experienced an increase in total unit weight of up to 8 kN/m^3 (51 pcf) during application of vertical stresses up to 76.7 kPa (1602 psf), as shown in Figure 3.2. The lower initial total unit weight after compaction obtained by Ghaaowd et al. (2017) compared to Humphrey and Manion (1992) could be due to the use of the small-scale vibratory compactor but also the larger particle size of the Type B TDA. No external stresses will be applied to the TDA layer in the example shown in Figure 1.1(b).

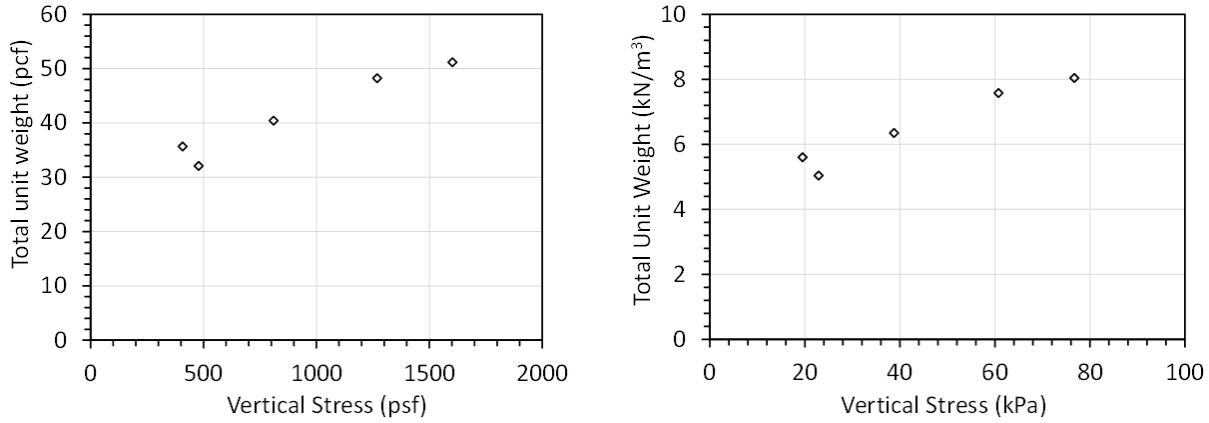

Figure 3.2: Total unit weight of TDA after applied vertical stress: (a) Imperial; (b) Metric.

The trends in unit weight with normal stress can be used to define the compression curve for Type B TDA, as shown in Figure 3.3 in both imperial and metric units. The void ratio, e was calculated using from the total unit weights of the TDA in Figure 3.2 assuming $\gamma_d = \gamma_t$ as follows:

$$e = \frac{G_s \gamma_w}{\gamma_d} - 1 \tag{3.4}$$

where the specific gravity G_s is 1.15 and γ_w is the unit weight of water. The compression curve for Type B TDA obtained from the data in Figure 3.2 is shown in Figure 3.3. The compression curve includes the average initial unit weight of Type B TDA after compaction of 5 kN/m^3 (31.8 pcf), which corresponds to an initial void ratio of 1.26. For comparison, the compression curve for a specimen of Type A TDA with a similar initial unit weight of 5.1 kN/m^3 (32.1 pcf) (specimen NY2) reported by Humphrey (2008) is also shown in this figure. The compression curves of both types of TDA are highly nonlinear. For the purposes of design, a bilinear envelope can be used for TDA as shown in Figure 3.3, with a recompression index of C_r of 0.1 for both TDA Type A and Type B, and a compression index of C_c = 0.45 for Type A TDA and C_c = 1.26 for Type B TDA. The intersection of the recompression and compression curves is an apparent yield stress, which is 2 kPa (42 psf) for Type A TDA and 20 kPa (418 psf) for Type B TDA. The apparent yield stress may change if the initial void ratio of the TDA after compaction is different than the values shown in Figure 3.3. The results of Humphrey (2008) shown in Figure 2.4 indicate that the compression index C_c for Type A TDA decreases slightly with increasing initial dry unit weight, while the recompression index C_r is not sensitive to the initial dry unit weight.

During placement of TDA in the field each lift will always have an initial vertical stress (defined at the center of a lift) that is smaller than the yield stress in Figure 3.3. However, the final stress due to application of overlying layers may be less than or greater than the yield stress. In these cases, the change in void ratio for each layer can be calculated as follows:

$$\Delta e = \begin{cases} -C_r log\left(\frac{\sigma_v{}'_{final}}{\sigma_v{}'_{initial}}\right), \sigma_v{}'_{final} < \sigma_v{}'_{yield} \\ -C_r log\left(\frac{\sigma_v{}'_{yield}}{\sigma_v{}'_{initial}}\right) - C_c log\left(\frac{\sigma_v{}'_{final}}{\sigma_v{}'_{yield}}\right), \sigma_v{}'_{final} > \sigma_v{}'_{yield} \end{cases} \tag{3.5}$$

where $\sigma_v{}'_{initial}$ is the initial vertical effective stress (calculated at the center of a TDA lift), $\sigma_v{}'_{yield}$ is the yield stress, and $\sigma_v{}'_{final}$ is the final vertical effective stress due to the weight of overlying layers or a surcharge (equal to the initial vertical stress plus the change in stress). The negative sign in Equation 3.6 implies that a decrease in void ratio will occur during an increase in vertical effective stress. During unloading, the TDA will rebound on a curve with a log-linear slope of C_r. It should be noted that the compression index C_c for Type B TDA is larger than that of most soils.

For example, using the correlation developed by Terzaghi and Peck (1948) (C_c = 0.009(LL-10)) for a clay with a liquid limit of LL = 50, the value of C_c is 0.36. More recently, Yarahuaman and McCartney (2023) developed a nonlinear hyperbolic relationship for the compression of TDA that can better capture the deformation response of TDA during compressive loads that also avoids the need to define the apparent yield stress in Equation 3.6.

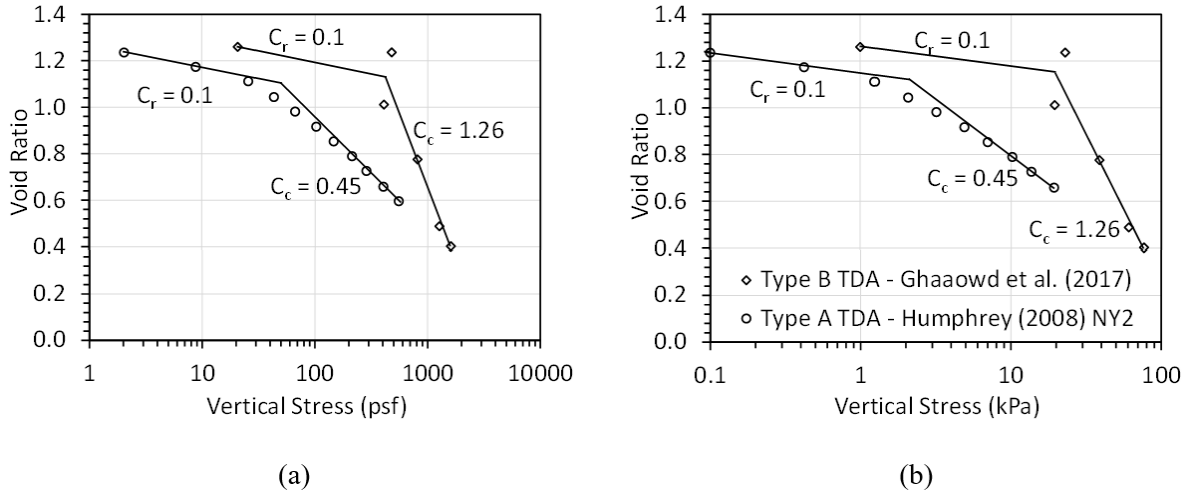

(a) (b)

Figure 3.3: Compression curves for Type B TDA: (a) Imperial; (b) Metric

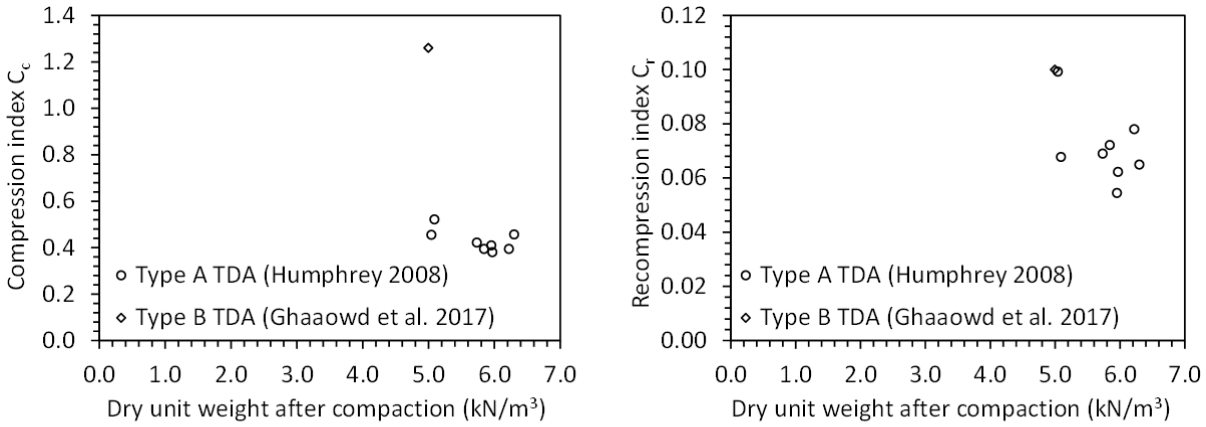

(a) (b)

Figure 3.4: Compression indices with initial unit weight: (a) Compression index; (b) Recompression index.

Internal and interface shear strength of TDA

The understanding of the shearing behavior of TDA, specifically that of Type B TDA with large particle sizes, is a topic that has evolved over time. While some studies used triaxial compression tests to study the shear shearing behavior of crumb rubber and TDA with small

particle sizes (Bressette 1984; Ahmed 1993; Benda 1995; Masad et al. 1996; Wu et al. 1997; Lee et al. 1999; Yang et al. 2002; Jeremić et al. 2004), most studies have used direct shear tests to characterize TDA with larger particle studies. Early studies like Humphrey and Sandford (1993); Humphrey et al. (1993), Foose et al. (1996) and Bernal et al. (1997) used relatively small direct shear devices with maximum areal dimensions of 300 mm and were limited in the displacement range that could be achieved (smaller than 90 mm) and the maximum particle size that could be characterized (smaller than 150 mm). Later studies like Gebhardt (1997) and Xiao et al. (2013) used larger boxes with maximum areal dimensions of 910 and 800, respectively, but were still limited in the maximum displacement range that could be achieved (230 and 180 mm, respectively) and the maximum particle size that could be characterized (432 and 75 mm, respectively). As the direct shear devices used in these studies could not always reach the peak shear strength within the maximum displacement, it was often difficult to consistently interpret the shear strength parameters of TDA. Ghaaowd et al. (2017) reviewed the shear strength parameters of TDA from the studies mentioned above (primarily Type A TDA) and found that the friction angle varied between 19 and 38 degrees. The studies reporting a low friction angle also reported apparent cohesion intercepts, reflecting that a linear relationship was fitted to a nonlinear failure envelope. In addition to not being able to consistently reach the peak shear strength of TDA occurring at large displacements, early studies did not consider the nonlinearity in the failure envelope for TDA over the range of vertical stresses encountered in lateral spreading applications.

To address the uncertainty in the shear strength parameters of TDA mentioned above and to permit the characterization of the shearing response of Type B TDA to large displacements over a wide range of normal stresses, Fox et al. (2018) developed a large-scale shearing device that could either be operated in direct shear mode or simple shear mode. This device was used to characterize the internal shear strength of TDA and the shear strength of TDA-concrete interfaces by Ghaaowd et al. (2017), the cyclic shearing response by McCartney et al. (2017), the shear strength of TDA interfaces with different soils by Ghaaowd et al. (2020), and the pullout of geosynthetic reinforcements from TDA by Ghaaowd and McCartney (2020).

The area-corrected shear stress-displacement curves from direct shear tests on Type B TDA reported by Ghaaowd et al. (2017) in Imperial and Metric units are shown in Figures 3.5(a) and 3.5(b), respectively. Due to the changes in normal stress that occur during direct shear tests, the curves in Figures 3.5(a) and 3.5(b) are not ideal for defining the point of shear failure. Instead, the

plots of the mobilized secant friction angle in Imperial and Metric units shown in Figures 3.5(c) and 3.5(d), respectively, are more suitable for interpreting the point of shear failure. At the peak of each of these curves the TDA has mobilized the maximum frictional resistance. Two observations can be drawn from these figures – a decrease in the peak secant friction angle with increasing initial normal stress indicating a nonlinear failure envelope, and a relatively large displacement at peak ranging from 337 to 439 mm (13.3 to 17.3 inches). These values indicate that TDA has a very ductile shearing response. Direct shear tests area always performed in drained conditions, which is suitable for characterizing the shearing behavior of TDA as it has high permeability and any shear-induced pore water pressures will drain rapidly. However, volume changes may occur during drained shearing of TDA, which are important to characterize for the development of advanced constitutive models. The vertical strain vs. horizontal displacement curves for Type B TDA measured during the direct shear tests are shown in Imperial and Metric units in Figures 3.5(e) and 3.5(f), respectively. Type B TDA tends to dilate after displacements of 131 to 284 mm (5.2 to 11.2 inches). Ghaaowd et al. (2017) also performed direct shear tests with different displacement rates and found that the shear strength was not sensitive to the shear displacement rate.

The shear failure envelopes for the Type B TDA internal direct shear test results from Ghaaowd et al. (2017) with the points at failure obtained from the maximum mobilized secant friction angle curves in Figures 3.5(c) and 3.5(d) are summarized in Figures 3.6(a) and 3.6(b) in Imperial and Metric units, respectively. In addition, the failure envelopes for interfaces between Type B TDA and concrete measured by Ghaaowd et al. (2017) and interfaces between Type B TDA and different soils measured by Ghaaowd et al. (2020) are also included in these figures for reference. The interfaces with different soils measured by Ghaaowd et al. (2020) all had separation geotextiles consistent with recommendations in ASTM D6270-20, although it should be noted that the TDA was observed to interact with the underlying soil through the separation geotextile. The shear strength of the Type B TDA is consistently higher than the interfaces with the other materials. As there was no source of apparent cohesion in the Type B TDA or the interfaces with different materials, nonlinear failure envelopes were fitted to each of the data sets in this figure using the shear strength model of Duncan et al. (1980):

$$\tau_f = \sigma_f tan\left(\phi_{sec}(\sigma_f)\right) \tag{3.6}$$

where τ_f is the shear strength defined at the point of maximum mobilized secant friction angle, σ_f is the vertical normal stress at failure, and $\phi_{sec}(\sigma_f)$ is the stress-dependent secant friction angle. The stress-dependent secant friction angle can be calculated using the following equation:

$$\phi_{sec}(\sigma_f) = \Delta\phi log\left({\sigma_f}/{P_{atm}}\right) + \phi_0 \tag{3.8}$$

where P_{atm} is atmospheric pressure (101.3 kPa or 2116 psf) and $\Delta\phi$ and ϕ_0 are fitting parameters that denote the change in secant friction angle with normal stress and the secant friction angle at a normal stress equal to the atmospheric pressure, respectively. For materials with a linear failure envelope, the value of $\Delta\phi$ is zero, and $\phi_{sec} = \phi_0$.

The parameters for the different failure envelopes are shown in Table 3.1. The value of ϕ_0 is the secant friction angle at a normal stress of P_a = 101 kPa while the value of $\Delta\phi$ describes how the secant friction angle decreases with the logarithm of normal stress. The Type B TDA itself had a nonlinear response, with a friction angle consistent with granular materials. For the range of vertical stresses expected in near-surface TDA deposits of 27 to 45 kPa, the secant friction angle calculated with the ϕ_0 and $\Delta\phi$ parameters in Equation 3.10 ranges from 35 to 39°. The interfaces between Type B TDA and clay and Type B TDA and aggregate were both nonlinear, while the interfaces between Type B TDA and concrete and Type B TDA and sand were both linear. A major difference between the failure envelopes shown in Table 3.1 and those for granular backfills used in MSE walls is the displacement at the peak failure conditions obtained from the curves in Figures 3.5(c) and 3.5(d). These displacements at peak are much greater than granular backfill soils, which typically reach a peak within the extents of a standard direct shear box for soils having a maximum displacement of 50 mm (2 inches).

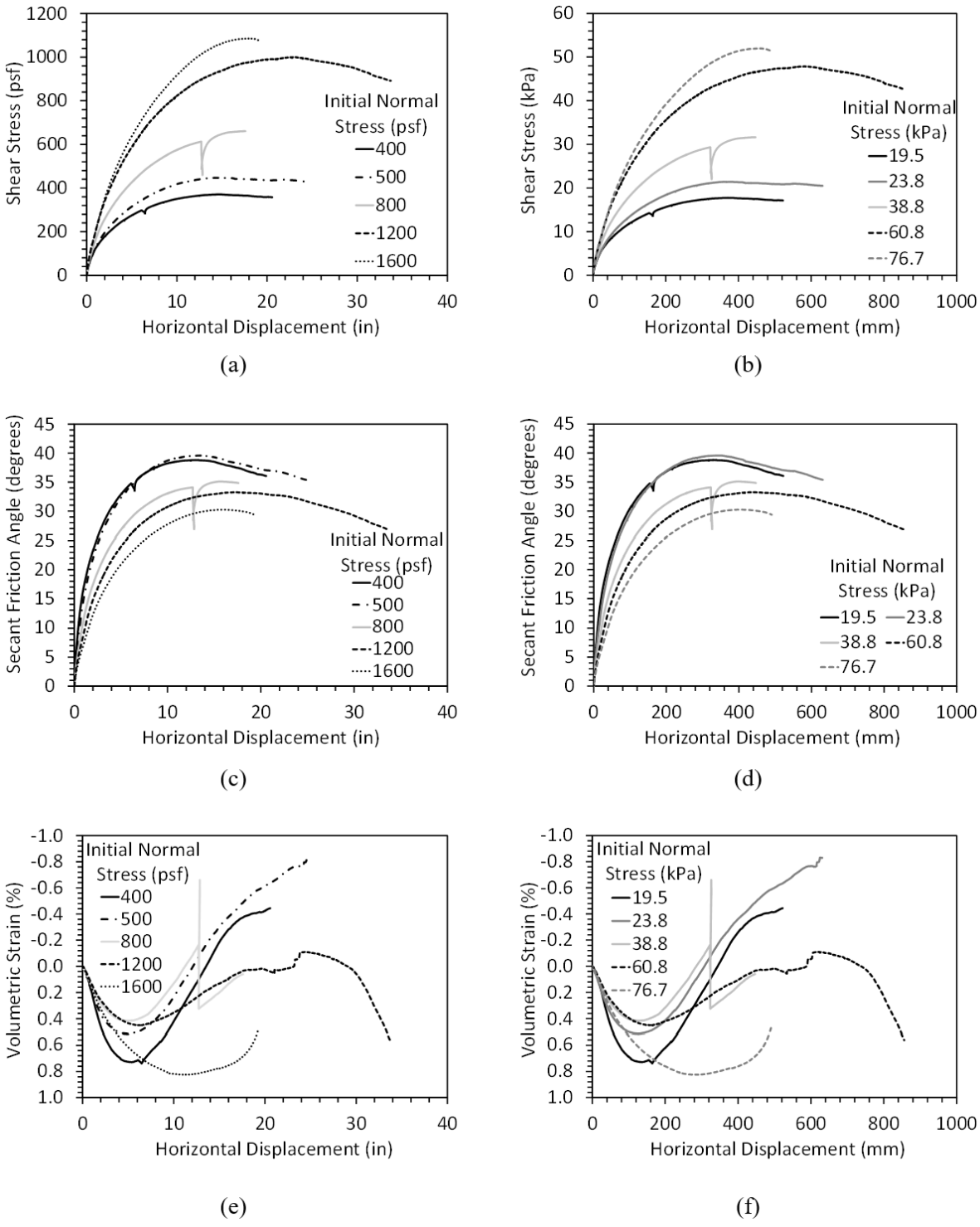

Figure 3.5: Type B TDA direct shear results: (a) Stress-displacement curves: Imperial; (b) Stress-displacement curves: Metric; (c) Secant friction angle mobilization curves: Imperial; (d) Secant friction angle mobilization curves: Metric; (e) Volumetric.

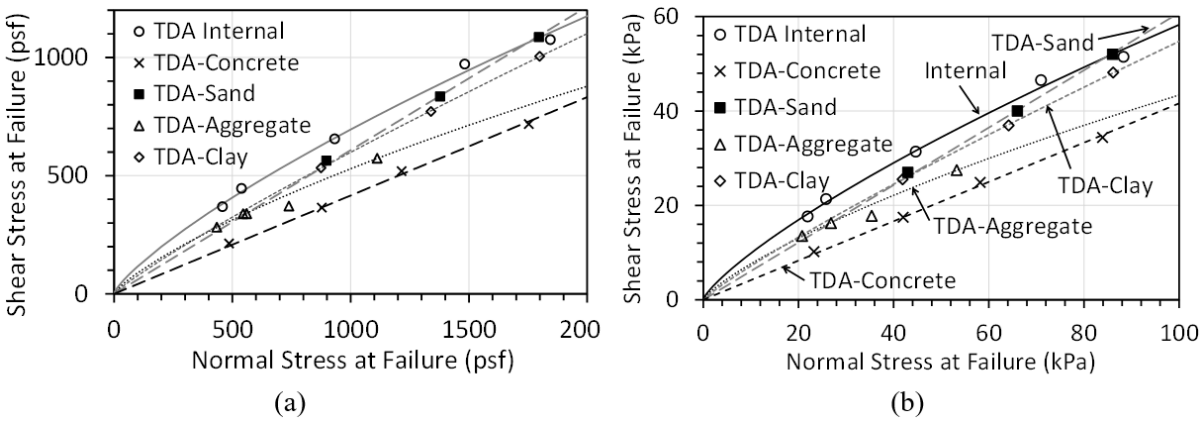

Figure 3.6: Shear failure envelopes for internal Type B TDA and interfaces between Type B TDA with different materials (Ghaaowd et al. 2017, 2020).

Table 3.1: Shear failure envelope and displacement parameters (Ghaaowd et al. 2017, 2020), Note: The symbol ϕ is used for both internal and interface friction angles.

Interface	Separation Geotextile	ϕ_0 (degrees)	$\Delta\phi$ (degrees)	Ave. Displacement at Peak (mm)	Ave. Displacement at Peak (inches)
TDA Internal	None	30.2	-14.4	385	15.2
TDA-Concrete	None	22.6	0.0	180	7.1
TDA-Aggregate	Woven	23.4	-13.9	244	9.6
TDA-Sand	Nonwoven	31.3	0.0	340	13.4
TDA-Clay	Nonwoven	28.7	-7.0	283	11.1

The dilation angle ψ is used to quantify the dilation (volumetric expansion) that occurs during shearing, and for the case of direct shear tests can be defined as follows:

$$\psi = \sin^{-1}\left(\frac{tan(\delta_v/\delta_h)}{2 + tan(\delta_v/\delta_h)}\right) \tag{3.8}$$

where δ_v is the vertical displacement and δ_h is the horizontal displacement. For the results shown in Figures 3.5(e) and 3.5(f), δ_v is the product of the volumetric strain and the height of the TDA layer (approximately 1500 mm), and the slope δ_v/δ_h should be defined after the initial compression when there is a tendency toward negative volumetric strains (i.e., for the test at a vertical stress of 19.5 kPa or 400 psf, the slope should be defined between displacements of 200 and 400 mm or 8 and 16 inches). Type B TDA also shows a small amount of dilation during shearing, as shown in Figures 3.5(e) and 3.5(f) and summarized in Figures 3.7(a) and 3.7(b). The dilation angle of TDA is relatively low and decreases with normal stress, with an average value of 2.2 degrees. The curves

in Figures 3.5(e) and 3.5(f) indicate that the onset of dilation typically does not occur until relatively large displacements that approximately half that required to reach the peak shear strength. The dilation angle may be needed when performing advanced finite element analyses.

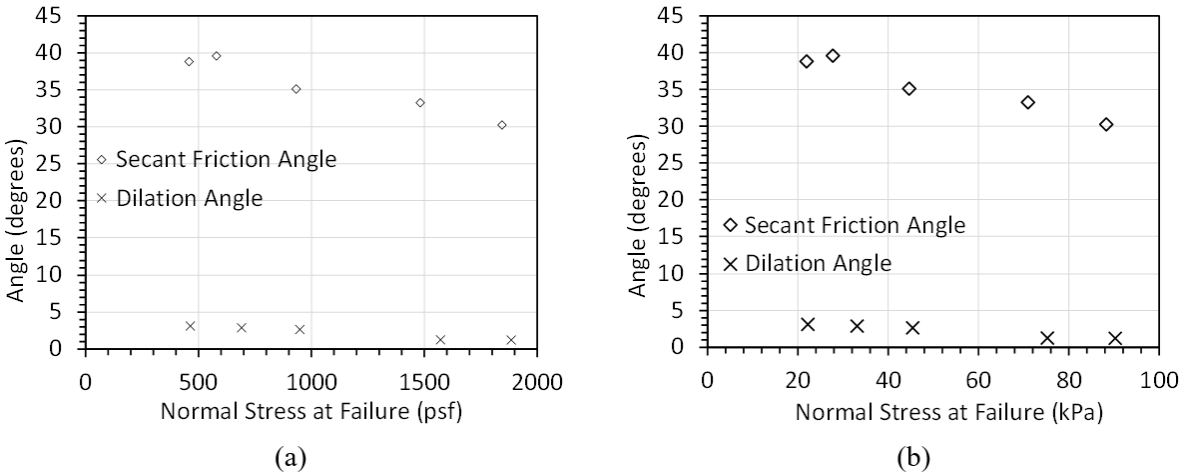

Figure 3.7: Comparisons between the secant friction angle and dilation angle measured for Type B TDA (Ghaaowd et al. 2017): (a) Imperial; (b) Metric.

Cyclic shearing response of TDA

The dynamic properties of TDA may be useful when performing advanced seismic analyses of TDA layers in lateral spreading applciations. The large-scale shearing device developed by Fox et al. (2018) can be configured to perform cyclic simple shear tests to determine the dynamic properties of TDA. McCartney et al. (2017) presented the results from cyclic simple shear tests on Type B TDA specimens in this device under different constant vertical stresses subjected to cyclic simple shear strain amplitudes ranging from 0.1 to 10%. The main outcome from these cyclic simple shear tests is the hysteretic shear stress vs. shear strain curve, which can be used to quantify the secant shear modulus and damping ratio as a function of the vertical stress and cyclic shear strain amplitude. The shear modulus was observed to increase nonlinearly with the vertical stress, as shown in Figure 3.8(a), but decrease nonlinearly with increasing shear strain amplitude. Figure 3.8(a) also includes power law relationships that were fitted to the secant shear modulus G vs. vertical stress σ_v data, having the following general form:

$$G = A\left(\frac{\sigma_v}{P_a}\right)^n \tag{3.9}$$

where P_a is the atmospheric pressure, and A and n are empirical fitting parameters. The damping ratios calculated from the area within the hysteretic shear stress vs. shear strain curves are shown in Figure 3.8(b). The damping ratios shown in this figure are greater than most granular soils, and a decreasing-increasing trend is observed with increasing shear strain amplitude instead of a monotonically increasing trend typically observed for soils.

The results in Figure 3.8(a) can be used to define a shear modulus reduction curve, which is a commonly used relationship in dynamic analyses. The shear modulus reduction curve model of Darandelli (2001) was fitted to the shear modulus data plotted as a function of the cyclic shear strain in Figure 3.9(a). This model has the following form:

$$\frac{\mathrm{G}}{G_{max}} = \left[1 + \left(\frac{\gamma_a}{\gamma_0(\sigma_v/P_a)^m}\right)^a\right]^{-1} \tag{3.10}$$

where G_{max} is the maximum secant shear modulus for a given vertical stress, γ_a is the cyclic shear strain amplitude, γ_0 is a reference shear strain, and a and m are fitting parameters. McCartney et al. (2020) estimated the relationship between G_{max} and σ_v using parameters A = 3800 kPa and n = 0.51, and used values of a = 0.75, γ_0 = 0.6, and m = 0.55 to fit Equation 3.13 to the secant shear modulus vs. cyclic shear strain amplitude data in Figure 3.9(a). Normalized G/G_{max} versions of the modulus reduction curves are shown in Figure 3.9(b). Although dynamic analyses typically require both a modulus reduction curve and a damping ratio vs. cyclic shear strain curve, the nonlinear shape of the damping ratio relationship in Figure 3.8(b) is difficult to capture with a fitting relationship. Instead, it is recommended to use an average value of damping ratio over the expected cyclic shear strain amplitude in advance dynamic analyses of of TDA layers.

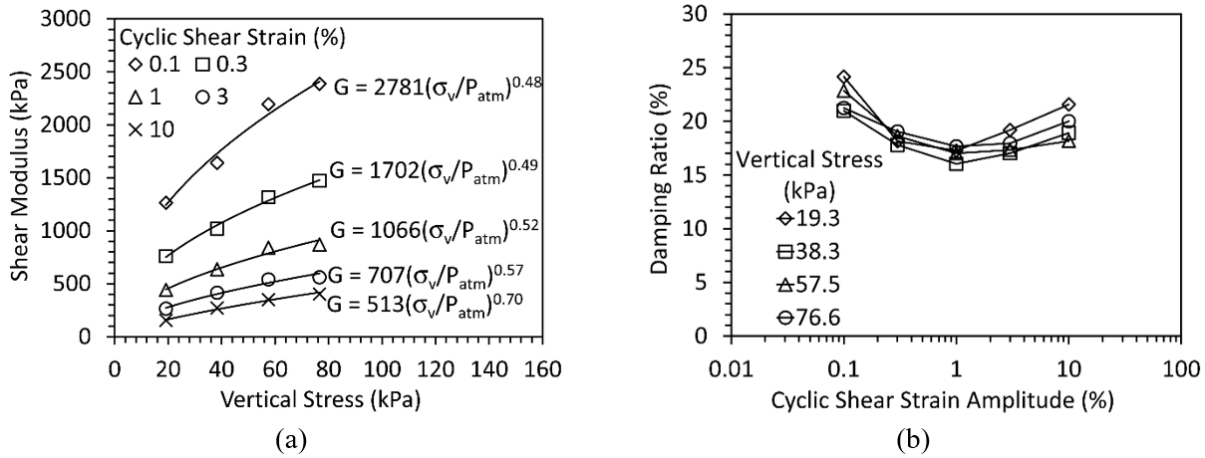

(a) (b)

Figure 3.8: Cyclic shearing response of Type B TDA under different vertical stresses and cyclic shear strains (McCartney et al. 2017): (a) Shear modulus; (b) Damping ratio.

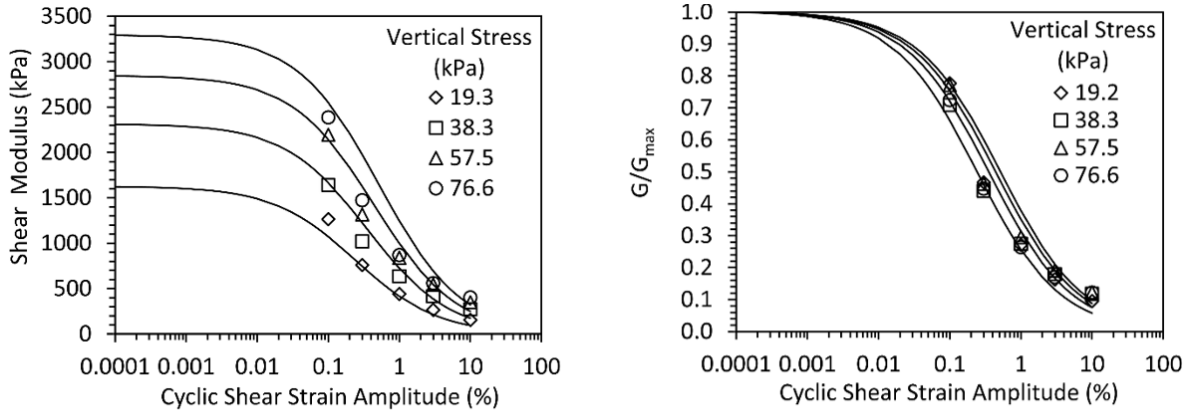

(a) (b)

Figure 3.9: Modulus reduction curves for Type B TDA (McCartney et al. 2017): (a) Fitted curves to measured data; (b) Normalized modulus reduction curves.

Chapter 4 EXPERIMENTAL TESTING PROGRAM

Testing Program Scope

The objectives of the experimental testing program are to understand the deformation response of steel pipe piles and cylindrical reinforced concrete piles during horizontal loading of a TDA layer having different widths *S* in Figure 1.1(b), and to use the pile bending response to develop *P-y* curves for different piles interacting with Type B TDA. A total of four specimens were tested at the University of California San Diego (UCSD) South Powell Laboratory as part of this project. During the tests on the steel pipe pile, the TDA layer was not fully removed and replaced again after each test due to the significant labor and time for material handling due to the size of the specimens. Instead, testing was performed using the smallest width first, after which the wall was retracted to a wider value of *S*, the TDA in the container was smoothed across the greater width, and additional TDA was incorporated to fill the container. The average TDA unit weight was obtained by measuring the top surface level of TDA after each test and weighing the amount of dry TDA added so that the initial weight and volume of the TDA layer is known. The TDA was not compacted during the experiments so that the it would have a low initial unit weight that would be as compressible as possible. The field application is also expected to involve a loose, uncompacted TDA layer placed within a trench on one or both sides of the bridge pile. The approach for preparing the TDA layers led to a 6% difference in the average unit weight of the TDA layers, and the initial unit weights were consistently near the lower bound of TDA unit weights expected in field applications (McCartney 2021). While the compression curve in Figure 3.3 indicates that the TDA unit weight is a function of the vertical stress, the loosely-placed TDA in these experiments is not expected to vary significantly with depth as the vertical stress range in the experiments is very small (0 to 15.6 kPa). The changes in the unit weight with vertical stress in this range are expected to follow the recompression line with negligible differences in this range.

Each specimen includes a 3 m-thick TDA layer surrounding the pile in the shape of a rectangular prism. Horizontal loads are applied quasi-statically using two actuators to a rigid moveable wall initially at a distance *S* from the pile. Movement of the rigid moveable wall imposes a horizontal stress on the TDA layer to replicate the downslope movement of the non-liquefiable crust in Figure 1.1(b). The three other sides of the TDA layer are constrained by rigid, stationary walls. The width *S* represents the distance between the moveable wall and the north face of the

pile. In this study, the width *S* varies from *3D* to 9*D* in the different tests where *D* is the diameter of the pile, as shown in Figure 4.1.

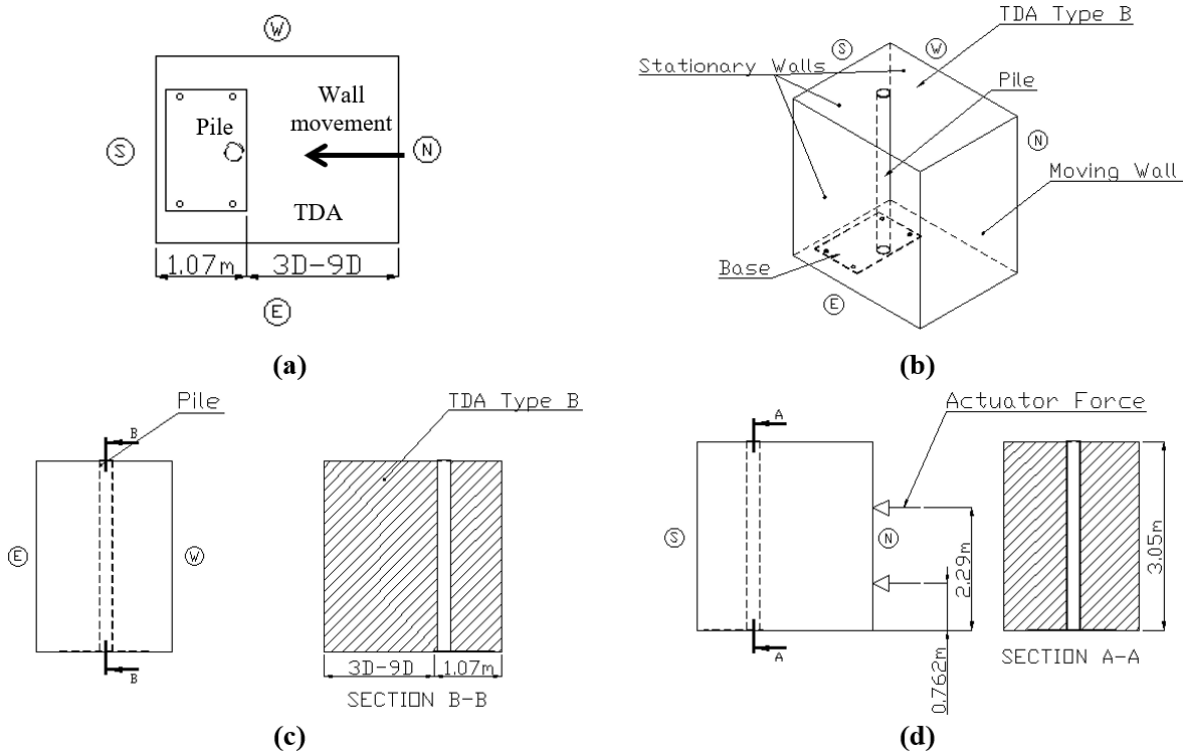

Figure 4.1. Specimen configuration: (a) Plan View, (b) Isometric view, (c) Front elevation view, and (d) Right side elevation.

Experimental setup

This project involved testing of four specimens that have different characteristics including two piles (reinforced concrete and a steel pipe pile) with different diameters and basal connections, widths of TDA in front of the pile *S*, and slightly different initial unit weights of the 3 m-thick uncompacted TDA layer. While the pile diameters evaluated in this study are smaller than those used in bridge applications, they are considered to follow the smaller diameters used in the previous shake table testing program by Qiu et al. (2023) and were selected so that measurable deformations would be observed to demonstrate the proof of concept of the compressible TDA buffer layer proposed tin this study. The characteristics of each specimen are detailed in Table 4.1. Three of the four specimens (QS01, QS02, and QS03) included a steel pipe pile attached to a rectangular steel plate. Four stiffeners were welded to the base of the pile and the steel plate base. The steel plate is anchored to the strong floor of the lab using four threaded rods having a diameter of 25.4 mm (one in each corner). Each of these three specimens has a different TDA spacing. The

fourth specimen (QS04) includes a cylindrical reinforced concrete pile attached to a rectangular prism of reinforced concrete. The reinforcement of the pile and rectangular prism was designed to avoid shear failure. The concrete and steel piles were not designed to be directly comparable, as the steel pile has a theoretical bending stiffness that is nearly 3 times greater than the concrete pile. Nonetheless, the testing program permits a general assessment of the behavior of the different pile materials interacting with the flexible TDA layer.

Table 4.1. Test specimen characteristics.

Specimen label	Pile type	Pile diameter	Pile base	Theoretical pile bending stiffness (EI)	TDA width, S	Unit weight of TDA
QS01	Steel pipe pile	$D_{in} = 203\ mm$ $D = D_{out} = 219\ mm$	50 mm-thick steel plate	6,032 kN.m^2	$660mm = 3.0D$	4.9 kN/m^3
QS02	Steel pipe pile	$D_{in} = 203\ mm$ $D = D_{out} = 219\ mm$	50 mm-thick steel plate	6,032 kN.m^2	$1461\ mm = 6.7D$	4.7 kN/m^3
QS03	Steel pipe pile	$D_{in} = 203\ mm$ $D = D_{out} = 219\ mm$	50 mm-thick steel plate	6,032 kN.m^2	$1880\ mm = 8.6D$	5.2 kN/m^3
QS04	Reinforced concrete pile	$D_{ext} = 254\ mm$ $D = 203\ mm$	Reinforced concrete prism	2,326 kN.m^2	$1226\ mm = 6.0D$	4.9 kN/m^3

As mentioned, three stationary walls constrained the displacement of the specimen in south, east, and west directions while the lateral loads were applied to the north side of the specimen through a moving wall attached to two actuators. The south stationary wall consisted in part of the strong wall of the lab which has a section of 1 m-thick heavily reinforced concrete. The east and west stationary walls consisted of a reinforced concrete block with a sectional thickness of 254 mm which is expected to provide a rigid lateral restraint. The blocks were anchored to the strong floor of the lab using post tensioned threaded rod of 38.1 mm diameter. The moving wall consisted of a 12.7 mm-thick steel plate stiffened with L-sections in vertical and horizontal orientations, as shown in Figure 4.2. The wall plate dimensions were 2.13 m long by 3.05 m wide.

To minimize the deflection of the plate from the at-rest soil pressure of the TDA, four vertical and two horizontal L-sections as stiffeners were welded to the plate. The vertical stiffeners are four equally spaced 4.48 m-long L-sections (L5”x2 7/8”x11/16”) sections welded with 6.35 mm fillet welds 0.254 m long at every 0.254 m spacing. The horizontal stiffeners are 2.03 m-long L-sections (L5”x2 7/8”x11/16”) sections located at both ends of the vertical stiffeners and are welded with 6.35 mm fillet welds 125 mm long at every 330 mm spacing. Although the moving wall is expected to provide a uniform lateral displacement response to the TDA layer it is not expected that the stress distribution will be uniform, with greater stresses expected at the bottom of the moving wall.

During testing, the moving wall is supported by two actuators hence it can remain in a vertical orientation. However, the moving wall could not be attached to the actuators during construction and between tests. Therefore, a temporary truss support was attached to the moving wall. The temporary truss has the objective of holding the moving wall when this last one was not attached to the actuators. It was also designed to withstand the active pressure generated by the TDA during construction. The temporary truss support is composed of two triangular trusses linked by two L-sections (L5”x3”x1/2”) and a portion of the vertical stiffeners of the moving walls, as shown in Figure 4.3. The truss members subjected to compression were checked against potential buckling. A steel mass having a weight of 6.67 kN was added to the back of the truss support to avoid overturning of the moving wall.

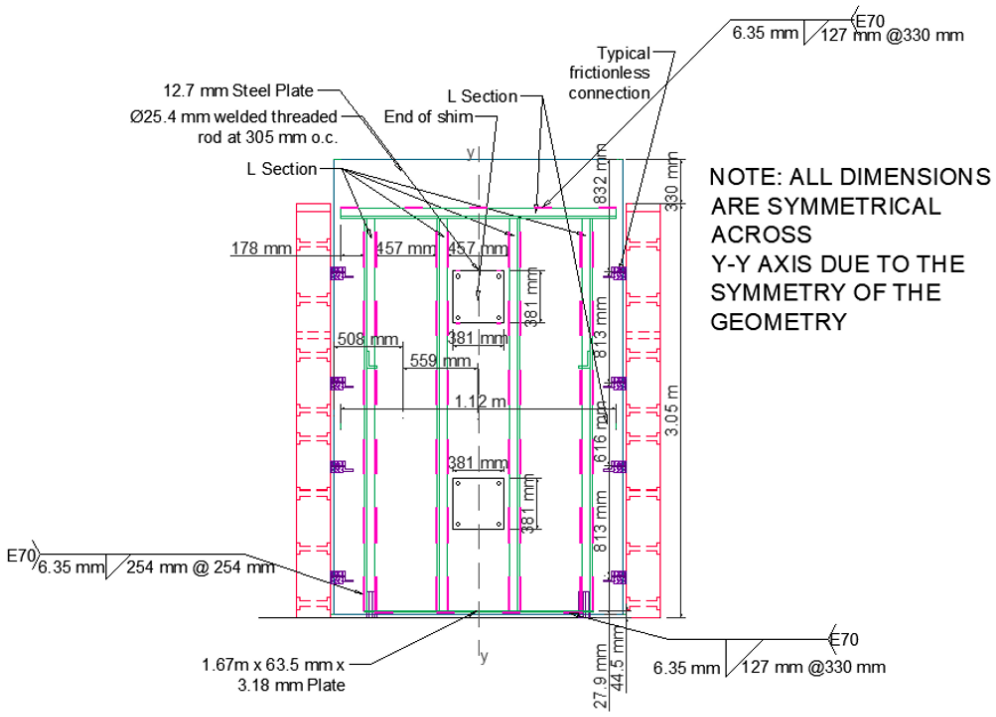

(a)

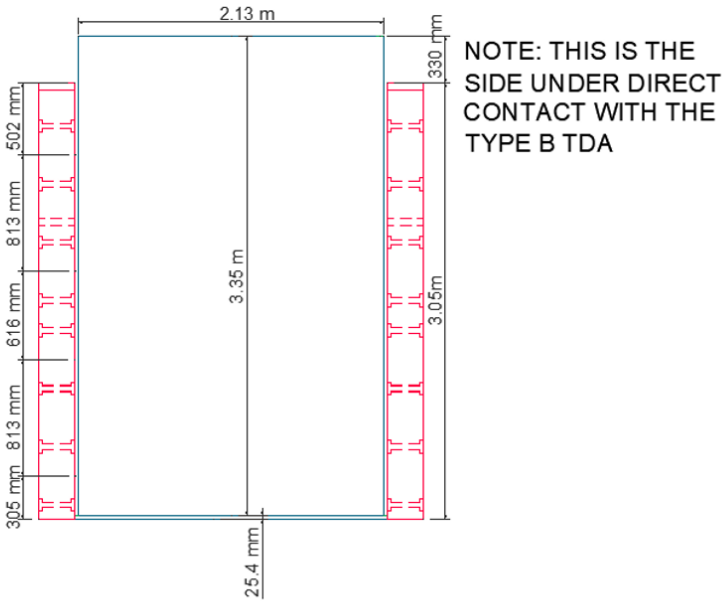

(b)

Figure 4.2.Stiffened moving wall: (a) Front elevation, and (b) Back elevation.

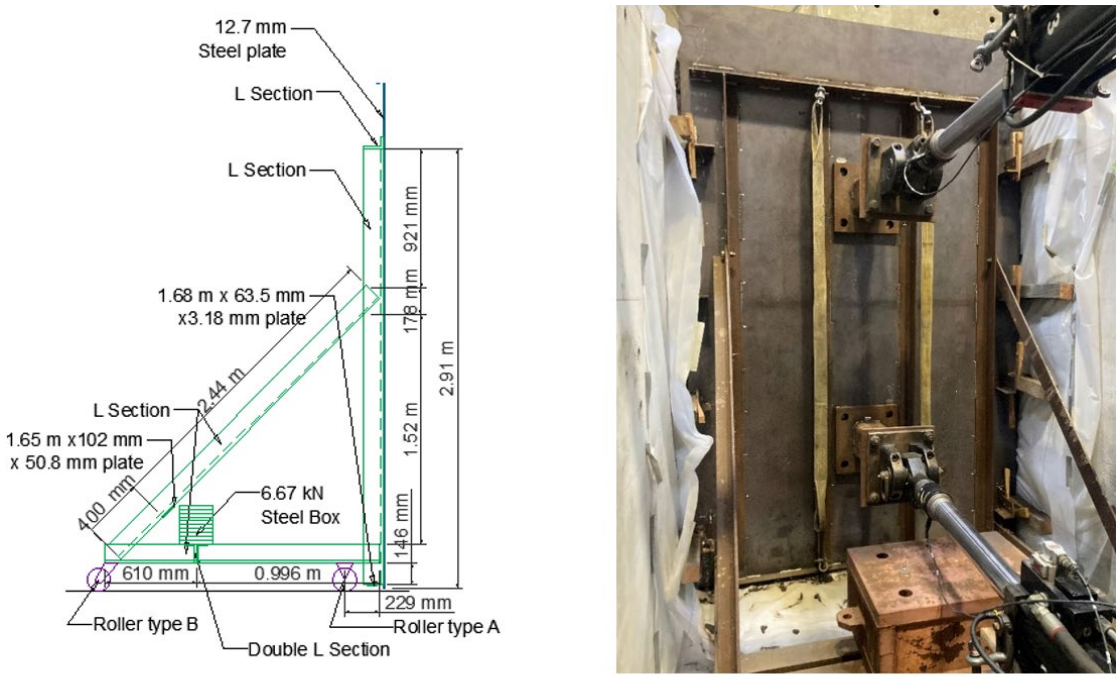

(a) **(b)**

Figure 4.3. Temporary truss support for moving wall.

The loading mechanism is shown in Figure 4.4. The moving wall was mobilized through the application of two actuators acting on the center of the plate at an elevation of 0.762 m and 2.29 m above the ground surface. Due to the different initial positions of the moving wall for the different specimens, and the stroke limit of the actuators, steel shims were added as extensions of the actuators. When switching from specimen to specimen, the steel shims would be interchanged or removed so the rest of the loading setup would not need to be altered. The details of the shims are illustrated in Figure 4.4. Two lengths L_s of shims were used, 0.61 and 1.22 m. One end of the actuators was attached to the shims while the other end was attached to a triangular reaction frame. The base of the reaction frame was attached to the strong floor of the lab using post-tensioned thread rods of 38.1 mm diameter to avoid slipping or overturning.

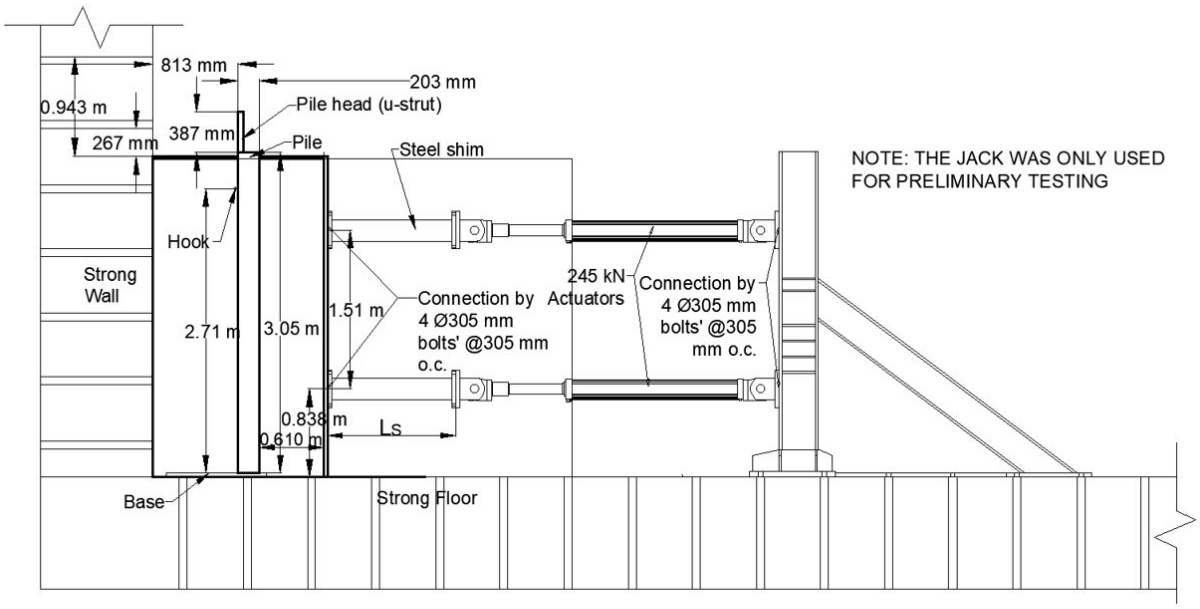

(a)

(b)

Figure 4.4. Horizontal loading setup: (a) General loading setup; (b) Photo of reaction frame and actuators

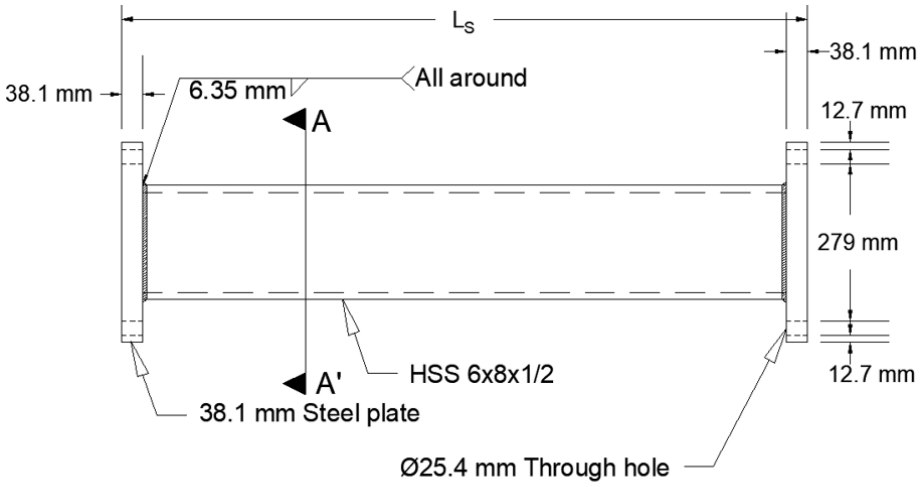

(a)

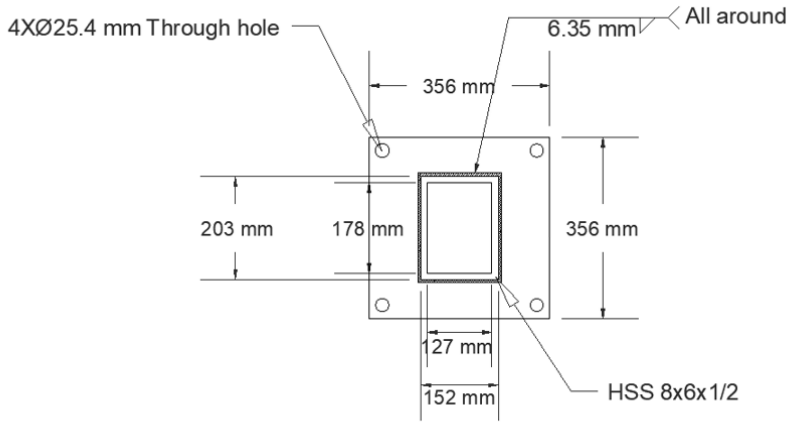

(b)

Figure 4.5. Steel shims Detail for Loading: (a) General side view, and (b) Cross Section

Instrumentation

The instrumentation in this project included steel strain gauges of 5 mm gauge length (FLA-5-11-7LT), string potentiometers (Model P- 5A/15A/25A/30A/40A from Rayelco), and a 44 kN load cell. The instrumentation layout can be categorized into groups. The first group includes a 254-mm stroke string potentiometer at the top of the pile to measure deflection. This group also includes the load cell that was also placed slightly below the string potentiometers which was only used during the preliminary testing (explained in the testing protocol section). The second group includes an array of strain gauge pairs spaced at 152.4 mm for specimens QS01, QS02, and QS03; and spaced at 203.2 mm for the QS04 specimen. The array of strain gauge pairs has the objective of measuring the axial strain generated by the flexural deformation of the pile. The measurements of each strain gauge pair were used to compute curvature at different depths of

the pile. The last group of instruments includes four 254-mm stroke string potentiometers attached close to the corners of the moving wall with the objective of its displacement and deformation. It is important to mention that both actuators are capable of measuring load and displacement hence they were also used to monitor the response of the wall as well. The instrumentation layout for specimens QS01, QS02, and QS03 is illustrated in Figure 4.6. The instrumentation layout for specimen QS04 is illustrated in Figure 4.7. Finally, the instrumentation layout for the moving wall is shown in Figure 4.8.

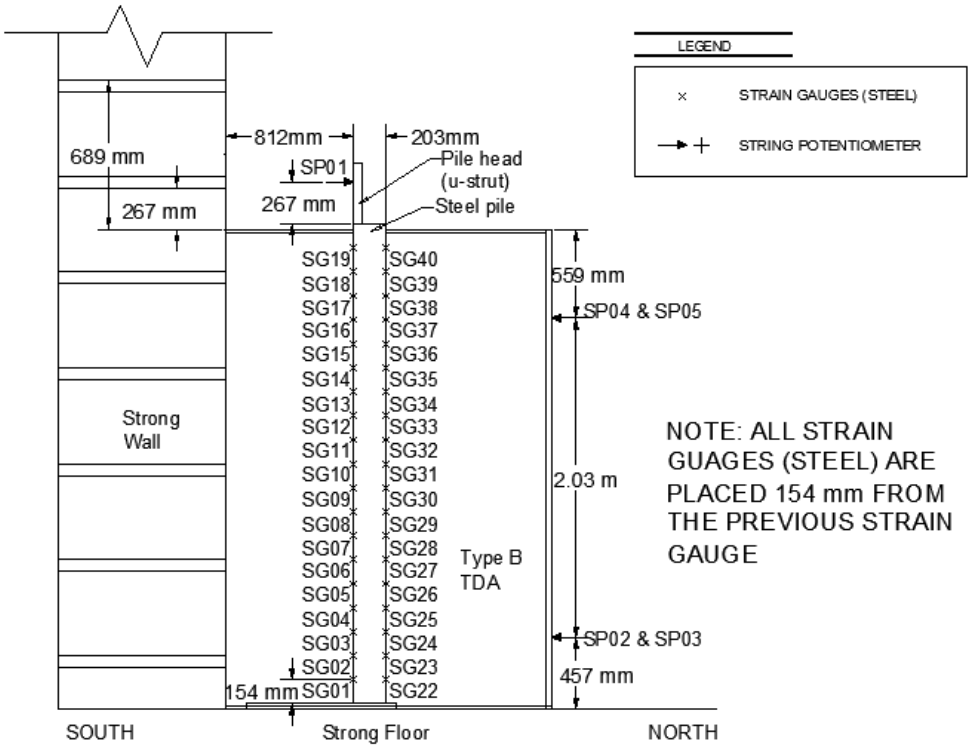

Figure 4.6. Instrumentation for specimens QS01, QS02, and QS03

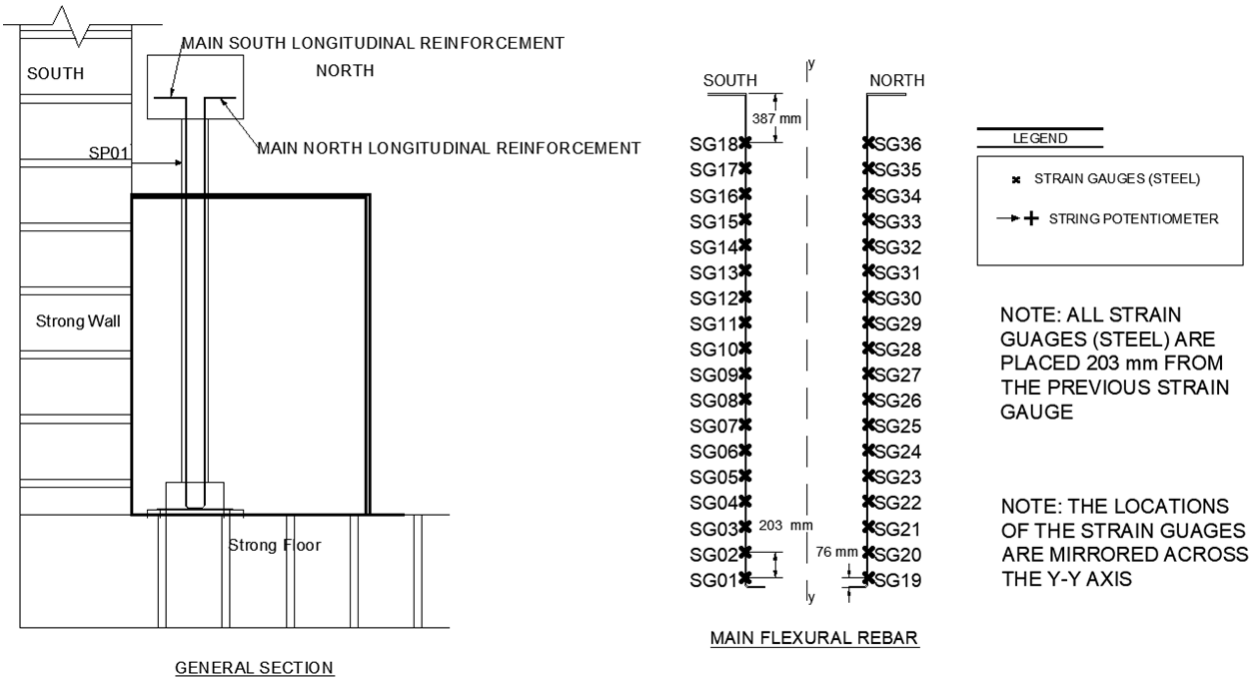

Figure 4.7. Instrumentation for specimen QS04

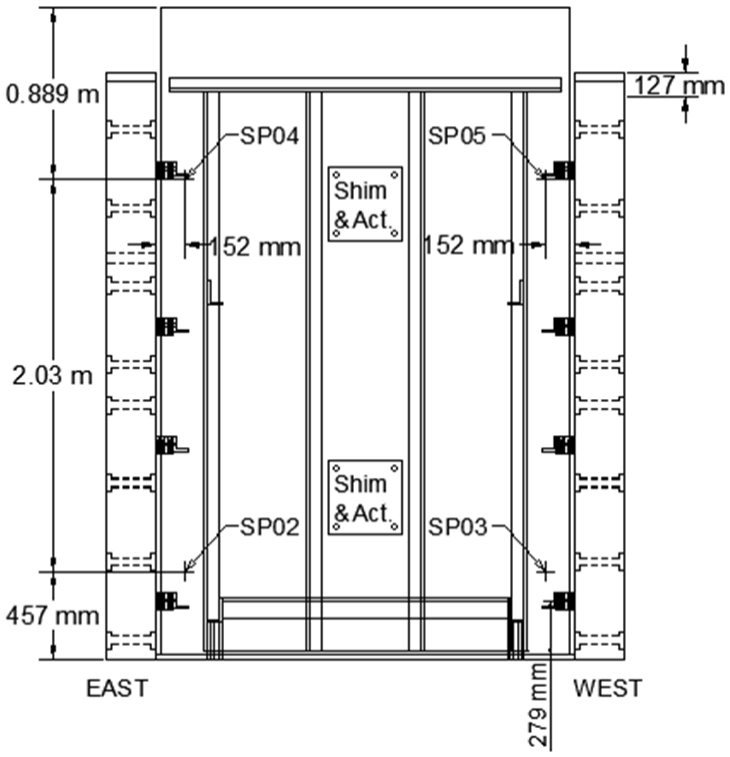

Figure 4.8. Instrumentation for moving wall.

Construction techniques

This section describes the materials and construction procedures used to set up the test specimens at the UCSD South Powell Laboratory. The construction procedures started with the preparation of the piles. The steel pile was built from a 3 m long SCH40 steel pipe pile welded to a steel base plate. Then, the strain gauge pairs were installed at 152 mm spacing from each other. The placement of the strain gauges was carefully conducted using a special adhesive, coating, and neoprene cover. Both are usually used for geotechnical testing of soils. Extra protection was added using two layers of foam and aluminum tape due to the high risk that the wires of the TDA represent, as illustrated in Figure 4.9 Once all the strain gauges were installed, the steel pile was placed and attached to the strong floor using post-tensioned threaded rods. Four stiffeners were welded at the base to avoid shear failure. The preparation of the reinforced concrete pile started with the design of its reinforcement, as illustrated in Figure 4.10. The rebar was fabricated by a local contractor and shipped to the lab. The assembling of the rebar for the rectangular prism, the cylinder of the pile, and the top mass is shown in Figure 4.11(a) and 4.11(b). The main flexural rebar in the north and south direction was instrumented with strain gauges. These strain gauges were installed with special adhesive and neoprene covering. The formwork was prepared carefully to withstand the stresses generated by the casting process, as illustrated in Figure 4.11(c). The casting of the pile was conducted as a single block using prefabricated 35 MPa concrete from a local plant. The final cast pile is shown in Figure 4.11(d).

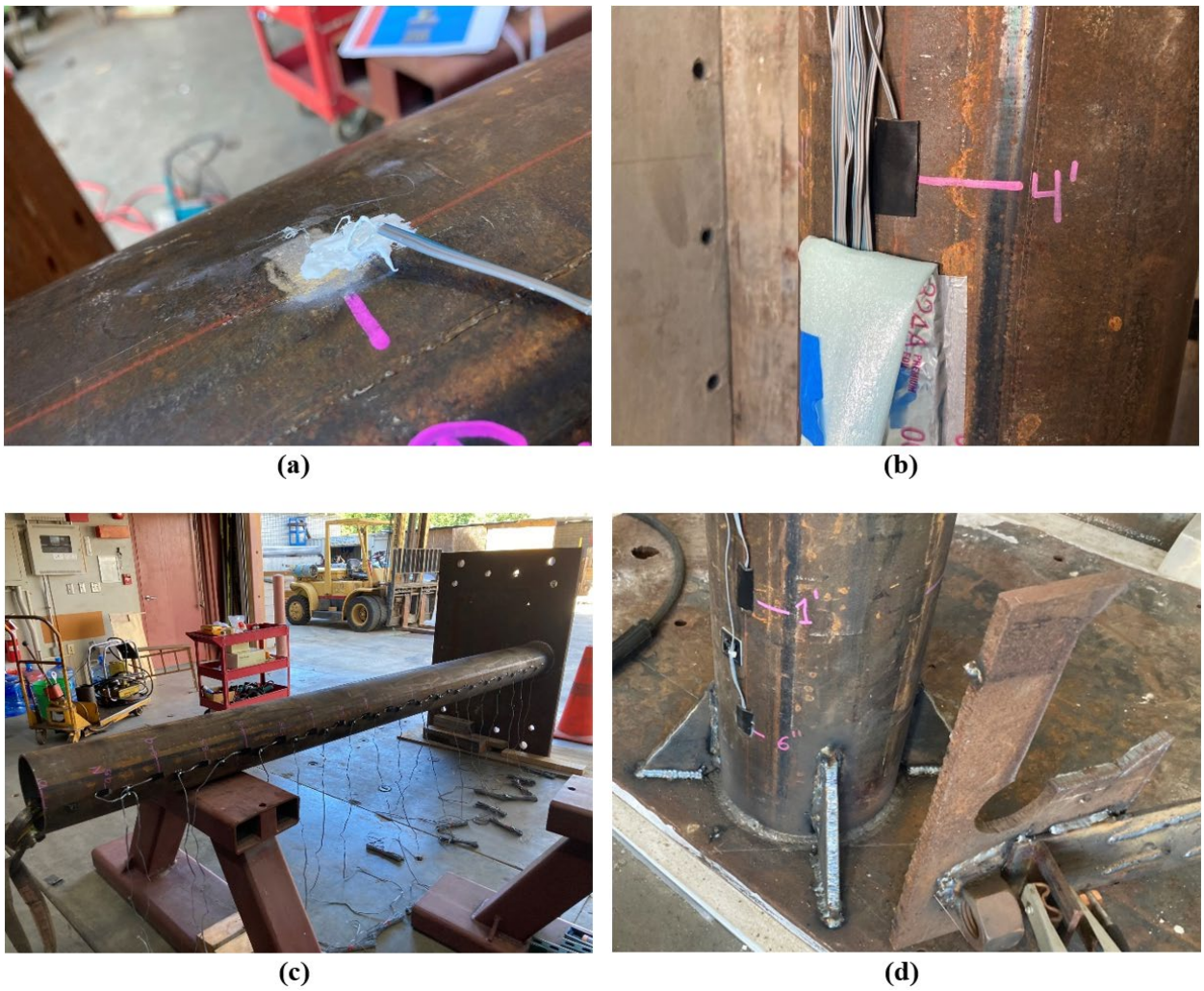

(a) (b)

(c) (d)

Figure 4.9. Preparation of steel pipe pile: (a) Installation of strain gauges, (b) Protection for strain gauges, (c) Instrumented steel pipe pile ready to be placed in testing location, and (d) Stiffeners at base of steel pipe pile.

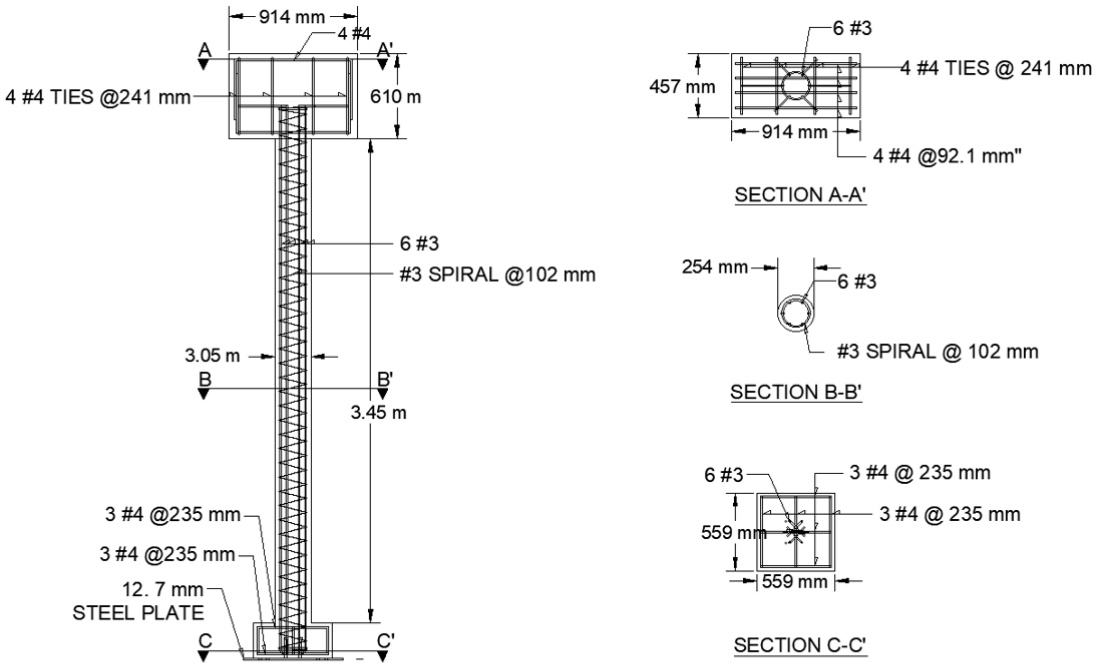

(a)

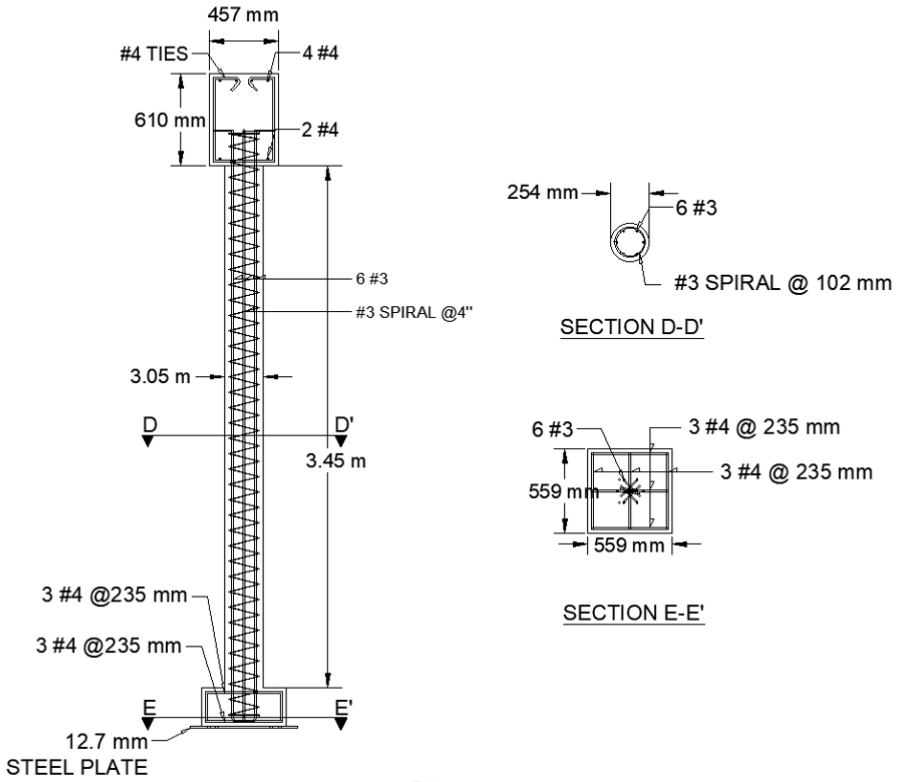

(b)

Figure 4.10. Reinforcement of concrete pile (a) Front View Orientation (b) Side View Orientation.

Figure 4.11. Preparation of reinforced concrete cylindrical pile: (a) Assembling of longitudinal reinforcement with spiral, (b) rebar for base rectangular prism, (c) Formwork before casting of pile, and (d) Cast pile.

At the same time when both piles were being prepared, the moving wall was built using a stiffened and temporary steel truss support. The north side of the moving wall was stiffened with multiple welded L-sections in both vertical and horizontal directions, as illustrated in Figure

4.12(a). The south side of the moving wall has a smooth clean surface which will be in contact with the TDA, as shown in Figure 4.12(b). A temporary truss support was attached to the moving wall to facilitate its mobility and installation, and to prevent overturning of the moving wall. Figure 4.12(a) shows a concrete block as a weight to counter the weight of the plate. This concrete block was replaced by a steel box with a similar weight for better versatility.

(a) (b)

Figure 4.12. Moving wall and truss support: (a) Front side and (b) Back side.

The next step was to prepare the stationary walls that compose the box intended to contain the pile and TDA. As previously mentioned, the stationary walls consisted of a portion of the strong wall of the wall and four concrete blocks. The pile was installed in the testing location right next to the strong wall. Then, the concrete blocks were placed on the east and west of the pile. The concrete blocks were attached to the strong floor using post-tensioned thread rods to withstand the horizontal stress generated by the load applied to the TDA. The base, east, and west sides of the box were covered by two layers of Visqueen plastic to reduce friction hence allowing the displacement of the TDA, as illustrated in Figure 4.13. At this time a preliminary test lateral pull

test was conducted with the installation of a hydraulic jack, a load cell, and string potentiometers on top of the pile.

(a) (b)

Figure 4.13. Specimen before filling of Type B TDA (a) Specimen QS01, and (b) Specimen QS04.

After the preliminary testing was finished, the placement of the TDA around the pile started with the placement of bags of TDA with the help of the lab crane. The specimens during the filling process are shown in Figure 4.14. The TDA in each had an average weight of 3.4 kN which was controlled by a load cell attached to the crane. Each bag generated a lift of around 80 mm thick. Multiple bags were placed in the box until reaching a total thickness of TDA of 3 m.

(a) (b)

Figure 4.14. Specimen during filling of Type B TDA (a) Specimen QS01; (b) Specimen QS04.

Once the container was full of TDA up to a height of 3 m, the actuators and extension shims were attached to the back of the moving wall, as illustrated in Figure 4.15. The actuators were connected to the reaction frame as well. String potentiometers were installed in the four corners of the back side of the moving wall as part of the last instrumentation stage. With the moving wall in place and connected to the actuators, the setup was ready to test. A few measurements of the initial position of the moving wall and reaction frame were taken as reference, and then the testing stage started. It is important to mention that between the testing of specimens, the actuators were separated from the shims. The shims were changed, and then the actuators were reattached to the shims which were connected to the moving wall. Following this procedure, the preparation time from test to test was significantly reduced.

(a)

(b)

Figure 4.15. Examples of constructed specimens: (a) QS02; (b) QS04.

Testing Protocol

The testing protocol included a preliminary testing stage and a main testing stage. The preliminary testing was performed to characterize the rocking stiffness of the base of the pile without the effect of the surrounding TDA. The preliminary testing consisted of a lateral load applied to the top of the pile using a jack and a load cell at the top of the pile. The preliminary testing was conducted before TDA was placed around each pile type. In other words, the preliminary testing was performed right before filling the TDA for specimens QS01 and QS04. Specimens QS02 and QS03 used the same pile as QS01, thus, no extra test was required. It is important to mention that the used jacks can only work under load-control type. A lateral load of 13 kN was applied to both specimens. The main testing protocol consisted of a single quasi-static loading and unloading rate for each specimen, as listed in Table 4.2. The load was applied using displacement-control mode to keep the moving wall fully vertical and to capture any softening generated in the pile-TDA system. The loading rate was low enough to avoid inertial effects. Quasi-static loading was used to represent the down-slope movement of a non-liquefiable crust that may occur after earthquake loading. The continuity and limit of the loading stage were mainly dependent on the load and stroke capacity of the actuators. An unloading stage was included to monitor the recovery response of TDA. Tests QS03 and QS04 were performed at a faster rate than the other tests to reduce the testing duration due to the large displacement applied. Further, the unloading rate was twice the load rate for all specimens to speed up the testing time which was deemed appropriate because the focus of this study was on the loading stage representative of downslope movement of a non-liquefiable crust. Ghaaowd et al. (2018) measured the shear strength of TDA at loading rates up to four times the highest loading rate used in this study and found that there were negligible rate effects on the shear strength of TDA. Accordingly, the different loading/unloading rates are not expected to affect the TDA compression response.

Table 4.2. Testing protocol for each specimen.

Specimen	Load application mode	Loading rate [mm/min]	Unloading rate [mm/min]
QS01	Displacement-control	7.62	15.24
QS02	Displacement-control	7.62	15.24
QS03	Displacement-control	12.70	25.40
QS04	Displacement-control	12.70	25.40

Chapter 5 EXPERIMENTAL RESULTS

Overview

The experimental results from this study are summarized in the following sections for the steel pile in three TDA layers having different widths *S*, and in Appendix D for the concrete pile in a TDA layer with a single width *S*. The results that are presented for each test include:

- Load-displacement curves for the two actuators attached to the rigid moveable wall;
- Average load on the wall versus the horizontal position of the four corners of the rigid moveable wall;
- Shear force at the base of the pile (the maximum force induced in the pile from the wall movement) versus the displacement at the head of the pile;
- Strain and curvature of the pile at different locations versus the induced shear force in the pile; and
- Heave of the TDA surface layer as measured by images of settlement plates on the TDA surface.

General comments on the testing results are presented in Section 5.6, and the results are interpreted in Chapter 6 to understand the deformation response of the steel and concrete piles in TDA and to determine *P-y* curves for preliminary analyses of lateral spreading mitigation.

Records from testing specimen QS01.

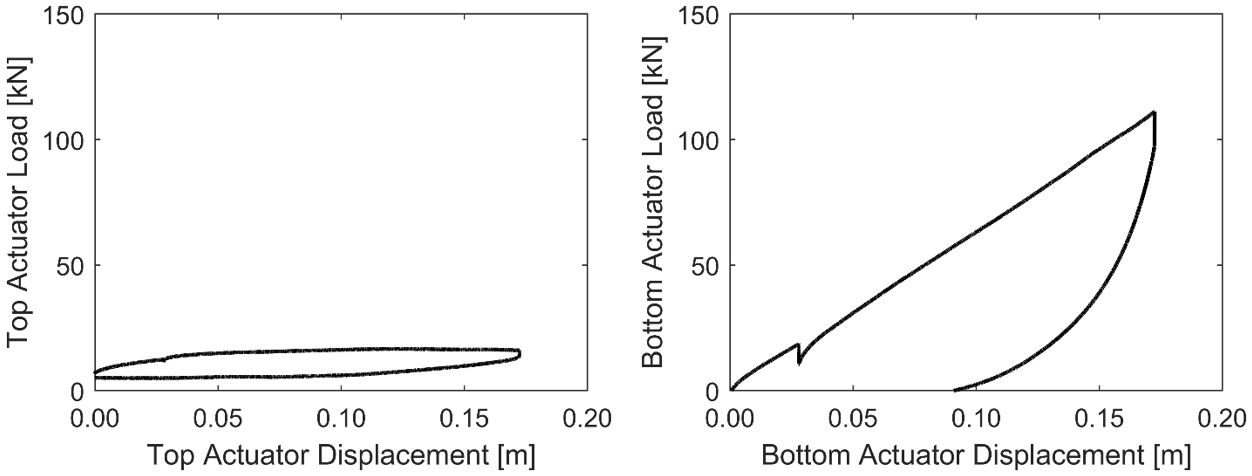

Figure 5.1. Actuator force-displacement curves: (a) Top actuator; (b) Bottom actuator.

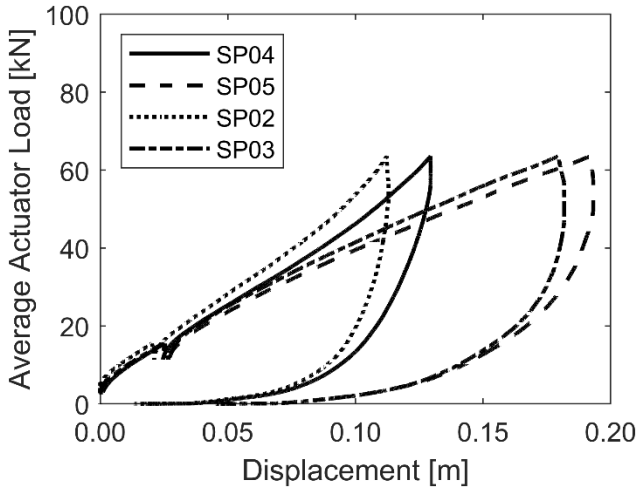

Figure 5.2. Load-deformation response of the steel wall at the four corners.

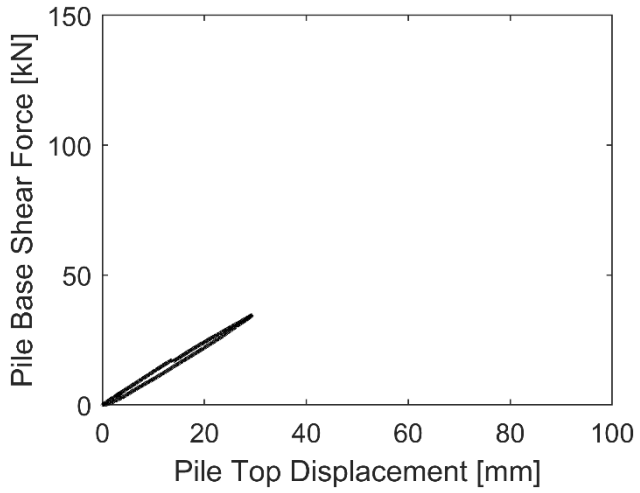

Figure 5.3. Pile top displacement response as a function of the known shear force at the base of the pile.

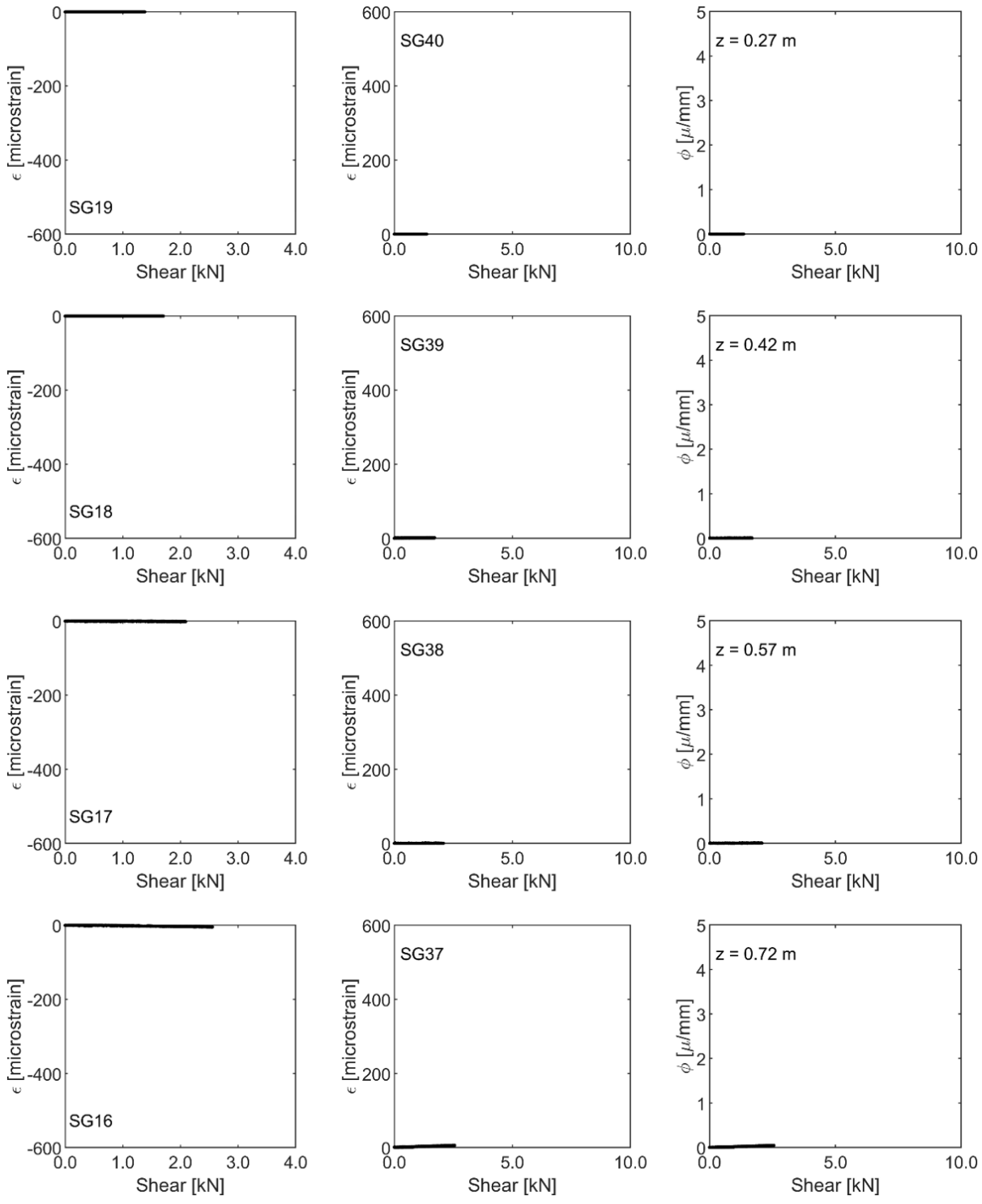

Figure 5.4. Measured strain and curvature at z = 0.27 to 0.72 m

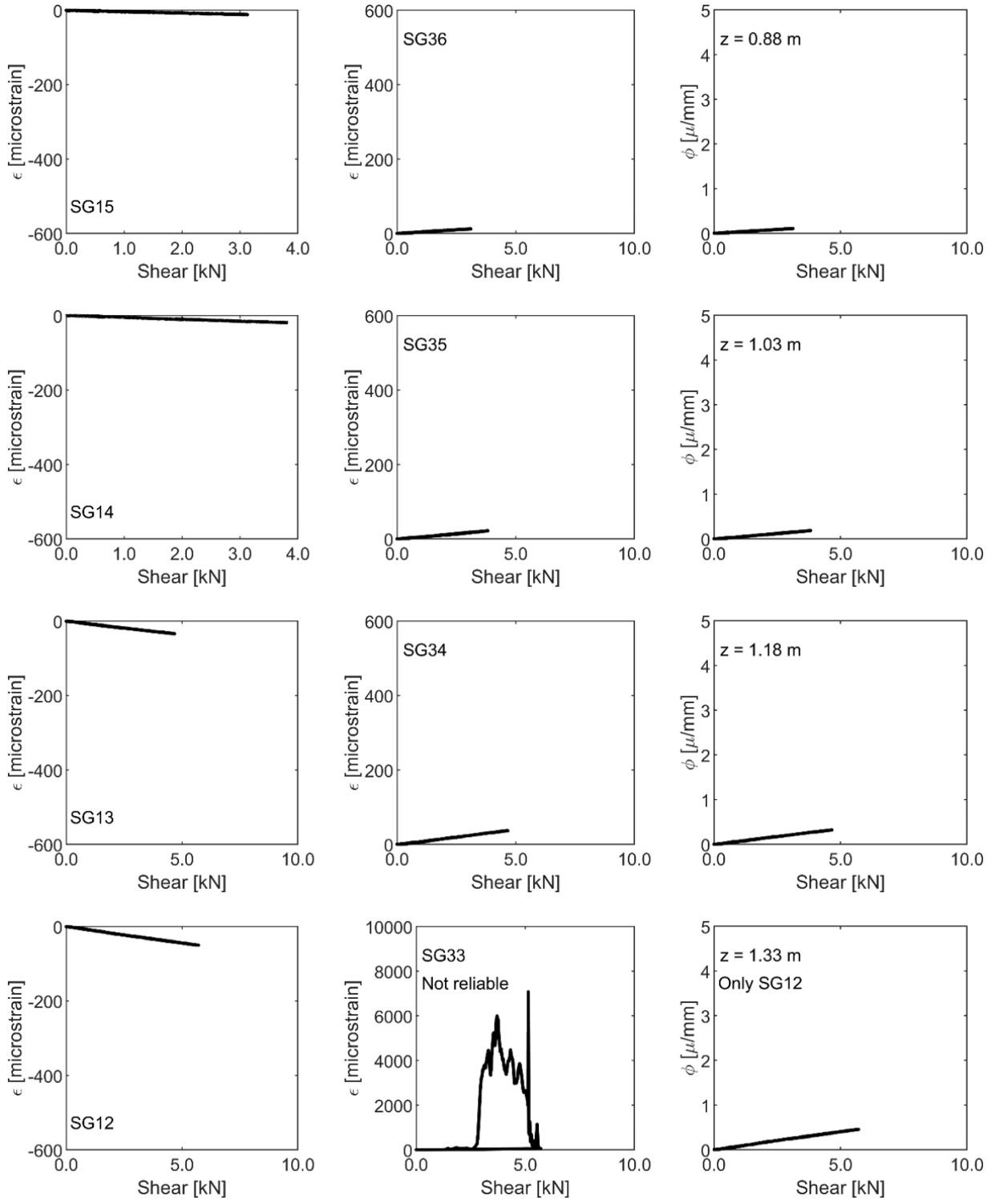

Figure 5.5. Measured strain and curvature at z = 0.88 to 1.33 m

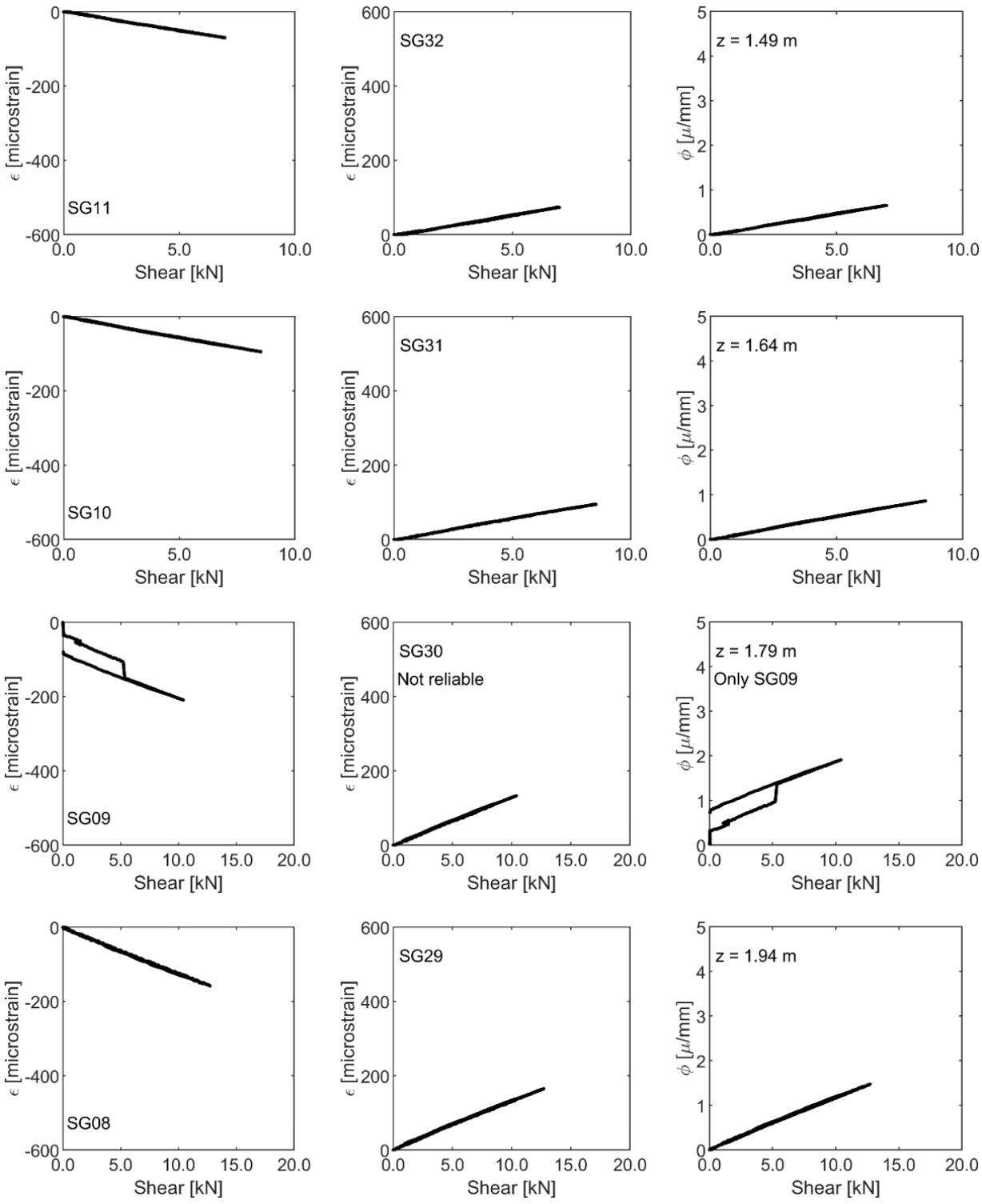

Figure 5.6. Measured strain and curvature at z = 1.49 to 1.94 m

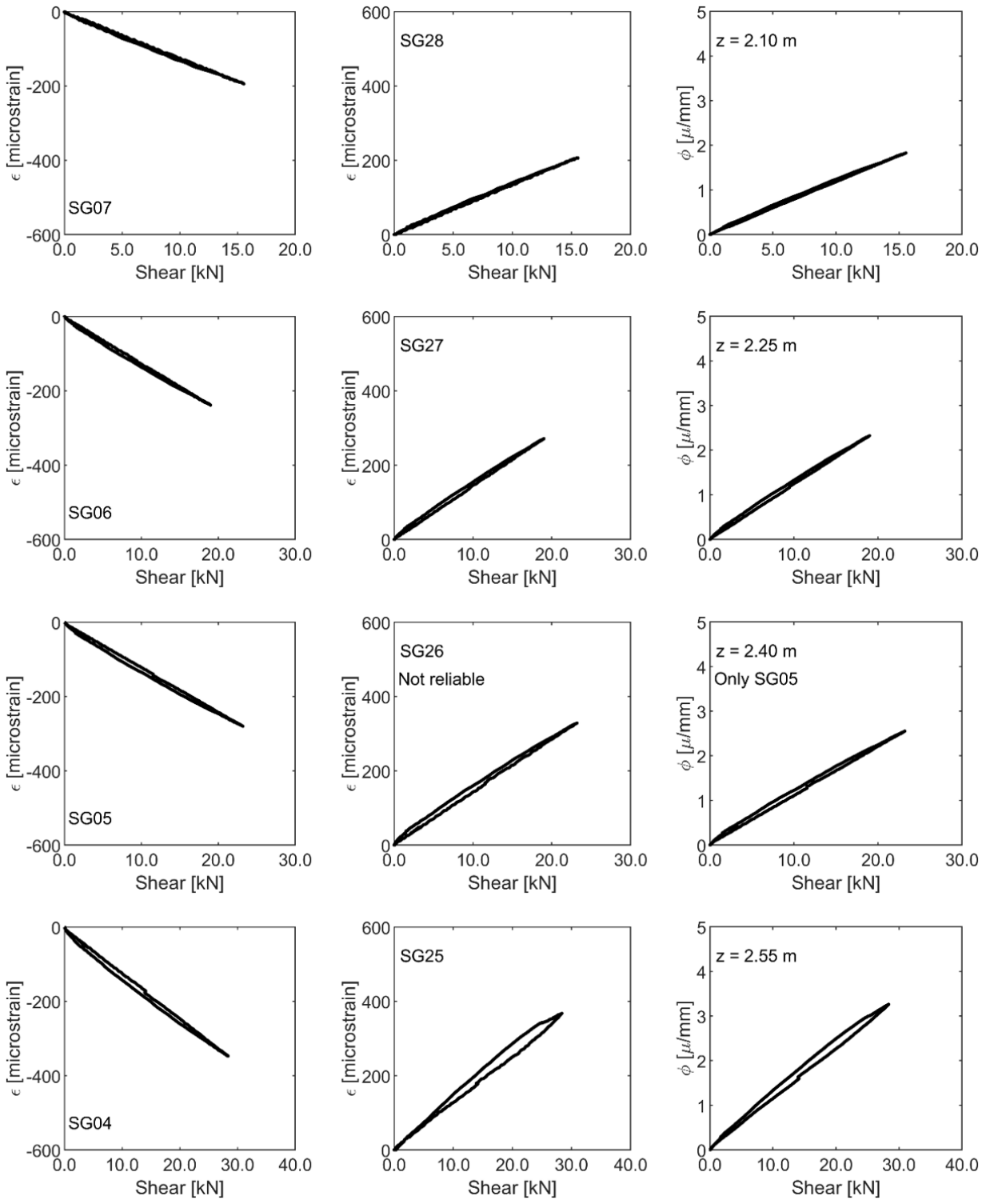

Figure 5.7. Measured strain and curvature at z = 2.10 to 2.55 m

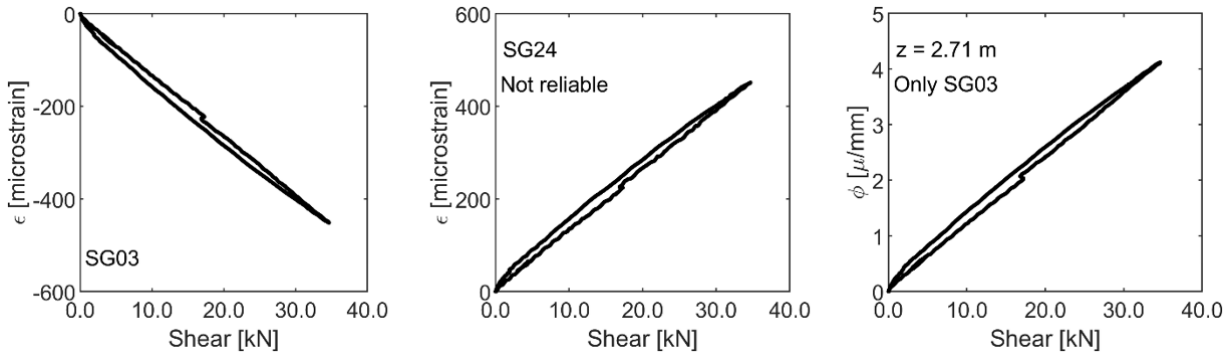

Figure 5.8. Measured strain and curvature at z = 2.71 m

(a) **(b)** **(c)**

Figure 5.9. Referential level of the TDA surface in specimen QS01 at: (a) Start of test, (b) Maximum load, and (c) End of test.

Records from testing specimen QS02.

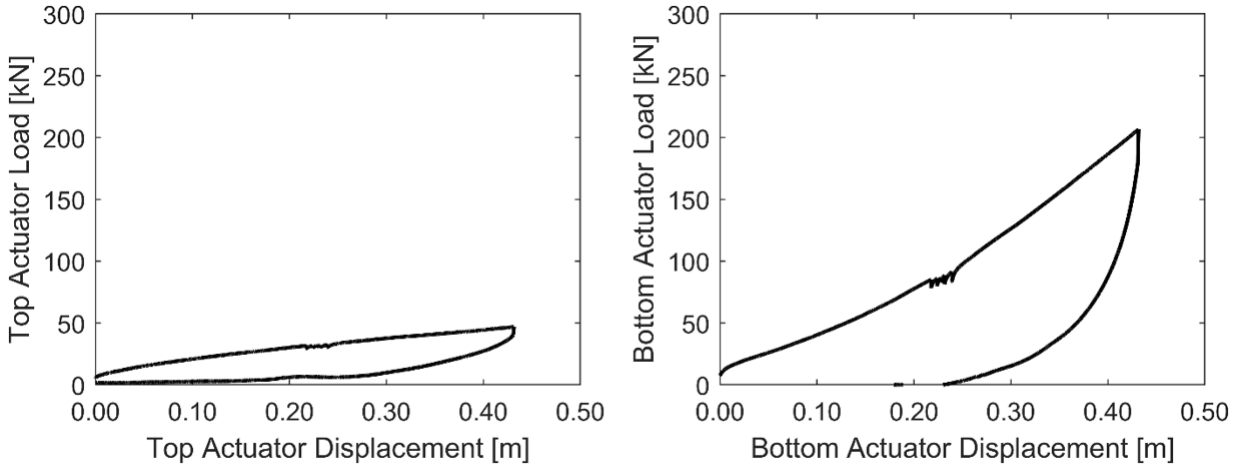

(a) **(b)**

Figure 5.10. Actuator force-displacement curves: (a) Top actuator; (b) Bottom actuator

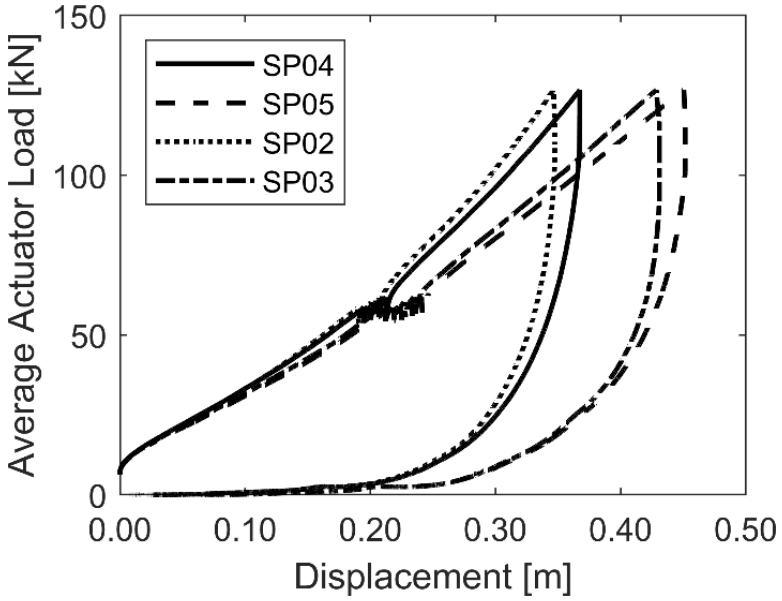

Figure 5.11. Load-deformation response of the steel wall at the four corners.

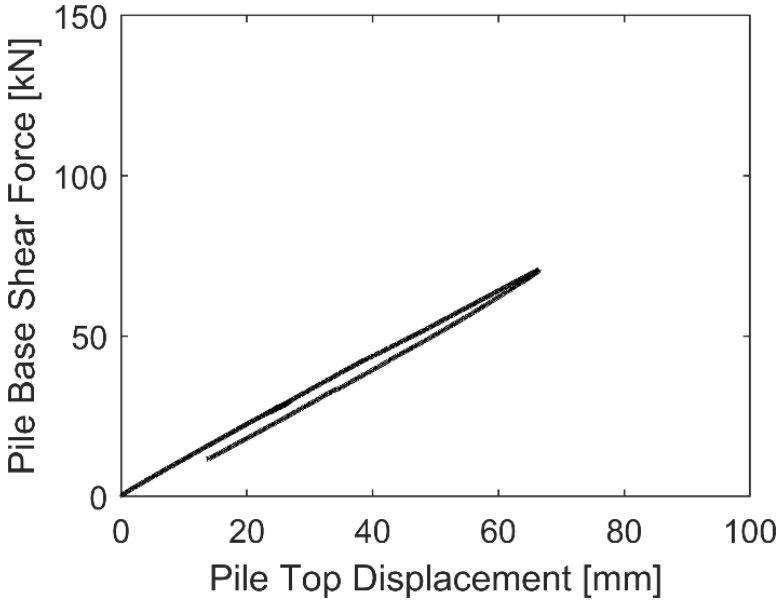

Figure 5.12. Pile top displacement response as a function of the known shear force at the base of the pile.

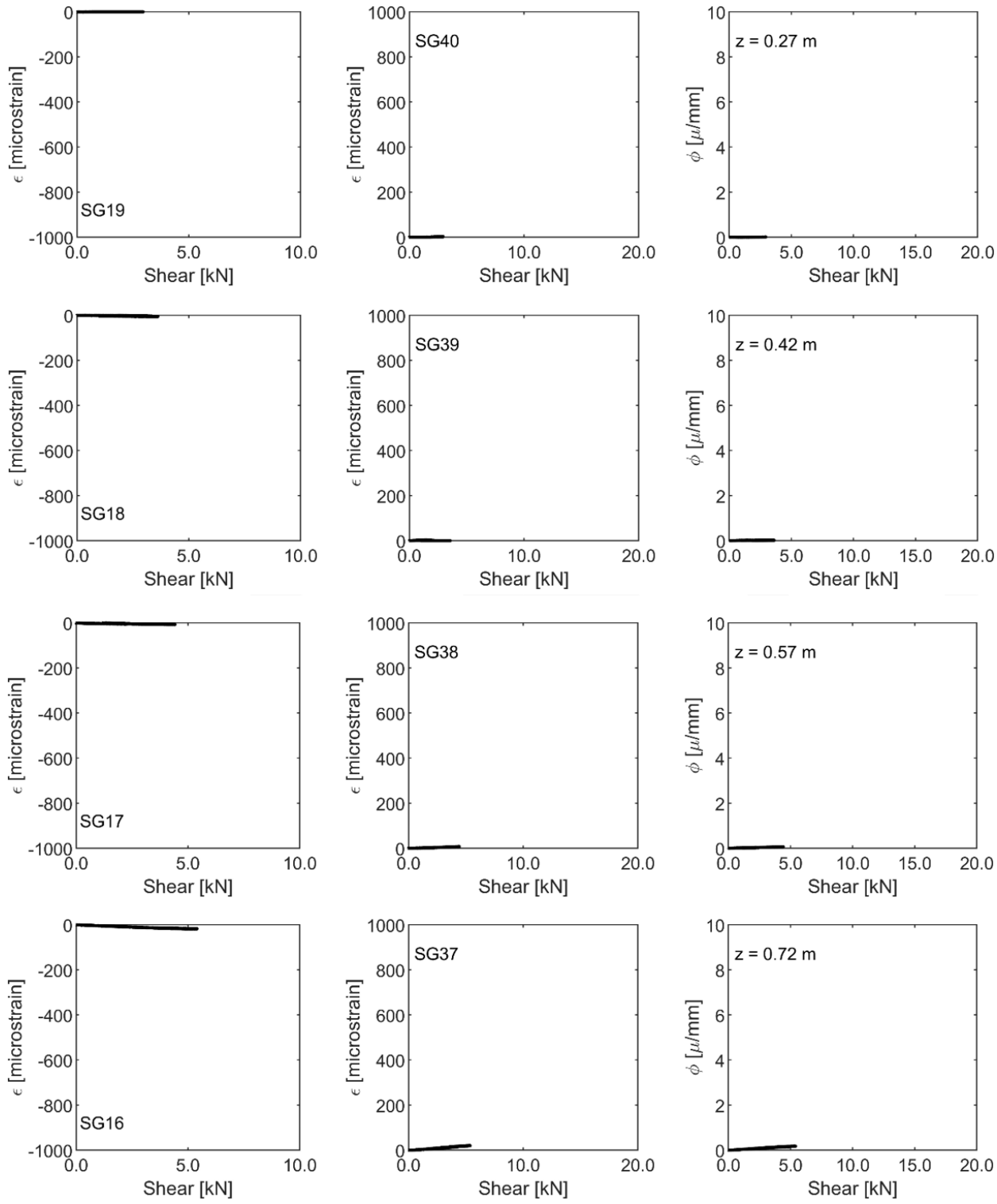

Figure 5.13. Measured strain and curvature at z = 0.27 to 0.72 m

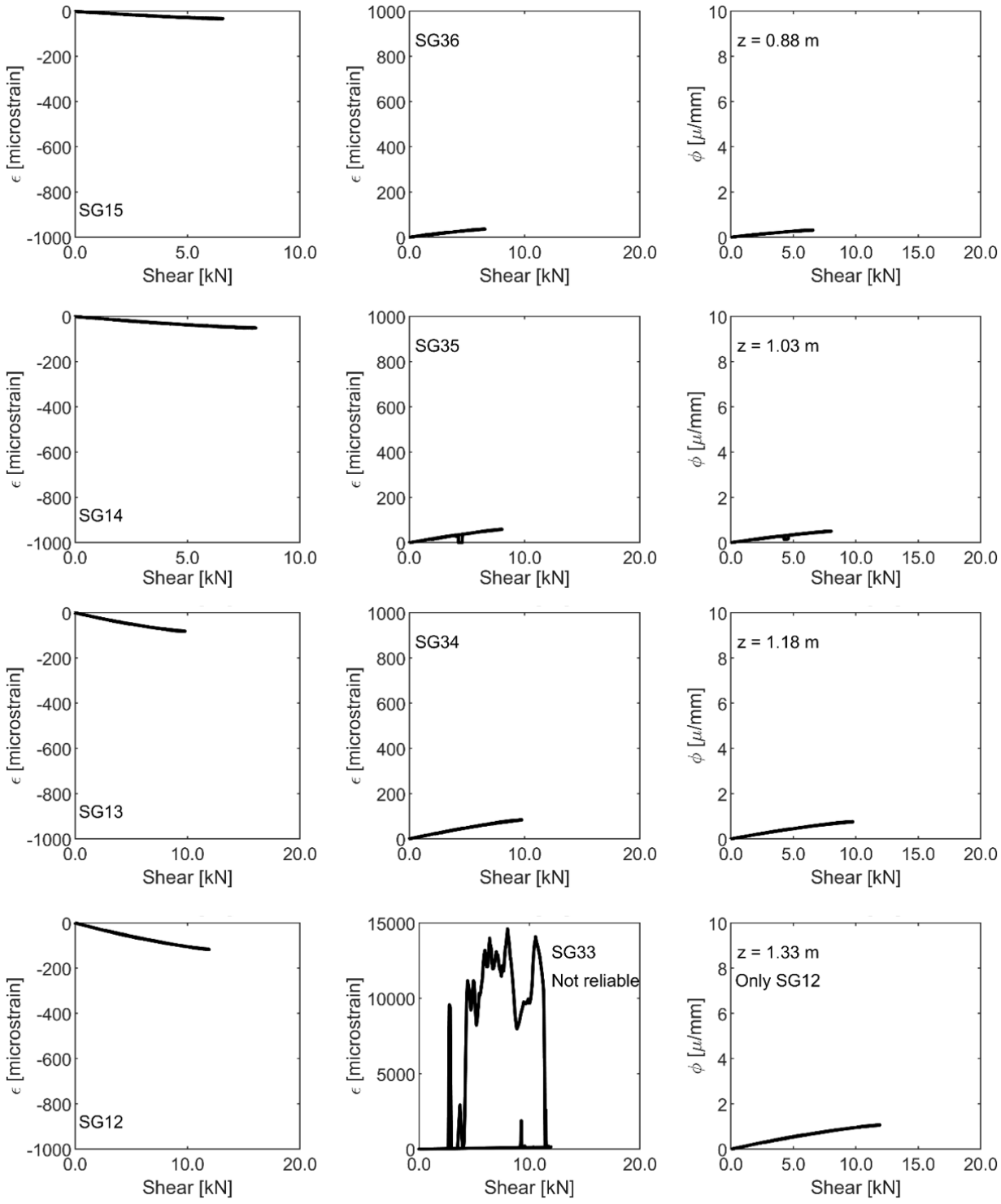

Figure 5.14. Measured strain and curvature at z = 0.88 to 1.33 m

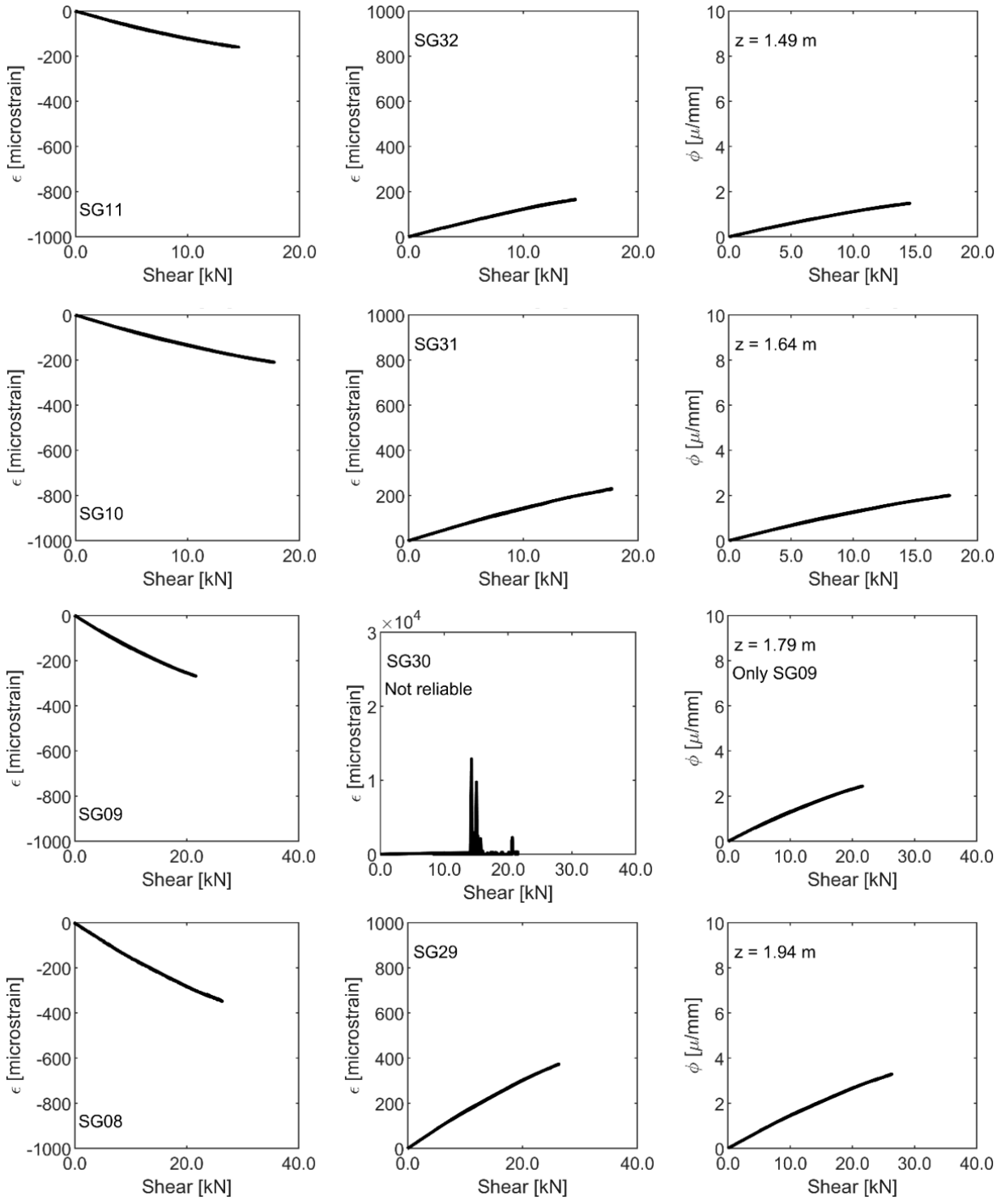

Figure 5.15. Measured strain and curvature at z = 1.49 to 1.94 m

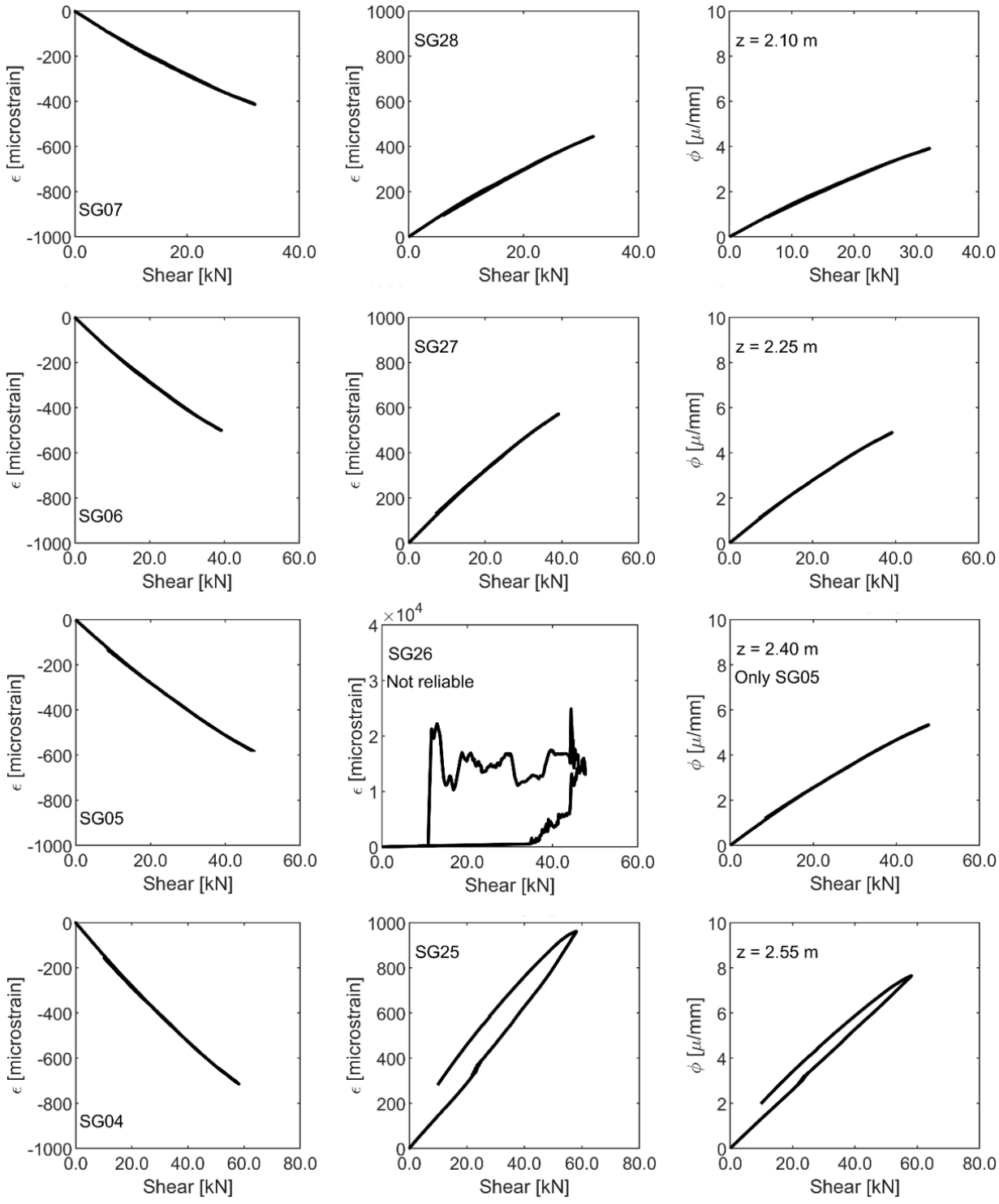

Figure 5.16. Measured strain and curvature at z = 2.10 to 2.55 m

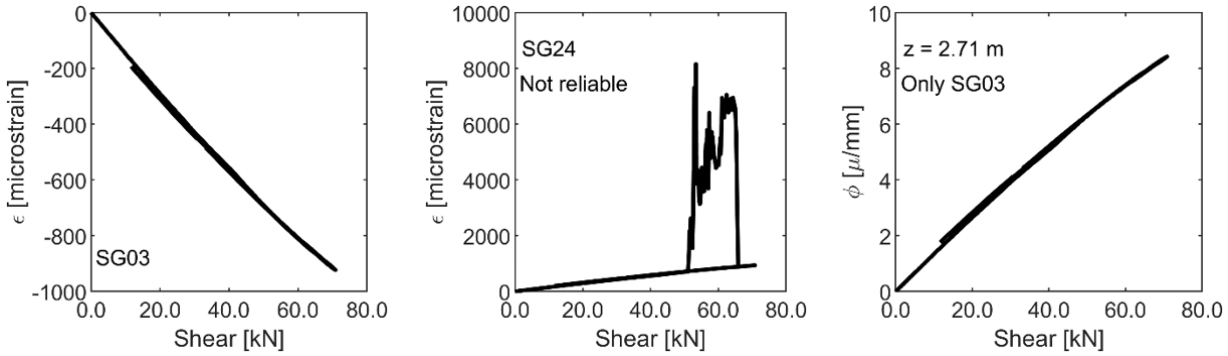

Figure 5.17. Measured strain and curvature at z = 2.71 m

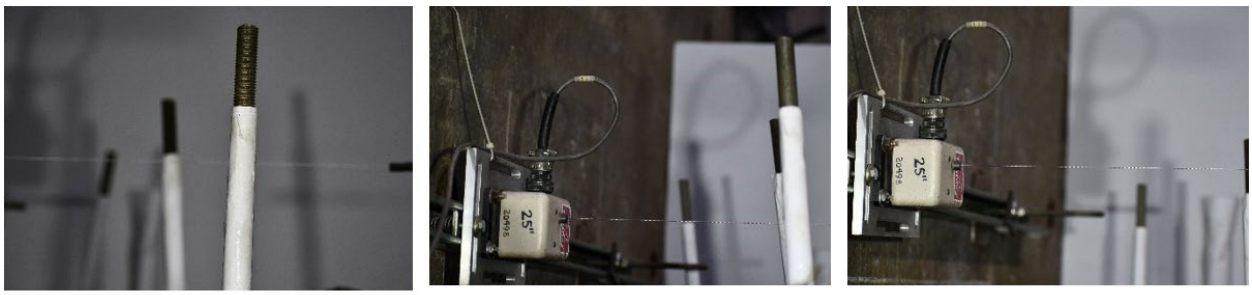

(a) **(b)** **(c)**

Figure 5.18. Referential level of the TDA surface in specimen QS02 at: (a) Start of test, (b) Maximum load, and (c) End of test.

Records from testing specimen QS03.

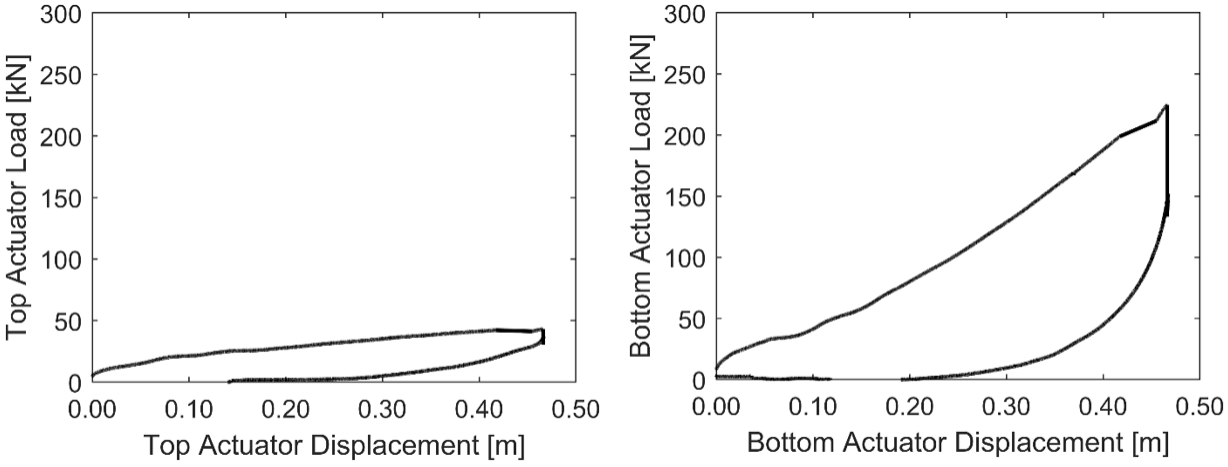

(a) **(b)**

Figure 5.19. Actuator force-displacement curves: (a) Top actuator; (b) Bottom actuator.

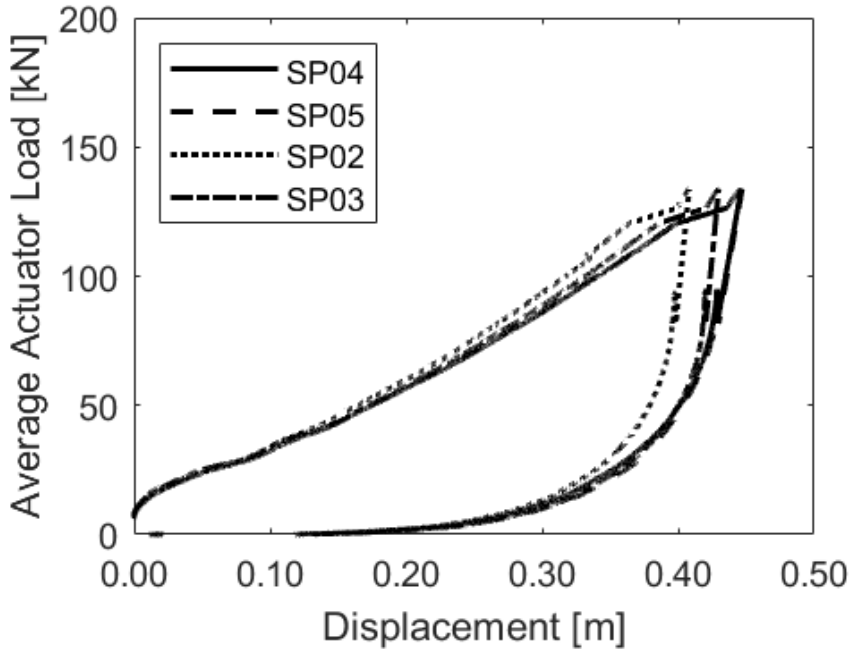

Figure 5.20. Load-deformation response of the steel wall at the four corners.

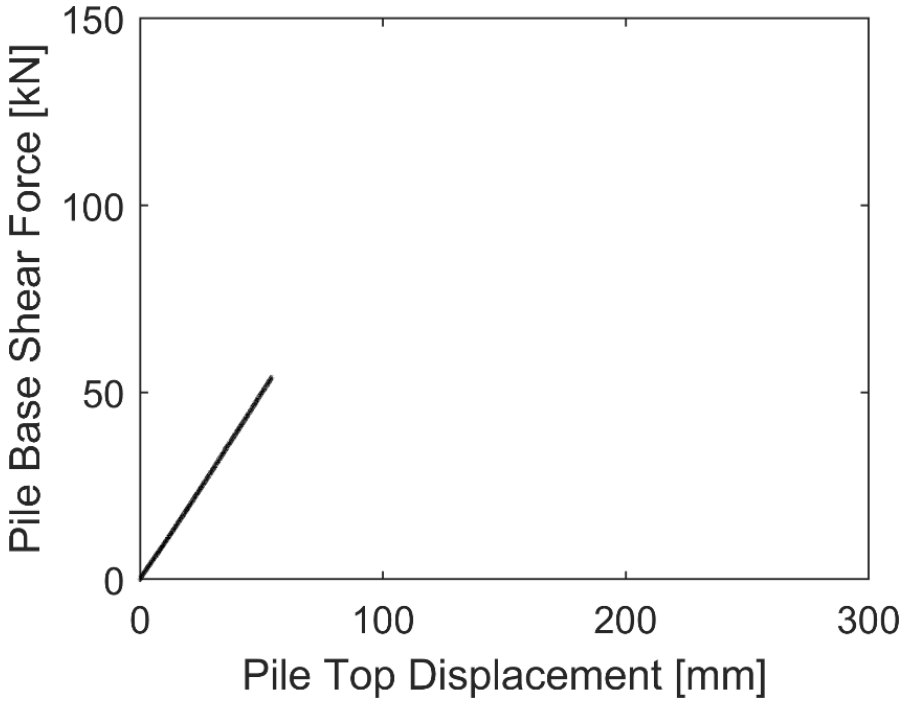

Figure 5.21. Pile top displacement response as a function of the known shear force at the base of the pile.

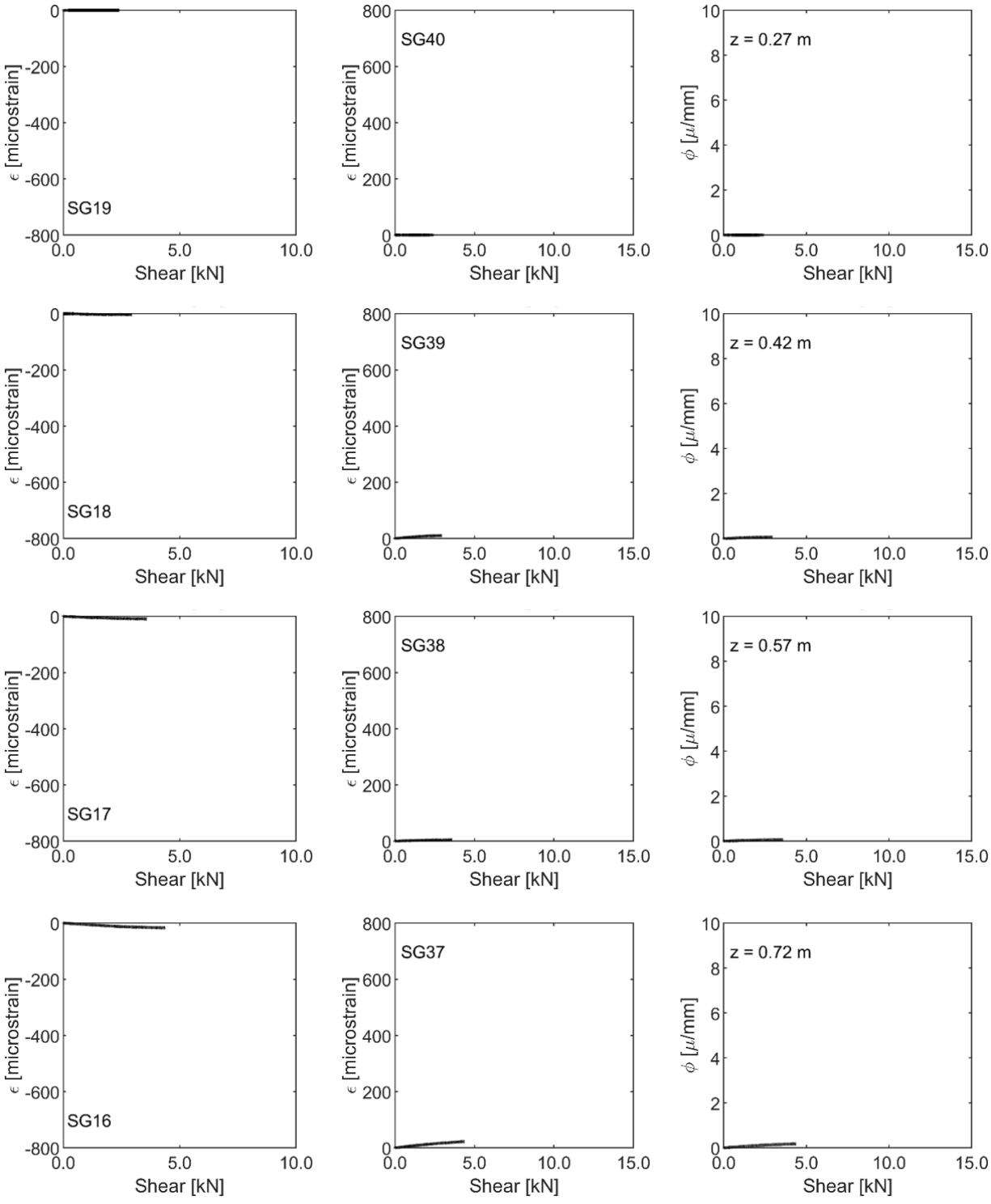

Figure 5.22. Measured strain and curvature at z = 0.27 to 0.72 m

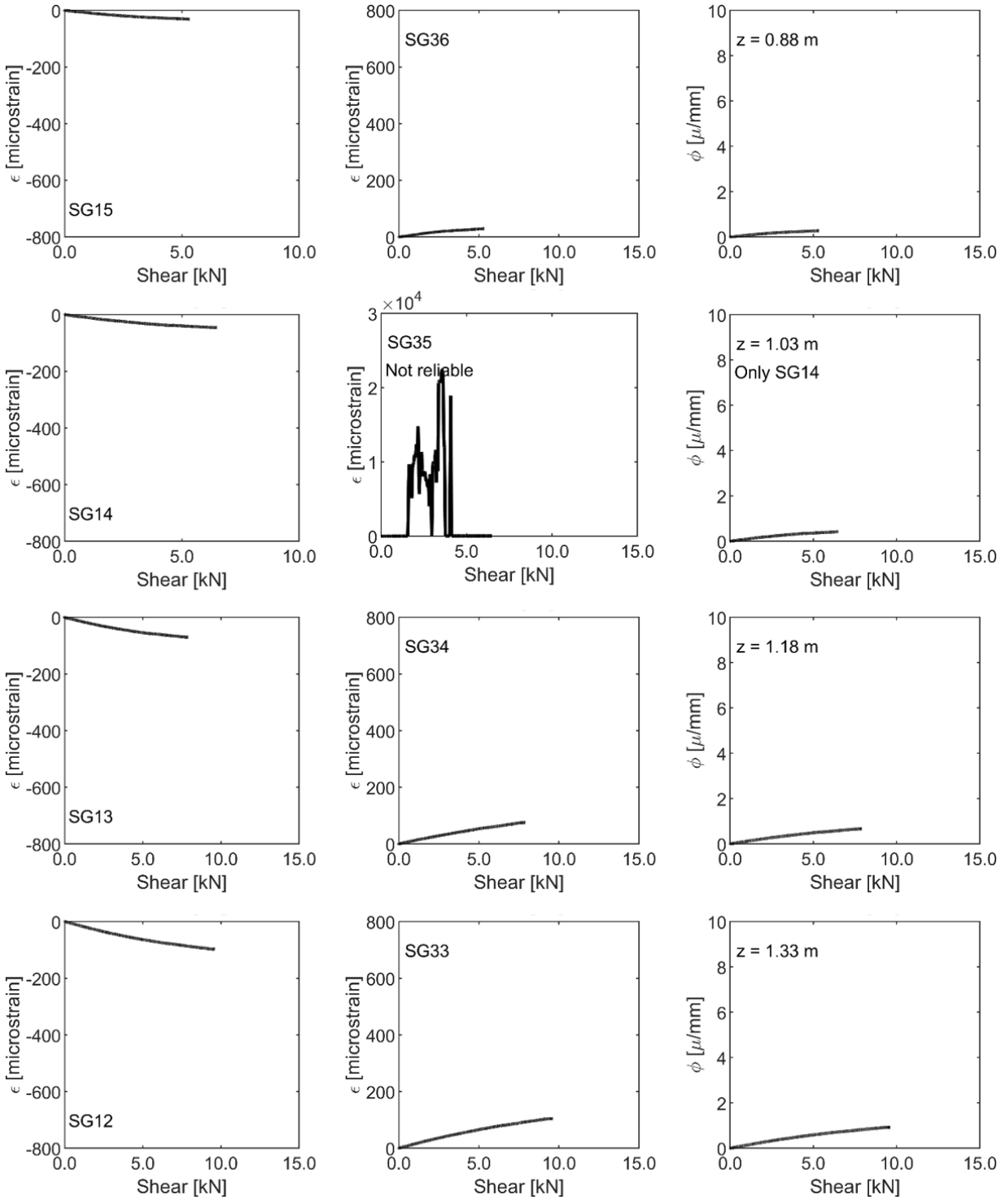

Figure 5.23. Measured strain and curvature at z = 0.88 to 1.33 m

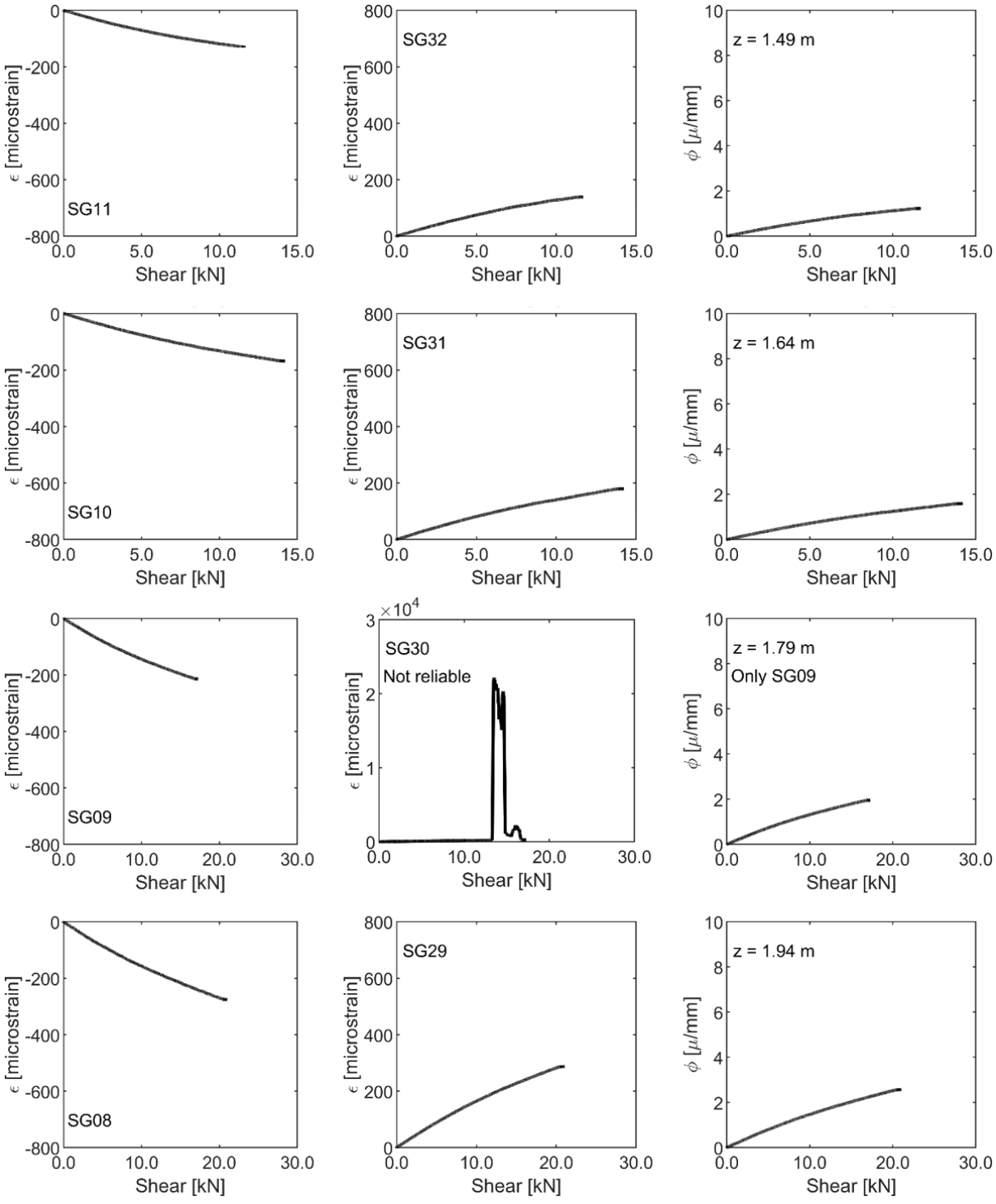

Figure 5.24. Measured strain and curvature at z = 1.49 to 1.94 m

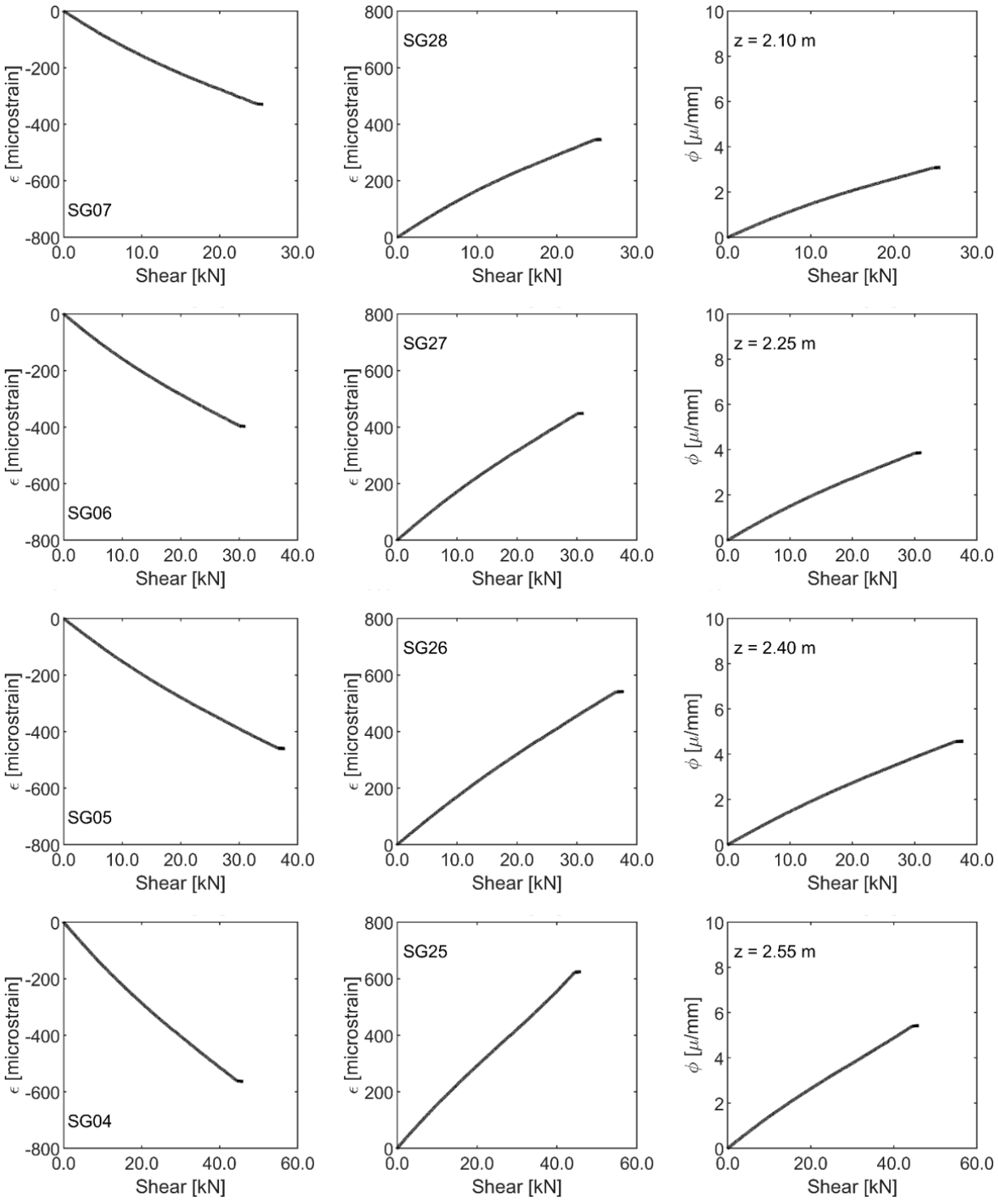

Figure 5.25. Measured strain and curvature at z = 2.10 to 2.55 m

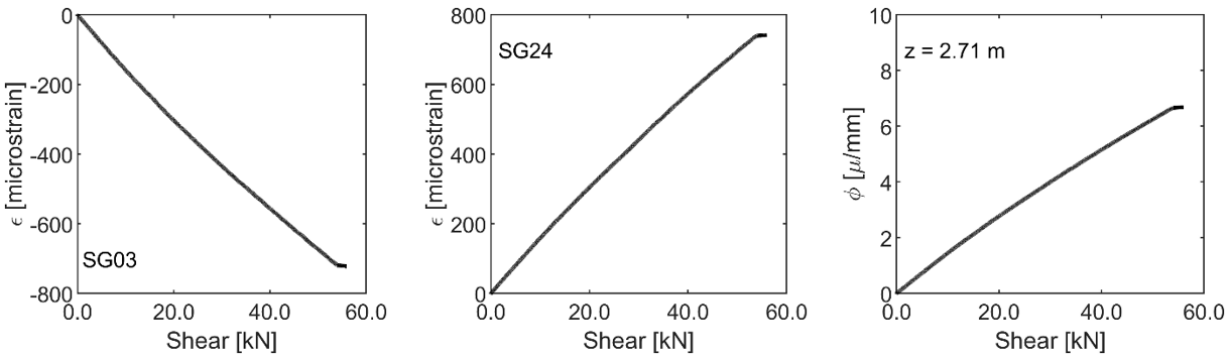

Figure 5.26. Measured strain and curvature at z = 2.71 m

(a) **(b)** **(c)**

Figure 5.27. Referential level of the TDA surface in specimen QS03 at: (a) Start of test, (b) Maximum load, and (c) End of test.

Records from testing specimen QS04.

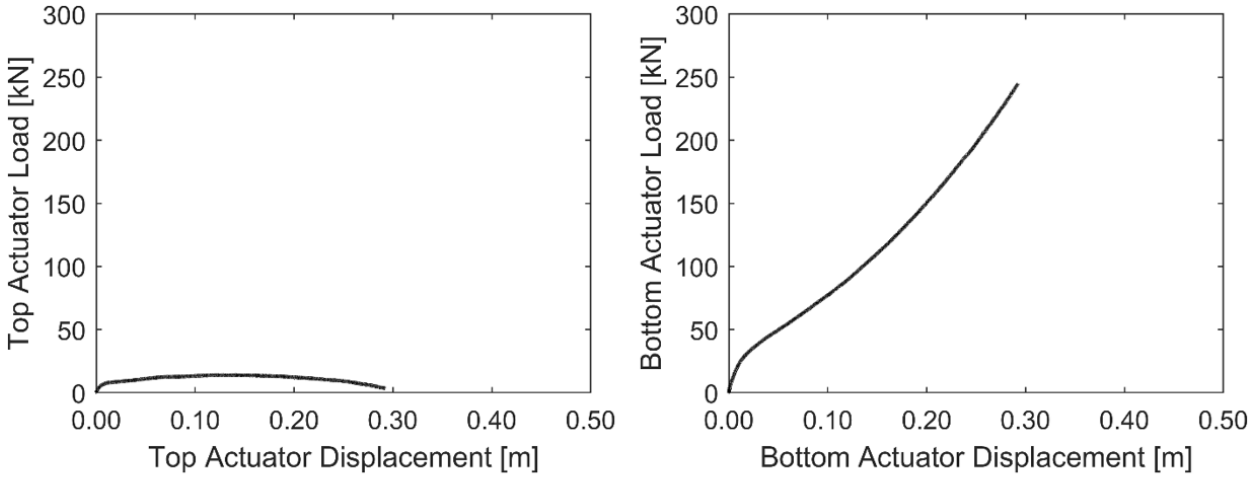

(c) **(d)**

Figure 5.28. Actuator force-displacement curves: (a) Top actuator; (b) Bottom actuator.

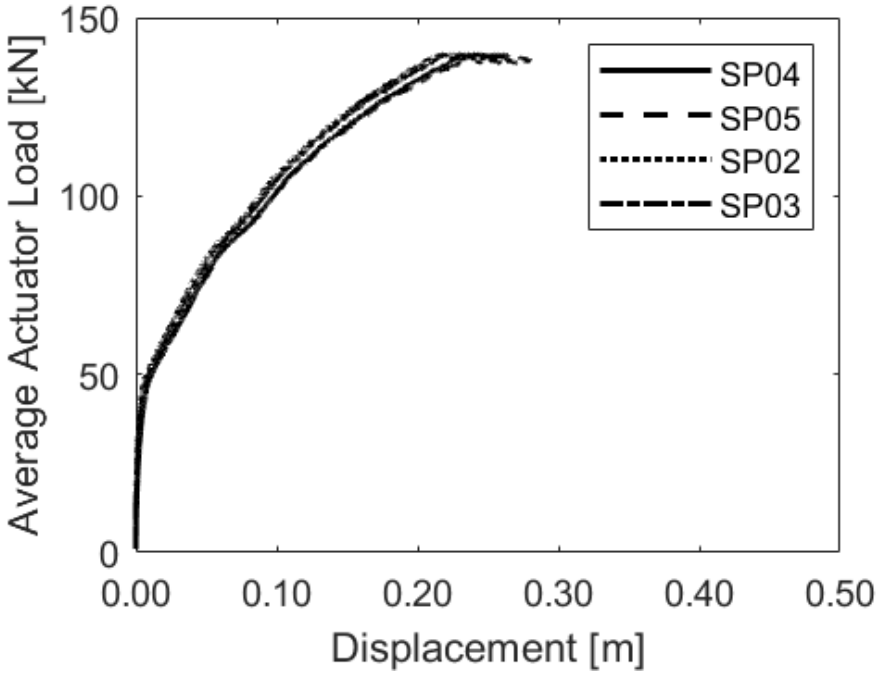

Figure 5.29. Load-deformation response of the steel wall at the four corners.

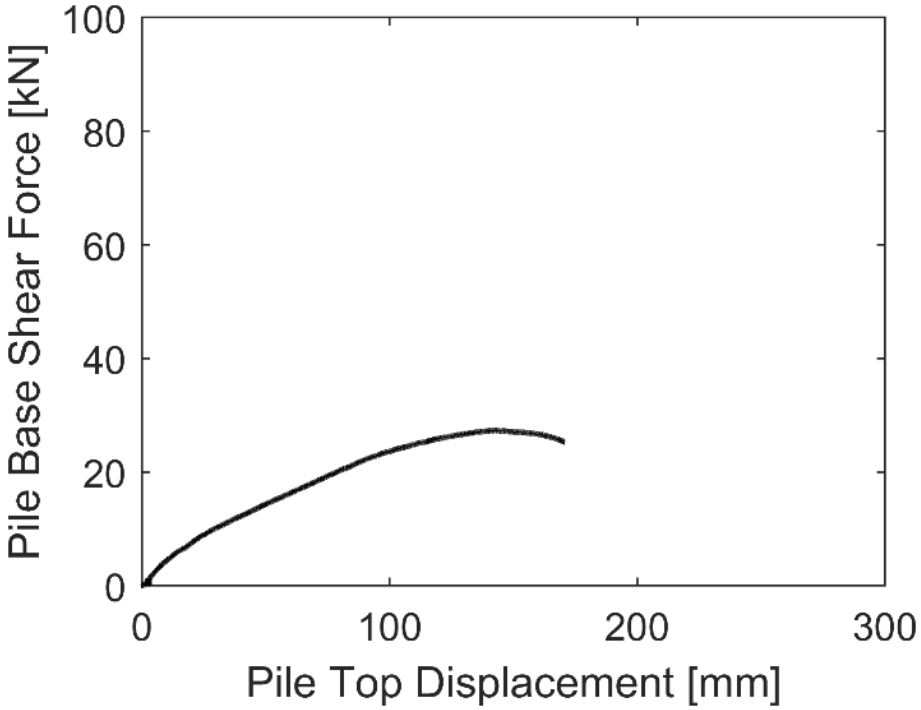

Figure 5.30. Pile top displacement response as a function of the known shear force at the base of the pile.

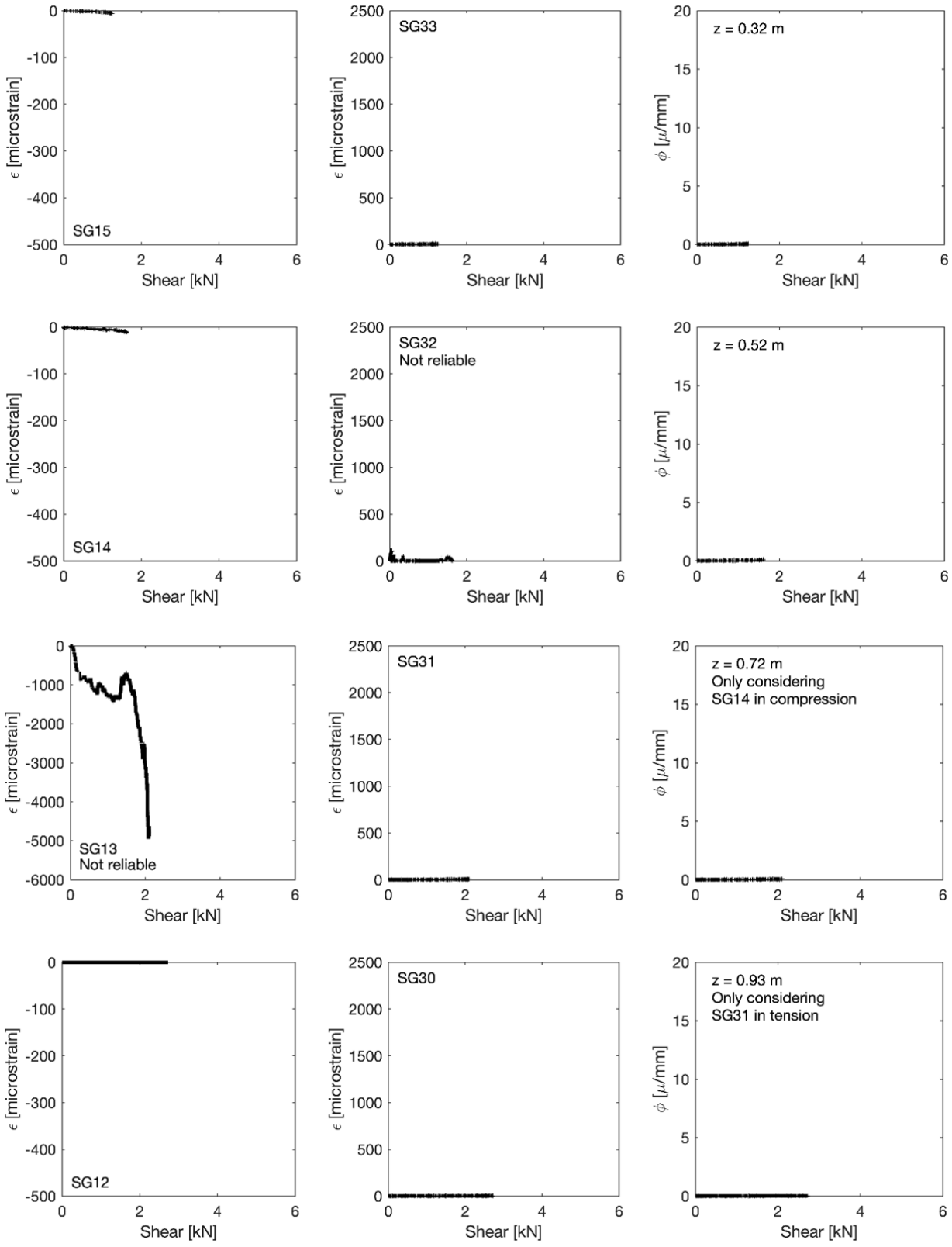

Figure 5.31. Measured strain and curvature at z = 0.32 to 0.93 m

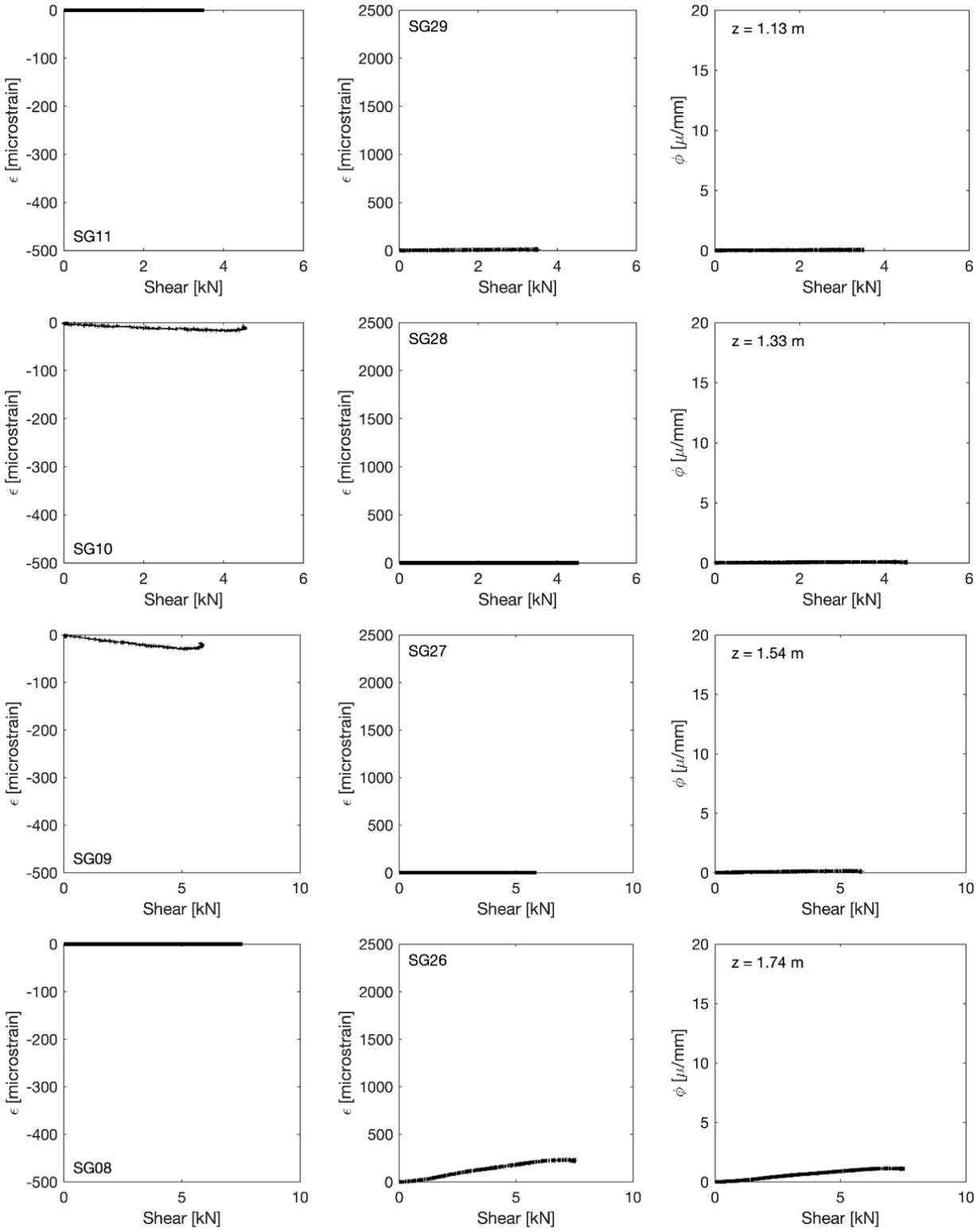

Figure 5.32. Measured strain and curvature at z = 1.13 to 1.74 m

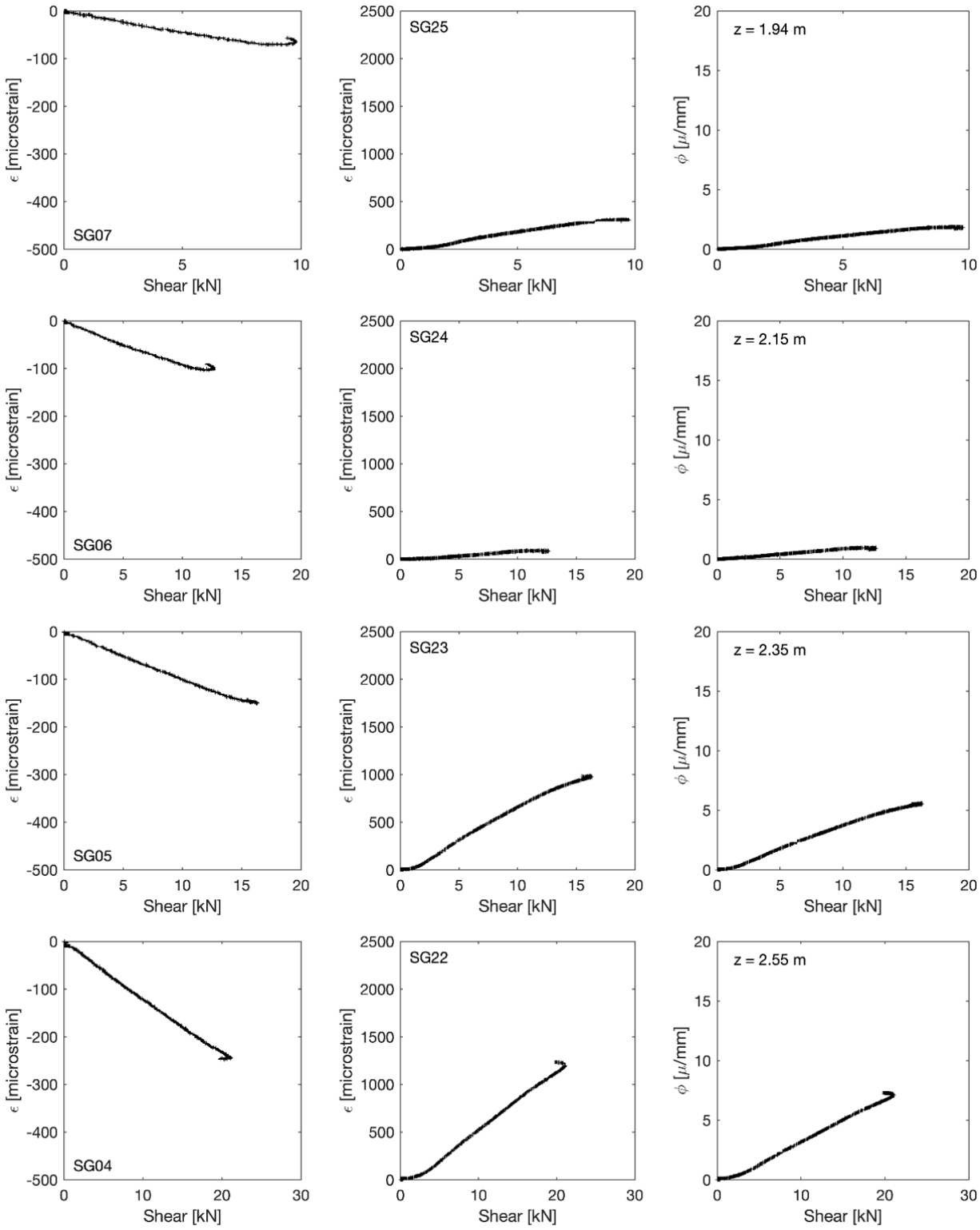

Figure 5.33. Measured strain and curvature at z = 1.94 to 2.55m

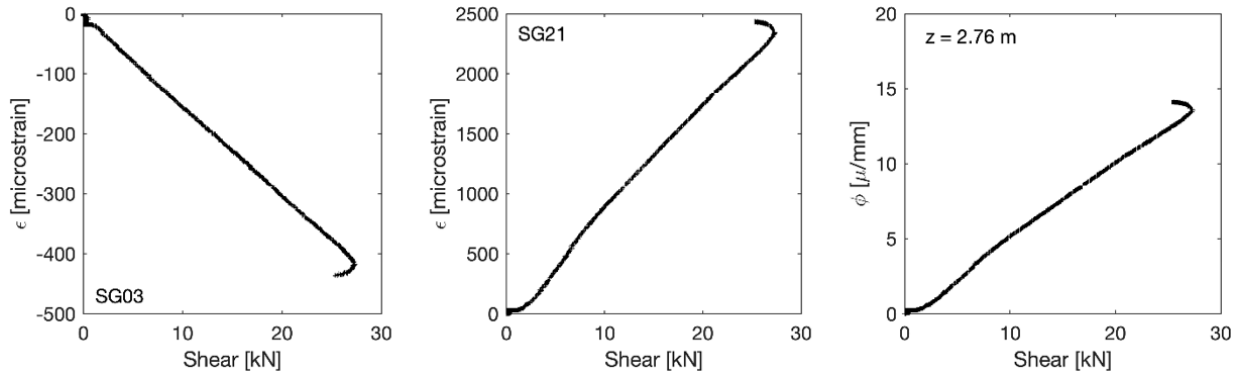

Figure 5.34. Measured strain and curvature at z = 2.76 m

General Comments of Results

Load-displacement curves for the two actuators attached to the rigid moveable wall

The two actuators were operated in displacement-control mode at the same displacement rate with the objective of maintaining the wall in a fully vertical orientation while pushing the TDA. This approach generated different loads in both actuators. The TDA is generally stiffer at larger depths, so the bottom actuator had to apply larger loads than the top actuator to maintain the same displacement. The maximum applied load is defined as the sum of the loads measured by both actuators. In Specimen QS01, the loading was stopped when one of the strain gages reached a value of 1200 me, which was estimated to be the theoretical yielding strain of the pile. However, later analysis indicated that the pile had not yielded and that greater loads could have been applied. In Specimens QS01, QS03, and QS04, the tests were continued until reaching the maximum capacity of the bottom actuator of 245 kN.

Average load on the wall versus the horizontal position of the wall corners

The moving wall shown in Figure 4.8 was heavily reinforced in the vertical direction and lightly reinforced in the horizontal direction. Due to the configuration of the wall, significant resources would have been required to heavily reinforce the wall in the horizontal direction. Therefore, instead of reinforcement, four string potentiometers were placed at the corners of the wall to measure the deflection of the wall. The measured wall displacements indicated almost null deflection in the vertical direction, but in specimens QS01 and QS02 deflections in the horizontal direction were measured on the order of 100 mm. For this reason, the average wall displacement was defined as the average of both actuator displacements. This was deemed to be a reasonable definition as the pile is located at the center of the wall so the TDA deformation in the vicinity of

the pile is associated primarily with the center of the moveable wall. In specimens QS03 and QS04, the moveable wall behaved in a rigid manner with negligible deformations in the vertical and horizontal directions.

Shear force at the base of the versus the displacement at the pile head

The pile head displacement was measured independently using a string potentiometer, which represents the maximum displacement of the pile as the head of the pile was unfixed and free to move while the base of the pile was fixed. It was not possible to measure the shear force at the head of the pile, so to generate a force-displacement curve the maximum shear force at the base of the pile was plotted against the pile head displacement. This force-displacement curve is thus not representative of the pile response but is useful to see the relative differences in pile displacement response in the four tests. In the three tests on the steel pile, this force-displacement curve indicates that the pile behaved in a linear elastic manner, while in the test on the concrete pile a yielding response was observed after a pile head displacement of 150 mm.

Strain and curvature of the pile at different locations versus induced shear force

The strain gages all behaved in a linear elastic manner in the different tests. In each of the tests one or two of the strain gages showed an erratic response indicating some damage during TDA placement. These damaged gages were not used in the analysis of pile bending.

Heave of the TDA surface layer

The settlement plates indicate that the TDA layer experienced some vertical heave during lateral compression. Three settlement plates on the TDA surface were used to monitor the heave. The settlement plates were placed on top of the TDA near the strong wall where the predominant heave was expected. Although the settlement plates were not attached to displacement sensors, they were monitored by a camera that took one picture per minute. The heave was formed non-uniformly along the entire surface of the TDA. The visual observation during testing and the pictures taken indicated that, upon loading, TDA particles near the surface of the layer moved laterally in the loading direction while progressively “heaving” upward. It was confirmed that the predominant heave occurred in the TDA nearest to the strong wall, with an average uplift of around 70 mm. During the unloading stage, the TDA moved in the same direction of unloading while settling. The final height of TDA was found to be lower than the initial height with a settlement of

around 40 mm (with respect to the initial height of the TDA). These results suggest that the TDA densified after testing. Further all specimens experienced a residual horizontal gap of 100 mm on average between the TDA and the pile top after unloading, as shown in the pictures in Figure 5.35. This gap might reduce the compression response of the TDA-pile system under cyclic loading, therefore, the conclusions from this project cannot be applied to cyclic loading.

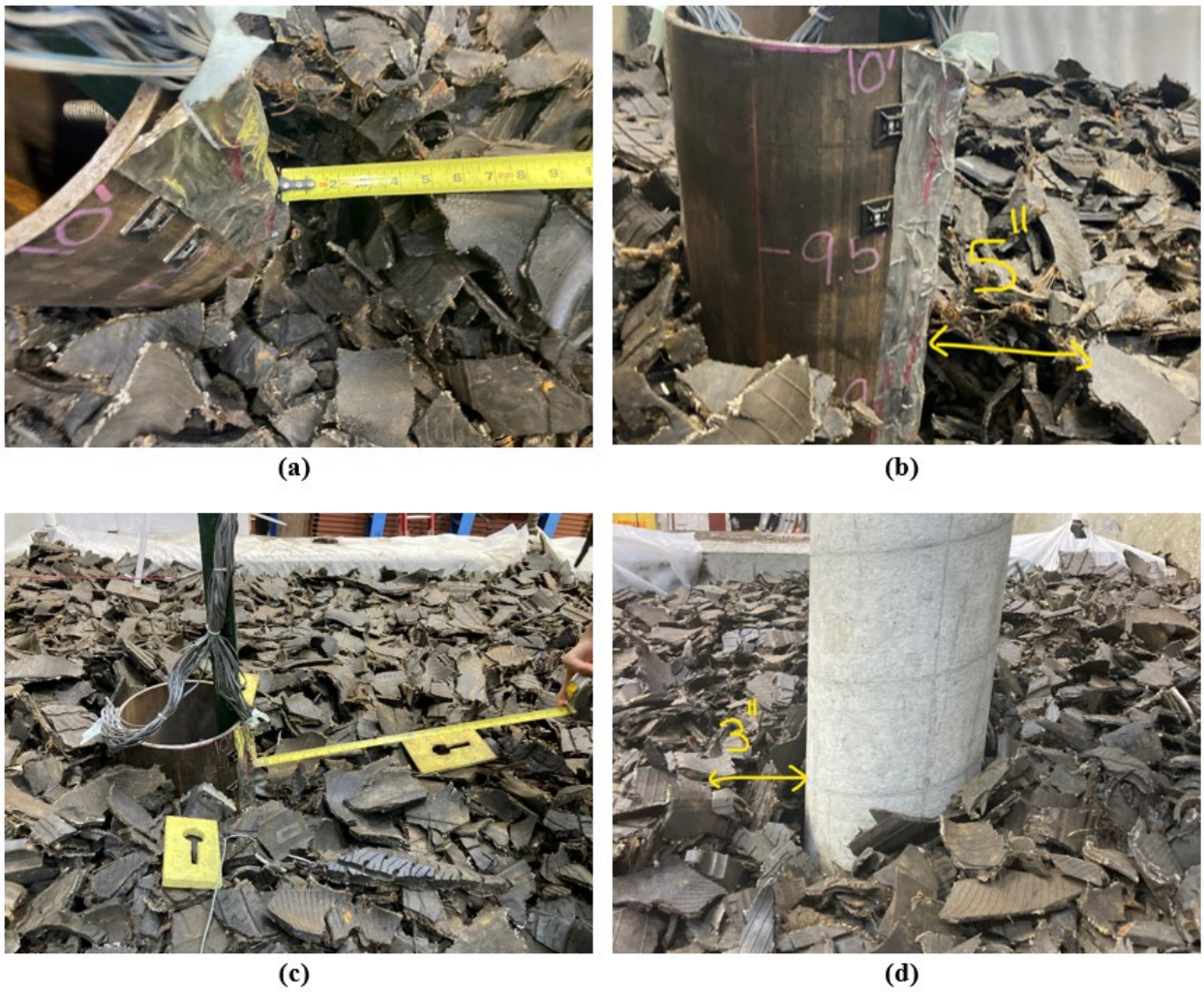

(a) (b)

(c) (d)

Figure 5.35. Residual gap after testing of specimens (a) QS01, (b) QS02, (c) QS03, (d) QS04.

Chapter 6 ANALYSIS

Lateral spreading analysis

The maximum displacements of the horizontal wall in the different tests can be assumed to represent the horizontal displacements of the non-liquefiable crust in an earthquake. The TDA layers evaluated in this study were able to absorb this horizontal displacement through a combination of both TDA compression and heave of the TDA surface. A summary of the deformation characteristics from the tests is shown in Table 6.1. As the tested piles have a fixed base, the TDA near the bottom of the pile experienced a compression that was equal to the same amount as the average wall displacement, which was nearly 0.5 m in Test QS03. The calculated shear force at the base of the pile was found to be significantly smaller than the maximum applied load, indicating that the TDA absorbs the applied stresses. As the head of the pile can deform during application of the horizontal displacements due to bending, the TDA compression at the pile head reflects the amount of deformation absorbed by the TDA that would have otherwise caused the pile to deform. The results from the first three tests on the steel pile indicate that when wall displacements up to 460 mm are applied to the TDA layer, only 62 mm of movement at the pile head occurred without causing the pile to yield. This corresponds to a TDA layer compression at the pile head of nearly twice the pile diameter. If the pile had been surrounded by a stiff soil layer experiencing lateral spreading, it is likely that a larger pile head displacement closer to the average wall displacement would have occurred. In the case of the concrete pile, a slightly lower average wall displacement was applied, but a large TDA compression at the pile head was still observed that is slightly less than twice the pile diameter. Overall, the summary of the deformation characteristics indicates that TDA is a flexible material that can accommodate large down-slope displacements of an un-liquefied crust and mitigate horizontal pressures on embedded piles.

Table 6.1. Summary of the deformation characteristics of the TDA layer during testing.

Test	Pile type	Pile diameter D (mm)	TDA width *S* (mm)	Max. applied load (kN)	Shear force at pile base (kN)	Average wall disp. (mm)	Pile head displ. (mm)	TDA compression at pile head (mm)
QS01	Steel pipe	219	660	130	40	175	32	143
QS02	Steel pipe	219	1461	250	60	420	74	346
QS03	Steel pipe	219	1880	260	55	460	62	398
QS04	Concrete	203	1226	250	25	300	166	134

Pile bending analysis

The experimental *P-y* curve can be developed from strain measurements along the pile shaft through the mathematical expression of the bending moment distribution to obtain the TDA reaction and lateral displacement along the pile. The bending moment (M) along the pile depth (z) can be calculated from recorded flexural strain measurements as follows:

$$M = \phi EI \tag{6.1}$$

where ϕ = curvature of the pile (the ratio of the difference between the compression and tension strains measured at a given depth to the distance between the two corresponding strain gauges, L^{-1}); M = bending moment at depth z (FL); and EI = flexural modulus of the pile (FL^2).

From the determined bending moment distribution along the pile, the TDA reaction (P) and lateral displacement (y) can be calculated using the following equations:

$$P = \frac{d^2M}{dz^2} \tag{6.2}$$

$$y = \int \left(\int \frac{M}{EI} dz \right) dz \tag{6.3}$$

where y = lateral deflection along the depth of the pile (L); M = bending moment at depth z (FL); EI = flexural modulus of the pile (FL^2); and P = TDA reaction per unit length of the pile (FL^{-1}).

It is important to mention that the computation of *P-y* relationships assumes a perfectly fixed base. Although the piles for all specimens were attached to the lab's strong floor with post-

tensioned rods, a minimum rocking was still expected. In case the *P-y* relationships are calculated with a non-perfectly fixed base, the rocking stiffness of the base shall be calculated. This rocking stiffness was characterized during the preliminary testing. The results indicate that the pile for specimens QS01, QS02, and QS03, has a rocking stiffness of 36.7 kN/rad. The rocking stiffness for the pile in specimen QS04 was found to be 12 kN/rad.

Only the most relevant results from the main testing stage are shown in this report body. The complete time-story records resulting from the main testing stage of all sensors are shown in Appendices A, B, C, and D. It is important to mention that a few strain gauges were categorized as non-reliable, and their measurements were excluded from the analysis. These details are listed in the appendices section. The reasons for these mismeasurements include the intrinsic high sensitivity of strain gauges and the potential effect of TDA particles bypassing the gauge protection system and physically contacting the strain gauge.

It is important to note that a typical practice of the experimental development of the *P-y* curves is to fit the measured bending moments to a curve that follows the expected moment distribution. Polynomial curves are typically used when the load is applied at the top of the pile (Choo and Kim 2016, Khati et al. 2020, Kim et al. 2004, Guo et al. 2014). For simplicity in data analysis, this report considers a horizontal uniformly distributed load applied to the TDA by the moving wall. This load can be assumed to generate a trapezoidal distribution in load on the pile due to the depth-dependent strength and compressibility of the TDA and the minimal deflection of the pile expected at greater depths. The moment distribution of a cantilever element with a trapezoidal distributed load follows an exponential trend along its depth. Therefore, an exponential curve is fitted to the moment distribution at each load step, given as follows:

$$M = ae^{bz} \tag{6.4}$$

where z is the depth and a and b are fitting parameters.

Another important aspect considered during the analysis of results is that the stiffeners and the concrete prism at the base of the piles generated a significant drop of curvature on the first two strain gauge pairs closest to the base. Although the computed moment can be compensated by increasing the moment of inertia at these points, the results suggested that the computed moments were not as reliable. Therefore, the analysis did not include the first two moment data points to

compute the shear and TDA reaction. As the shear force and TDA reaction are derivatives of the moment with respect to the depth, one data point is lost at each differentiation.

The pile response for each specimen is shown in terms of curvature, moment, shear force, TDA reaction, and deflection along the depth of the pile reached maximum total load (sum of the forces of both actuators). The pile bending response analysis for specimen QS01 is shown in Figure 6.1. Specimen QS01 was laterally loaded until reaching a theoretical yield strain which was assumed to occur at 1200 με. During testing a strain gauge reached the tensile yield strain hence the loading protocol was stopped, and then the unloading stage started. Later analysis of the results from QS01 indicate that the pile had not yielded at this strain. Specimen QS02 was laterally loaded until the maximum load capacity of the bottom actuator was reached, which was 245 kN. Then, the unloading stage started. The pile bending response analysis for specimen QS02 is shown in Figure 6.2. The pile bending response analysis for specimen QS03 is shown in Figure 6.3. Specimen QS03 was also laterally loaded until the maximum load capacity of the bottom actuator was reached. In this test, the top actuator kicked back 76 mm when the loading stage finished and disconnected slightly before reaching the max load, so only the loading stage results were considered in the analysis. The pile bending analysis results for specimen QS are shown in Figure 6.4. Specimen QS04 was also laterally loaded until the maximum load capacity of the bottom actuator was reached. Due to the concrete yielding observed during loading, only the loading stage results are considered in the analysis of QS04.

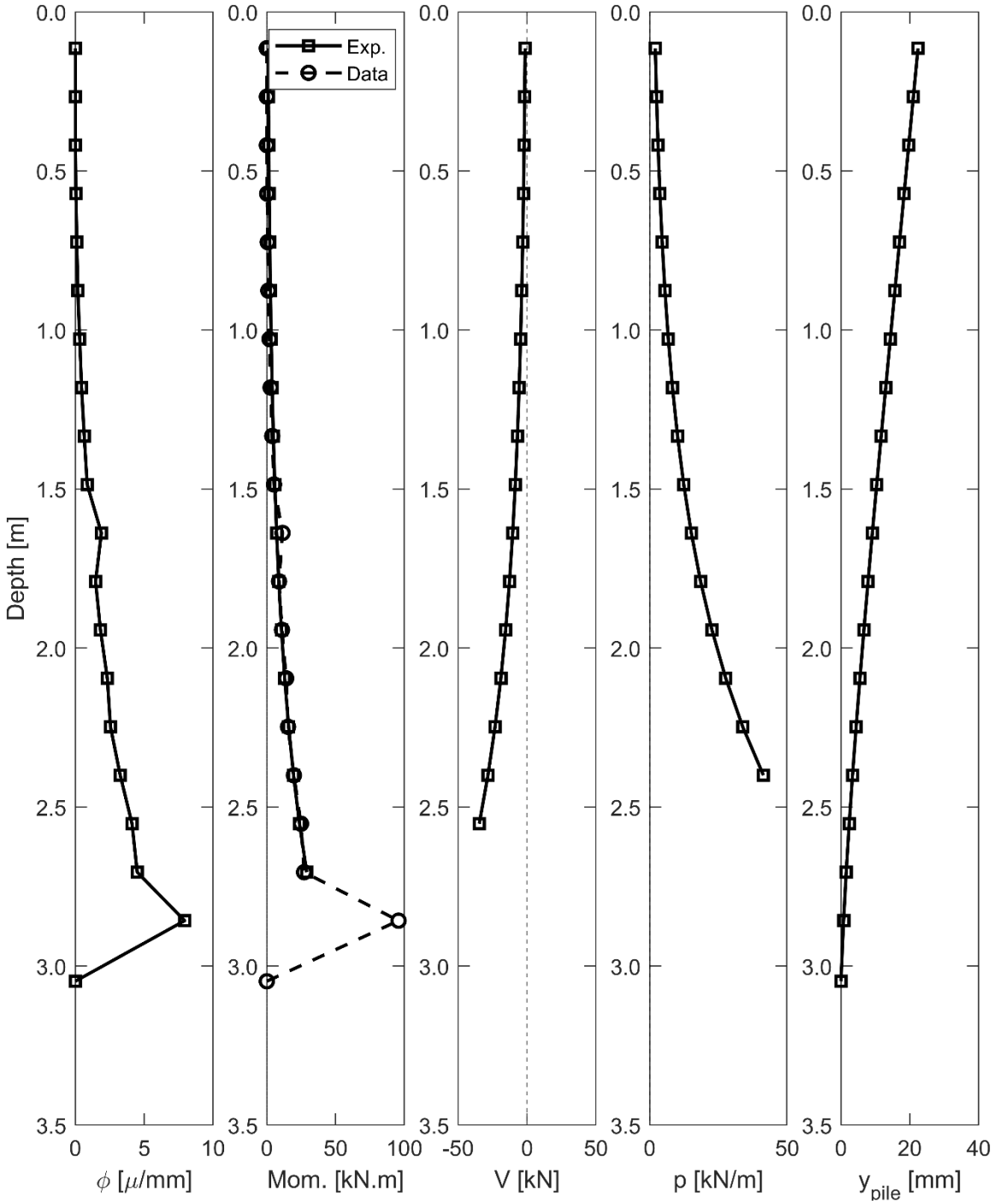

Figure 6.1. QS01 pile response at max total load (Exp. = exponential fit to the moment data).

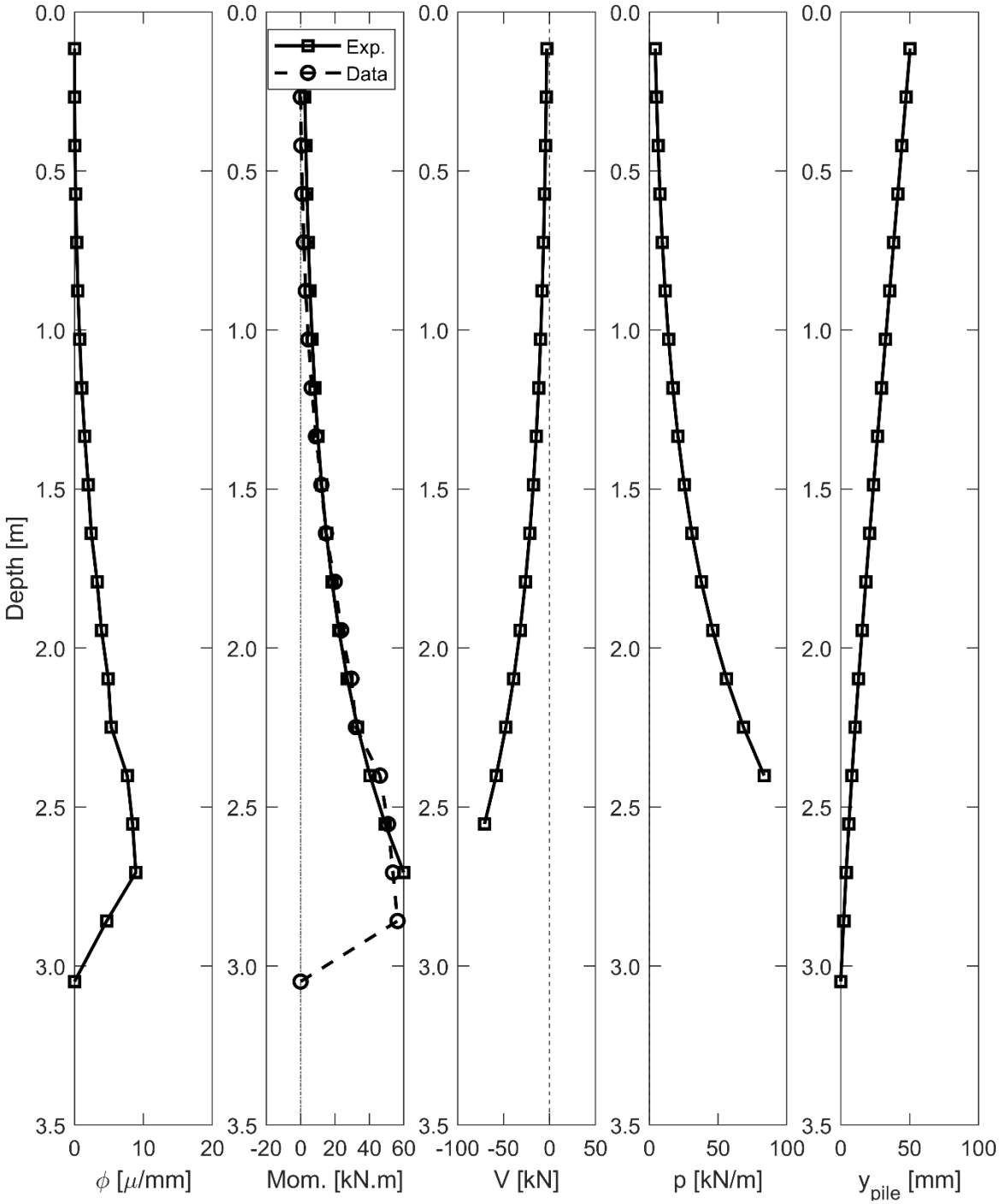

Figure 6.2. QS02 pile response at max total load (Exp. = exponential fit to the moment data).

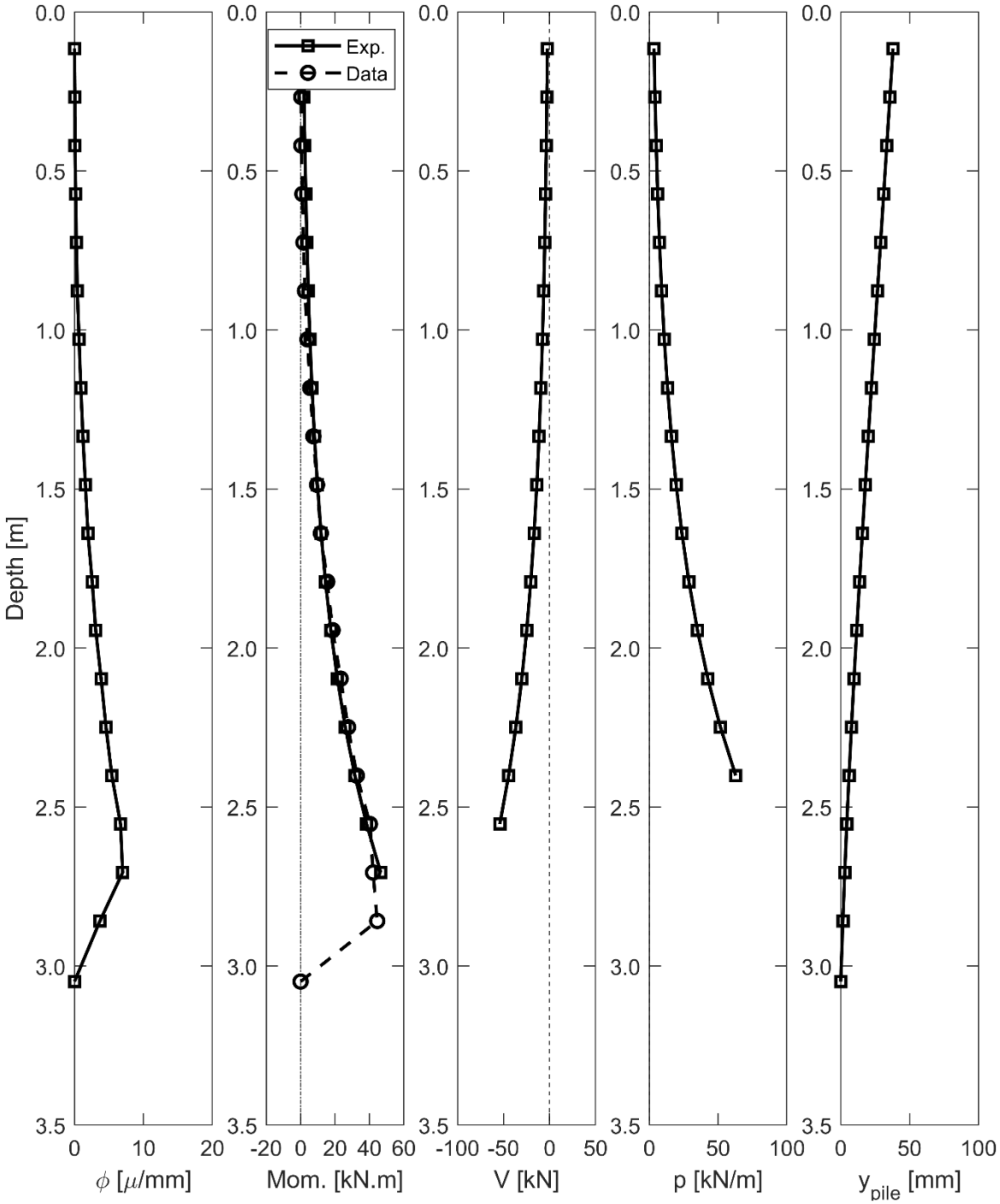

Figure 6.3. QS03 pile response at max total load (Exp. = exponential fit to the moment data).

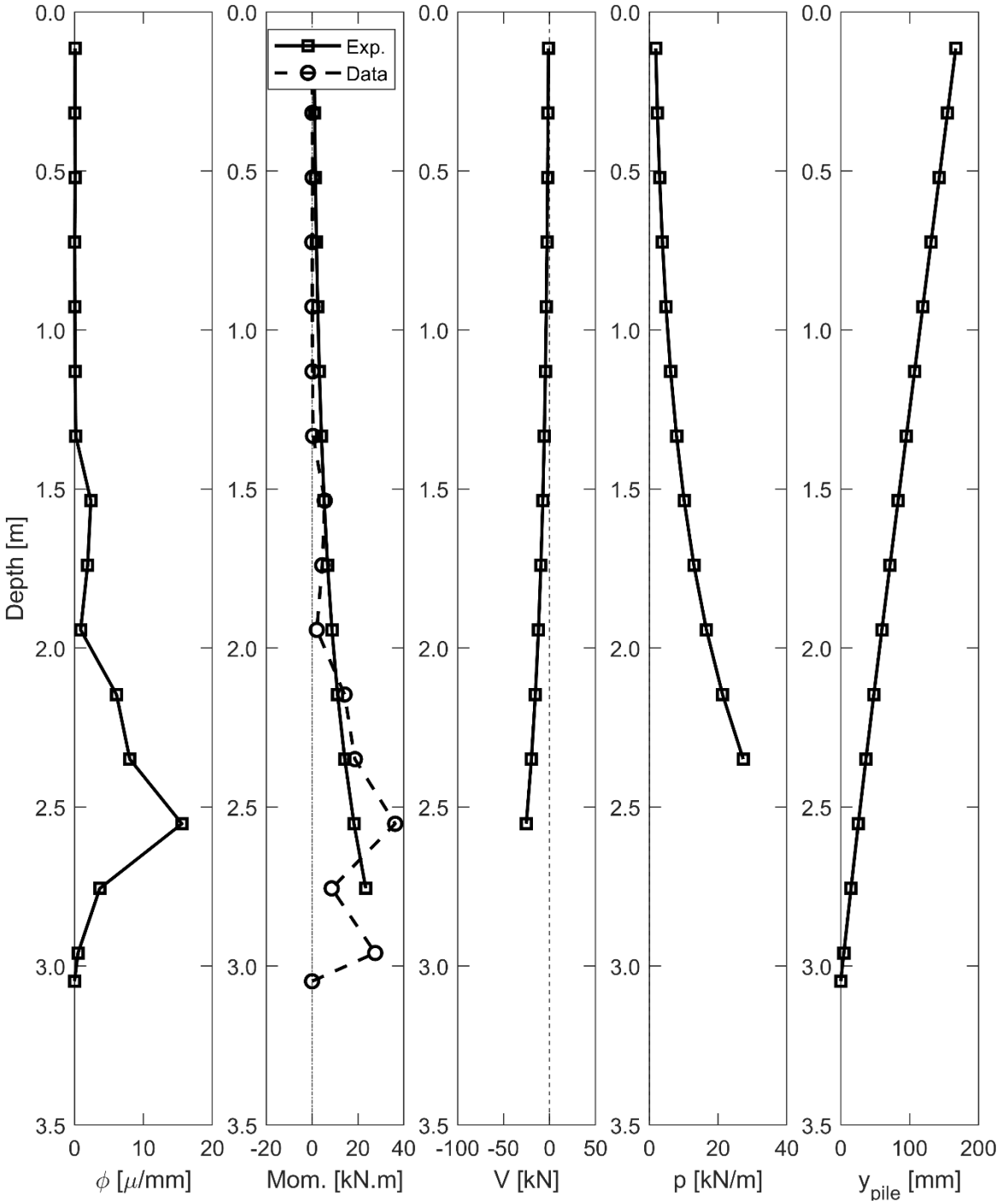

Figure 6.4. QS04 pile response at max total load (Exp. = exponential fit to the moment data).

Overall, the results indicate that the curvature and moment are more predominant at larger depths for all specimens, which is expected for a cantilever element. The results also suggest that the exponential curves successfully capture the measured moment distribution along the pile. The shear force and TDA reaction distributions show an exponential increase along the depth with similar maximum amplitudes. The steel pipe pile did not experience yielding in any of the tests. On the other hand, the reinforced concrete pile experienced two small cracks having a thickness of approximately 0.1 mm above the base rectangular prism, as shown in Figure 6.5. These cracks likely led to the post-peak softening response observed in the plot of pile head displacement vs. shear force at the base of the pile in Figure 5.30.

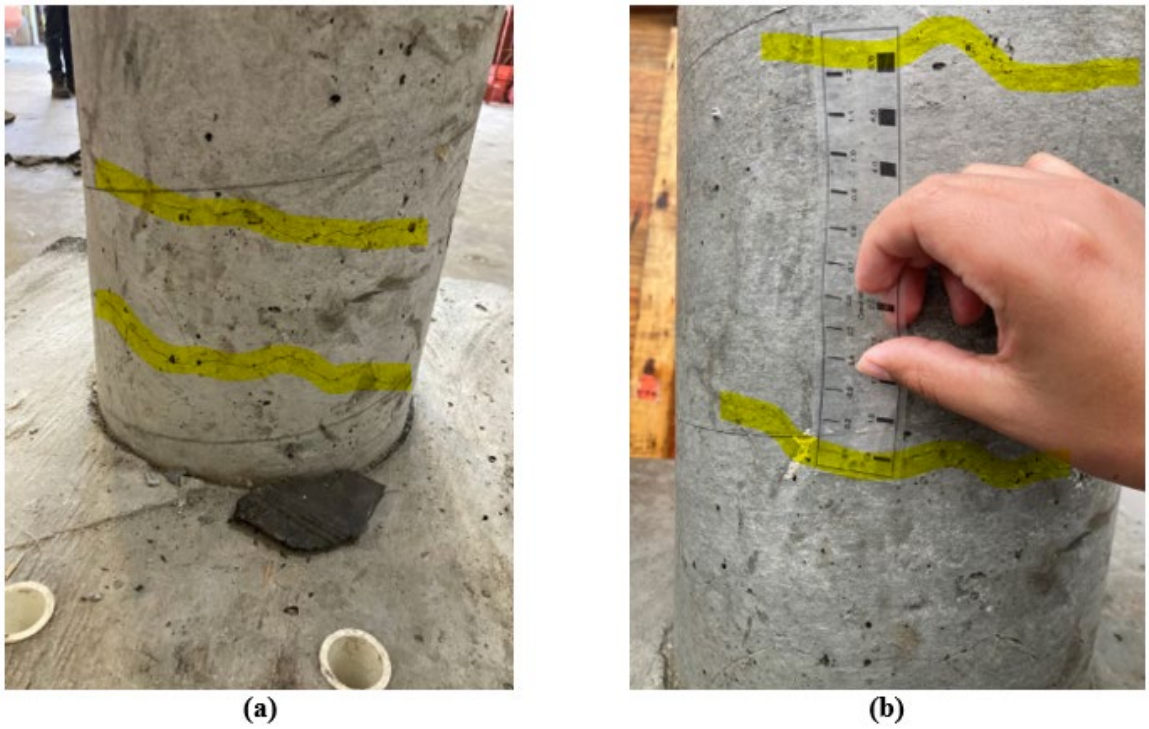

Figure 10Figure 6.5. Cracking of concrete cover of the reinforced concrete pile in Test QS04: (a) General view; (b) Close-up view showing measurement of cracks

A comparison of the maximum pile curvature, moment, shear force, TDA reaction, and deflection for all specimens is shown in Figure 6.6. Regarding the effect of the TDA spacing *S* on the pile response, it was found that the smaller the spacing *S*, the larger the bending moment, shear force, TDA reaction, and larger pile deflection was achieved. This relationship could indicate that the increase in spacing generates a larger portion of the induced horizontal stresses to be taken by

the TDA and a lower portion by the pile itself. This finding suggests that the larger the spacing of TDA, the lesser stress will affect the pile.

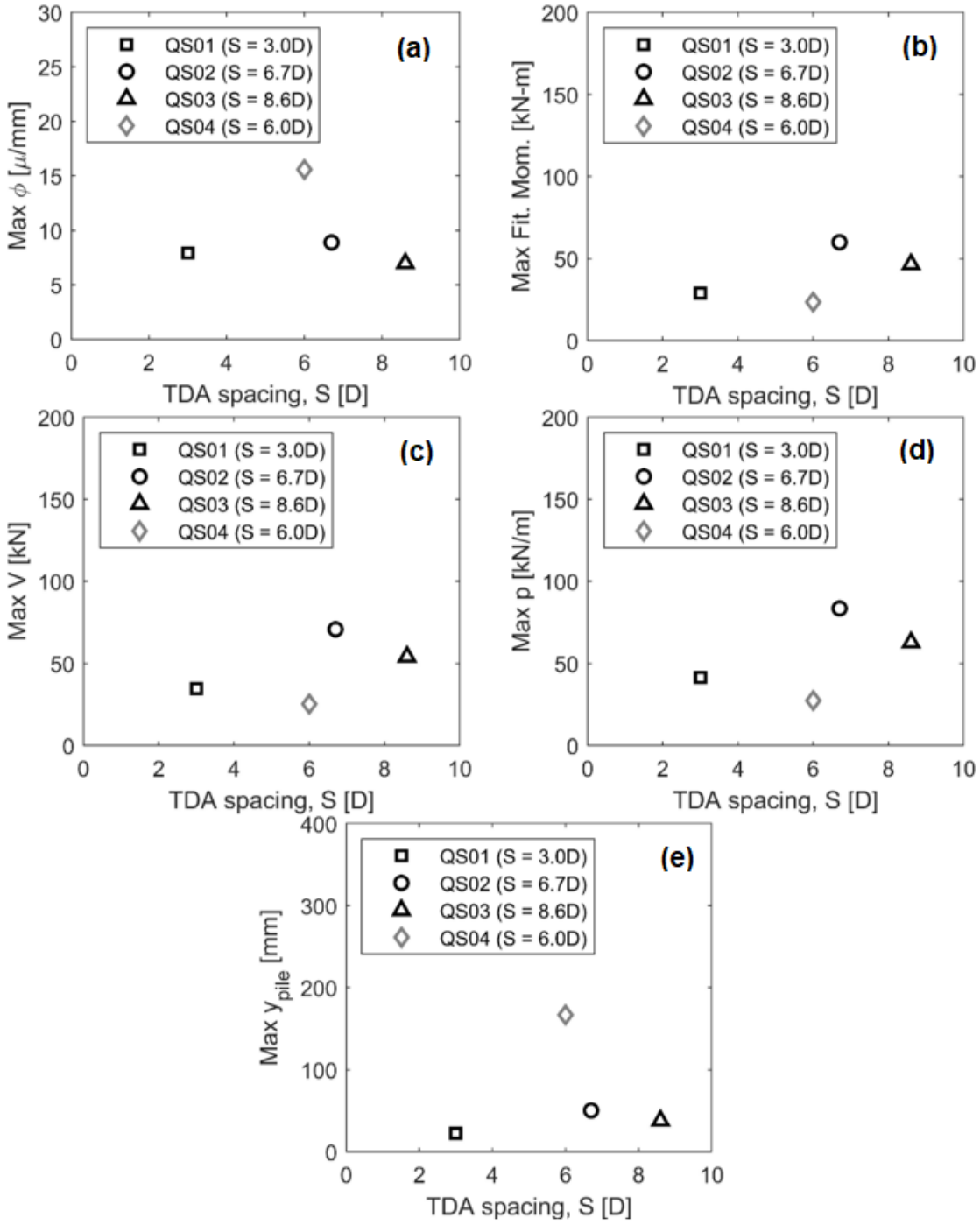

Figure 6.6. Analysis of max pile response parameters for all specimens, (a) Maximum curvature, (b) Maximum moment, (c) Maximum shear, (d) Maximum TDA reaction, and (e) Maximum displacement.

Regarding the pile type effect, the curvature and deflection experienced by the reinforced concrete pile (Specimen QS04) was 77% and 245% larger than the steel pile with the most similar TDA spacing (Specimen QS02), respectively. The moment was estimated considering a bending stiffness (*EI*) of 2,326 kN.m^2 and 6,032 kN.m^2 for the reinforced concrete and the steel pile, respectively. The estimation results indicate that the reinforced concrete experienced lower moments, shear forced, and TDA reaction than the steel pile. These results suggest that the reinforced concrete pile is more flexible than the steel piles. This response is supported by the theory that flexible elements undergo larger deflection but attract lower shear forces and moments.

***P-y* relationships**

The pile response analysis was the first step before the development of the *P-y* relationships. The next step was to characterize the response of the moving wall displacements using the string potentiometers SP01, SP02, SP03, and SP04, and the measurements from both actuators. In the tests on Specimens QS01 and QS02, it was observed the moving wall behaved rigidly in the vertical direction but experienced a deflection of around 100 mm on the sides in the horizontal direction. Therefore, due to the proximity to the pile, only the displacement measurements of the actuators located at the center of the moving wall were used for computing the displacement of the wall y_{wall} that was used in the computation of the *P-y* relationships. The displacement of the TDA *y* was then computed as follows:

$$y = y_{wall} - y_{pile} \tag{6.5}$$

where positive displacement represents shortening and negative, lengthening. The resulting mobilized *P-y* relationships for specimens QS01, QS02, QS03, and QS04, are shown in Figures 6.7, 6.8, 6.9, and 6.10, respectively. The P-y curves shown in these figures were generated for vertical stresses representing different depths within the TDA layers ranging from 0.5 to 12.5 kN/m^2 for the steel pile and from 0.6 to 11.5 kN/m^2 for the reinforced concrete pile. The vertical stresses were calculated considering the average unit weights of each specimen reported in Table 4.1. The unloading-reloading spikes observed in Figures 6.7 and 6.8 were due to periodic stopping of the horizontal loading to check the status of instruments, but these do not affect the overall interpretation of the *P-y* curves. At the end of the loading stage, unloading was only evaluated for Specimens QS01 and QS02 due to issues with the top actuator in Specimen QS03 and yielding of the concrete in Specimen QS04.

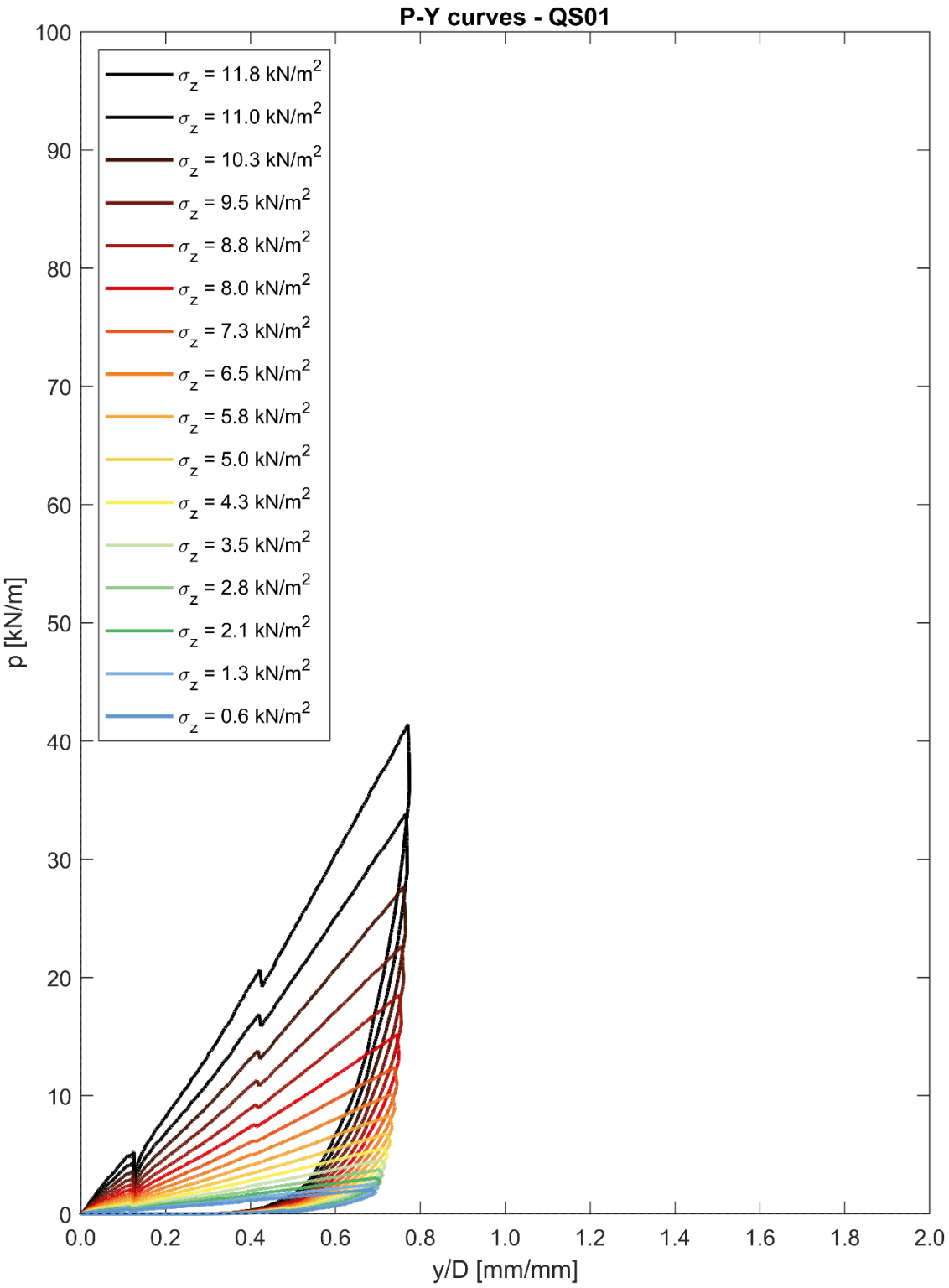

Figure 6.7. Mobilized *P-y* curves from specimen QS01

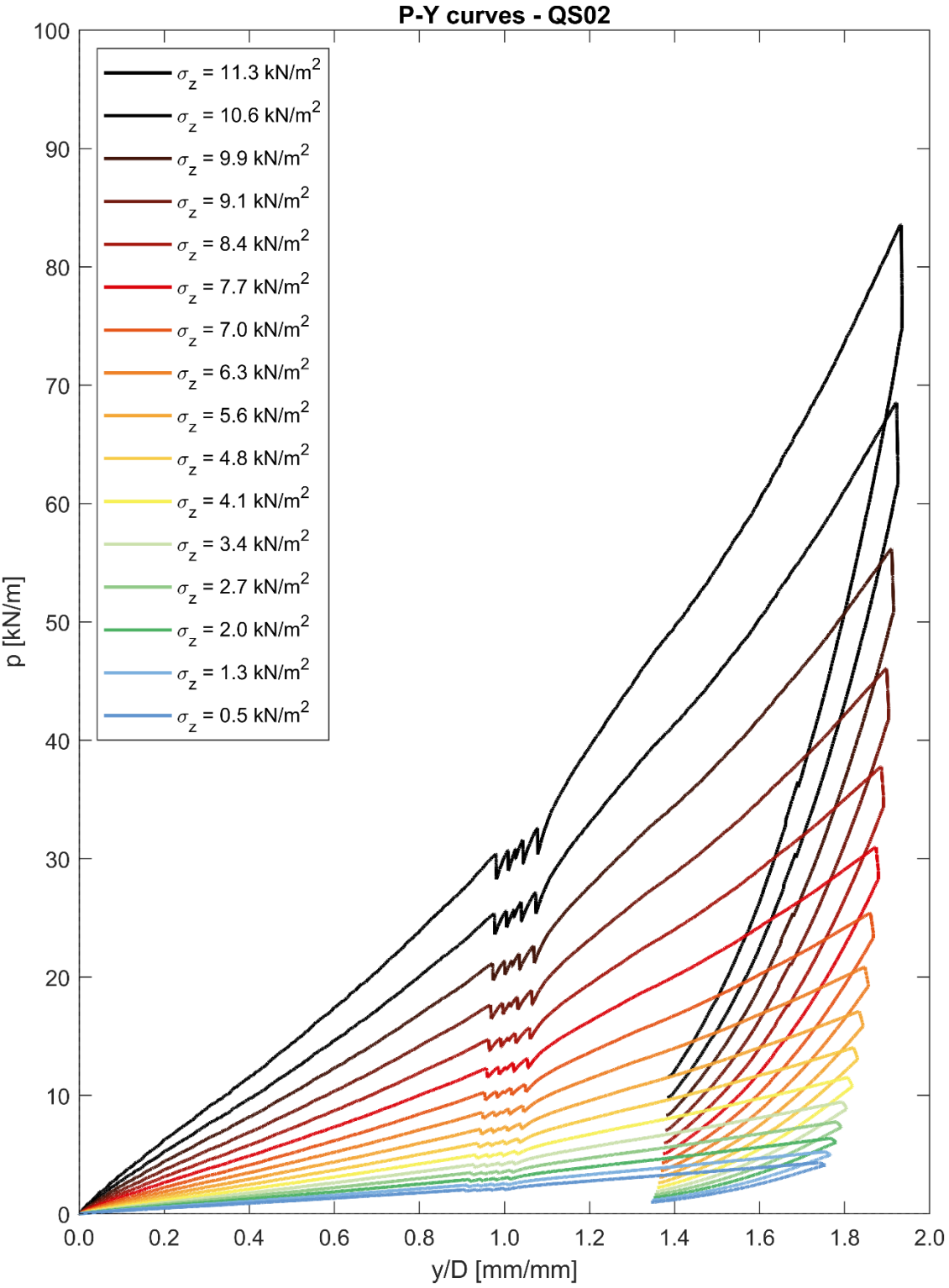

Figure 6.8. Mobilized *P-y* curves from specimen QS02

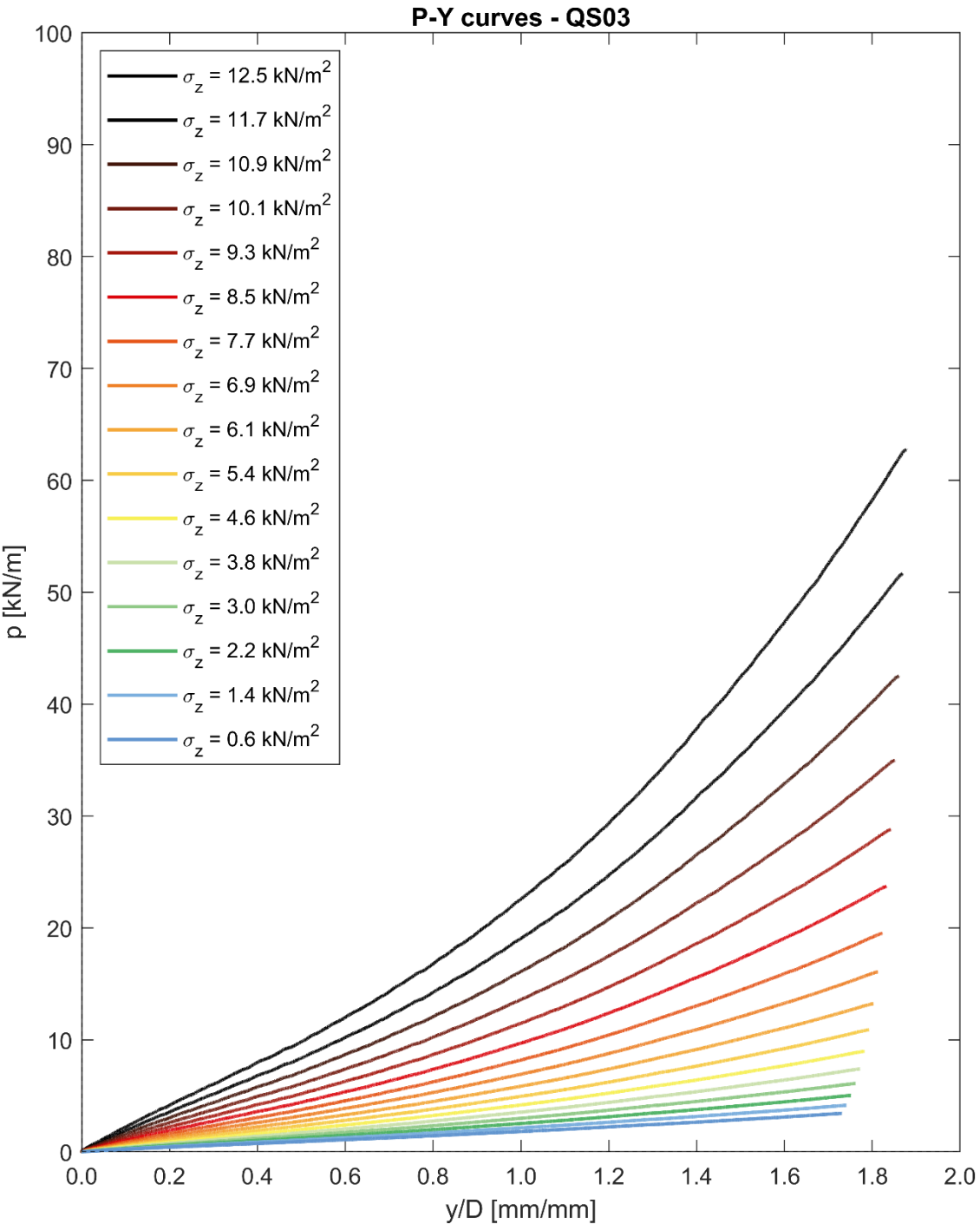

Figure 6.9. Mobilized *P-y* curves from specimen QS03

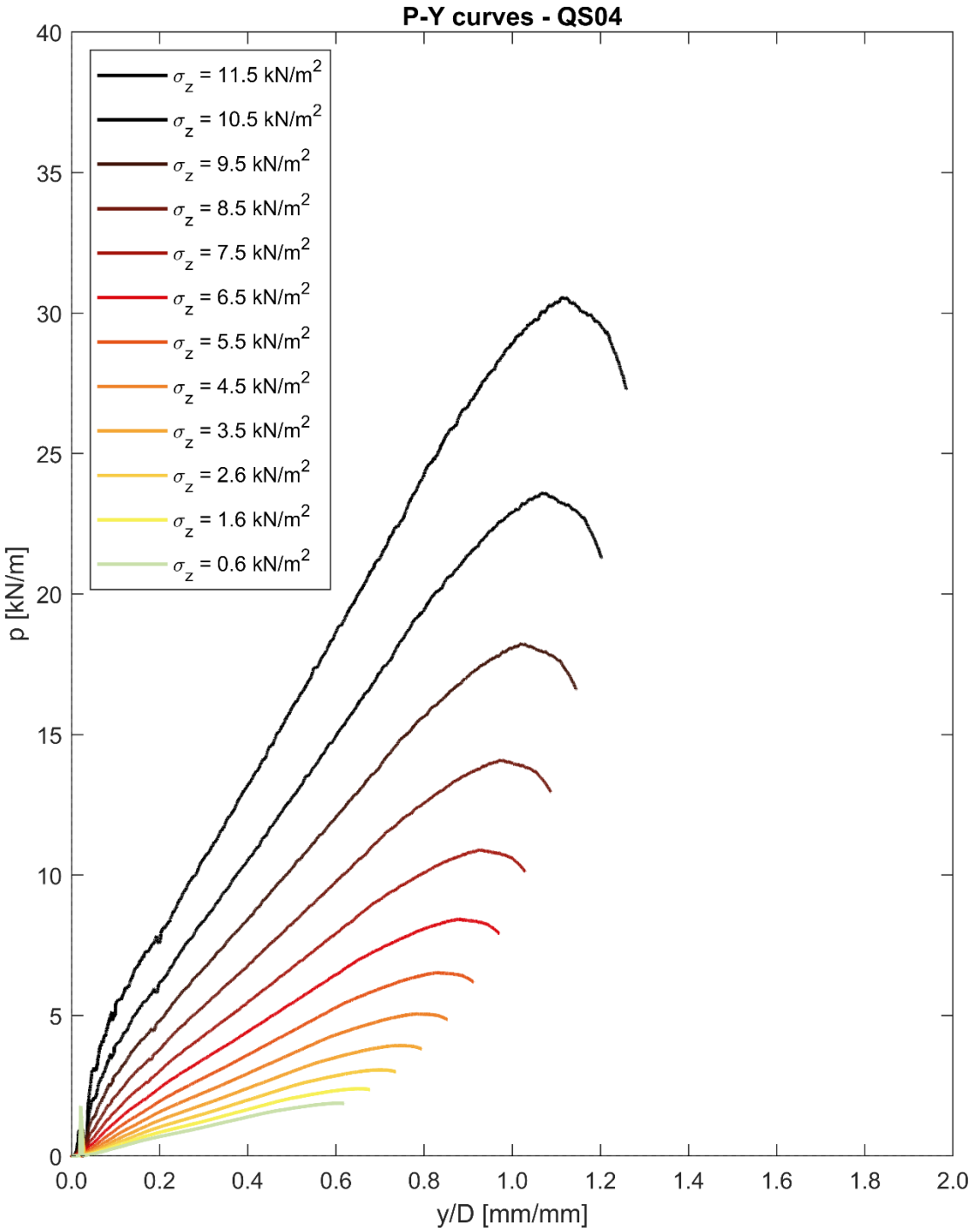

Figure 6.10. Mobilized *P-y* curves from specimen QS04

The computed *P-y* relationships indicate that the higher the vertical stress (or depth within the TDA layer), the higher the TDA reaction and the lower the deflection. The higher TDA reaction at larger depths is partly because the TDA has increasing strength with depth, as expected for

pressure-dependent geomaterials. In addition, the smaller deformations at larger depths are explained by the typical deflected shape of a cantilever pile with more deflection at the top and less deflection at the bottom. The *P-y* relationships for the steel piles indicate a strengthening trend of the pile reaction with the increase of TDA deformation that is concave upwards in some situations. This trend is common in high void ratio materials like TDA, as observed by Yarahuaman and McCartney (2023). Stress densifies the material generating an increase in modulus. The *P-y* relationships for the concrete pile show an overall linear trend before reaching a maximum TDA reaction followed by softening. The softening could be caused by the cracking of the concrete cover discussed in the previous subsection.

Comparing the mobilized *P-y* curves for different vertical stresses for the steel pile in Figures 6.7 to 6.9 with those for the concrete pile in Figure 6.10 indicate that the pile type plays a significant role in the response of TDA under horizontal loads. The variable known as TDA reaction modulus E_{py} is typically used to measure the "stiffness" of the *P-y* curves following the ratio as follows:

$$E_{py} = P/y \tag{6.6}$$

A comparison of the TDA reaction modulus for all specimens as a function of the vertical stress is shown in Figure 6.11. The results in this figure indicate that the TDA reaction modulus versus vertical stress relationship follows an exponential increasing trend for all specimens. This indicates that the head of the pile will experience less induced stress than the base of the pile (due to both the greater strength of the TDA deeper in the layer and the fixed base condition of the pile). Further, it is also observed that the smaller the TDA spacing, the higher the TDA reaction modulus. This relationship indicates that the more TDA between the load application point and the pile, the lesser stress affects the pile. Moreover, the results suggest that the specimen with the reinforced concrete pile generates a lower TDA reaction modulus than the steel pile. Comparing the steel pipe piles with different TDA spacing and considering QS01 as baseline reference (S = 3.0D), it is found that a TDA spacing of S = 6.7D generates the maximum TDA reaction modulus 29% larger than the maximum TDA reaction modulus with a spacing of 3.0D. In addition, the maximum TDA reaction modulus when S = 8.6D is 60% larger than the maximum TDA reaction modulus at S = 3.0D. Comparing the steel pipe pile to the reinforced concrete pile with similar width S = 6.0-6.7D

(specimens QS02 and QS04), it is observed that the use of a steel pipe pile generates a maximum TDA reaction modulus 85% greater than the one using a reinforced concrete pile.

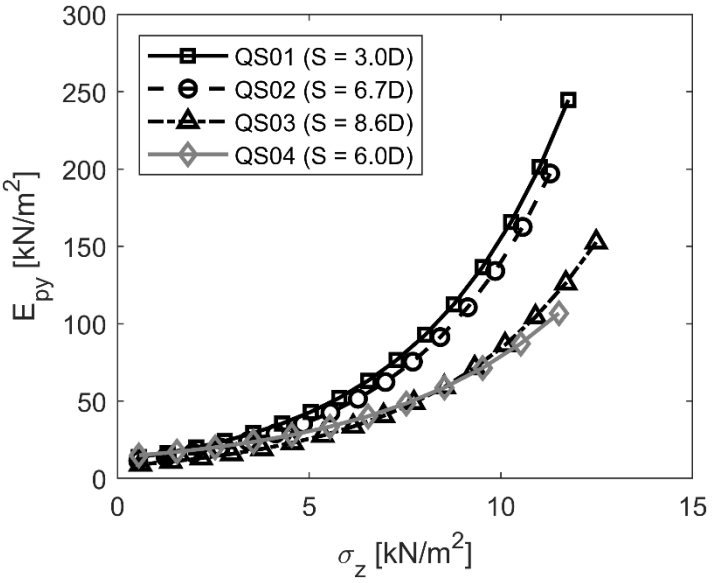

Figure 6.11. Analysis of TDA reaction modulus for all specimens.

Chapter 7 CONCLUSIONS AND OPPORTUNITES FOR FUTURE RESEARCH

The results from this study demonstrate that the layer of TDA installed next to a fixed-base pile will absorb significant horizontal displacements at the pile head location up to nearly 2 pile diameters for the steel pile and the concrete pile without causing yielding, with shear forces induced in the pile being only up to 25% of the applied forces. The TDA layer absorbs the displacements through a combination of compression and surface heaving. Results from the experiments indicated that larger lateral displacements could have been applied in some of the tests. Overall, the tests in this study help to demonstrate the feasibility of using a flexible material like TDA upslope from a bridge foundation system to mitigate the effects of lateral spreading. The *P-y* curves developed in this study for the small-diameter piles may be used for preliminary proof of concept studies to determine the site-specific pile deformation response in response to an expected amount of lateral spreading displacement and TDA layer compression. Future research can integrate the lateral loading analysis enabled by this research into a bridge system analysis that evaluates the magnitude of lateral spreading displacements expected for a given earthquake and the actual dimensions and end restraints of bridge piles. For example, further experimental or numerical analyses are necessary to interpret the effects of the pile diameter and pile toe boundary conditions expected in actual bridge foundation systems on the shape of the *P-y* curve, which can be first calibrated against the experimental results reported in this study.

Additionally, the following specific conclusions can be drawn from this study:

- Under the lateral loads applied to the TDA and transmitted to the pile, the steel pipe pile having an exterior diameter of 203 mm was found to experience less deflection and curvature but more bending moment and shear force than the reinforced concrete pile with a diameter of 254 mm.
- Regarding the effect of the TDA width *S* between the point on load application point and the pile, it was observed that the smaller the TDA width *S*, the larger the demands on the pile in terms of curvature, bending moment, shear force, and deflection. This relationship indicates that larger TDA widths *S* contribute to a larger portion of the horizontal stresses to be sustained by the TDA and a lesser portion by the pile itself. Nonetheless, all the TDA widths investigated in this study have positive effects on the pile response considering the applied horizontal displacements to the TDA layer.

- The developed *P-y* relationships show an overall non-linear response for all specimens. The specimens with steel pipe piles showed a slight strengthening trend, which is common for high void ratio materials such as TDA. The specimen with the reinforced concrete pile showed a linear trend until reaching its peak where some softening occurred presumably due to the cracking of the concrete cover. In summary, the results suggest that when the more rigid the pile is, the TDA response dominates a greater portion of the *P-y* relationship.
- The TDA reaction modulus E_{py} is a variable used to quantify the "stiffness" of the *P-y* relationships. It was found that the TDA reaction modulus increases exponentially with the increase of vertical stresses on the TDA. This means that the *P-y* relationship will be stiffer at larger depths.
- The TDA spacing between the point of the lateral load applications and the pile generated has a significant influence on the *P-y* curves which can be quantified by comparing the TDA reaction modulus. The smaller the spacing of the TDA layer, the larger the TDA reaction modulus will develop on the pile, and vice versa. Larger TDA layer spacings are recommended in practice which will not result in significant financial implications due to the low cost of the recycled TDA material.
- The effect of the pile type also has a significant impact on the *P-y* relationships which was quantified by comparing specimens QS02 and QS04. The specimen with the steel pipe pile generated a TDA reaction modulus that was 85% greater than the specimen with the reinforced concrete pile at the maximum vertical stresses tested in this project.
- This project applied a quasi-static lateral load to all testing specimens in only the north to south direction. After unloading, a residual gap of approximately 100 mm was observed between the pile head and the TDA in the north direction. This gap could affect the compression response of the TDA in case a reverse load was applied to the pile in the south to north direction. Therefore, the extrapolation of these results in cyclic loading applications should be conducted very carefully and may require further experiments. However, lateral spreading events are expected to correspond to a monotonic downslope compression response.

Chapter 8 REFERENCES

Ahmed, I. (1993). Laboratory Study on Properties of Rubber Soils. Report No. FHWA/IN/JHRP-93/4, Purdue University, West Lafayette, Indiana.

Ahmed, I. and Lovell, C.W. (1993). "Rubber soils as lightweight geomaterials." Transportation Research Record. 1422, 61-70.

Ahn, I., Cheng, L., Fox, P.J., Wright, J., Patenaude, S., and Fujii, B. (2014). "Material properties of large-size tire derived aggregate for civil engineering applications." Journal of Materials in Civil Engineering, DOI: 10.1061/(ASCE)MT.1943-5533.0001225, 04014258.

American Society for Testing and Materials. (2011). ASTM D3080: Standard Test Method for Direct Shear Test of Soils under Consolidated Drained Conditions. ASTM International, West Conshohocken, PA.

American Society for Testing and Materials. (2019). ASTM C136 / C136M-19: Standard Test Method for Sieve Analysis of Fine and Coarse Aggregates. ASTM International, West Conshohocken, PA.

Arduino, P., Ashford, S., Assimaki, D., Bray, J., Eldridge, T., Frost, D., Hashash, Y., Hutchinson, T., Johnson, L., Kelson, K. and Kayen, R. (2010). "Geo-engineering reconnaissance of the 2010 Maule, Chile earthquake." GEER Association Report No. GEER-022, 1.

Arroyo, M., San Martin, I., Olivella, S. and Saaltink, M.W. (2011). "Evaluation of self-combustion risk in tire-derived aggregate fills." Waste Management. 31(9-10), 2133-2141.

Ashford, S.A., Boulanger, R.W., Brandenberg, S.J. and Shantz, T. (2009). "Overview of Recommended Analysis Procedures for Pile Foundations in Laterally Spreading Ground." In TCLEE 2009: Lifeline Earthquake Engineering in a Multihazard Environment, 1-8.

Ashford, S.A., Boulanger, R.W. and Brandenberg, S.J. (2011). "Recommended design practice for pile foundations in laterally spreading ground." Pacific Earthquake Engineering Research Center. University of California, Berkeley, Calif. PEER Rep, (2011/04).

Aygün, B., Dueñas-Osorio, L., Padgett, J.E. and DesRoches, R. (2010). "Efficient longitudinal seismic fragility assessment of a multispan continuous steel bridge on liquefiable soils." Journal of Bridge Engineering, 16(1), 93-107.

Bernal, A., Salgado, R., Swan Jr., R.H. and Lovell, C.W. (1997). "Interaction between tire shreds, rubber-sand and geosynthetics." Geosynthetics International. 4(6), 623-643.

Berrill, J.B., Christensen, S.A., Keenan, R.P., Okada, W. and Pettinga, J.R. (2001). "Case study of lateral spreading forces on a piled foundation." Geotechnique, 51(6), 501-517.

Bosscher, P.J., Edil, T.B., and Eldin, N. (1993). "Construction and performance of shredded waste tire test embankment." Transportation Research Record. 1345, 44-52.

Bosscher, P.J., Edil, T.B., and Kuraoka, S. (1997). "Design of highway embankments using tire chips." Journal of Geotechnical and Geoenvironmental Engineering. 123(4), 295-304.

Boulanger, R.W., Chang, D., Brandenberg, S.J., Armstrong, R.J. and Kutter, B.L. (2007). "Seismic design of pile foundations for liquefaction effects." In Earthquake Geotechnical Engineering, 277-302. Springer, Dordrecht.

Bressette, T. (1984). Used Tire Material as an Alternate Permeable Aggregate. State of California, Department of Transportation, Division of Engineering Services, Office of Transportation Laboratory, Sacramento, CA.

CalRecycle. (2016). Usage Guide: Tire-Derived Aggregate (TDA). Publication # DRRR 2016-01545. California Department of Resources Recycling and Recovery (CalRecycle). Sacramento, CA.

CalRecycle. (2017). Report to the Legislature, Five-Year Plan for the Waste Tire Recycling Management Program (Ninth Edition covering Fiscal Years 2017-2018 to 2021-2022). Publication # DRRR-2017-01610. California Department of Resources Recycling and Recovery (CalRecycle). Sacramento, CA.

CalRecycle. (2019). California Waste Tire Market Report: 2018. Publication # DRRR-2019-1654. California Department of Resources Recycling and Recovery (CalRecycle). Sacramento, CA.

CalRecycle. (2020). California Waste Tire Market Report: 2019. Publication # DRRR-2020-1691. California Department of Resources Recycling and Recovery (CalRecycle). Sacramento, CA.

Cheng, D.X., Zhang, K., Cavender, Z., Giles, M., Thor, J., and Joslin, K. (2021). Tire Derived Aggregate Handbook. 3rd Edition. Report to California Department of Resources Recycling and Recovery.

Choo, Y.W., and Kim, D. (2016). "Experimental development of the *P-y* relationship for large-diameter offshore monopiles in sands: Centrifuge tests". *Journal of Geotechnical and Geoenvironmental Engineering*, 142(1), 04015058.

Cubrinovski, M., Bradley, B., Wotherspoon, L., Green, R., Bray, J., Wood, C., Pender, M., Allen, J., Bradshaw, A., Rix, G. and Taylor, M. (2011). "Geotechnical aspects of the 22 February 2011 Christchurch earthquake." Bulletin of the New Zealand Society for Earthquake Engineering, 44(4), 205-226.

Cubrinovski, M., Winkley, A., Haskell, J., Palermo, A., Wotherspoon, L., Robinson, K., Bradley, B., Brabhaharan, P. and Hughes, M. (2014). "Spreading-induced damage to short-span bridges in Christchurch, New Zealand." Earthquake Spectra, 30(1), 57-83.

Dickson, T.H., Dwyer, D.F., Humphrey, D.N. (2001). "Prototype tire-shred embankment construction." Transportation Research Record, 1755, National Research Council, Transportation Research Board, Washington, D.C. pp. 160-167.

Edil, T.B. and Bosscher, P.J. (1994). "Engineering properties of tire chips and soil mixtures." Geotechnical Testing Journal, 17(4), 453-464.

El-Emam, M., and Bathurst, R.J. (2007). "Influence of reinforcement parameters on the seismic response of reduced-scale reinforced soil retaining walls." Geotextiles and Geomembranes, 25(1), 33-49.

Federal Highway Administration, U.S. Department of Transportation. (1998). User Guidelines for Waste and Byproduct Materials in Pavement Construction. Publication Number: FHWA-RD-97-148.

Feng, Z.Y. and Sutterer, K.G. (2000). "Dynamic properties of granulated rubber/sand mixtures." ASTM Geotechnical Testing Journal. 23(3), 338–344.

Finney, B.A. (2018). Exothermic Behavior of Tire Derived Aggregate Fills Subject to Periodic Wetting with Fresh and Saline Water. California Department of Resources Recycling and Recovery (CalRecycle), Sacramento, CA. In Press.

Finney, B.A. and Maeda, R.K. (2016). Evaluation of Tire Derived Aggregate as a media for Stormwater Treatment. Publication # DRRR-01625. California Department of Resources Recycling and Recovery (CalRecycle), Sacramento, CA.

Foose, G.J., Benson, C.H., and Bosscher, P.J. (1996). "Sand reinforced with shredded waste tires." Journal of Geotechnical Engineering. 122(9), 760-767.

Fox, P.J., Thielmann, S.S., Sanders, M.J., Latham, C., Ghaaowd, I., and McCartney, J.S. (2018). "Large-scale combination direct shear/simple shear device for tire-derived aggregate." ASTM Geotechnical Testing Journal. 41(2), 340-353. DOI: 10.1520/GTJ20160245.

Gebhardt, M.A. (1997). Shear Strength of Shredded Tires as Applied to the Design and Construction of a Shredded Tire Stream Crossing, M*S* Thesis, Iowa State University.

Geisler, E., Cody, W.K., and Niemi, M.K. (1989). "Tires for subgrade support." Annual Conference on Forest Engineering, Coeur D'Alene, ID. 1-5.

Geosyntec. (2008). Guidance Manual for Engineering Uses of Scrap Tires. Prepared for Maryland Department of the Environment. Geosyntec Project No.: ME0012-11.

Ghaaowd, I., McCartney, J.S., Thielmann, S., Sanders, M. and Fox, P.J. (2017). "Shearing behavior of tire derived aggregate with large particle sizes. I: Internal and concrete interface direct shear behavior." *ASCE Journal of Geotechnical and Geoenvironmental Engineering*. 143(10), 04017078.

Ghaaowd, I., Fox, P.J. and McCartney, J.S. (2020). "Shearing behavior of the interfaces between tire derived aggregate and three soil materials." ASCE Journal of Materials in Civil Engineering. 32(6), 04020120.

Guo, F., Lehane, B.M., and Ju, J. (2014). Experimentally derived CPT-based *P-y* curves for soft clay. *In Proceedings of the 3rd International Symposium on Cone Penetration Testing* (pp. 1021-1028).

Hamada, M., Isoyama, R. and Wakamatsu, K. (1996). "Liquefaction-induced ground displacement and its related damage to lifeline facilities." Soils and Foundations, 36(Special), 81-97.

Hoppe, E.J. (1998). "Field study of shredded-tire embankment," Transportation Research Record No. 1619, Transportation Research Board, Washington, DC. 47-54.

Humphrey, D.N. (1996). Investigation of Exothermic Reaction in Tire Shred Fill Located on SR100 in Ilwaco, Washington. Report to Federal Highway Administration, Washington, DC.

Humphrey, D.N. (2008). "Tire derived aggregate as lightweight fill for embankments and retaining walls." Scrap Tire Derived Geomaterials – Opportunities and Challenges. Hazarika and Yasuhara (eds). Taylor and Francis, London. 59-81.

Humphrey, D.N., Whetten, N., Weaver, J., Recker, K., Cosgrove, T.A. (1998). "Tire shreds as lightweight fill for embankments and retaining walls." Prof. Conference on Recycled Materials in Geotechnical Applications. Geotechnical Special Publication (GSP) 79, ASCE, Reston, Virginia. 51-65.

Humphrey, D.N., Sandford, T.C., Cribbs, M.M., Gharegrat, H., and Manion, W.P. (1992). Tire Chips as Lightweight Backfill for Retaining Walls - Phase I. Report to the New England Consortium, 137 pp.

Humphrey, D.N. and Manion, W.P. (1992). "Properties of tire chips for lightweight fill." Grouting, Soil Improvement and Geosynthetics, R.H. Borden, et al., eds., ASCE, Vol. 2, 1344-1355.

Humphrey, D.N. and Nickels, W.L., Jr. (1997). Effect of tire chips as lightweight fill on pavement performance." Proc. 14th International Conference on Soil Mechanics and Foundation Engineering. Vol. 3: 1617-1620. Balkema, Rotterdam.

Humphrey, D.N. and Sandford, T.C. (1993). "Tire chips as lightweight subgrade fill and retaining wall backfill." Symposium on Recovery and Effective Reuse of Discarded Materials and By-products for Construction of Highway Facilities. Denver, Colorado. 1-20.

Humphrey, D., Sandford, T., Cribbs, M., and Manion, W. (1993). "Shear strength and compressibility of tire chips for use as retaining wall backfill." Transportation Research Record. Transportation Research Board, Washington, DC. 1422, 29–35.

Jeremić, B., Putnam, J., Sett, K., Humphrey, D., Patenaude, S. (2004). "Calibration of elastic–plastic material model for tire shreds." GeoTrans 2004. ASCE. 760-767.

Khati, B.S., Sawant, V.A., and Gupta, A. (2020). "Development of *P-y* Curves from Experimental Studies on Piles near Sloping Ground". *Geo-Congress 2020*. Reston, VA: American Society of Civil Engineers. pp 64-72.

Kim, B.T., Kim, N.K., Lee, W.J., and Kim, Y.S. (2004). “Experimental load–transfer curves of laterally loaded piles in Nak-Dong River sand”. *Journal of Geotechnical and Geoenvironmental Engineering*, 130(4), 416-425.

Ledezma, C. and Bray, J.D. (2010). “Probabilistic performance-based procedure to evaluate pile foundations at sites with liquefaction-induced lateral displacement.” Journal of Geotechnical and Geoenvironmental Engineering, 136(3), 464-476.

Ledezma, C., Hutchinson, T., Ashford, S.A., Moss, R., Arduino, P., Bray, J.D., Olson, S., Hashash, Y.M., Verdugo, R., Frost, D. and Kayen, R. (2012). “Effects of ground failure on bridges, roads, and railroads.” Earthquake Spectra, 28(S1), S119-S143.

Lee, J.H., Salgado, R., Bernal, A., and Lovell, C.W. (1999). “Shredded tires and rubber-sand as lightweight backfill.” Journal of Geotechnical and Geoenvironmental Engineering. 125(2), 132–141.

Mahgoub, A. and El Naggar, H. (2019). "Using TDA as an engineered stress-reduction fill over preexisting buried pipes. Journal of Pipeline Systems Engineering and Practice. 10(1): 04018034.

Manion, W.P. and Humphrey, D.N. (1992). “Use of tire shreds as lightweight and conventional embankment fill, Phase I – laboratory.” Technical Paper 9I-I, Technical Services Division, Maine Department of Transportation, Augusta, ME.

Matsuoka, H., Liu, S., Sun, D., and Nishikata, U. (2001). “Development of a new in-situ direct shear test.” Geotechnical Testing Journal. 24(1), 92–102.

McCartney, J.S. (2021). Design of Mechanically Stabilized Tire Derived Aggregate (MSTDA) Retaining Walls. Report DRRR-2023-1717 to CalRecycle. 97 p.

McCartney, J.S., Ghaaowd, I., Fox, P.J., Sanders, M., Thielmann, S., and Sander, A. (2017). “Shearing behavior of tire derived aggregate with large particle sizes. II: Cyclic simple shear behavior.” *ASCE Journal of Geotechnical and Geoenvironmental Engineering*. 143(10), 04017079.

McGann, C.R. and Arduino, P. (2014). “Numerical assessment of three-dimensional foundation pinning effects during lateral spreading at the Mataquito River Bridge.” Journal of Geotechnical and Geoenvironmental Engineering, 140(8), 04014037.

McGann, C. R. and Arduino, P. (2015). “Numerical assessment of the influence of foundation pinning, deck resistance, and 3D site geometry on the response of bridge foundations to demands of liquefaction-induced lateral soil deformation.” Soil Dynamics and Earthquake Engineering, 79, 379-390.

McGann, C.R. (2020). “Parametric Assessment of Equivalent Static Procedure Accounting for Foundation-Pinning Effects in Analysis of Piled Bridge Abutments Subject to Lateral Spreading.” Journal of Geotechnical and Geoenvironmental Engineering, 146(7), 04020055.

Qiu, Z., Lu, J., Ebeido, A., Parayancode, A., Elgamal, A., and Martin, G.R. (2023). Analysis of Lateral Spreading Effects on Bridge Foundations. Final Report Submitted to the California Department of Transportation (Caltrans) under Contract No. 65A0548.

Qiu, Z., Ebeido, A., Almutairi, A., Lu, J., Elgamal, A., Shing, P.B. and Martin, G. (2020). “Aspects of bridge-ground seismic response and liquefaction-induced deformations.” Earthquake Engineering & Structural Dynamics, 49(4), 375-393.

Seed, R.B., Dickenson, S.E., Riemer, M.F., Bray, J.D., Sitar, N., Mitchell, J.K., Idriss, I.M., Kayen, R.E., Kropp, A., Harder, Jr. L.F. and Power, M.S. (1990). “Preliminary report on the principal geotechnical aspects of the October 17, 1989 Loma Prieta earthquake,” Report No. UCB/EERC-90/05, UC Berkeley, Berkeley, CA.

Shin, H., Arduino, P., Kramer, S.L. and Mackie, K. (2008). “Seismic response of a typical highway bridge in liquefiable soil.” In Geotechnical Earthquake Engineering and Soil Dynamics IV, 1-11.

Skempton, A.W. (1961). “Effective stress in soils, concrete, and rocks.” Pore Pressure and Suction in Soils. Butterworths, London. 4-16.

Stark, T.D., Reddy, K.R. and Marella, A. (2010). “Beneficial use of shredded tires as drainage material in cover systems for abandoned landfills.” Journal of Hazardous, Toxic, and Radioactive Waste Management. 14(1), 47-60.

Strenk, P.M., Wartman, J., Grubb, D.G., Humphrey, D.N., and Natale, M.F. (2007). “Variability and scale-dependency of tire-derived aggregate.” Journal of Materials in Civil Engineering. 19(3), 233–241.

Tandon, V., Velazco, D.A., Nazarian, S., and Picornell, M. (2007). “Performance monitoring of embankments containing tire chips: Case study.” Journal of Performance of Constructed Facilities. 21(3), 207–214.

Terzaghi, K. and Peck, R.B. (1948). Soil Mechanics in Engineering Practice. John Wiley.

Tokimatsu, K. and Asaka, Y. (1998). “Effects of liquefaction-induced ground displacements on pile performance in the 1995 Hyogoken-Nambu earthquake.” Soils and Foundations, 38(Special), 163-177.

Turner, B., Brandenberg, S.J. and Stewart, J.P. (2013). “Evaluation of collapse and non-collapse of parallel bridges affected by liquefaction and lateral spreading,” Proc. 10th International Conf. on Urban Earthquake Engin., Center for Urban Earthquake Engineering, March 1-2, 2013, Tokyo Institute of Technology, Tokyo, Japan.

Turner, B.J., Brandenberg, S.J. and Stewart, J.P. (2016). “Case study of parallel bridges affected by liquefaction and lateral spreading.” Journal of Geotechnical and Geoenvironmental Engineering, 142(7), 05016001.

Tweedie, J.J., Humphrey, D.N., and Sandford, T.C. (1998a). “Full scale field trials of tire shreds as lightweight retaining wall backfill, at-rest conditions.” Transportation Research Record. 1619, 64-71.

Tweedie, J.J., Humphrey, D.N., and Sandford, T.C. (1998b). “Tire shreds as retaining wall backfill, active conditions.” Journal of Geotechnical and Geoenvironmental Engineering. 124(11), 1061-1070.

USTMA. (2020). 2019 U.S. Scrap Tire Management Summary. U.S. Tire Manufacturers Association. Washington, D.C.

Verdugo, R., Sitar, N., Frost, J.D., Bray, J.D., Candia, G., Eldridge, T., Hashash, Y., Olson, S.M. and Urzua, A. (2012) “Seismic performance of earth structures during the February 2010 Maule, Chile, earthquake: dams, levees, tailings dams, and retaining walls.” Earthquake Spectra, 28(S1), S75-S96.

Wotherspoon, L., Bradshaw, A., Green, R., Wood, C., Palermo, A., Cubrinovski, M. and Bradley, B. (2011). “Performance of bridges during the 2010 Darfield and 2011 Christchurch earthquakes.” Seismological Research Letters, 82(6), 950-964.

Wright, J. (2015). Cost Benefit Assessment: Evaluation of Tire-Derived Aggregate Against Alternate Fill Options for Civil Engineering Applications. CalRecycle. June 2015.

Wu, W.Y., Benda, C.C. and Cauley, R.F. (1997). "Triaxial determination of shear strength of tire chips." Journal of Geotechnical and Geoenvironmental Engineering. 123(5), 479-482.

Wu, P.K., Matsushima, K., and Tatsuoka, F. (2007). "Effects of specimen size and some other factors on the strength and deformation of granular soil in direct shear tests." Geotechnical Testing Journal. 31(1), 1- 20.

Xiao, M., Bowen, J., Graham, M., and Larralde, J. (2012). "Comparison of seismic responses of geosynthetically-reinforced walls with tire-derived aggregates and granular backfills." Journal of Materials in Civil Engineering. 24(11), 1368-1377.

Xiao, M., Ledezma, M., and Hartman, C. (2013a). "Shear resistance of tire-derived aggregate using large-scale direct shear tests. Journal of Materials in Civil Engineering. 04014110-1-8.

Xiao, M., Bowen, J., Ghraham, M., and Larralde, J. (2013b). "Comparison of seismic responses of geosynthetically reinforced walls with tire-derived aggregates and granular backfills." Journal of Geotechnical and Geoenvironmental Engineering. 24(11), 1368-1377.

Xiao, Y., Nan, B., McCartney, J.S., and Liu, H. (2019). "Thermal conductivity of sand-tire shred mixtures." ASCE Journal of Geotechnical and Geoenvironmental Engineering. 145(11), 06019012.

Yang, S., Lohnes, R.A., and Kjartanson, B.H. (2002). "Mechanical properties of shredded tires." Geotechnical Testing Journal. 25(1), 44-52.

Yarahuaman, A. and McCartney, J.S. (2023). "Large-scale testing of the static one-dimensional compression response of tire-derived aggregate." *GeoCongress 2023*. Los Angeles, CA. Mar. 26-29. GSP 341. ASCE, Reston, VA. 593-603.

Yarahuaman, A., and McCartney, J.S. (2024). "Large-scale seismic response testing of shallow foundations embedded in tire-derived aggregate for geotechnical seismic isolation." Soil Dynamics and Earthquake Engineering. 177, 108417. DOI: 10.1016/j.soildyn.2023.108417.

Youd, T.L. (1993). “Liquefaction-induced damage to bridges.” Transportation Research Record, 1411, 35-41.

Zhang, Y., Conte, J.P., Yang, Z., Elgamal, A., Bielak, J. and Acero, G. (2008). “Two-dimensional nonlinear earthquake response analysis of a bridge-foundation-ground system.” Earthquake Spectra, 24(2), 343-386.